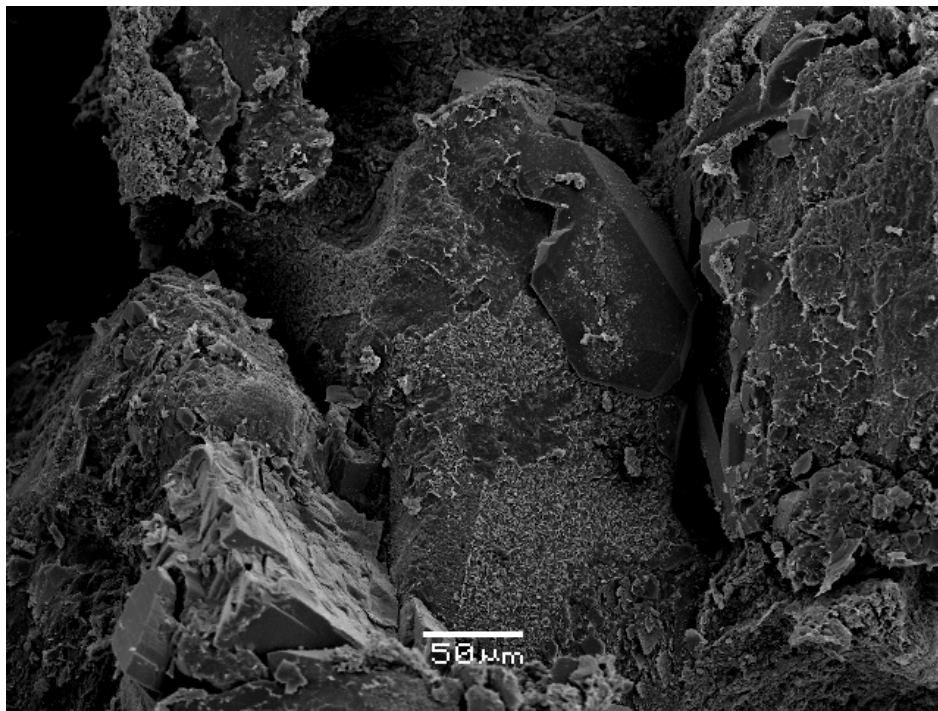


Master Thesis in Geosciences

Diagenesis and reservoir quality of Triassic sandstones in the Central Graben, Norwegian sector

A mineralogical, petrographical and petrophysical approach

Anders Wold Skovli



UNIVERSITY OF OSLO

FACULTY OF MATHEMATICS AND NATURAL SCIENCES

Diagenesis and reservoir quality of Triassic sandstones in the Central Graben, Norwegian sector

A mineralogical, petrographical and petrophysical approach

Anders Wold Skovli



Master Thesis in Geosciences

Discipline: Petroleum Geology and Petroleum Geophysics

Department of Geosciences

Faculty of Mathematics and Natural Sciences

UNIVERSITY OF OSLO

01.06.10

© **Anders Wold Skovli, 2010**

Tutor(s): **Jens Jahren (UiO) and Brit Thyberg (UiO)**

This work is published digitally through DUO – Digitale Utgivelser ved UiO

<http://www.duo.uio.no>

It is also catalogued in BIBSYS (<http://www.bibsys.no/english>)

All rights reserved. No part of this publication may be reproduced or transmitted, in any form or by any means, without permission.

Keywords: Diagenesis; Reservoir quality; Central Graben; Grain-coating chlorite; XRD

Acknowledgements

I would like to thank my supervisors Associate Professor Jens Jahren and Dr. Brit Thyberg for always being supportive and available during this master thesis and making me become more interested in working with reservoir geology. I also appreciate Phd Student Tom Erik Maast for encouraging discussions and for providing me with important data for this thesis.

A special thanks to Professor Knut Bjørlykke for aiding me in the sandstone petrology world and for constructive discussions and valuable feedbacks.

I would also like to thank Tom McKie, Professor Johan Petter Nystuen, Associate Professor Dag Karlsen, Claus Beyer, Knut Pederstad for stimulating discussions regarding the Triassic in the North Sea.

I would like to acknowledge (Berit Løken Berg, Muriel Marie Laure Erambert, Turid Winje and Mofak Naoroz) for technical assistance during my XRD and SEM analysis. A special thanks to Berit Løken Berg for always being available for technical questions regarding XRD analysis and to Dr. Ray Ferrel for technical feedback regarding XRD interpretation. I would also thank Phd Student Binyam Lema Alemu for introducing me to sample preparation of XRD and Professor Henning Dypvik and Dr. Elin Kalleson for assistance during taking picture of the thin sections. I also appreciate the support of Dr Michel Heeremans for help setting up Petrel and Petromod and also thanks to Professor Leiv Gelius for letting me use the program Hampson Russel.

Special thanks go also to Marit Sørli and Kristin Rangnes staffs at the library of Department of Geoscience. They have been very service-minded during this study.

Lunch breaks and endless coffee breaks will be missed with everyone from room 214. Special thanks to my fellow students Eirik Hjelseth, Maren Kleven and Jonas Enoksen for social and scientific discussions.

Big thanks for the patience and support from my family and their attempt to improve my work. A special thanks to my little sister, Nina Wold Skovli, for always being motivating and supportive.

University of Oslo
01.06.2010

Anders Wold Skovli

Abstract

This study examines the diagenesis and reservoir quality of Triassic sandstones in the Central Graben, Norwegian sector. Cored reservoir intervals from four wells (6/3-1, 7/8-4, 7/11-8, 7/11-9) have been examined by petrophysical- (wire line logs, cross plots), petrographical- (SEM-BSE, SEM-SEI) and mineralogical analysis (XRD, modal analysis).

The sandstones are fine grained moderately sorted subrounded to subangular with an average subarkosic composition ($Q_{85}F_{11}R_4$). A wide range of diagenetic minerals has been identified: quartz, chlorite, smectite, kaolin, illite, dolomite, calcite, ankerite and pyrite.

Intergranular volume – quartz cement relationships have been used to predict the effect of grain size, grain shape, compaction (mechanical and chemical) and grain coating on compaction. An increase of 7% average quartz cement in sandstones between well 6/3-1 (2,9 – 3.1 km) and 7/8-4 (4,1 km) is caused by the temperature difference of about 40°C. Kaolin is found in the shallow well (6/3-1). Kaolin could also have been present in the deeper wells (7/8-4, 7/11-9, 7/11-8) but may have been dissolved and replaced by illite. More quartz cement is found in very fine grained sandstones than in medium grained sandstones, which is related to higher surface area for quartz cementation.

Early carbonate cement common and may be an important fluid flow barrier. Mapping the distribution of carbonate cement was done by comparing XRD data together with petrophysical data and interpreting log responses. The distribution of carbonate cement is facies dependant within floodplain associated facies with most likely pedogenic origin. Authigenic iron rich chlorite occurs as both pore-filling and grain coats. High porosities are found in sandstone with minor amount of chlorite typical of grain coating chlorite, thus grain coating chlorite has most likely prevented precipitation of quartz overgrowths. Authigenic illite reduces the permeability by pore-bridging. Morphological evidence suggests smectite to be the precursor of both chlorite and illite. Authigenic kaolin in the Upper Triassic channel associated facies indicates leaching due to meteoric water flow in permeable rocks. Presence of detrital kaolin in combination with authigenic kaolin suggests a more humid climate towards the end of Triassic and into the Jurassic.

Table of Contents

ACKNOWLEDGEMENTS.....	5
ABSTRACT.....	6
1. INTRODUCTION	10
1.1 INTRODUCTION.....	11
1.2 PURPOSE AND METHODS	11
1.3 STUDY AREA	12
2. GEOLOGICAL FRAMEWORK.....	13
2.1 INTRODUCTION.....	14
2.2 STRUCTURAL SETTING.....	16
2.3 LITHOSTRATIGRAPHIC SETTING	19
2.3.1 <i>Sequence stratigraphic setting</i>	20
2.4 TRIASSIC DEPOSITIONAL SYSTEM.....	21
2.5 PALAEOGEOGRAPHY	22
2.5.1 <i>Palaeoclimate in the Triassic</i>	23
3. METHODS AND MATERIALS.....	25
3.1 WELL INFORMATION AND DATA SET	26
3.1.1 <i>Well 6/3-1</i>	26
3.1.2 <i>Well 7/8-4</i>	27
3.1.3 <i>Well 7/11-8</i>	28
3.1.4 <i>Well 7/11-9</i>	28
3.2 WIRE LINE LOGGING	29
3.3 XRD	31

3.3.1	<i>XRD Bulk analysis</i>	33
3.3.2	<i>XRD Clay fraction analysis</i>	34
3.3.3	<i>Volume percentage or XRD percentage</i>	35
3.4	SEM.....	36
3.4.1	<i>Elemental analysis on pore-coating clay material</i>	36
3.5	THIN SECTION.....	37
3.5.1	<i>Point counting</i>	38
3.5.2	<i>Intergranular Volume</i>	38
3.6	UNCERTAINTIES.....	39
3.6.1	<i>XRD uncertainties</i>	39
3.6.2	<i>Thin section uncertainties</i>	39
3.6.3	<i>Petrophysics</i>	40
4.	MINERALOGICAL AND PETROGRAPHICAL DESCRIPTION	41
4.1	INTRODUCTION.....	42
4.2	THIN SECTION ANALYSIS.....	42
4.2.2	<i>Point counting</i>	46
4.2.3	<i>IGV</i>	48
4.2.4	<i>Importance of sorting</i>	48
4.3	XRD.....	51
4.3.1	<i>XRD Bulk</i>	51
4.3.2	<i>XRD Clay fraction</i>	55
4.3.3	<i>Fe content of chlorite from XRD diffractogram</i>	59
4.4	COMBINING XRD AND THIN SECTION DATA.....	59

4.5	SEM.....	63
4.5.1	<i>Secondary Electron Image (SEI).....</i>	63
4.5.2	<i>Backscattered Electron Image (BSI).....</i>	68
4.5.3	<i>Fe content of Chlorite by SEM-SEI.....</i>	73
5.	PETROPHYSICAL DATA.....	74
5.1	INTRODUCTION.....	75
5.2	WIRE LINE LOG.....	75
5.2.1	<i>Log quality.....</i>	75
6.2.2	<i>Cross plots.....</i>	<i>Error! Bookmark not defined.</i>
6.	DISCUSSION.....	87
6.1	CLAY MINERALS.....	88
6.1.1	<i>Kaolin.....</i>	88
6.1.2	<i>Illite.....</i>	91
6.1.3	<i>Chlorite.....</i>	94
6.2	CARBONATE CEMENTATION	98
6.3	QUARTZ CEMENTATION.....	102
6.4	IGV.....	105
7.	CONCLUSION.....	108
8.	REFERENCES	110
	APPENDIX.....	118

1. Introduction

1.1 Introduction

This thesis will investigate reservoir quality and diagenesis ultimately linked to facies and provenance (Bjørlykke 2010) and physical properties related to Triassic sandstones within the Central Graben in the North Sea. Special emphasis will be on mineralogical composition in the Skagerrak Formation. Skagerrak Formation is a proven reservoir with abnormal high porosities (e.g Beryl/Nevis and Judy fields (Goldsmith et al. 2003)).

The Reservoir quality for reservoir rocks changes all the time during diagenesis and predictions regarding reservoir quality are needed prior to drilling (Bjørlykke 1998). Predictions for the effect of mechanical compaction can be based on experiments, but the chemical processes influencing diagenesis are harder to predict (Bjørlykke et al. 1989, Bloch and Helmold 1995, Lander and Walderhaug 1999). The present day subsiding basins can be seen upon as a laboratory and data can be provided by core material and mineralogical analysis of the rock. Changes in porosity and permeability can only be predicted if the processes that influence these parameters are understood (Bjørlykke 1999).

1.2 Purpose and methods

The main purpose of this thesis is to characterize the cored reservoir interval in well 6/3-1, 7/8-4, 7/11-9 and 7/11-8 in the Central Graben. Most of the attention will be given to well 6/3-1 due to the higher amount of data available. The focus of this work is to understand the controlling factors for reservoir development and mineralogical composition distribution and understand how compaction affects rocks physical properties in natural occurring sediments. Distribution and the source of clay minerals will be investigated and related to facies and palaeoclimate. The thesis will also investigate the variation of the intergranular volume (IGV) and relate it to clastic diagenesis and reservoir quality.

Following methods will be used:

- Mineralogical and petrographical analysis (thin sections, SEM, XRD)
- Petrophysical evaluation (wire-line logs)

1.3 Study area

The study area is located in the Central Graben within the North Sea in block 6/3, 7/8 and 7/11 (Figure 1-1). Both block 6/3 and 7/8 are part of Jæren High, that is situated in the complex area where the Central Graben, the Ling Depression, The South Viking Graben and the Witch Ground Graben converge (Figure 1-1). The Jæren High is a eastward-tilted fault block at base Zechstein level (Høiland et al. 1993). Block 7/11 is located in the Cod Terrace (Figure 1-1), that has been heavily affected by the Triassic salt tectonics (Gowers et al. 1993).

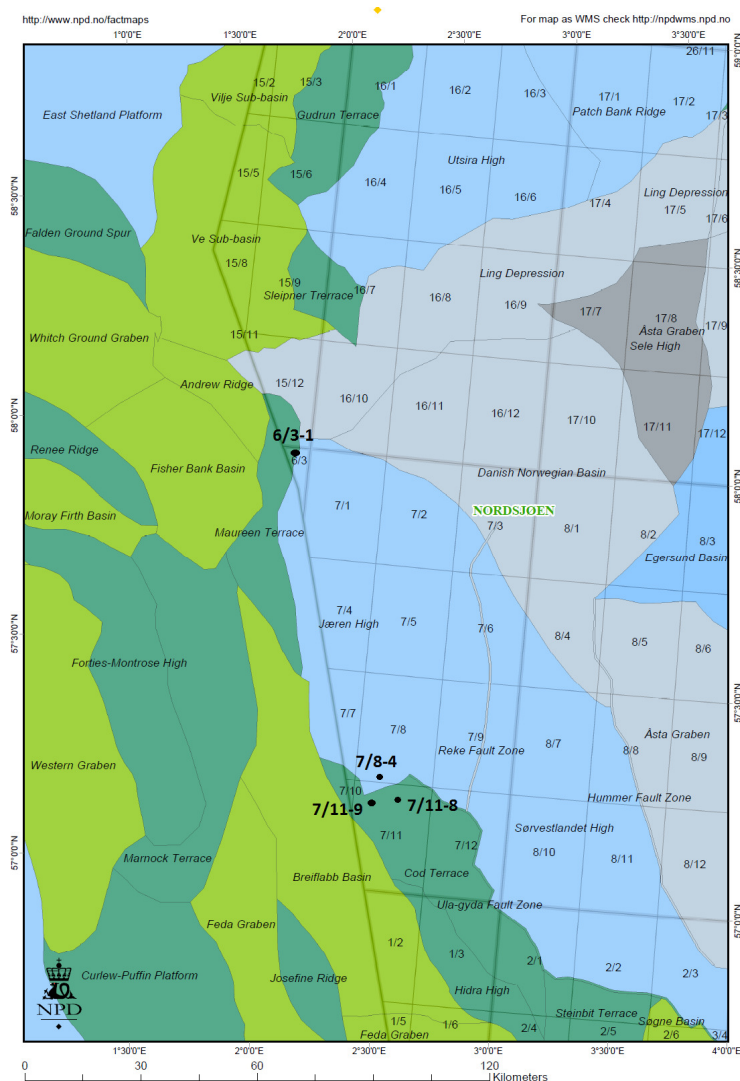


Figure 1-1. Structural element map of the study area (Block 6/3, 7/8 and 7-11). Black dots indicate well locations. Map modified from (NPD 2010)

2. Geological framework

2.1 Introduction

This chapter will focus on the geological framework regarding the Central Graben that is located in the middle and southern part of the North Sea (Figure 2-1).

The Norwegian Central Trough was first defined as a structural element by Rønnevik et al. (1975). The official nomenclature used to describe the study area is ‘Central Trough’, although ‘Central Graben’ has become more accepted as a loosely defined area of extensional faulting (Gowers et al. 1993). In this thesis the expression ‘Central Graben’ will be used to describe the study area.

The North Sea basin has a prolonged extensional history that began in the Devonian with extension of the Caledonian crust. Later Permo-Triassic and Jurassic – Early Cretaceous rifting events together with thermal subsidence contributed to the generation of the sedimentary basins seen in the North Sea (Ziegler 1975, Sclater and Christie 1980, Ziegler 1980, Ziegler and Van Hoorn 1989, Ziegler 1990, Bartholomew et al. 1993, Glennie 1998, Erratt et al. 1999, Zanella and Coward 2003). The structures seen in the North Sea basin is mainly a function of the Jurassic – Early Cretaceous rifting event. Deformation of the North Sea basin continued in Late Cretaceous – Cenozoic due to tectonic inversion and a period of uplift in the Cenozoic (Zanella and Coward 2003).

For an extensive review regarding petroleum geology of the North Sea the author recommend the Millennium Atlas (Evans et al. (2003) and references therein) and the Petroleum geology of the North Sea (Glennie (1998) and references therein).

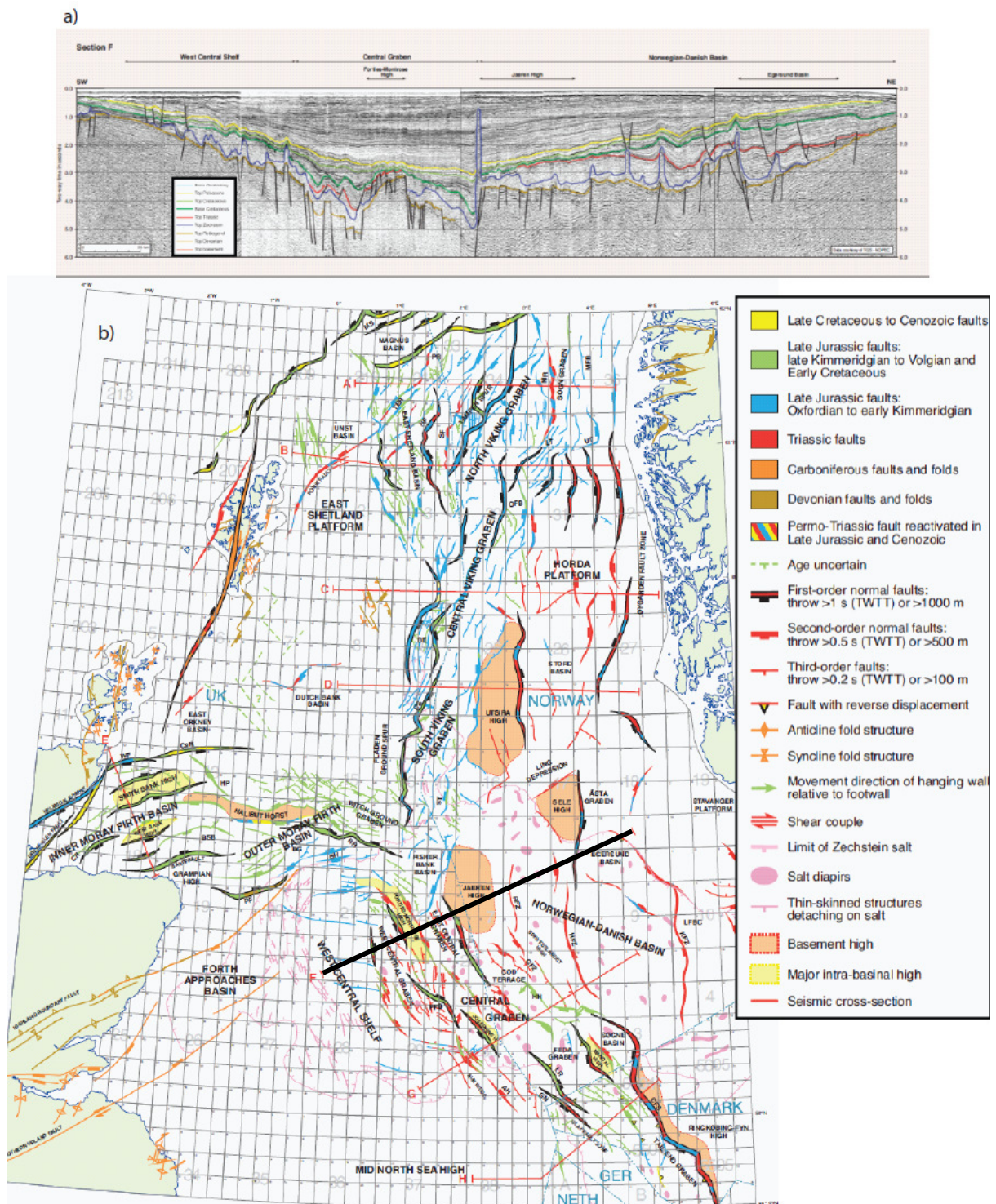


Figure 2-1. a) Regional seismic cross section F (see black line in b) for location of the seismic cross section) displaying the characteristic halokinetic deformation within the Central Graben by movement of the Zechstein salt b) Structural framework of the North Sea modified after Zanella and Coward (2003)

2.2 Structural setting

The Central Graben belongs to the southern arm of the triple junction Viking Graben, the Central Graben and the Moray Firth basins (Figure 2-1). In contrast to the Viking Graben and the Moray Firth basins the Central Graben is more symmetrical in character (Zanella and Coward 2003). The symmetrical character of the basin was used to describe a pure shear model by Mckenzie (1978).

The NW-SE graben system, belonging to the Central Graben, was active during the Mesozoic rifting and subsidence. Several narrow discontinuous structural highs and lows can be seen within the Graben and are characteristic for the UK and the Norwegian sector (Skjerven et al. 1983). Even though the Central Graben is symmetrical it has a complicated tectonic history that involves polyphase tectonics and oblique/strike slip movements and structural inversion (Sears et al. 1993). The reason for its complexity is believed to be caused by interplay of changing extensional kinematic regimes and Palaeozoic structural grain (Erratt et al. 1999). Several models have been made trying to explain the structural framework of the basin with little consensus. This thesis will base the structural framework on work done by Gowers et al. (1993).

According to Gowers et al. (1993) the structural development of the Central Graben (Norwegian sector) can be divided into three main stages:

- 1) Late Turassic to middle Jurassic flexural uplift
- 2) Late Jurassic to early Cretaceous fragmentation
- 3) Late Cretaceous to Tertiary flexural subsidence

Prior to these stages the Central Graben was a part of the Norwegian-Danish basin during the deposition of the Zechstein and the Triassic succession.

The first stage is heavily affected by extensive halokinetic deformation that took place during the Triassic. The halokinetic movements created salt highs/ridges with intervening blocks of Triassic sediments resting on thin salt or on Permian pre-salt sediments (Gowers et al. 1993).

Movement of the salt has been a major factor influencing the distribution of the reservoirs within the Central Graben (Smith et al. 1993). In both Breiflagg basin and the Feda Graben (Figure 1-1) there seem to be less Triassic remaining than in the surrounding area due to erosion related to gentle basin-wide flexuring (Gowers et al. 1993). The Triassic depocentres had been eroded by the middle Jurassic which represents an episode of thermal doming and erosion of the central North Sea area (McKie et al. 2010). The doming was in response of a mantle plume-induced thermal uplift (McKie et al. 2010).

The second stage involves initiation of tectonics specific to the Central Graben. Geometrical analysis of sequences within the Central Graben of Oxfordian to early Volgian age indicate symmetrical subsidence of individual fault blocks with minimal rotation and salt movement. By the beginning of the Volgian faulting became more dominant and individual fault blocks rotated. The rotated fault blocks got eroded on the footwall and deposited on the hangingwall. The rotational tectonics ended in the late Volgian and the following regional subsidence caused drowning of the rotated fault blocks. Renewed subsidence is indicated by the distribution of Lower Cretaceous sediments. It is believed that the subsidence is of syn-depositional age and that the Lower Cretaceous sediments were deposited in a series of basins created by the end of Jurassic. The basins created by early Cretaceous subsidence are partially fault bounded; flexure bounded and has an undisturbed internal configuration. The geometry of the inversion-related structures is related to previously established normal faulting.

The third stage is related to the thermal subsidence (after McKenzie(1978)) in the late Cretaceous due to thermal cooling of the crust. The thermal subsidence is centered in Breiflabb basin but cannot be seen in either Søgne Basin or Tail End Graben (Figure 2-1).

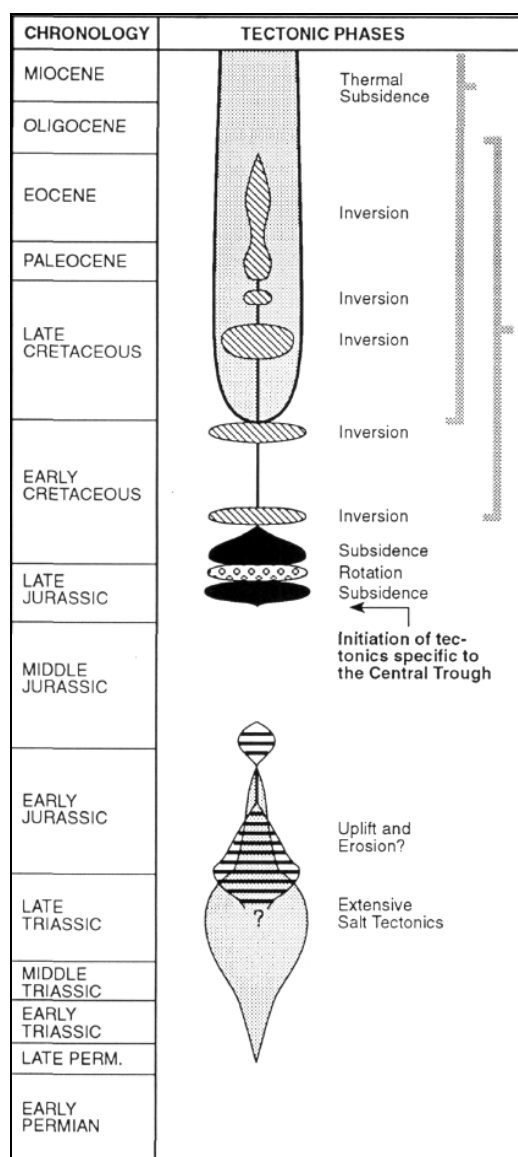


Figure 2-2. Structural evolution describing different tectonic phases observed in the Central Graben (modified from Gowers et al. 1993)

2.3 Lithostratigraphic setting

The Central North Sea has been divided into an informal Triassic group comprising of the Skagerrak Formation and Smith Bank Formation (Deegan and Scull 1977)(Figure 2-3).

The Smith Bank Formation (Figure 2-3) was deposited during Early Triassic to late Triassic and represents a range of distal continental environments where fine grained predominantly fine grained clastics were deposited (Deegan and Scull 1977). The Smith Bank Formation comprises of thick red sequences with a wide density-neutron log (Goldsmith et al. 1995).

The Skagerrak Formation (Figure 2-3) represents thick sandy sequence of fluvial origin deposited in middle to late Triassic (Deegan and Scull 1977). The depositional model for Skagerrak Formation has evolved from braidplain model (Hodgson et al. 1992) to a more diverse type of dryland depositional styles with some cases being wetland environment. The palaeogeographic reconstructions indicate that the fluvial system of the Skagerrak Formation is terminal in character (McKie et al. 2010).

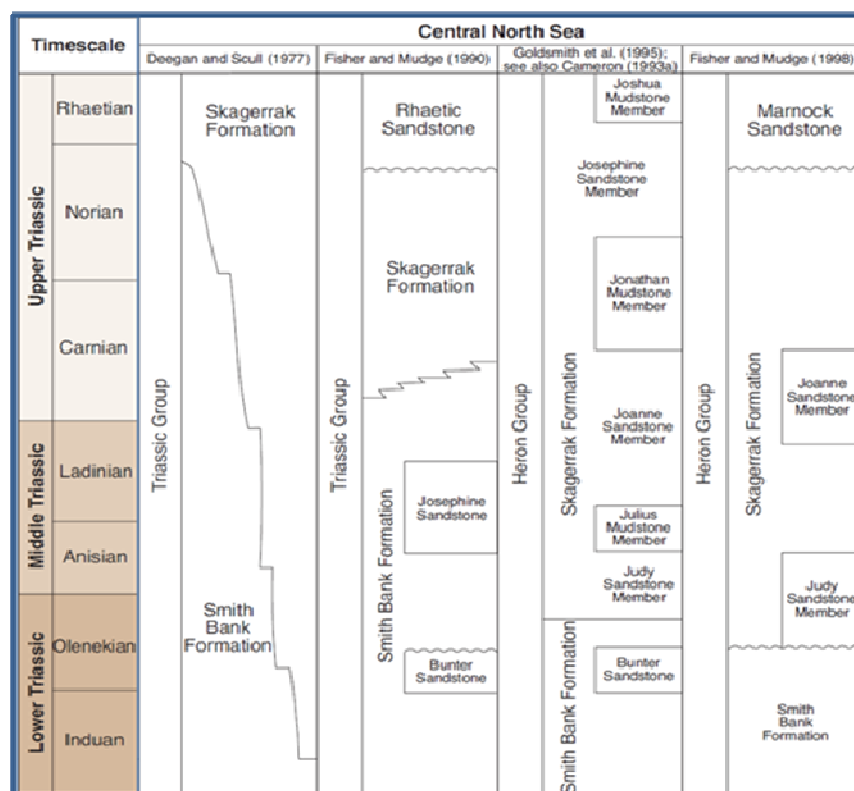


Figure 2-3. Stratigraphic overview of the Triassic in the Central North Sea. The precise chronostratigraphic overview of the formation is uncertain. Modified after Goldsmith et al.(2003)

2.3.1 Sequence stratigraphic setting

A Triassic sequence stratigraphic subdivision for the Central North Sea was proposed by Smith (1993) based on variations in gross depositional setting through time. It was later modified by Goldsmith et al. (2003) which presented a more detailed sequence stratigraphic subdivision. The sequence stratigraphic framework consists of six sequences termed Tr00-Tr50 (Figure 2-4) based on wireline log and lithostratigraphic correlation (Goldsmith et al. 2003).

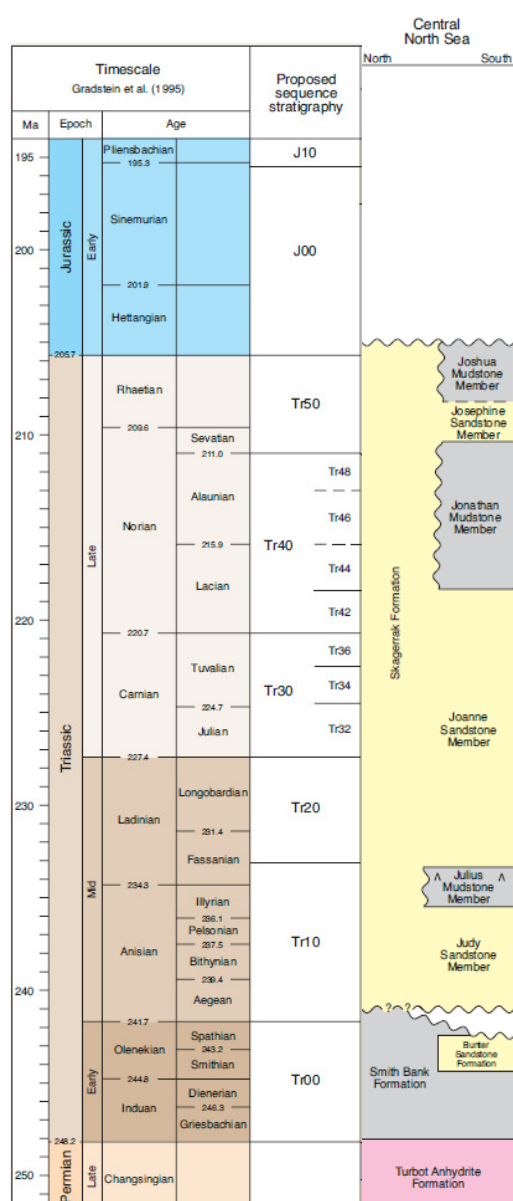


Figure 2-4. Proposed sequence stratigraphy of the Central North Sea by Goldsmith (2003) based on work done by Smith et al.(1993) and Goldsmith et al.(1995) and references therein

2.4 Triassic depositional system

Thick alluvial successions with no apparent marine penetration from the southern North Sea dominate the Triassic deposition in the central North Sea (Goldsmith et al. 2003). The lacking evidence for aeolian activity or evaporite deposition and palynological evidence from shales within Skagerrak Formation indicate episodic wetland conditions (Goldsmith et al. 2003, McKie et al. 2010). Presence of redbeds, calcic and vertic palaeosols, aeolian deposits and evaporites in the surrounding area suggest semi-arid conditions.

The Triassic deposition was controlled by the halokinetic generation of accommodation space initiated by salt movements and salt reduction through surface dissolution. The sediment packages deposited in the synforms is termed pods (Smith et al. 1993). Hodgson et al. (1992) suggest that the Smith Bank Formation was deposited in the topographic lows (within the synforms) and that Skagerrak Formation sheet floods were deposited over and between these salt pods. Reduction of water volume-down fan by evaporation and infiltration and weaker flow strength formed proximal-to-distal facies belts. The proximal facies are associated with the Skagerrak Formation and the distal facies are associated with the Smith Bank Formation (Goldsmith et al. 2003).

Palaeocurrent data in combination with provenance information indicate axial flow to the south east and transverse flow, from Fennoscandian towards the south west probably reflecting the source area to be a combination of both Scottish Highland and Fennoscandian derived streams (McKie and Williams 2009, McKie et al. 2010).

The depositional setting is interpreted by McKie et al. (2010) in the central North Sea area to comprise of ephemeral to intermittent streams in relatively dry climatic setting which formed an endoheric drainage into basinal playa and marshes (Figure 2-5). Individual drainage systems cannot be identified due to insufficient stratigraphic resolution.

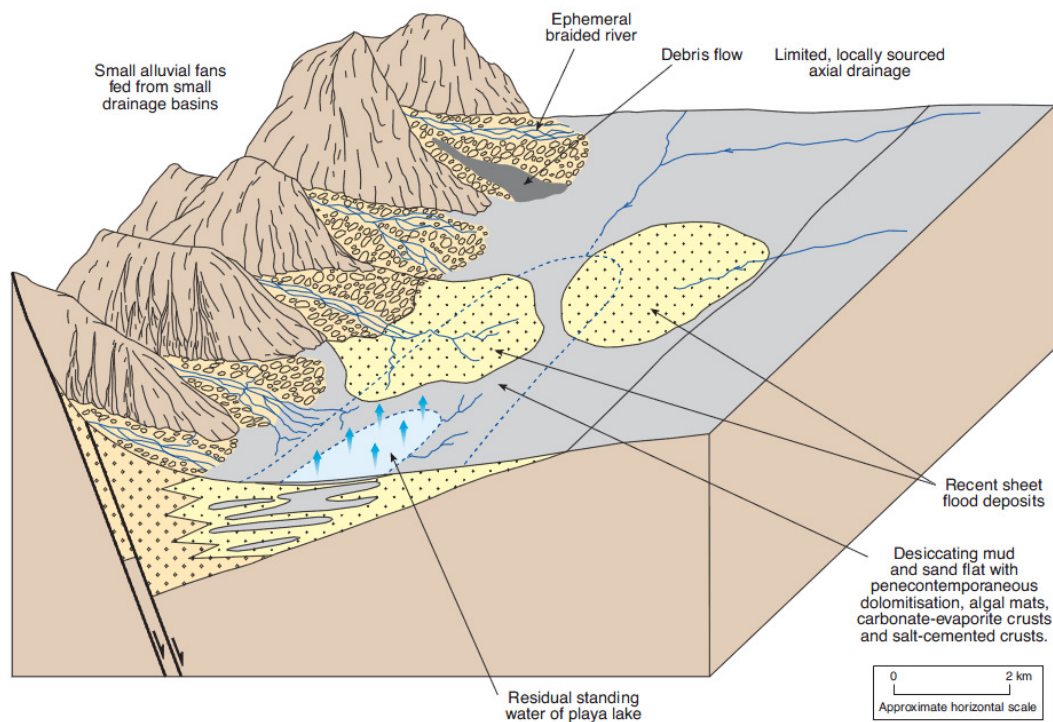


Figure 2-5. Simplified depositional system of Early Triassic (Pers. Comm. Johan Petter Nystuen, March 2010) (Marshall and Hewett 2003)

2.5 Palaeogeography

During the Triassic all land masses were gathered into the supercontinent called Pangea with the surrounding Indo-Pacific Ocean extending from 85°N to 90°S, symmetrical from the equator (Ziegler 1990). Palaeomagnetic data suggested that the European plate drifted northwards where the central part moved from a subtropical to moderate palaeolatitudes. Rough estimates suggest movement of 25° to the north and anticlockwise rotation of 30° during the Triassic (Feist-Burkhardt et al. 2008).

Systematic trends in the dispersal of sandy fluvial detritus across NW Europe has been mapped as broad facies belts and represented as regional trends (Figure 2-6). Notice that there is no marine influence in the study area.

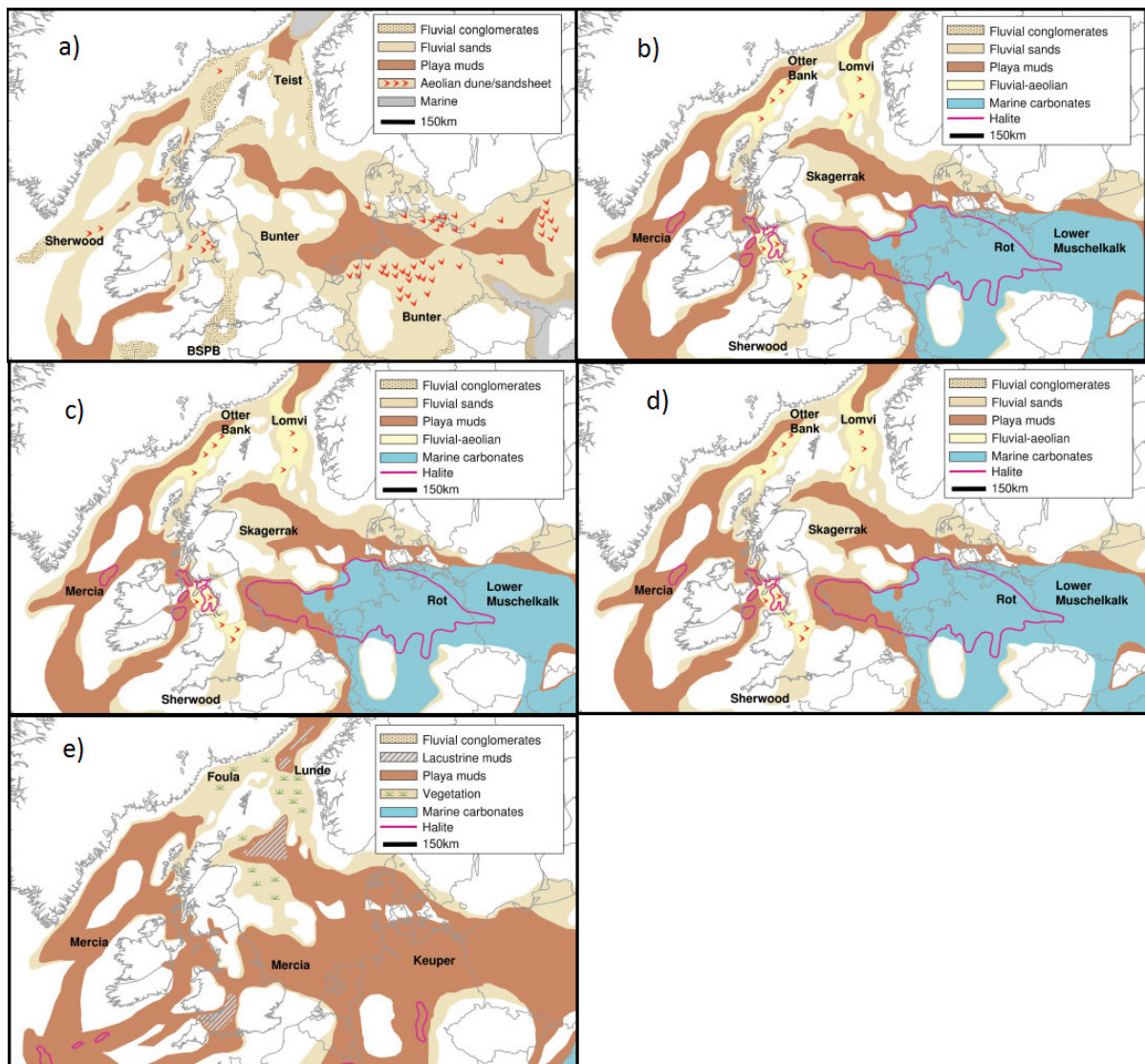


Figure 2-6. Palaeogeographical reconstruction of the Triassic over NW Europe adapted from McKie and Williams (2009). a) Early Triassic (Olenekian), b) Middle Triassic (Anisian), c) Middle Triassic (Ladinian), d) Late Triassic (Carnian) and e) Late Triassic (Norian)

2.5.1 Palaeoclimate in the Triassic

In most sedimentary basins the climate is the primary allogenic control on sedimentation. Palaeoclimate is therefore reflected in the stratigraphic succession of both chemical and siliciclastic sedimentary rocks. Indications for dry periods are presence of carbonate, evaporite, vertisols and aridisols while coal beds or leached paleosols indicate a wetter climate (Cecil 1990). The Triassic sandstones in the North Sea were deposited in an

arid to semiarid climate (Figure 2-7) and contain mostly illite/smectite with subordinate kaolinite (Bjørlykke and Aagaard 1992).

The formation of Pangea had a strong influence on the climate and the zonal circulation pattern would be disrupted (Parrish 1993). The large area of exposed land with symmetry around the equator and relative position to the Tethys is thought to have favored formation of the megamonsoon that was optimal in the Triassic (Parrish 1993).

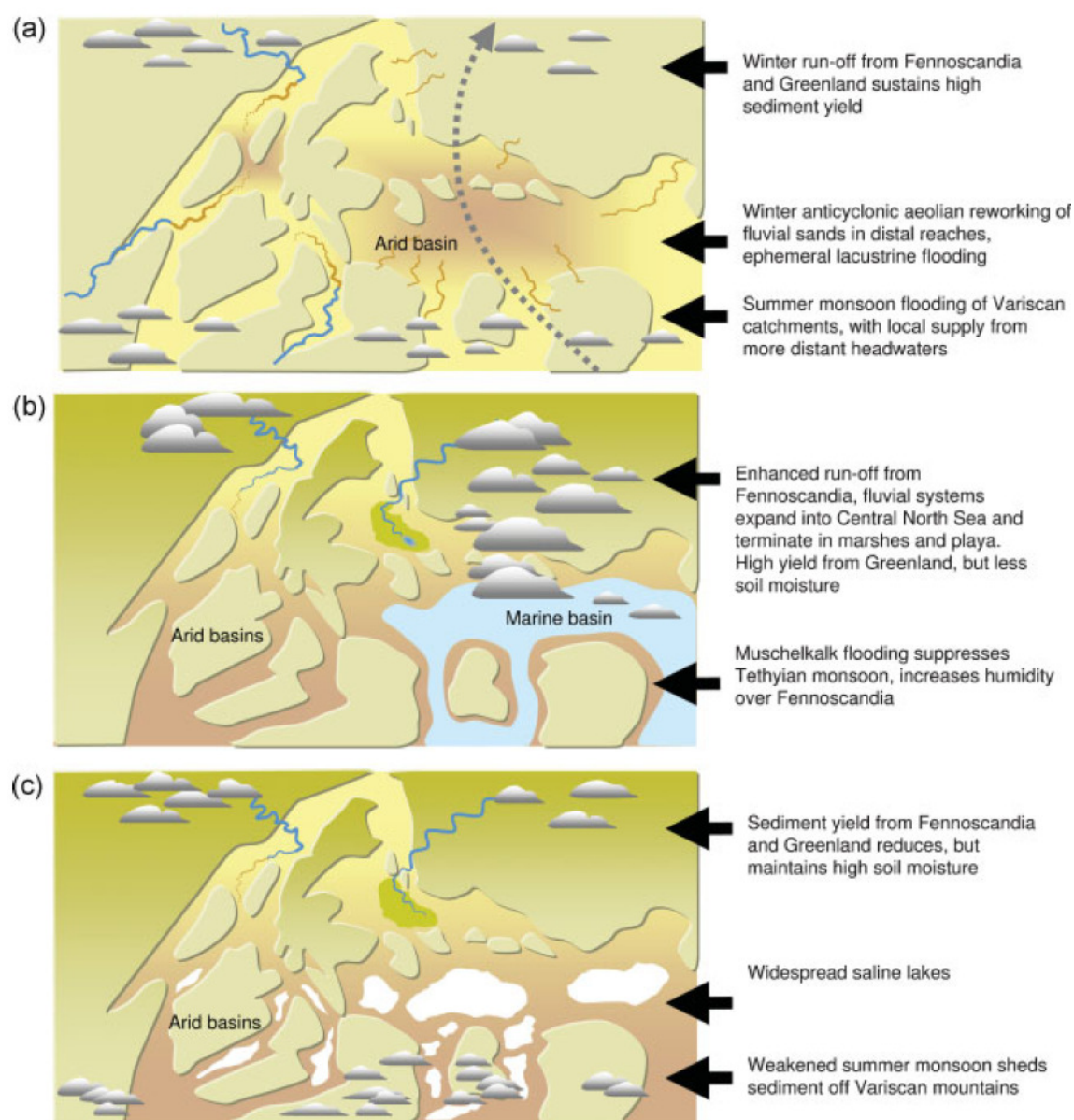


Figure 2-7. Main conceptual model of climatic changes in NW Europe (McKie and Williams 2009). a) Early Triassic, b) Middle Triassic, c) Late Triassic

3. Methods and materials

3.1 Well information and data set

Well information is gathered from The Norwegian Petroleum Directorate Fact Pages (NPD 2010) and Petrobank. Samples from well 6/3-1, 7/8-4, 7/11-9 and 7/11-8 have been investigated. Two burial history plots have been made for two wells (6/3-1 and 7/8-4). Well 6/3-1 will be given the most attention because it has the biggest data set with a total of 91 samples investigated, while well 7/8-4 has the second biggest with 28 samples (Table 3-1). The small data set in well 7/11-9 (10 samples) and 7/11-8 (11 samples) will be briefly discussed.

3.1.1 Well 6/3-1

Well 6/3-1 was a wildcat well drilled in the Pi-structure in the north-western part of block 6 in the Jæren high (Figure 1-1). The well is close by the UK-Norwegian median line and the UK Drake field (block 22/5 UK sector). The main objective was the Jurassic and Triassic sandstones (Skagerrak Formation) with Paleocene sandstones and Upper Cretaceous as secondary objectives. It was drilled 2nd November 1984 and discovered oil and gas/condensate at 2965m (mRKB) with oil/water contact at 3037m (mRKB).

Burial history with isotherm graphs has been made with the purpose of identifying areas of diagenetic alteration of minerals due to a change in thermodynamic state. Figure 3-1 has been made with information gathered from the NPD website (NPD 2010). The burial history of this figure is made to illustrate the rapid subsidence that happened in recent time (Cenozoic), as the burial during Mesozoic is stable and mainly a function of the Triassic succession. Most of the Early Jurassic deposition was probably eroded by the Mid-Jurassic uplift (Høiland et al. 1993), however erosional events have been excluded in the model because of uncertainties with the amount being eroded thus making the burial history very simplistic.

The cored reservoir interval of well 6/3-1 is between 2967-3116mRKB which according to the burial history is between approximately 120-130°C (Figure 3-1).

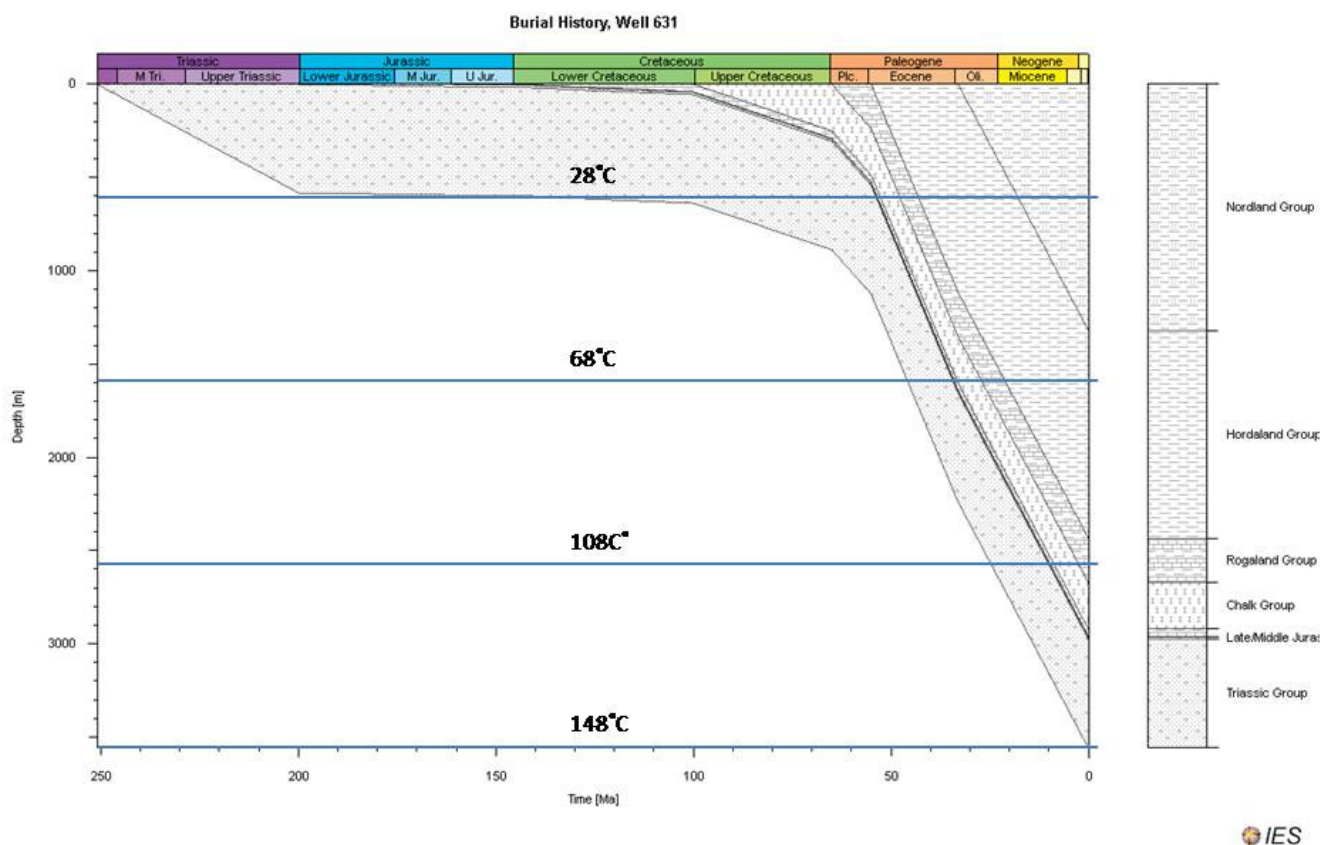


Figure 3-1 Simplified burial and temperature history of well 6/3-1 showing high burial rates in the Cenozoic compared to the Mesozoic. Erosional events are excluded in the model and temperature gradient is based on the bottom hole temperature of 148°C at 3560TD and a geothermal gradient of 40 °C/km (assuming seafloor temperature of 4°C)

3.1.2 Well 7/8-4

Well 7/8-4 is a wildcat well drilled in the northern flank of the Central Graben (Figure 1-1). The main objective was sandstone in Late Jurassic sand at 3840m (mRKB) and secondary target in isolated sands in the Triassic. The prospect was within a structural/stratigraphic trap on the north flank of a Triassic fault block. The well was drilled 20th February 1985 and turned out to be dry. Figure 3-2 is a more complex burial/temperature history with multiple erosional events. The temperature history has been calibrated against vitrinite reflectance. The burial history in the Mesozoic is dominated by the Triassic succession with an initial fast burial to 4km until the end of Triassic, thereby continued by a slow burial rate until the Cenozoic. As more sediments were deposited in the Cenozoic the Triassic succession got

more deeply buried, with a top Triassic around 3.8km depth. The cored reservoir interval lies around 3.8km corresponding to a temperature of 150-165°C.

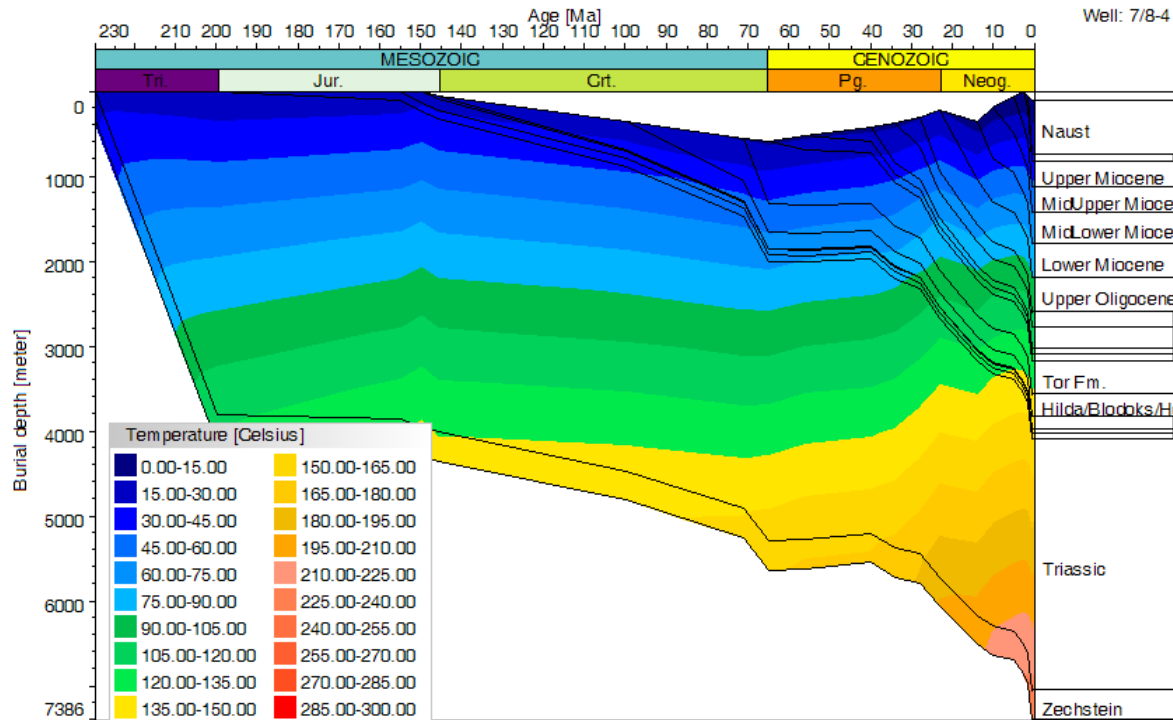


Figure 3-2. Burial and temperature history of well 7/8-4. (Data given by Tom Erik Maast)

3.1.3 Well 7/11-8

Wildcat well 7/11-was drilled in the Cod Terrace in Central Graben. The well had a primary objective in Late Jurassic sandstones and secondary objective in Triassic sandstones. The well was planned to penetrate a strong intra Triassic reflector at 4550+100m (mRKB). The Well ended up dry 12th December 1983.

3.1.4 Well 7/11-9

The 7/11-9 well is located in the Cod Terrace and designed to test sedimentary sequences that was thought to be related to the Upper Jurassic sandstones in the 7/11-5 Mime Discovery. The main objective was the Upper Jurassic sandstone. The well ended up abandoned on 9th March 1986.

Table 3-1. Well overview showing the sample distribution. *Data provided by Tom Erik Maast.

Well	XRD (bulk)	XRD(clay fraction)	Thin section	SEM
6/3-1	36	18	31	10
7/8-4	17	6	5*	0
7/11-8	4	2	5*	0
7/11-9	3	3	4*	0
Samples investigated	60	29	45	10

3.2 Wire line logging

Wire line logging measures physical properties of the rock penetrated by a well. Modern logging tool measures several different properties at the same time and most of them require direct contact with the rock. The logs can therefore be quality controlled by the use of a caliper log that measures the borehole diameter, in case the logging tool loses its contact with the rock.

All information regarding wire line logs has been gathered from Asquith and Krygowski (2004) unless stated otherwise. Following logs have been used in this thesis:

- Electric logs
 - Resistivity log (R) measures resistance between electrodes that are in contact with the rock in the well
- Radioactivity logs
 - Gamma log (GR) is the result of the naturally occurring gamma radiation in the rock (potassium, thorium and uranium)
 - Neutron Porosity log (NPHI) measures hydrogen content in the rock (related to porosity)

- Density log (RHOB) records the electron density of the rock that is related to the true bulk density
- Acoustic logs
 - Sonic transit time log (DT) records the time to send a P-wave from one end of the logging tool to the other end. High transit time is related to slow velocity of the rock
- Caliper log
 - Measure width of the borehole and can identify loosely consolidated areas and can be used for QC (quality control) of the measurements requiring direct contact with the rock in the borehole.

Combinations of logs are called composite logs where data from the same depths from one log on one axis is plotted next to data from another log on another axis. In this thesis the NPHI – RHOB cross plot have been used to identify shale and sand dominating areas. The NPHI is calibrated to a water saturated limestone. Increasing NPHI with no change in RHOB is interpreted as an increase in shale content. Another cross plot used to identify lithologies is the LMR cross plot (Anderson et al. 2001).

Porosity can be estimated from wire line bulk density.

$$\rho_b = \phi \rho_f + (1 - \phi) \rho_{ma}$$

where:

ρ_b is the measured bulk density,

ρ_f is the matrix density,

ρ_{ma} is the density of the fluid filling the pores (usually mud filtrate),

The equation can be rearranged to.

$$\Phi = (\rho_{ma} - \rho_b) / (\rho_{ma} - \rho_f)$$

If ρ_{ma} and ρ_f are known the total formation porosity from the measured bulk density ρ_b can be estimated. For this thesis the matrix density is assumed to be 2,65 g/cm³ and fluid density of 1.02g/cm³.

3.3 XRD

X-ray diffraction (XRD) analyses are used for detailed mineralogical screening. A monochromatic X-ray is transmitted on a crystal lattice and the diffraction depends on the crystal lattice structure. In the lab the angle of incidence from the X-ray will vary and reflections will be registered according to the incidence angle. The angles correspond to lattice distances related to different planes and are registered in a diffractogram. Each mineral will give its own unique pattern, however, some may overlap. The theory behind this method is based on Bragg's Law (equation 4-1). For a more thorough review of the basics and history behind XRD see Moore and Reynolds (Moore and Reynolds 1997).

$$n\lambda = 2d \sin \theta \quad \text{equation 4-1 (after Bragg and Bragg (1913))}$$

The relationship among the wavelength of the radiation λ , angle θ between the incident beam of radiation and the parallel planes of atoms causing the diffraction, and the spacing d between these planes is called Bragg's law (Bragg and Bragg 1913, Moore and Reynolds 1997).

Both semi quantitative XRD analysis and qualitative XRD analysis was carried out in this thesis. An overview of the samples can be found in Table 3-2. The qualitative identification procedure begins by identifying the mineral that explains the highest peak, then confirming it by finding the positions of the weaker peaks for the same mineral. When all peaks associated with the mineral is found, they can be excluded and the procedure repeats itself until all peaks can be explained. Error in peak position might occur, thus requires an internal standard. For this thesis Corundum has been added as an internal standard in order to identify and calibrate possible phase shifts or intensity differences. The output of the qualitative analysis is a glance of which reflections are due to clay minerals and which can be explained by other minerals. Reynolds and Moore (1997) suggested using integrated intensities for semi-quantification. In MacDiff the Pseudo Voigt function has been used for this purpose.

The integrated intensities were multiplied by in house weight factor standards based on the work done by Ramm (1991) (Table 3-3). The output of this method is used to identify semi-quantitative trends in the mineralogical composition with respect to depth. For more detailed

information regarding quantitative analysis see Hillier (2003). Moore and Reynolds (1997) and Snyder and Bish (1989).

It important to note that a there is a single procedure for preparing the XRD bulk analysis (section 4.3.1) and the XRD clay fraction analysis (section 4.3.2). By following a specific procedure for each method comparisons within the set can be made easier. This is especially important for semi-quantitative analysis where phase shifts and intensities have to be corrected.

All samples were processed at the University of Oslo, Department of Geology by using a Philips X'Pert MPD diffractometer with Cu-Ka radiation. The diffractometer was set to 40kV/50mA. The MacDiff software program was used to analyze the data.

Table 3-2 Overview of all the core samples in this thesis sorted by XRD number. Notice that well 7/8-4 has two XRD number intervals due to different sample takers. All the samples presented in this table has been analyzed for whole rock (bulk) composition, additional clay fraction analysis are bolded. *Samples from Tom Erik Maast. mRKB = meter relative to Kelly bushin.

Well	mRKB	XRD nr	Well	mRKB	XRD nr	Well	mRKB	XRD nr
7/11-8	3728,36	6440*	6/3-1	2967,7	6487	6/3-1	3069,1	6511
	3735,7	6441*		2972,85	6488		3074	6512
	3736,7	6442*		2977,65	6489		3079,05	6513
7/8-4	3743,95	6443*		2979,65	6490		3080,15	6514
	3825,6	6444*		2982,65	6491		3085	6515
	3831,25	6445*		2987,4	6492		3090,46	6516
	3831,6	6446*		2992,65	6493		3095,38	6517
	3832	6447*		2996,65	6494		3100,65	6518
7/11-9	3845,65	6448*		3002,32	6495		3105,65	6519
	4183,66	6449*		3005,35	6496		3109,65	6520
	4186,7	6450*		3011,35	6497		3113,63	6521
	4191,85	6451*		3016,77	6498		3115,65	6522
7/8-4	3825,68	6475		3020,72	6499			
	3826,35	6476		3022,65	6500			
	3830	6477		3023,42	6501			
	3832	6478		3028,77	6502			
	3834	6479		3033,65	6503			
	3837	6480		3039,72	6504			
	3840,15	6481		3042,65	6505			
	3843,15	6482		3047,65	6506			
	3845,05	6483		3052,66	6507			
	3850,2	6484		3055,3	6508			
	3855,05	6485		3060,65	6509			
	3858	6486		3064	6510			

Table 3-3. XRD identification scheme with weight factors (WF) for semi quantitative representation after Ramm (1991) and Peltonen et al. (2008).

Mineral	d-spacing	WF
Bulk		
"Total clay	4,5	20
Quartz	3,34	1
Plagioclase	3,19	4,2
K-feldspar	3,24	3,7
Calcite	3,04	1,6
Dolomite/ankerite	2,89-2,90	1,2
Siderite	2,79	4
Pyrite	2,71	2
Clay fraction (EG)		
Smectite/ IS	17	0,5
Illite	10	1
Kaolinite	7	1
Chlorite	7	1

Kaolinite and Chlorite overlap at 7\AA and the relative percentage of each clay mineral has to be semi quantified. This is done by looking at the slow scan in XRD_c run 2 where peaks at $3,54/54\text{\AA}$ (chlorite (004)) and $3,57/58\text{\AA}$ (kaolinite 002) are present. A straight baseline is drawn and the intensity peaks are measured. If both kaolinite and chlorite is present peak decomposition is required. The relative abundance of both kaolinite and chlorite is determined and can be calculated from the integrated area of 7\AA that represents both minerals.

3.3.1 XRD Bulk analysis

XRD Bulk analysis was carried out on 60 samples from three different wells (Table 3-2). The XRD Bulk analysis was carried out as follows:

- Samples are crushed in a pestle or a mortar to a size of $< 2\text{mm}$
- Samples are put into a grinder where the sample is mechanically crushed, by both impact and friction, into a homogenous material

- 20% Corundum was added to the sample (preferable 2 gram of sample size was added 0,5 gram of Corundum)
- The crushed sample was then pulverized for 3-5 minute (depending on sample size) in a McCrone micronizing mill. Distilled water was added in the mill (1gram = 7-10 milliliter, 2,5gram = 20 milliliter). For more information regarding use of micronizer see O'Connor and Chang (1986) and Moore and Reynolds (1997)
- The pulverized wet material was filtered by a vacuum filter apparatus provided by the MilliporeTM Corporation (see Moore and Reynolds (1997) for more information). The filter used is a cellulose nitrate filter with a pore size of 0.45 μ m
- The filter with the sample was air dried for at least 24 hours
- The dried sample is disaggregated in an agate mortar and pressure packed into an aluminum sample holder to produce random whole rock mounts

The sample is now ready to be analyzed by the diffractometer.

The scanning program set for the XRD bulk analysis is as following:

Bulk FORCE: 2-65 °2 θ Step: 0,02 °2 θ 3 seconds per step.

3.3.2 XRD Clay fraction analysis

XRD clay fraction analysis was carried out on 25 samples (Table 3-2).

- Crushed sample material (without any Corundum) is put into a small beaker glass
- 300 ml of distilled water was added in the beaker glass with the sample and stirred for one minute
- Each sample was given 10 minutes of ultrasound treatment in a Bandelin Sonorex RK102 transistor in order to disperse the clay particles. Samples with high clay content was left overnight
- 100 ml of distilled water and 10-15 ml of Calgon was added to the sample
- Samples were stirred for one minute and left in suspension for 3 ½ hour (theory based on falling velocity being the result of the particle diameter (see Stoke's Law (Stokes 1851))
- Everything above roughly 175 ml mark on the beaker glass was siphoned into a small plastic container
- The wet material was filtered by a vacuum filter apparatus provided by the MilliporeTM Corporation (see above for reference)
- The filtered samples were treated with 0,1 M MgCl₂ and distilled water
- Samples were then air dried and placed on silica glass slides with the aid of a small aluminum cylinder making the sample oriented

The sample is now ready to be analyzed in the diffractometer.

The samples underwent three treatments and four different XRD runs.

Treatment 1: Air dried

XRD_a run 1: Fast scan 2 - 45 °2θ, step 0,06 °2θ, 3 seconds per step

XRD_c run 2: Slow scan across 3,53/54Å (Chlorite) – 3,57/58Å (Kaolinite)
reflection 24 - 26 °2θ, step 0,01 °2θ, 4 seconds per step

Treatment 2: Ethylene glycol vapor. Sample was left in an exsiccator overnight

XRD_e run 3: 2 - 35 °2θ

Treatment 3: Heating (550°C).

XRD_h run 4: 2 – 30 °2θ

3.3.3 Volume percentage or XRD percentage

In this thesis the mineral abundance will be presented as XRD percentage. The XRD percentage is only a relative amount that may vary but still will give mineralogical trends. A more time consuming method based on full pattern matching has not been done due to time restrictions.

3.4 SEM

Secondary electron microscopy (SEM) is method images the sample surface in very high resolution. A SEM-JEOL JSM 6460LV equipped with a Link eXL energy dispersive spectrometer (EDS) was used for petrographical examination by both BSE (backscattered electrons) and SEI (secondary electrons) on selected sandstone samples. The identification was done by using a combination of EDS and SEM atlas (Welton 1984). Three main types of samples were examined by SEM: gold coated stubs, carbon coated thin sections and carbon coated carbon bricks.

3.4.1 Elemental analysis on pore-coating clay material

Bulk samples of sandstone with high amount of pore-coating clay are gently rolled around into a mortar with ethanol. The ethanol containing the clay minerals are then transferred by pipette onto a polished carbon brick and later carbon coated. The pore-coating material is now coated by carbon and can be investigated by SEM with minimum background noise. An elemental analyzes are carried out the software INCA and atomic% are used to calculate the chemical formulae of the respective pore-coating material.

In this thesis two chlorite coated sandstone samples were examined by elemental analyzes in SEM (3065,65mRKB and 3115,65mRKB).

3.5 Thin section

Thin sections are about 30 µm thin consisting of epoxy impregnated sediments (rock). They provide detailed information about rock texture and mineralogy, however they cannot provide us with information of grains smaller than about 5 µm. A general description of all the thin sections used in this thesis can be found in Appendix II. This description is based on: lithology, average grain size, most common grain shape, sorting, framework connection and other remarks of interest. An overview of which samples that was examined can be seen in Table 3-4. The degree of sorting is divided into good- (well-) ,moderate- and poorly sorted which are modified after Longiaru (1987) (Figure 3-3). For grain sizes the common Wentworth scale is used.

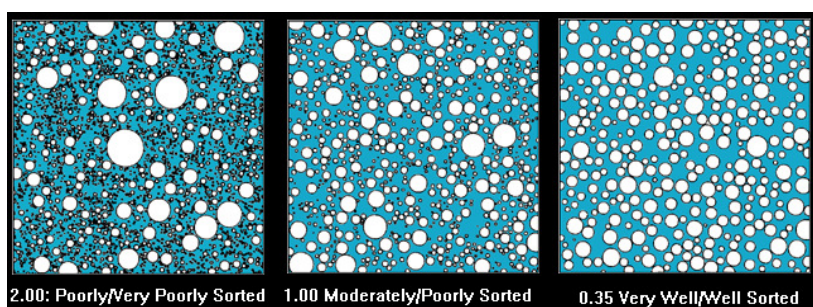


Figure 3-3. Degree of sorting taken from Choh et al. (2003) that is modified after Longiaru (1987)

Table 3-4. Thin sections for the study area. All depths are in mRKB. Bolded samples have been point counted. *Data given by Tom Erik Maast

Well	Depth	Well	Depth	Well	Depth
6/3-1	2967,7	6/3-1	3042,65	7/11-8	3726,08*
	2972,85		3047,65		3728,36*
	2977,65		3052,66		3735,7*
	2979,65		3055,3		3736,7*
	2982,65		3060,65		3743,95*
	2987,4		3069,1	7/8-4	
	2992,65		3074		3825,6*
	2996,65		3079,05		3831,25*
	3002,32		3080,15		3831,6*
	3005,35		3085		3832*
	3016,77		3090,16		3845,65*
	3020,72		3095,38	7/11-9	
	3023,42		3100,65		4183,66*
	3028,77		3105,65		4186,7*
	3033,65		3109,65		4191,85*
	3039,72		3115,65		4192,6*

3.5.1 Point counting

Point counting has been performed on a Nikon Optiphot-Pol petrographic microscope with both plain polarized light (PPL) and cross polarized light (XPL). Exactly 200 points have been counted with the aid of a Swift automatic counter in 31 thin sections (Table 3-4).

Eight different parameters were counted for:

1) Quartz, 2) Feldspar, 3) Rock Fragments, 4) Matrix, 5) Carbonate cement, 6) Primary porosity, 7) Quartz cement and 8) Secondary porosity. Adams et al.(1986) have been used excessively for identification of the different parameters. For more information regarding point counting see Galehouse (1971) and Weltje (2002).

3.5.2 Intergranular Volume

From the information gathered in Point counting (see above) we can calculate the IGV(InterGranular Volume). IGV is an important parameter for measuring compaction in sandstone. It is equivalent to intergranular primary porosity (measure of the space between framework grains) and averages around 40-45 volume percent. IGV varies to a limited degree with sorting and does not vary with particle size. It should be noted that the 2D representation through a thin section gives an apparent variation in grain size. Grain contacts may also be out of the plane of the thin section (Lundegard 1992, Ehrenberg 1995).

$$\text{IGV (\%)} = V_{\text{intergranular porosity}} + V_{\text{intergranular cement}} + V_{\text{detrital matrix}}$$

3.6 Uncertainties

Uncertainties regarding different methods are just as important as the method itself.

3.6.1 XRD uncertainties

XRD intensities can be influenced by differences in particle size, orientation and multiple reflections for each mineral.

The use of Corundum as an internal standard is new for this department, however it is not a new method (Snyder and Bish 1989). The purpose of using an internal standard is to detect and calibrate possible shifts in phases and correction of intensities.

The use of a dry grinder (such as the one used in this thesis) should be avoided according to Hillier (2003) due to the risk of damaging the clay minerals. Prolonged grinding might also create new clay-sized-minerals. An alternative method would be the freeze-thaw method, this however takes too much time to be applied in this thesis (see Hillier (2003) and references therein).

The cellulose nitrate filter used for both clay fraction analysis and bulk analysis had expired over eight years ago (October 2002). The effect of using an expired filter did not seem to affect the result and is considered to have a negligible impact.

3.6.2 Thin section uncertainties

Interpretation of the thin sections is in a strong degree dependant of experience. Due to limited experience by the author in sandstone petrology the results should be looked upon as indications and rough trends only. It should also be noted that some thin sections were of poor quality. Both extensive quartz fractures and yellowish color of the quartz (due to too thick thin section) were present in some samples (Appendix IIc). Some samples also had an increase in pore space towards the thin section edges, implying artificial porosity.

Uncertainty arise when conventional microscopy is used for quantification of quartz cement instead of SEM/CL as studies show that percentages of quartz cement determined by conventional methods are overestimated where quartz cement is present in high proportions and underestimated where quartz cement is less abundant (Evans et al. 1994).

3.6.3 Petrophysics

The assumption of a standard bulk density of $2,65 \text{ g/cm}^3$ and fluid density of 1.02 g/cm^3 is very simplified since the bulk composition from the cored interval in well 6/3-1 and 7/8-4 is subarkosic, meaning the bulk density should be adjusted for every 5 meter (common cutting sampling interval). The fluid density of well 6/3-1 is highly variable as the well is defined as oil find with an oil/water contact at 3037mRKB.

4. Mineralogical and Petrographical description

4.1 Introduction

This chapter will present the results and observations done by XRD, SEM and Thin section analysis by methods described in Chapter 4.

4.2 Thin section analysis

A general description of 31 thin sections from well 6/3-1 has been made (Appendix II).

Intra Draupne Formation

The upper three samples (Intra Draupne Formation) consist of matrix dominated framework with varying grain sizes from silt to fine sand. The sorting is generally poor and grain shape range between subangular and subrounded. Presence of polycrystalline sutured quartz and undulose extinction have been interpreted to suggest both metamorphic and magmatic source (Adams et al. 1986).

Skagerrak Formation

The remaining 28 samples belong to the Triassic Skagerrak Formation. The samples are poor to well sorted with varying lithology from shale to sandstone. Generally they are grain dominated framework with moderately sorted subrounded-subangular fine sandstone. A wide range of feldspars have been identified (perthite, albite, microcline and orthoclase). Both polycrystalline quartz and undulose extinction are present indicating a source area of both magmatic and metamorphic origin (Adams et al. 1986). Good porosity occurs in thin sections where a black rim, hematite or chlorite, coating is visible around the grains (2992,65 mRKB and 3105,65 mRKB). Local occurrence of pressure solution between quartz and mica is present (3039,72 mRKB). Abundance of fine grained rhombic dolomite cement is observed in 3042,85 mRKB indicating cementation of shallow origin. The cemented thin section also has an abnormal high IGV, indicating dissolution of grains and precipitation of cement. A mosaic texture of pore-filling calcite can be seen at 3039,72 mRKB where available porosity has been filled by calcite and dolomite crystals increase in size away from

the grains. Figure 4-1 illustrate two samples with low porosity where the sample from 3028,77 mRKB is a well sorted siltstone with parallel mica bonds and 3023,42 mRKB having local calcite cemented areas and polymodal grain size. Presences of sutured boundaries in detrital quartz indicate presence of the diagenetic effect have been interpreted to be caused by pressure-solution along grain-to-grain contacts.

Some enlarged pictures have been taken of selected thin section samples with 10X magnification (Figure 4-2). Both PPL (Plane Polarized Light) and XPL (Cross Polarized Light) images have been taken of 2992,65 mRKB and 3039,72 mRKB while only PPL has been taken of 3039,72 mRKB and 3052,66 mRKB. Several compaction related deformation structures are visible such as sutured quartz along grain-to-grain contact areas and ductile deformation of mica. Porosity reducing effects such as carbonate cementation and quartz overgrowth severely reduce the reservoir quality. Some minor provenance features can also be interpreted such as quartz with an abnormal notch in the structure perhaps caused by dissolution of quartz and replacement of calcite cement or corrosion in humid soil. Another provenance identified features are recrystallized metamorphic quartz that's been identified by having equant and relatively straight borders and extinction.

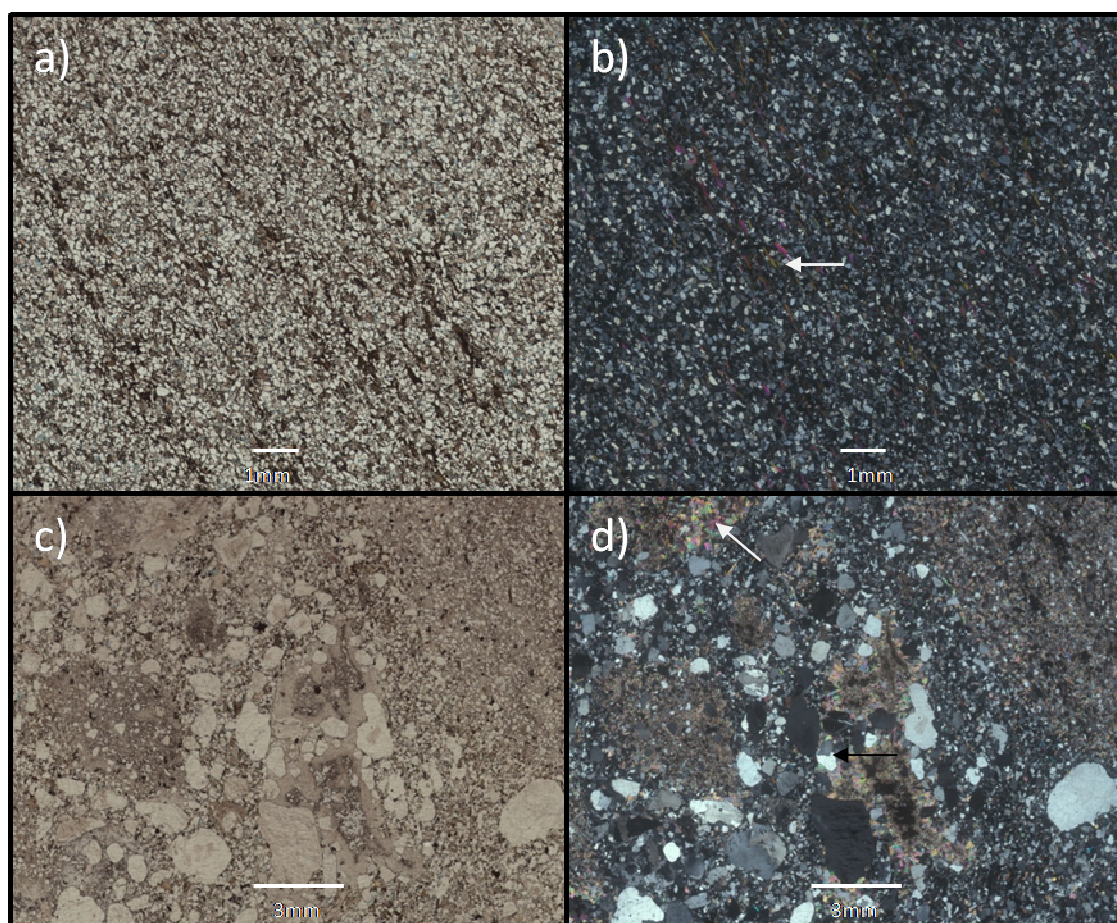


Figure 4-1. Scanned thin sections with white bar for scale. a) Siltstone with laminated mica (3028,77 mRKB PPL), b) Same as a) but in XPL. Notice presence of parallel oriented mica (white arrow), c) Grain supported poor sorted fine sandstone from 3023,42 mRKB (PPL) with local areas of cementation, d) Same as c) but in XPL. White arrow points toward calcite cemented area while the black arrow points towards sutured quartz

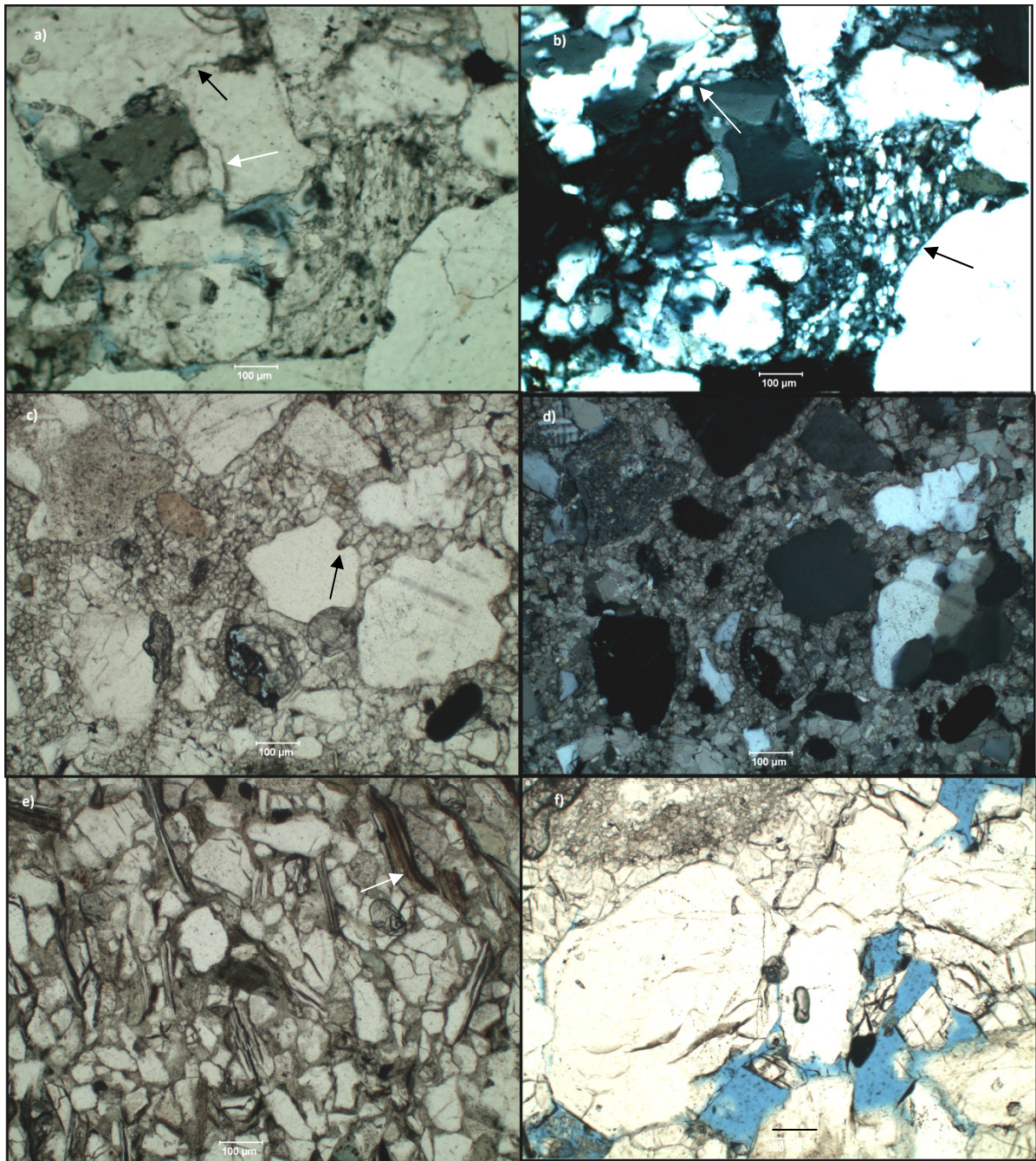


Figure 4-2. Microscope images taken from a 10x thin section (same scale for all images). a) Quartz overgrowth (white arrow) and stylolite (pressure solution)(black arrow), b) XPL of a) Polycrystalline quartz (chert?, black arrow) and recrystallized metamorphic quartz (polycrystalline quartz with equant boarders and relatively straight boarders and extinction, white arrow), c) Extensive dolomite cementation filling surrounding a quartz grain with an anomalous notch in the grain surface due to partial replacement of quartz by dolomite cement (alternatively corrosion in humid soil) at 3039,72 mRKB depth, d) XPL of c) Microcline with its characteristic twinning (uppermost left) and polycrystalline quartz (far right), e) 3052,66 mRKB depth with poorly sorted very fine sandstone with high content of matrix (mica). Ductile deformation is evident by bending mica (white arrow), f) 3069,10 mRKB depth with localized carbonate cement (upper left) and open pore space (lower right). Black line is 10µm

4.2.2 Point counting

Modal analysis (200 points per section) has been performed on 30 samples belonging to 6/3-1, 7/8-4, 7/11-9 and 7/11-8 (See appendix IIb). Both wackes and arenites are present in the study area (Figure 4-3 and Figure 4-4). Within the wackes the most abundant composition is feldspathic wackes, while among the arenites the feldspathic arenites and quartz arenite are the most abundant. It should be noted that a great number of untwinned albite in well 6/3-1 might have been misinterpreted as quartz, making the true composition more likely to be feldspathic arenites. Both the matrix content and the Jurassic samples have been excluded in the average composition calculation where average value of each well and average value of all the wells have been plotted (Figure 4-5). The dominantly petrographic classifications of all the sandstones are subarkosic.

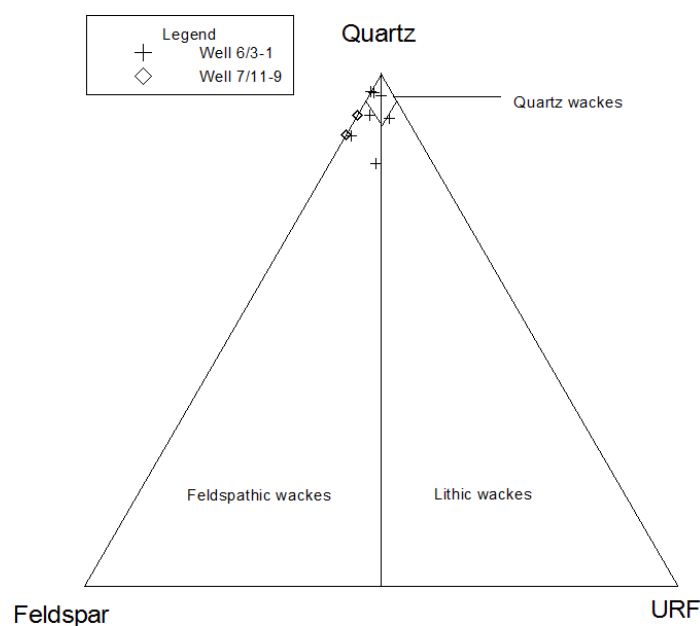


Figure 4-3. Petrographic classification of wackes (matrix >10%) in the study area. Wackes are only present in well 6/3-1 and 7/11-9

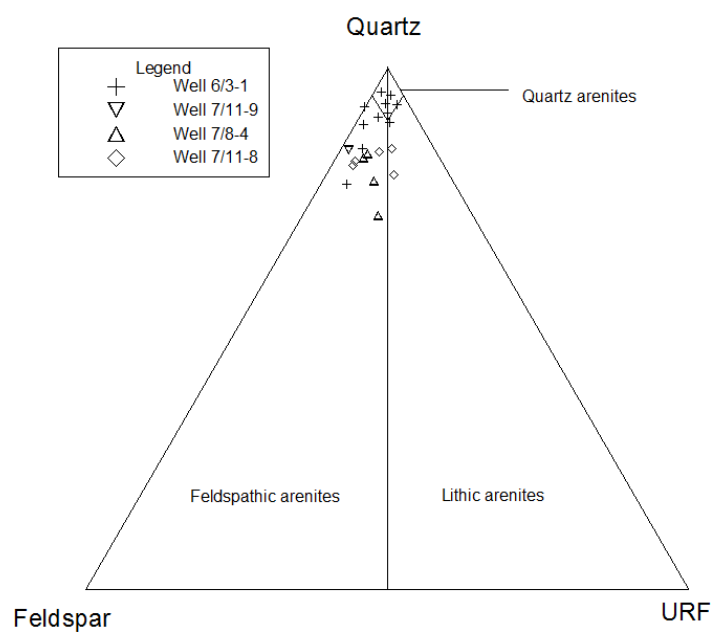


Figure 4-4. Petrographic classification of arenites (matrix < 10%) in the study area.

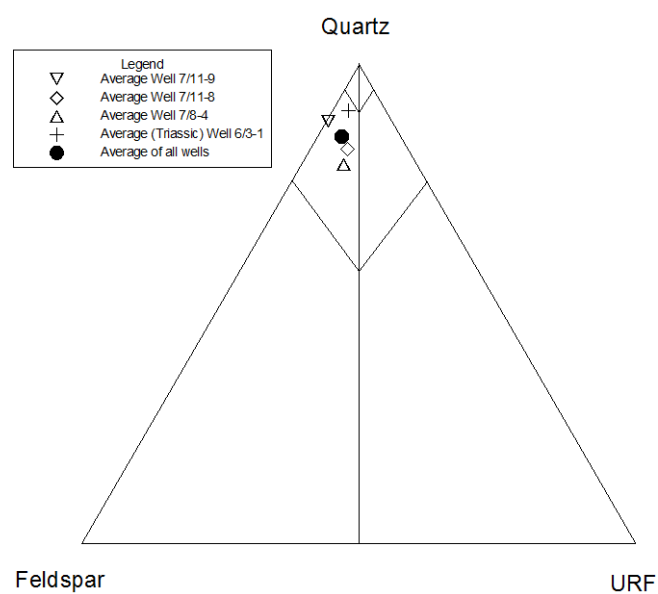


Figure 4-5. Petrographic classification of average values (excluding Jurassic samples and matrix content) in the study area for all the wells. All wells end up with an average subarkosic composition

4.2.3 IGV

IGV was calculated and presented in Figure 4-6. The Jurassic samples from well 6/3-1 has been removed. The average IGV of well 6/3-1 for the Triassic samples is 35% and range between 20% – 70%. The majority constituent in sample from 3039,7 mRKB is dolomite cementation. The less IGV variable well 7/8-4, 7/11-9 and 7/11-8 ranges mostly between 20% - 50% with averages in same well order of: 30%, 34% and 39%.

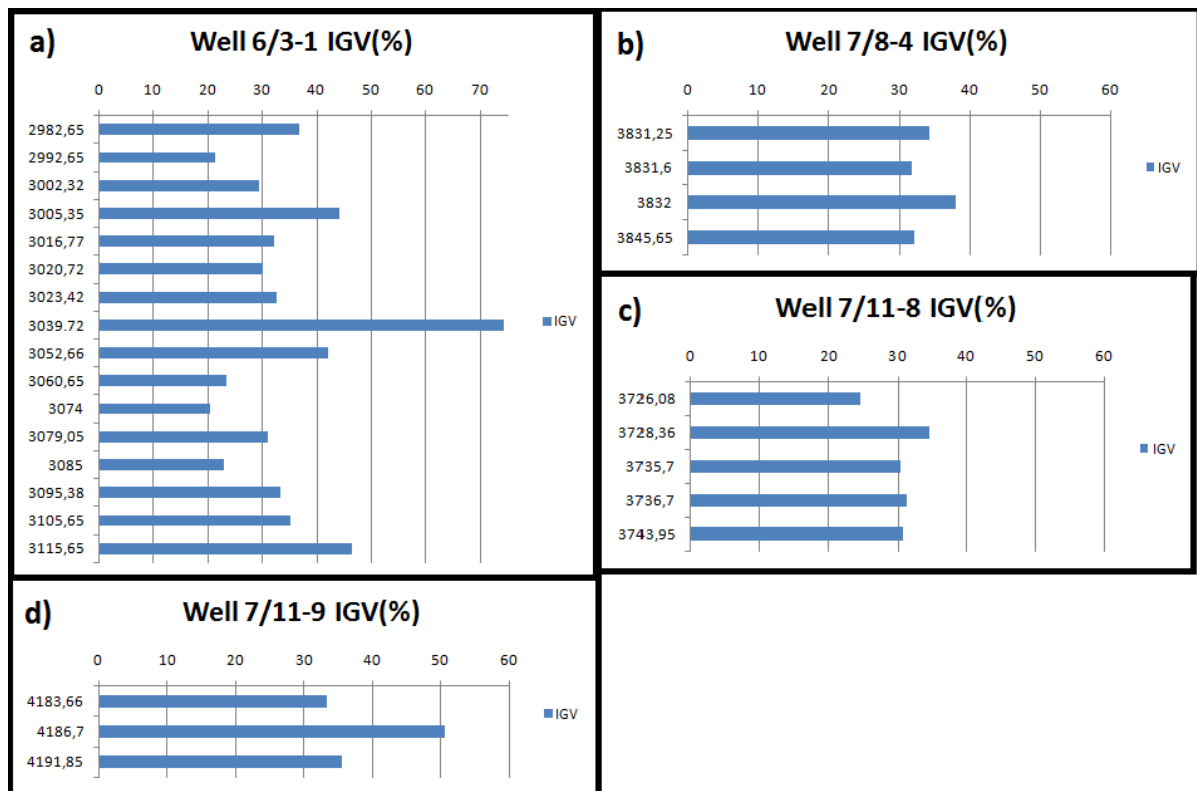


Figure 4-6. Intergranular volume from all the wells. Depth on Y axis while IGV is on the X axis. a) Well 6/3-1 with the biggest dataset showing variations in IGV with depth, b) Well 7/8-4, c) Well 7/11-9, d) Well 7/11-8. Caliche identified samples from well 7/8-4, 7/11-8 and 7/11-9 has been excluded but can be found in appendix IIb)

4.2.4 Importance of sorting

Thin sections from well 6/3-1 were grouped semi-qualitatively by eye in a microscope according to the degree of sorting (bad, moderate or good)(Appendix II). The sorting was also correlated with the conventional core description (NPD 2010). Three statistical plots were made with sorting against porosity/total clay and IGV (Figure 4-7b–Figure 4-9).

Porosity values from point counting (both primary and secondary) were plotted against the degree of sorting (Figure 4-7). It should be noted that both the poor and moderate sorted samples has roughly 4% average porosity with varying 95% confidence interval depending on the spread of data and the number of samples. The good sorted samples show a higher mean porosity but also a larger 95% confidence interval due to small sample size and varying porosity values. A trend is difficult to predict from these samples although an impression that higher porosities are found with high degree of sorting is plausible.

From the bulk XRD data a total clay value from each sample was obtained. This value is highly semi-quantitative as the 4.5Å peak fail to include all the clay minerals within the sample, but is a good estimate, and thus will be referred to as XRD%. A decreasing value of total clay XRD% is visible with higher degree of sorting (Figure 4-8). The 95% confidence interval for poorly sorted samples is big in comparison with good sorted samples implying higher certainty in good sorted samples than in the bad sorted samples.

For the IGV(%) against sorting the trend is unclear (Figure 4-9). The bad sorted has a mean IGV of 35% while both moderate and good sorted samples has a mean of 30%. The large uncertainty is evident by the 95% confidence interval that range between 15-45% for the good sorted to about 25%-35% for the moderate sorted. One would expect higher IGV with higher degree of sorting, due to higher porosities (IGV) for well sorted than poor sorted, but this is not evident from samples in well 6/3-1.

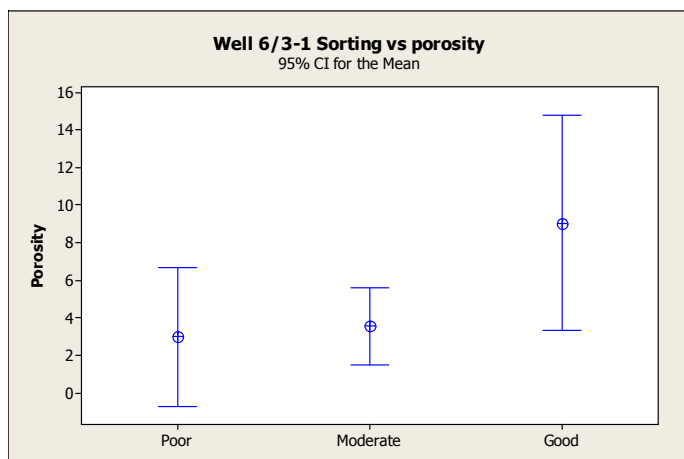


Figure 4-7. Sorting plotted against porosity (from point counting) with a 95% confidence interval and the mean. Sample size: $N_{\text{poor}}=5$, $N_{\text{moderate}}=7$ and $N_{\text{good}}=5$.

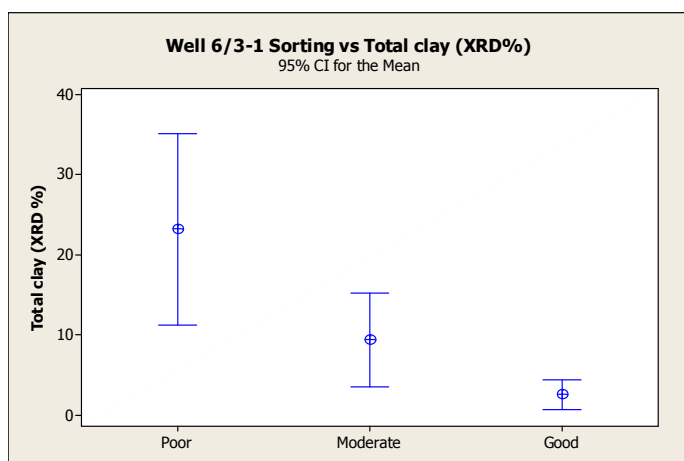


Figure 4-8. Relationship between sorting and Total Clay (XRD %) show both the mean and 95% confidence interval. Sample size: $N_{\text{poor}}=12$, $N_{\text{moderate}}=12$ and $N_{\text{good}}=7$

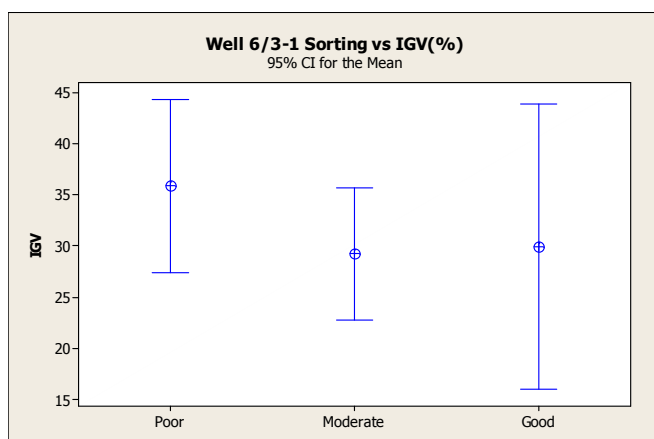


Figure 4-9. Relationship between sorting and IGV (%). Notice big spread in 95% CI implying big uncertainties, however high IGV seem to favor poorly sorted sediments. Sample size: $N_{\text{poor}}=5$, $N_{\text{moderate}}=7$ and $N_{\text{good}}=5$

4.3 XRD

This section will include both the results from XRD Bulk and Clay fraction analysis according to methods in section 4.4. A total of 60 samples have been analyzed and an overview of them can be found in table 4-2.

4.3.1 XRD Bulk

No clay minerals has been identified in the bulk analysis, instead a “total clay” value will represent the abundance of clay minerals within one sample. Both well 7/11-8 (Figure 4-10) and 7/11-9 (Figure 4-11) contain less than 5 samples from a small interval (<20) and thus only provides us with a vague insight in the bulk mineralogical composition. Well 6/3-1 and 7/8-4 have been sampled at a larger interval and provide us with a better insight of mineralogical variation with depth.

In well 7/11-8 (Figure 4-10) the mineralogical composition in order of abundance with average values are: Quartz (57 XRD%), Plagioclase (22 XRD%), K-feldspar (12 XRD%), “Total clay” (7 XRD%), Dolomite/Ankerite (<1 XRD%), Calcite (<1 XRD%), Siderite (<1 XRD%) and pyrite (<1 XRD%). It should be noticed that the sample at 3743,95 mRKB contain no “total clay”, which is in reality not the case. The reason for the 0% is most likely related to the fact that “total clay” is just an estimate of the total clay content and not the true total clay content.

The mineral composition for well 7/11-9 is only represented by three samples in a thickness of 7 meters (Figure 4-11). Mineralogical in order of decreasing abundance with average values the minerals are: Quartz (50 XRD%), Plagioclase (19 XRD%), K-feldspar (13 XRD%), “Total clay” (10 XRD%) and Dolomite/Ankerite (6 XRD%). We also observe a localized sharp increase in Dolomite/Ankerite in 4191,85 mRKB most likely related to a cemented interval.

Fourteen samples have been taken from well 7/8-4 with one sample duplicated due to different sample takers (3832 mRKB) (Figure 4-12). Mineral composition with decreasing order of abundance and average value is: Quartz (32 XRD%), Plagioclase (24 XRD%),

“Total clay” (19 XRD%), Dolomite/Ankerite (15 XRD%), K-Feldspar (8 XRD%), Siderite (<1 XRD%) and pyrite (<1 XRD%). There seems to be an inverse relationship between presence of Dolomite/Ankerite XRD% and Feldspar (XRD%) (K-feldspar XRD% + Plagioclase XRD %). A quality control on the data can be performed by comparing the two samples, taken by different sample takers, from the same depth (3832mRKB) assuming homogeneous sample. There is a significant correlation in these two samples with a Pearson correlation value of 0,991 and a P-value of 0, indicating good repeatability for the method.

Well 6/3-1 was most extensively sampled and thereby provides the most detailed mineralogical evolution with depth (Figure 4-13). The cored reservoir interval from well 6/3-1 contains both Jurassic and Triassic strata and the author find it practical to divide the results from well 6/3-1 in two. It should also be mentioned that the entire Early Jurassic strata is missing, creating an unconformity at 2978mRKB. Only three samples represent the Jurassic with heterogeneous composition

The mineralogical composition with decreasing order of abundance for the Triassic samples in well 6/3-1 is: Quartz (47 XRD%), Plagioclase (20 XRD%), “Total clay” (14 XRD%), K-Feldspar (12 XRD%), Dolomite/Ankerite (6 XRD%), Calcite (3 XRD%), Pyrite (<1 XRD%) and Siderite (<1 XRD%). As with both well 7/11-9 and 7/8-4 there are local areas of high XRD % of total clay and Dolomite/Ankerite.

Well 6/3-1 and 7/8-4 shows a decreasing maturity with depth based on quartz/feldspar ratio (Figure 4-14) . The quartz and feldspar values are based on XRD due to a bigger sample number and less biased by the interpreter. The quartz/(quartz + feldspar) ratio for well 6/3-1 ranges from 1 to 0,38 with an average of 0,59. Well 7/8-4 has an average quartz/feldspar ratio of 0,51 and range from 0,63 to 0,39.

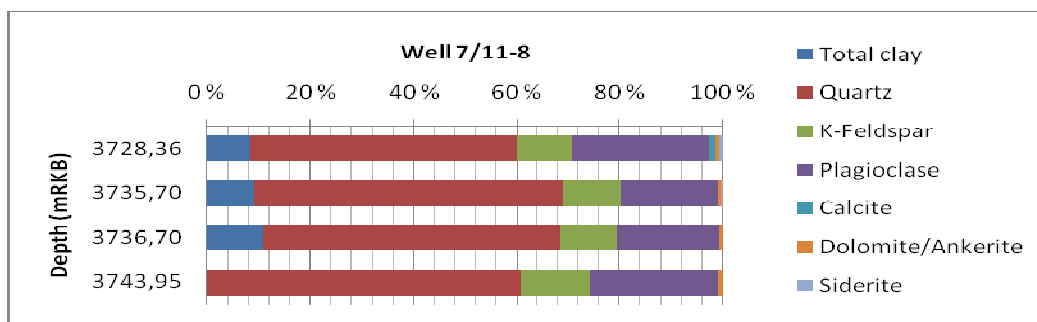


Figure 4-10. XRD bulk composition of samples from well 7/11-8

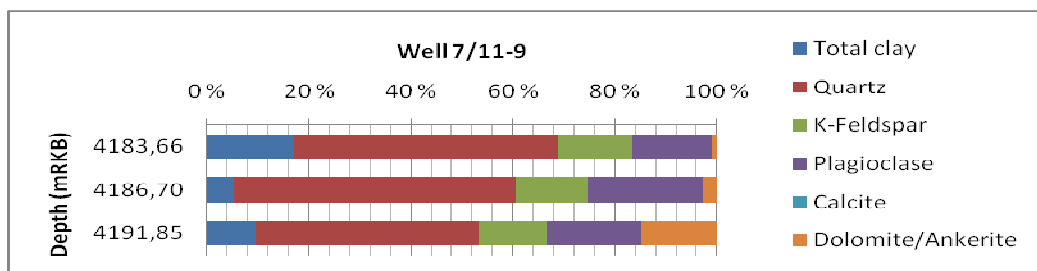


Figure 4-11. XRD bulk composition of samples from well 7/11-9

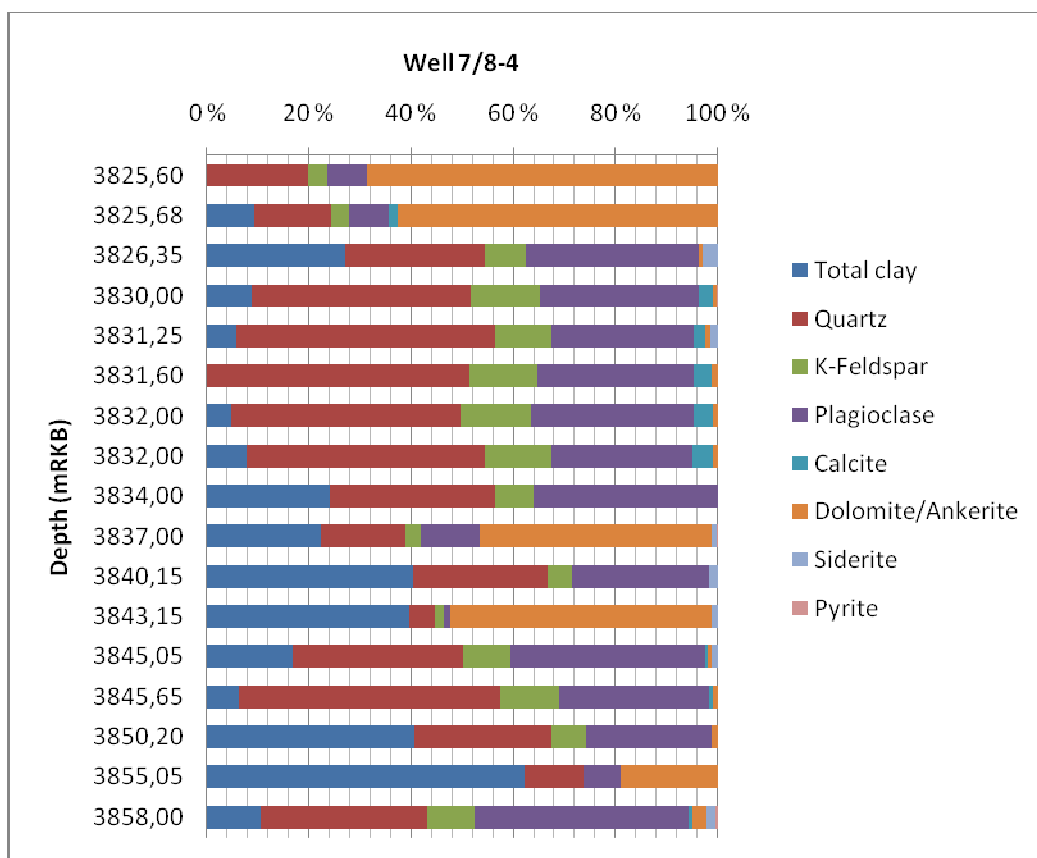


Figure 4-12. XRD bulk composition of samples from 7/8-4. Notice two samples from 3832 mRKB (from two different sample takers) showing a good correlation

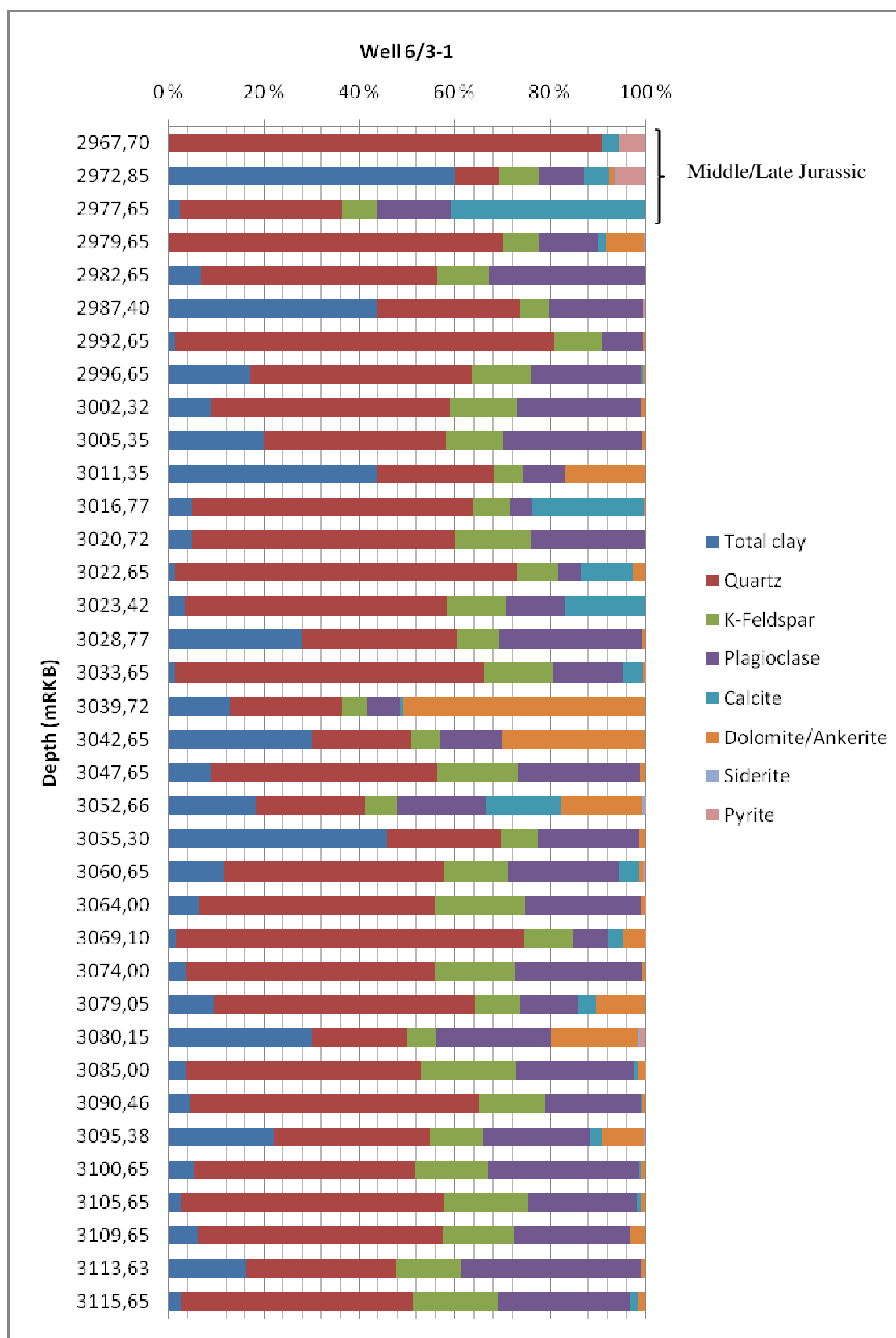


Figure 4-13. XRD bulk composition of samples from well 6/3-1

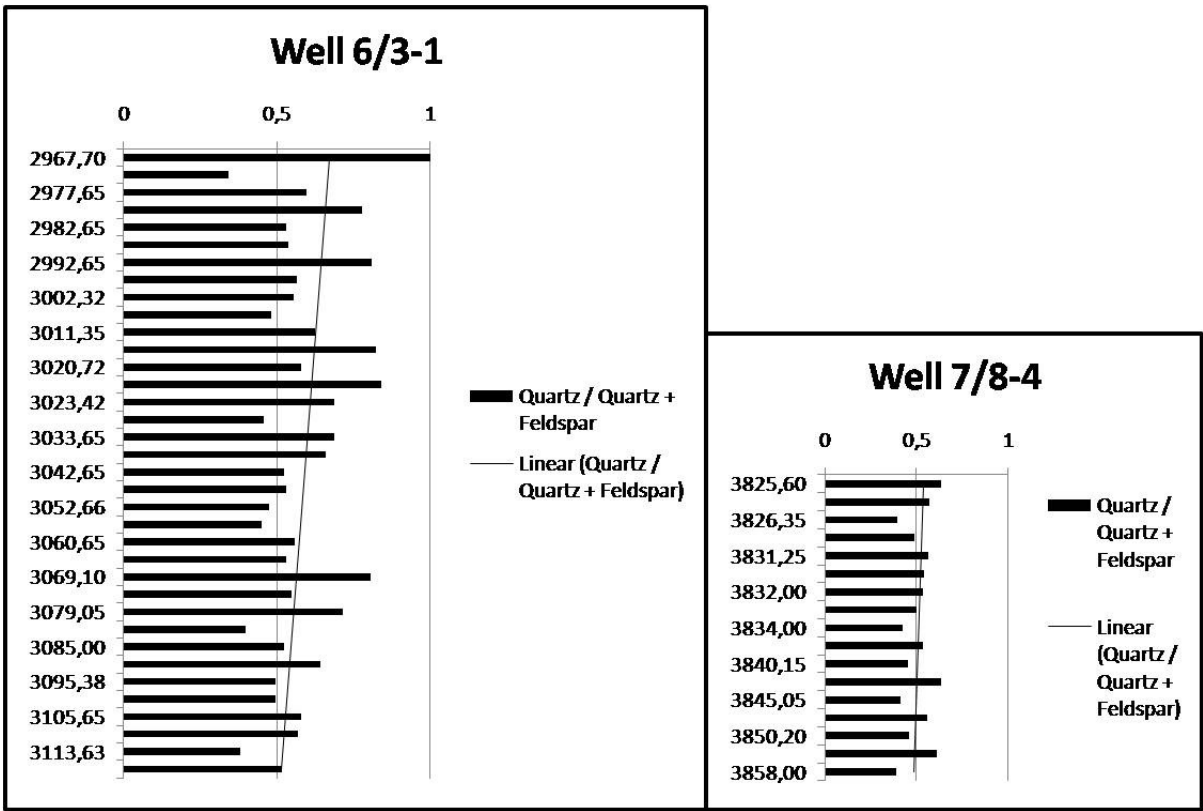


Figure 4-14. Quartz / Quartz + Feldspar ratio in well 6/3-1 and 7/8-4. The data is taken from XRD bulk A value of 1 implies mature sandstone while a value of 0 implies immature sandstone

4.3.2 XRD Clay fraction

A total number of 29 XRD clay fraction samples were analyzed with the purpose of identifying the abundance of each clay mineral group (Smectite group, Illite group, Chlorite group) with the exception of the Kaolin group where only the clay mineral kaolinite is represented. When relating to the most abundant clay mineral within a sample it is only with respect to the clay fraction analysis and not the bulk fraction. The amount of clay minerals in each sample is related to the “total clay” XRD % in the bulk analysis (XRD Bulk).

Both chlorite and illite are present in well 7/11-8 (Figure 4-15) and 7/11-9 (Figure 4-16) with the majority being chlorite. It is difficult to deduce trends with few samples however well 7/11-8 seems to have a dominance of chlorite (>90 XRD%) while well 7/11-9 is more influenced by illite.

In well 7/8-4 (Figure 4-3 there seems to be a downward increase in illite (from 90 XRD% chlorite and 10 XRD% illite to a roughly 20 XRD% chlorite and 80 XRD% illite). Two samples also stand out with almost the same proportion illite and chlorite (3845,05mRKB and 3858,00mRKB). Trace amount of smectite / Illite/smectite can be seen in 3845,05mRKB.

Well 6/3-1 provides the most detailed clay mineralogical development with 18 samples covering roughly 140 meters (Figure 4-18). The first sample belongs the Middle/Late Jurassic (2977,65 mRKB) displaying a 90 XRD% chlorite and a 10 XRD% illite content. Within the Triassic section three main clay minerals with decreasing order of abundance and average values: chlorite (53 XRD%), illite (35 XRD%) and kaolinite (12 XRD%). The amount of chlorite and illite seem to vary with depth with some intervals being dominated by chlorite and others by illite. It is worth noticing that kaolinite is only present in and above 3028,77 mRKB and below 2977,65mRKB with two upward increasing trends. It should also be noticed that one sample is without any kaolinite (within the “kaolinite”) interval.

A clay mineral distribution overview(excluding smectite and mixed layer clays) shows the dominant clay mineral group to range between chlorite and illite, however some samples show an abundance of kaolinite (Figure 4-19). The kaolinite seems to be restricted from 3028,77 mRKB to 2979,65 mRKB with two upward increasing of kaolinite sequences.

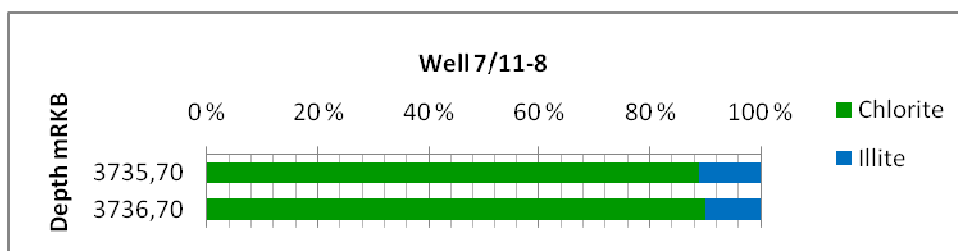


Figure 4-15. XRD clay fraction composition from well 7/11-8

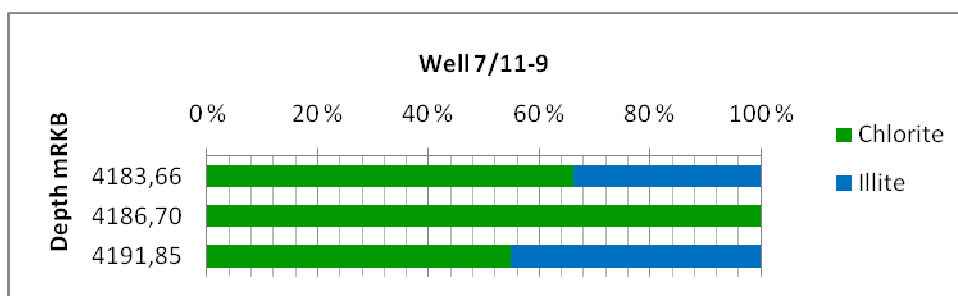


Figure 4-16. XRD clay fraction composition of samples from well 7/11-9

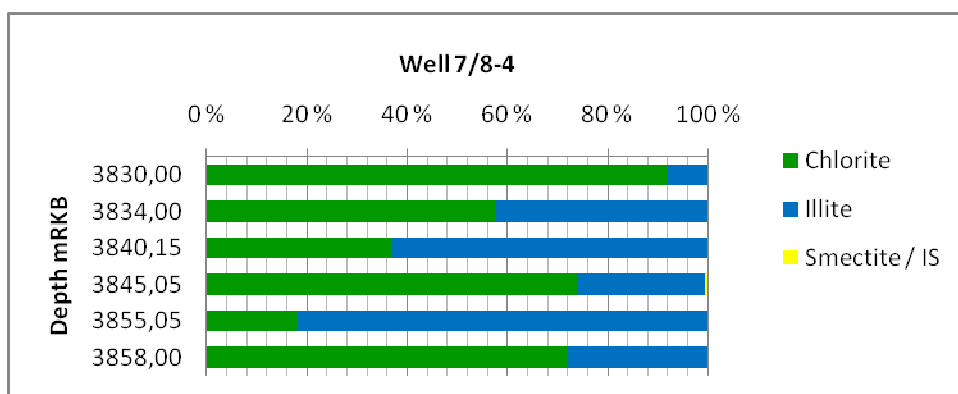


Figure 4-17. XRD clay fraction composition of well 7/8-4. Notice presence of Smectite/IS at 3845.05 mRKB

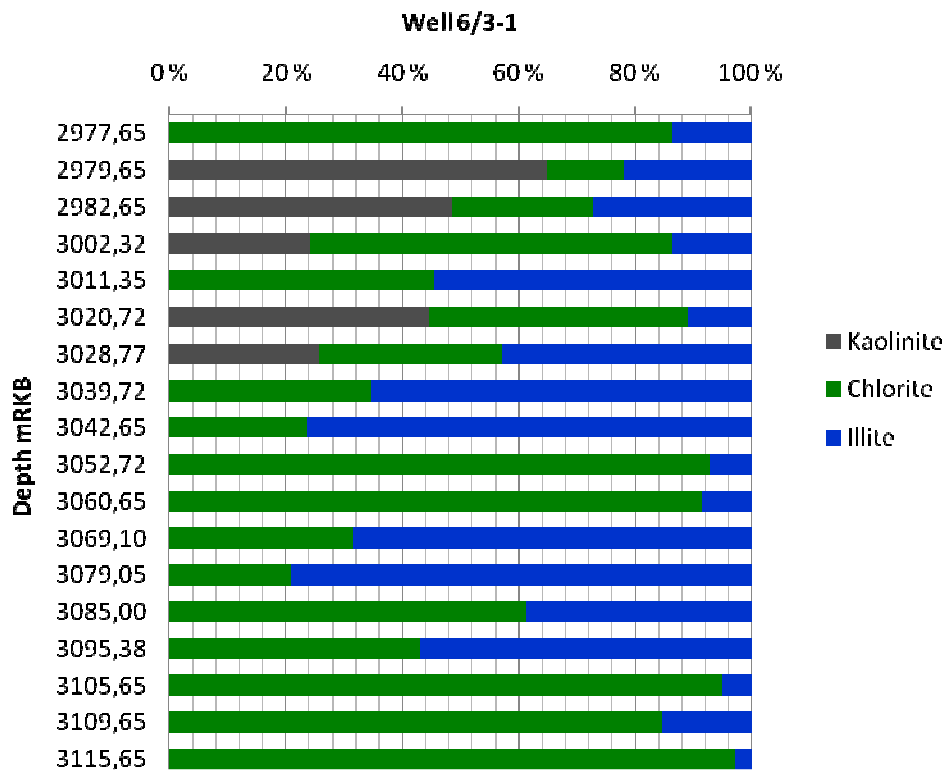


Figure 4-18. XRD clay fraction composition of well 6/3-1

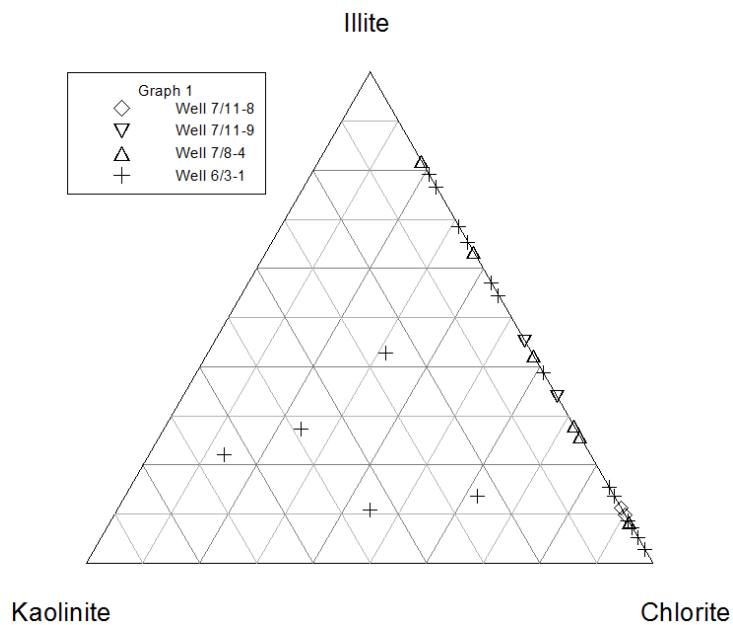


Figure 4-19. Ternary plot of the three most dominating clay minerals within the study area

4.3.3 Fe content of chlorite from XRD diffractogram

Fe content of two samples, 3115,65 mRKB and 3060,76 mRKB, have been determined based on the method after Moore and Reynolds (1997). The samples were chosen by three reasons. Firstly, a pore-coating material, assumed to be chlorite, and high porosities was identified in both thin sections (Appendix II). Secondly both samples showed high odd numbered reflections on the XRD diffractograms (Appendix Ib) implying high Fe chlorites according to Moore and Reynolds (1997). Thirdly, according to the XRD analysis high amounts of chlorite in the clay fraction is present in both samples (>90 XRD%, Figure 4-18). The amount of Fe in the octahedral position is 3 in the sample from 3115,65 mRKB and 4 in the sample from 3060,65 mRKB.

4.4 Combining XRD and thin section data

Simple relationship between mineralogy and porosity has been made to identify trends in well 6/3-1 (Figure 4-20) XRD% values less than 5% of Calcite and Dolomite/Ankerite favors higher porosities while above this high porosities are rare. Decreasing Illite XRD% favor higher porosities high porosities are found where illite is below 3 XRD%. As with Illite, low XRD% of chlorite (<5 XRD%) is needed to see high porosities, although the data is more spread than in illite.

A simplified log from the most densely sampled logs (well 6/3-1 and 7/8-4) illustrates the trends in mineralogical distribution with depth (Figure 4-21 and Figure 4-22). It should be noticed that only samples that have been analyzed by both XRD bulk and XRD clay fraction have been added. The lithology logs are simplified and based on core description logs from the completion logs. It should be noted that the lithology logs have been upscaled and areas with high amount of clay (even though it the logs say sand) is caused by the upscaling since small beds of 0.5m shale is present and have been sampled and analyzed by XRD.

In well 7/8-4 the trends in clay mineral abundance is evident with a fairly constant chlorite content and varying illite XRD%. An increase in illite and dolomite/ankerite XRD% can be seen around 3855mRKB together with a decrease in feldspar content.

Due to access of more samples well 6/3-1 displays several trends with increasing depth. There is a relationship between the amount of dolomite/ankerite with the amount of illite and chlorite, which increases at an expense of feldspar (mainly plagioclase) and quartz. High porosities are located where the amount of clay minerals and dolomite/ankerite and calcite is low while the opposite is true for low porosities.

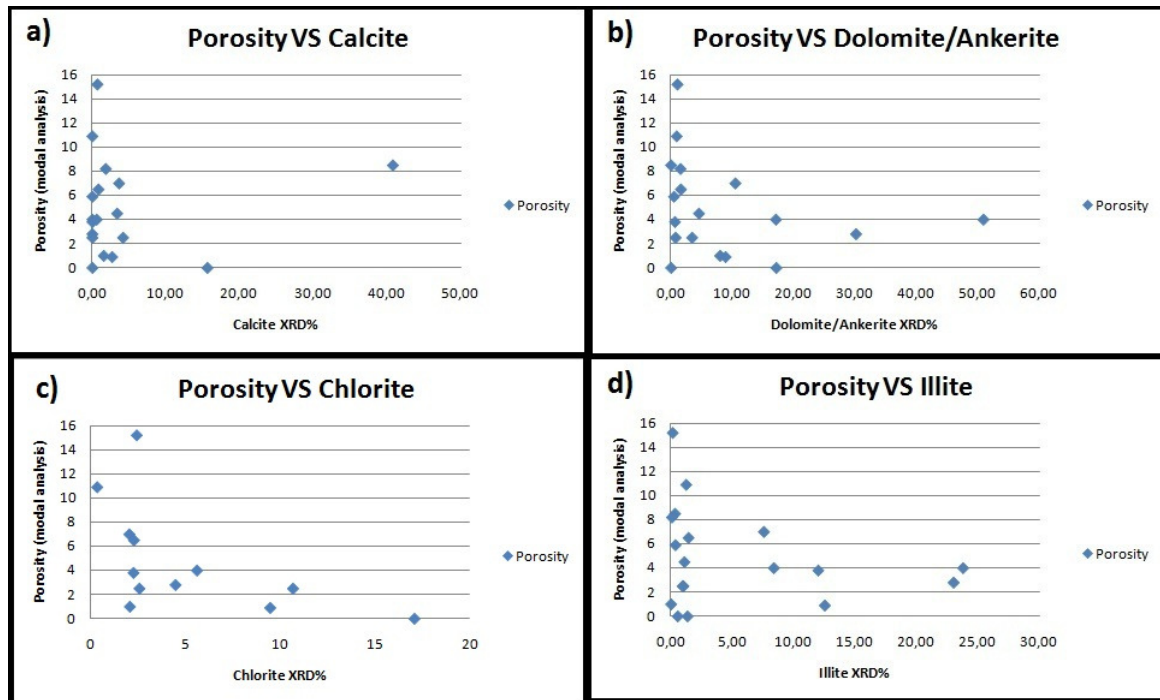


Figure 4-20 Specific minerals against modal analysis porosity estimation in well 6/3-1. NB real porosity is always higher than modal analysis porosity due to microporosity. a) Porosity plotted against calcite notice possible anomaly at 40 % calcite XRD %, b) Porosity plotted against Dolomite/Ankerite XRD %, c) Porosity plotted against chlorite XRD %, d) Porosity plotted against illite XRD %

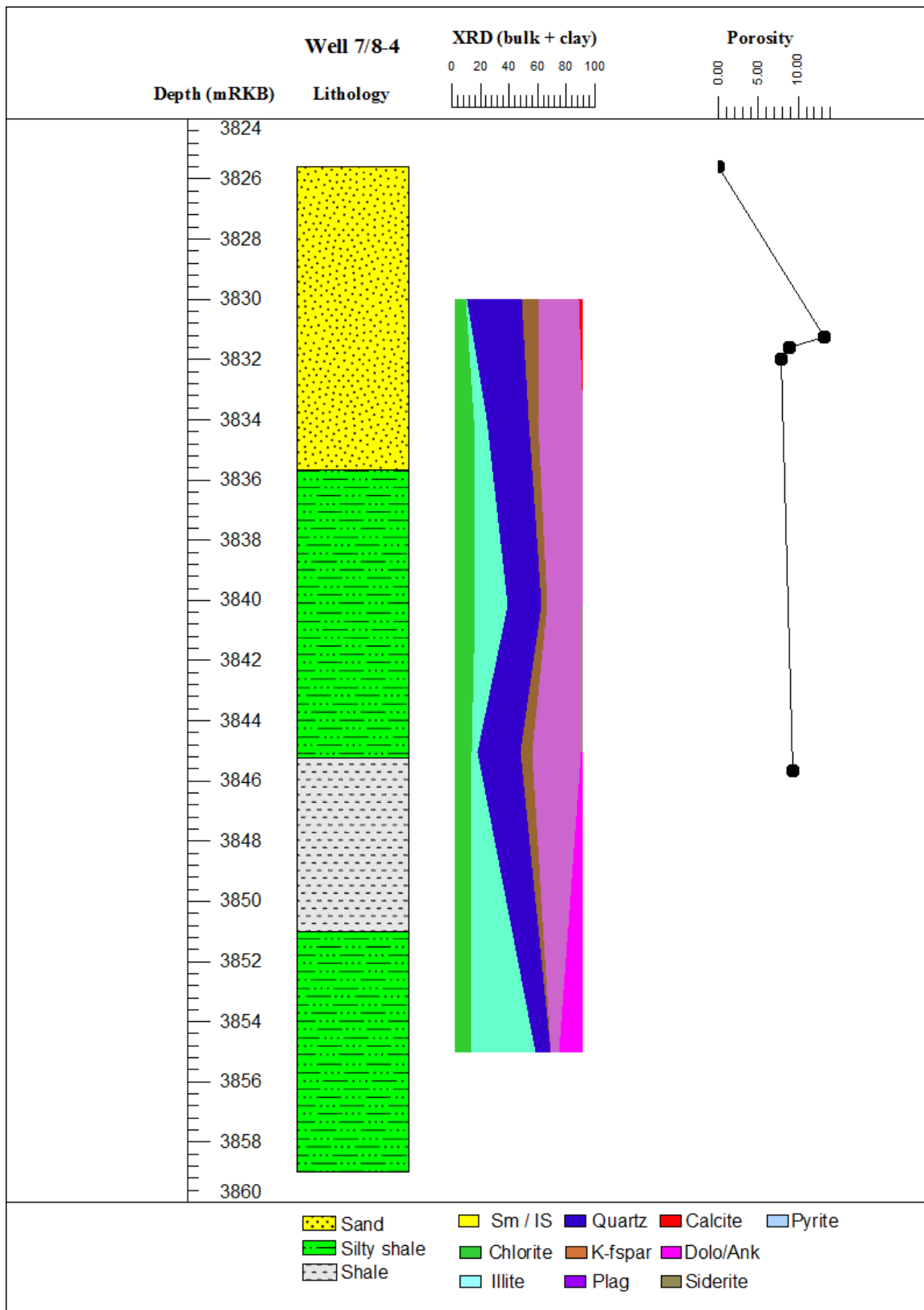


Figure 4-21. Simplified lithology log from well 7/8-4 with a complete XRD data description (both clay fraction- and bulk data) and porosity from modal analysis

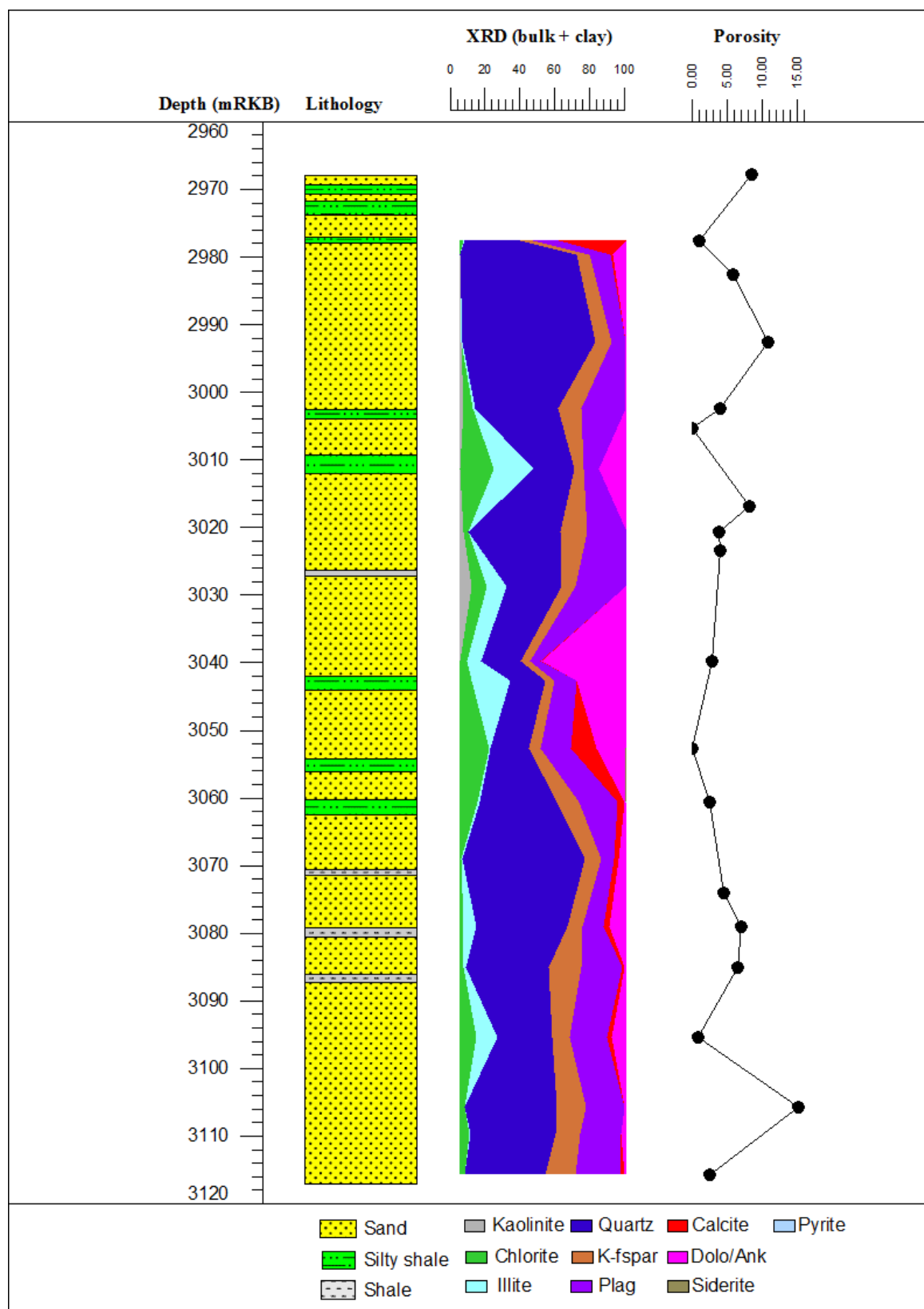


Figure 4-22. Simplified lithology log from well 6/3-1 with a complete XRD data description (both clay fraction- and bulk data) and porosity from modal analysis

4.5 SEM

Eight samples, from well 6/3-1, of both cemented and porous sandstones, have been examined by SEM with the purpose of identifying clay morphology and mineral associations. All minerals identified in Figure 4-23 to Figure 4-30 have been confirmed by the use of energy dispersive spectrometer (EDS). A wide range of minerals have been identified in random order: Kaolin, illite, chlorite, smectite, apatite, biotite, calcite, ankerite, dolomite, feldspar and quartz.

4.5.1 Secondary Electron Image (SEI)

Five porous sandstone samples (gold coated “stubs”) have been investigated by SEI. The samples have been presented with increasing burial depth (2992,65 mRKB – 3069 mRKB).

In the sample from 2992,65 mRKB (Figure 4-23) three main types of clay can be identified: chlorite, kaolin and illite. All the clay minerals in this sample occur as pore-filling between detrital quartz. The morphology of the clay minerals that can be recognized is the characteristic authigenic booklet shaped kaolin and platy illite possibly from a smectite precursor due to the platy morphology. A small piece of calcite can be seen on top of a quartz overgrowth next to pore-filling platy chlorite.

From the depth of 3016,77 mRKB (Figure 4-24) presence of quartz overgrowth and interstratified illite/smectite rim cement with a pore-bridging morphology is seen. The distribution of the rim cement seems to within a limited area.

Extensive chlorite coating with honeycomb morphology is seen in Figure 4-25 at 3022,65 mRKB burial depth. The coating did not cover the entire grain thus haven't prevented quartz overgrowth to occur. The quartz overgrowth fills in the porespace and reduces reservoir quality. Other clay minerals such as smectite and illite have been identified with a platy pore-bridging morphology although the illite is more fibrous in some areas. Feldspar is also seen with dissolution along cleavage planes.

At a depth of 3069,10 mRKB (Figure 4-26) both illite and illite/smectite has been identified. The illite occurs as both platy and fibrous and fills in the pore space with a fibrous

morphology. Quartz overgrowth can be seen in the space between two detrital feldspars. Some feldspars has also been extensively dissolved along its crystallographic axis.

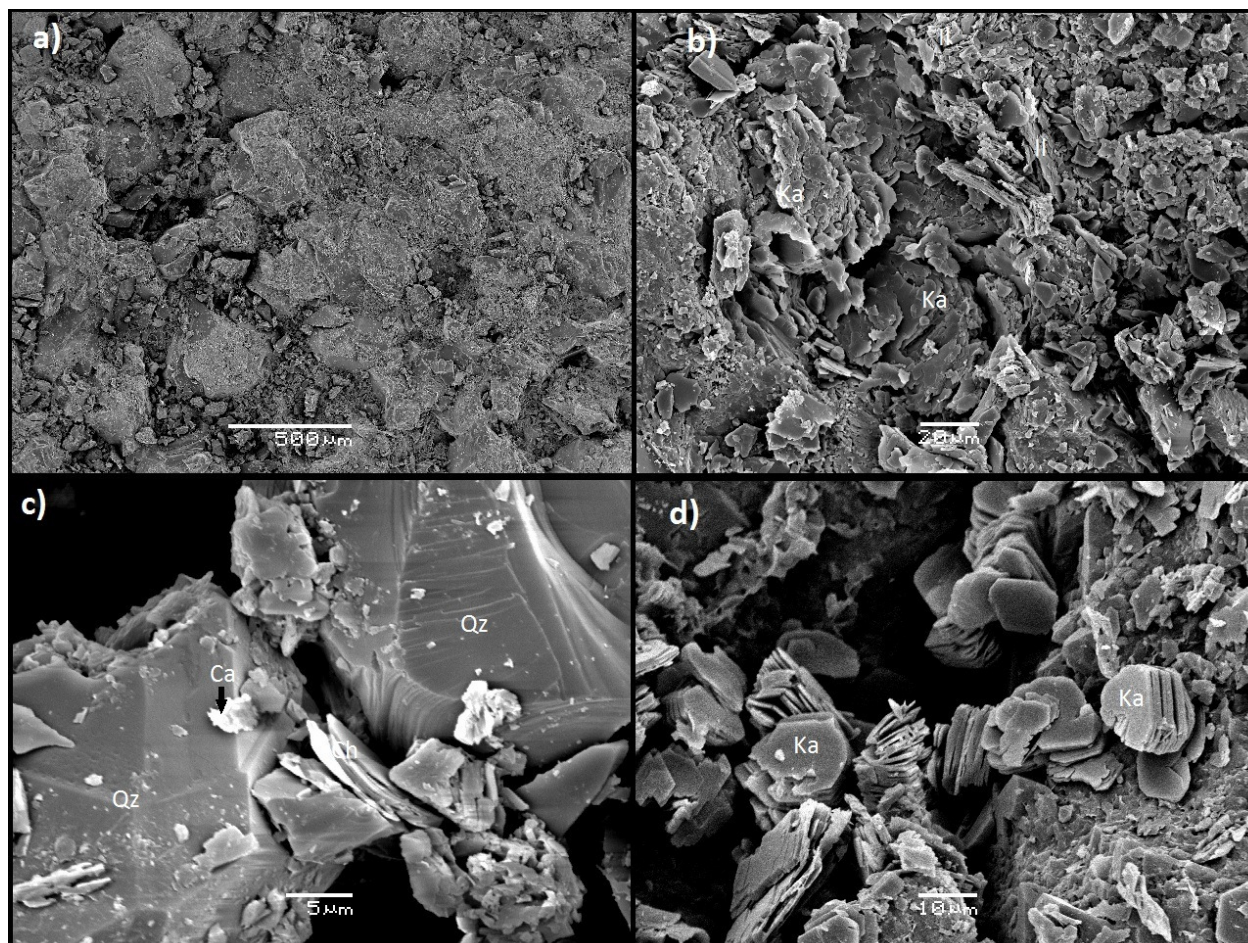


Figure 4-23. SEM-SEI images of sample from 2992,65 mRKB. a) Overview of the sample showing good sorted subrounded-subangular medium grained sandstone with pores (black area) and matrix, b) Close-up of porefilling, possibly, detrital kaolin (Ka) and authigenic illite (Il), c) Detrital quartz (Qz) with pore-filling chlorite (Ch) and presence of calcite (Ca), d) Authigenic kaolin with the characteristic booklet shape

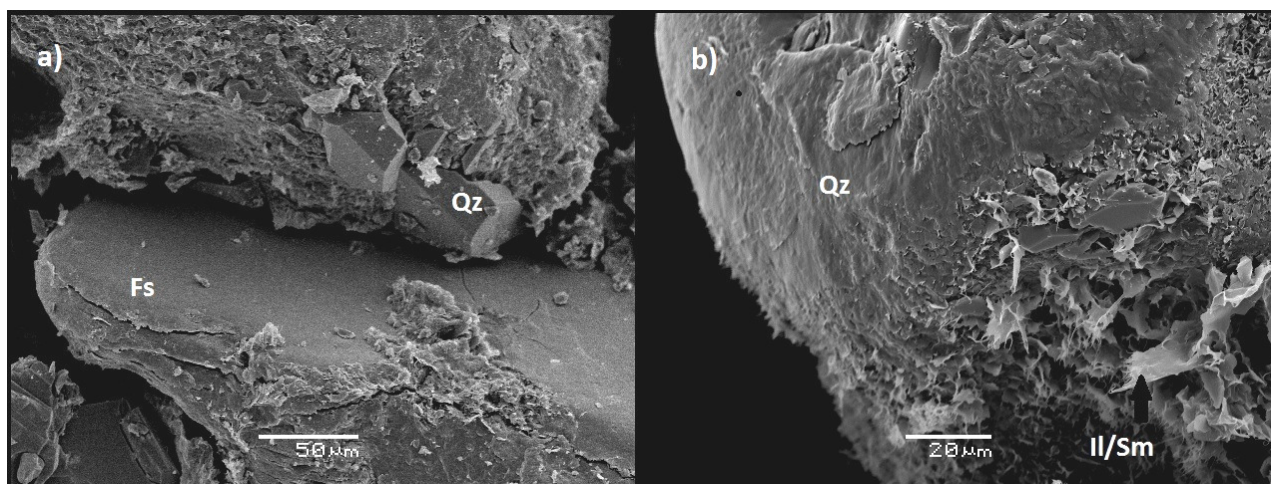


Figure 4-24 . SEM-SEI images of sample from 3016,77 mRKB. a) Quartz overgrowth (Qz) next to a detrital feldspar (Fs), b) Illite/smectite rim cement (Il/Sm) with a pore-bridging morphology

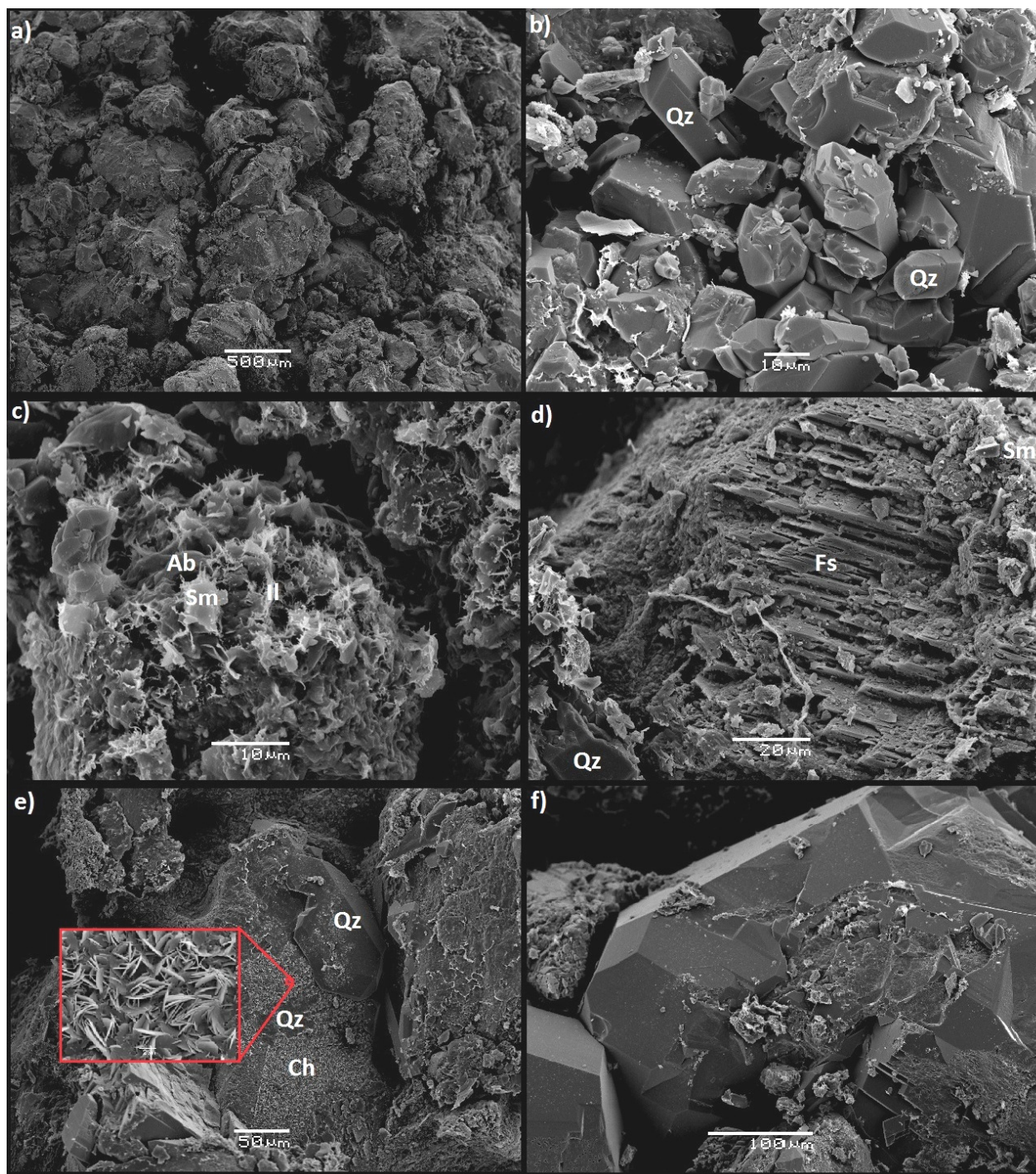


Figure 4-25. SEM-SEI images of sample from 3022,65 mRKB. a) Overview of coarse grained moderately sorted sandstone, b) Randomly oriented authigenic euhedral quartz grains (Qz), c) Albite (Ab), smectite (Sm) and illite(II) coating a detrital grain, d) Dissolved feldspar (Fs) suggesting that dissolution process was surface-reaction controlled along selected lattice planes, e) Extensive chlorite (ch) coating on a detrital quartz (Qz) grain with quartz overgrowth on it. Enlarged area displays the characteristic honeycomb morphology of chlorite. White line for scale in the enlarged is 2μm, f) Large quartz overgrowth filling the pore space

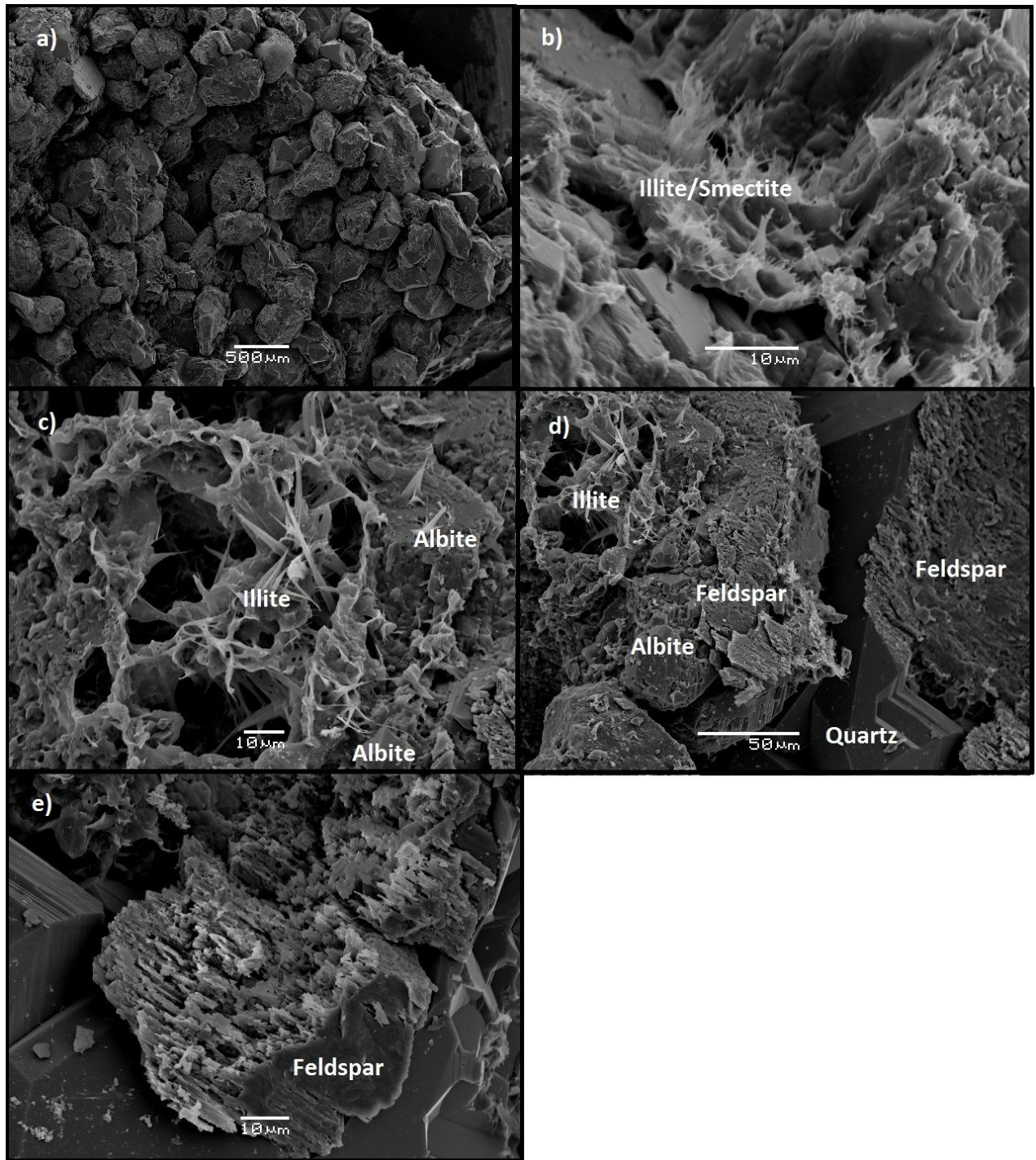


Figure 4-26. SEM-SEI images of sample from 3069, 10 mRKB. a) Overview image of clean good sorted medium grained sandstone, b) Pore-bridging illite/smectite (Il/Sm) on a detrital grain, c) Fibrous illite along albite, d) Fibrous illite and quartz overgrowth on detrital feldspar, e) Extensively dissolved feldspar along its crystallographic axis

4.5.2 Backscattered Electron Image (BSI)

Three sandstone samples were studied by BSI due to presence of cement and varying reservoir qualities within the thin sections.

In the sample from 2996,65 mRKB (Figure 4-27) several heavy minerals can be identified: rutile, apatite, barite, zircon and pyrite. The presence of pyrite can often be seen next to or within cleavage planes of biotite. A deformed biotite and fractures within the grain is visible. Pore-filling kaolin can also be seen filling up open pore space and pore throat, severely reducing permeability and porosity. There is also several oversized pores (could not be a part of primary porosity) that indicate dissolution of unstable minerals (for instance feldspar or rock fragments) have taken place.

At 3023,42 mRKB similar relationship between biotite and pyrite can be seen (Figure 4-28). Three generations of cements have been identified: calcite, ankerite and dolomite. The calcite cement is most abundant with patches of dolomite and ankerite. The calcite cemented sample seems unaffected by compaction. Among the clay minerals pore-filling authigenic kaolin is present, having a reducing effect on reservoir quality.

Extensive examination of points around a feldspar overgrowth can be seen in Figure 4-29 where calcite cement, quartz and biotite is present. The difference in EDS spectrum 1 and spectrum 2 clearly illustrate the composition of feldspar overgrowth and detrital feldspar where barium is often found in detrital feldspar. The feldspar overgrowth seems to have nucleated into porespace thus believed to predate the calcite cement.

Pore-filling chlorite and illite can be seen in the sample from 3016,77mRKB (Figure 4-30). Minor fracturing indicates mechanical compaction at grain-to-grain contacts. The fracturing usually occurs in weak zones and can be used to recognize different minerals (for instance feldspar). The importance of secondary porosity caused by dissolution of feldspar is seen as it is mostly unaffected by the pore-filling chlorite and illite. Presence of barite next to dissolved feldspar might be due to contamination from drilling mud.

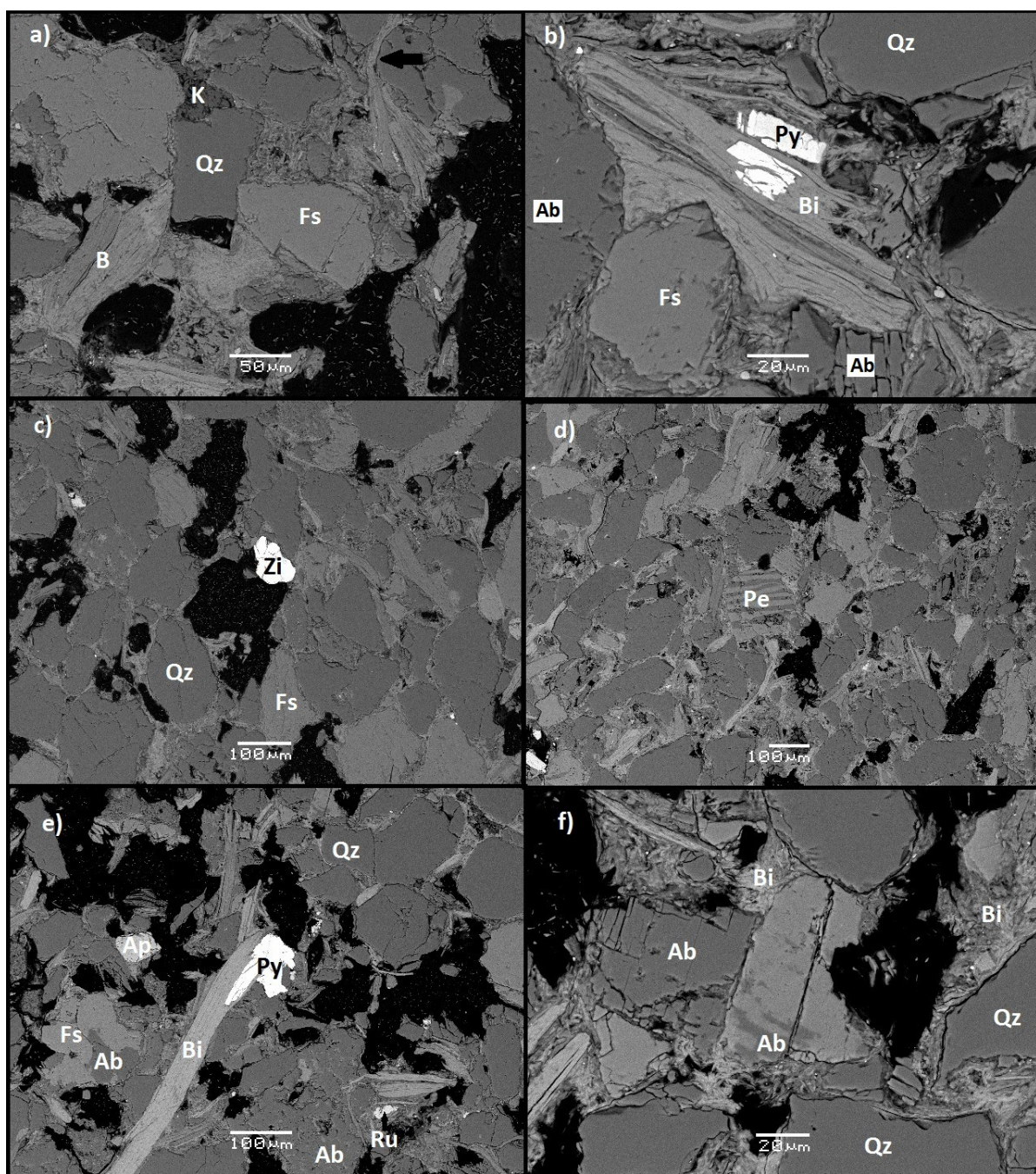


Figure 4-27. BSI image from 2996,65 mRKB a) pore-filling kaolinite (K) with biotite (B) quartz (Qz) and feldspar (Fs). Notice ductile bending of mica (black arrow), b) deformed biotite with pyrite (Py), large albite (Ab) grains are also visible, c) Accessory mineral Zircon (Zi), present within the sandstone d) Perthite with irregular veins, e) Accessory mineral pyrite, rutile (Ru) and pyrite (Py) seen in the sample. Notice albitization (Ab) lowermost left, f) Albitization (Ab) of feldspar and porefilling deformed biotite

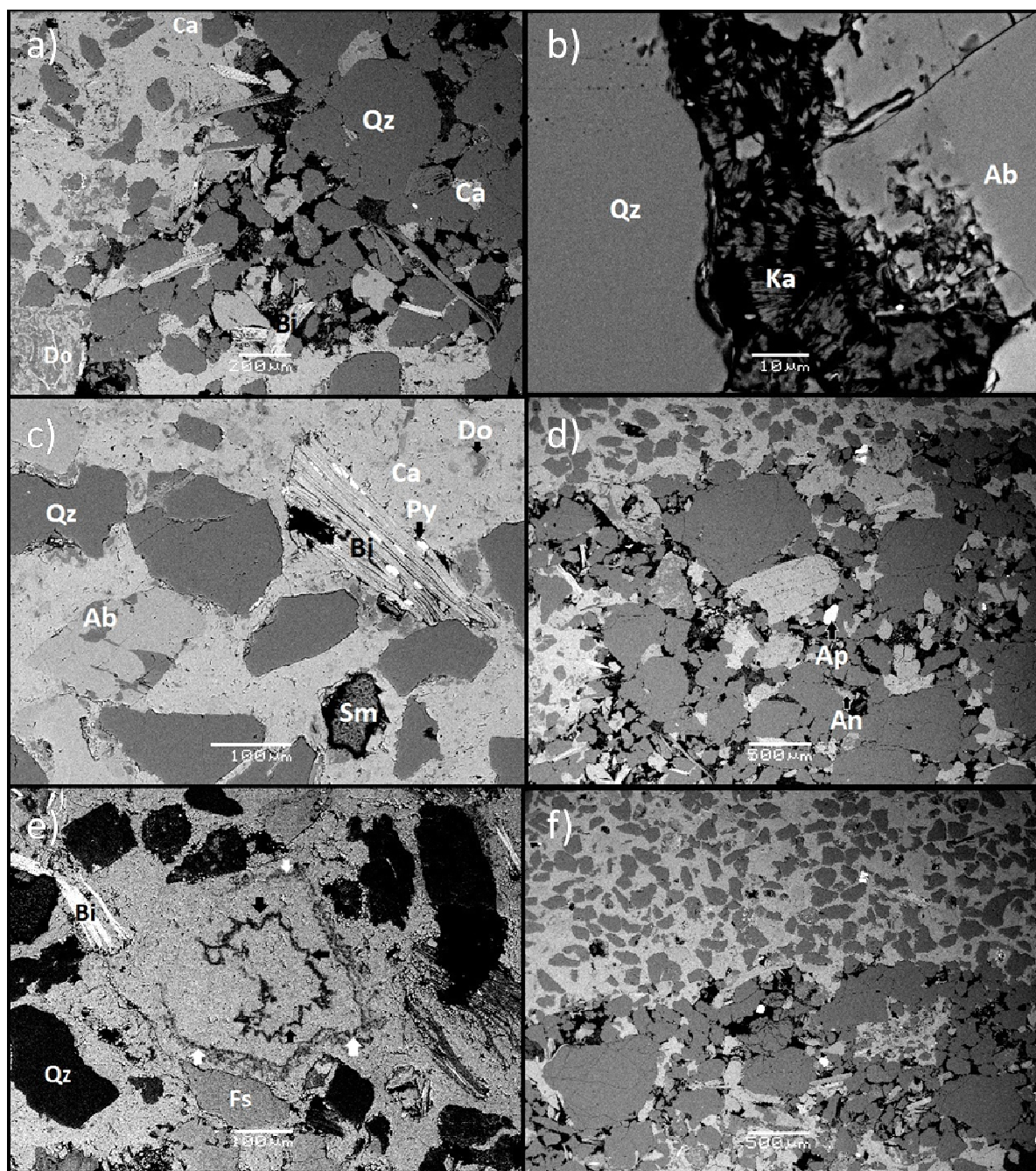


Figure 4-28. BSI image of 3023,42 mRKB. a) Area of extensive cementation (both calcite(Ca) and dolomite(Do) and a uncemented area, b) Pore-filling kaolinite between quartz and albite, c) Biotite with local concentration of pyrite. Smectite present within a cluster (Sm) in the calcite cement. Albitization is also present, d) Small amounts of ankerite (An) seen within the calcite cement, e) Dissolved grain filled with cement outlined by ankerite cement (black arrows), and a second rim of dolomite (white arrows) f) Sudden change in cementation and grain size (boundary?)

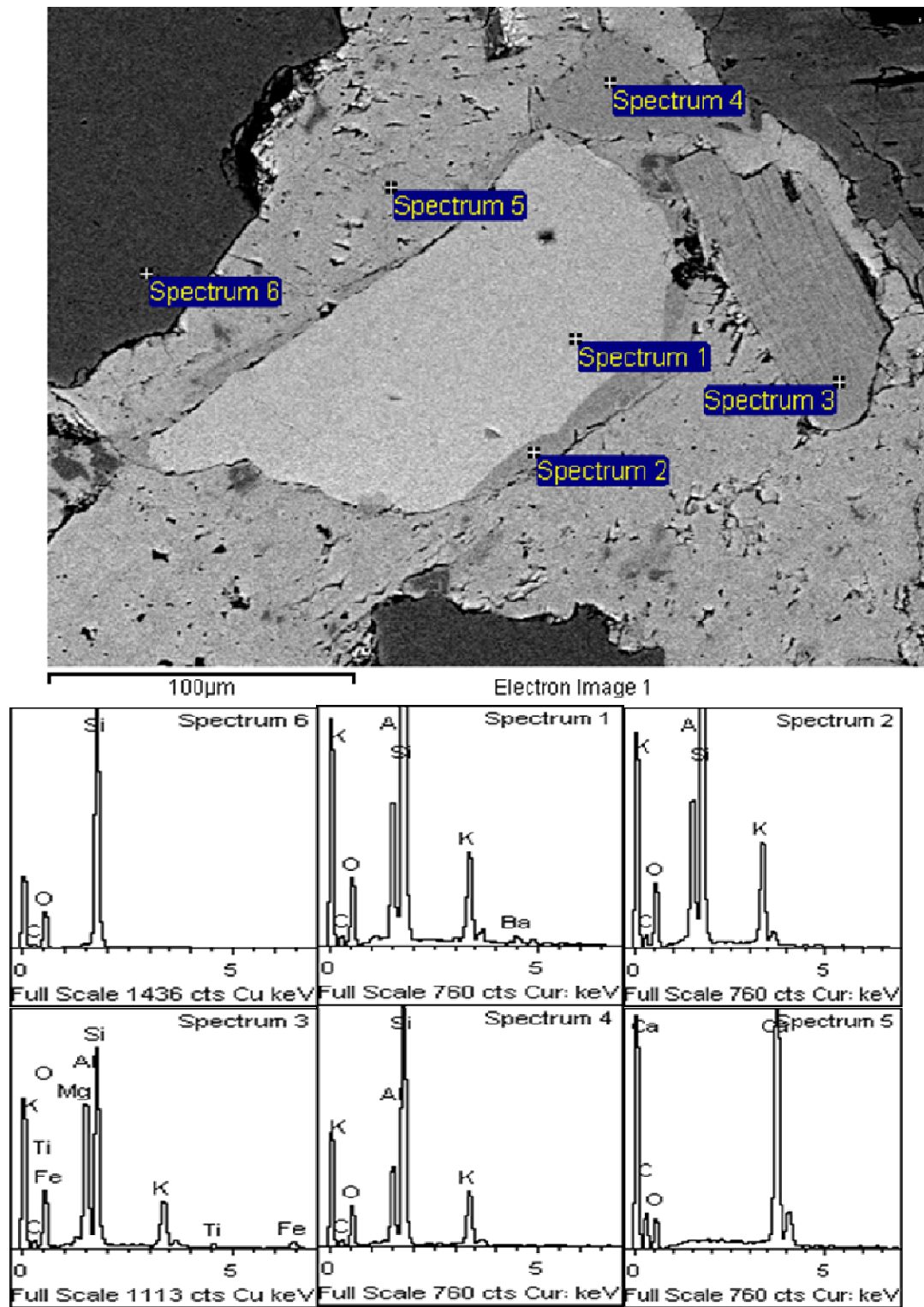


Figure 4-29. Feldspar overgrowth (spectrum 2) pre-dating calcite cement (spectrum 5) at 3023,42mRKB. Notice presence of barium in detrital feldspar (spectrum 1) in comparison to the feldspar overgrowth. Spectrum 3 is identified as biotite while spectrum 6 is a detrital quartz grain

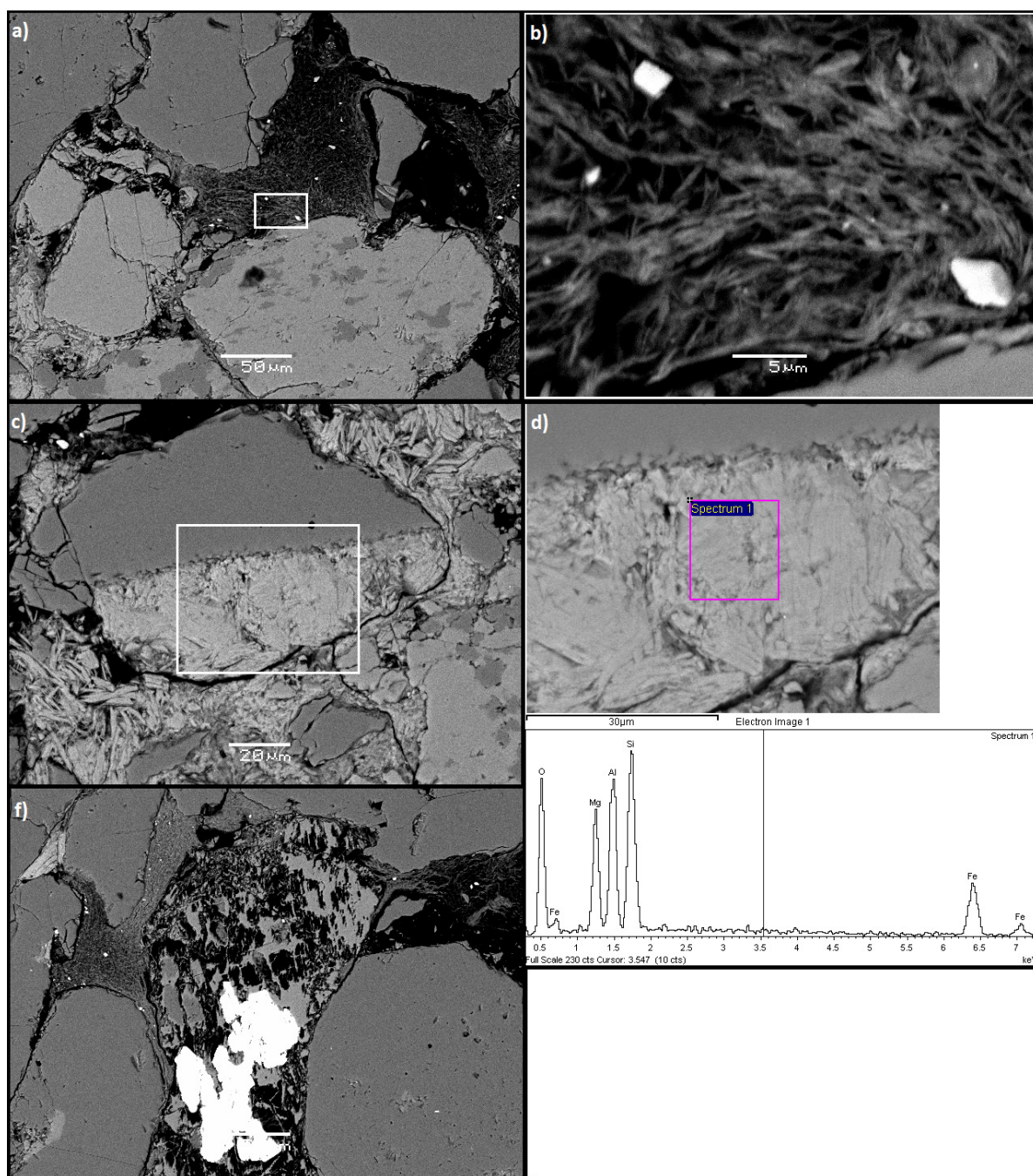


Figure 4-30. Sample from 3016,77 mRKB. a) Pore-filling clay mineral next to partly albitized feldspar. Presence of fractured grains indicate mechanical compaction, b) Enlarged area from a) showing the needle like pore-filling properties of Illite, c) Possible rock fragment consisting of quartz and chlorite mineral. Notice the pore-filling properties of chlorite surrounding the rock fragment d) Enlarged area from c) showing the EDS spectrum of a selected area (spectrum 1) characteristic of chlorite, f) White bar for scale is 50μm. Pore-filling illite present between silica grains on left side while a heavily dissolved feldspar with barite (white color) in the middle

4.5.3 Fe content of Chlorite by SEM-SEI

Bulk samples from the samples investigated in 4.3.4 were examined by SEM-SEI based on the method in section 3.4.1 (3115,65 mRKB and 3060,65 mRKB). The amount of Fe in 3115,65 mRKB is 2,31 while 3060,65 mRKB has a Fe content of 2,39.

Chlorite				
Chlorite : Fe / (Fe+Mg)				Average composition
Sample	Average	Max	Min	(Mg _{1,91} , Fe _{2,31} , Al _{1,43}) (Al _{0,72} , Si _{3,28}) O ₁₀ (OH) ₈
3115,65(n=11)	0,55	0,64	0,42	
3060,65(n=15)	0,61	0,72	0,34	

5. Petrophysical data

5.1 Introduction

This chapter will investigate the physical properties related to the cored reservoir intervals in the study area. Data from 7/11-8 and 7/11-9 will not be petrophysically investigated as the small amount of XRD samples only provides us with an impression rather than mineralogical trends that can be compared with the log response. The main purpose for the petrophysical logging is to estimate porosity and identify lithologies from the logs.

5.2 Wire line log

Wire line log analysis has been used to estimate porosity, lithology and fluid content. Permeability and porosity values from core plugs are unavailable from well 6/3-1 but present in well 7/8-4.

Caliper, sonic transit time, neutron porosity, density, deep and shallow induction, gamma log and porosity derived from density have been plotted in Figure 5-1 to provide with a general overview. Lithologies are illustrated by NPHI/RHOB cross plot where yellow color indicates sand and green color indicates shale.

5.2.1 Log quality

The caliper log has been used to identify trouble areas regarding the log quality. All of the anomalous porosity spikes can be related to enlarged hole size found in the caliper log. The enlarged hole size reduces the quality of the density (density pad not in contact to the rock) and neutron porosity (attenuation by borehole fluids). The enlarged hole size caused by cavings is likely to be associated with shale units.

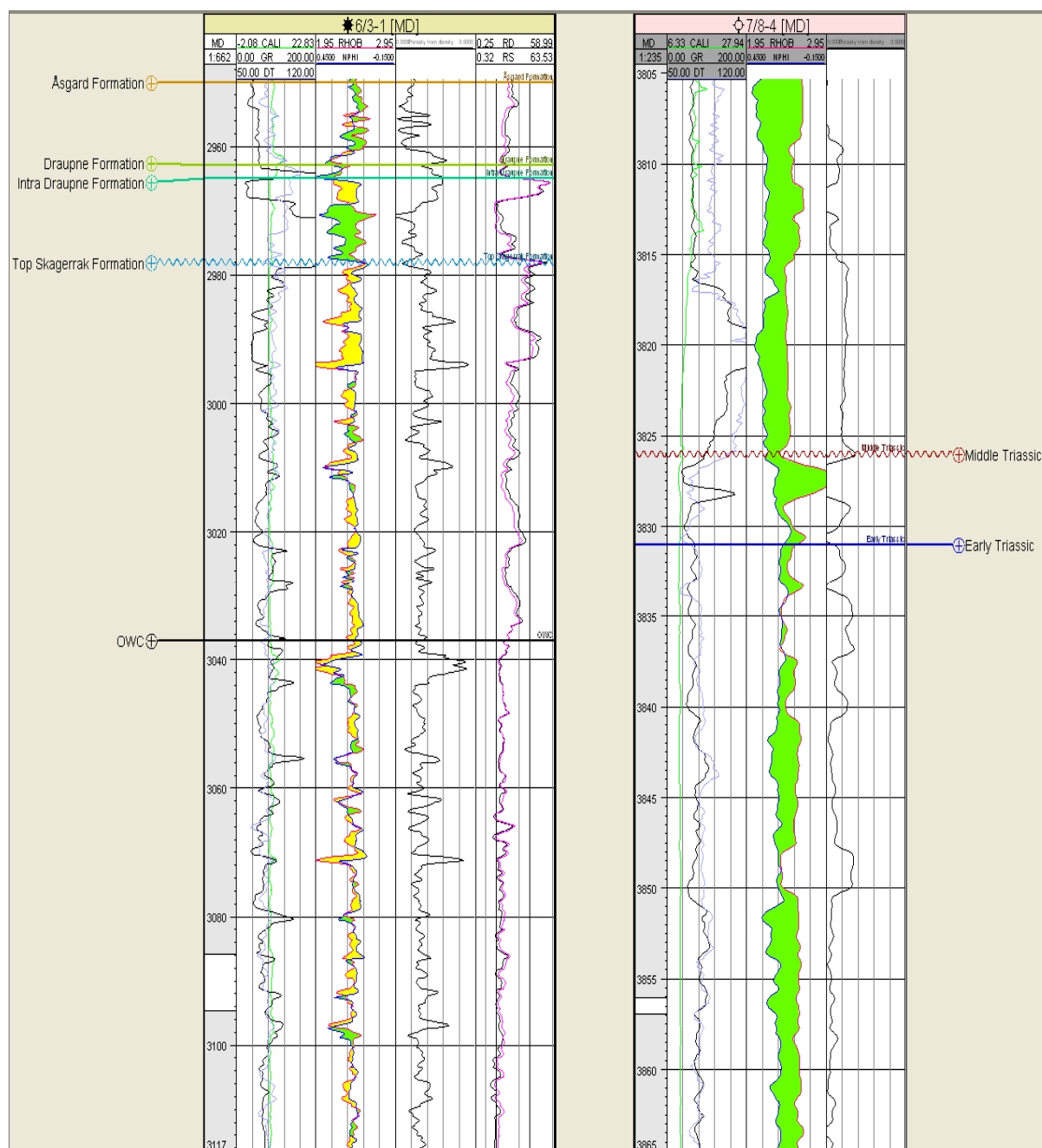


Figure 5-1. Wireline log overview of well 6/3-1 with proven OWC(Oil-Water contact) and 7/8-4. Notice different depths. Yellow color indicates sand while green indicate shale. Porosity values are located in track 3 based on density-porosity relationship.

Well 6/3-1 consists of interbedded shale and sand with cemented areas indicated by low density (and spike in porosity). Several dirtying-up trends can be seen in the GR log indicating an upward decrease in energy, probably related to fluvial channel infill assuming continental deposits. Abrupt shifts in energy at both base and top at 2990mRKB indicating either fluvial sandstone units. Notice that this boxcar trend is capped between two low density (high porosity) units, possibly related to carbonate cement or flooding surfaces. Most of the high gamma readings can be found on top of a dirtying upward trend. The fluid content has been confirmed to be water filled below OWC (by completion log) and this is also reflected in the resistivity log. This again implies presence of porosity and at least decent permeability within these hydrocarbon filled zones.

Well 7/8-4 Shows an irregular trend (GR) most of the time indicating a frequent changes in energy.

5.2.2 Cross plots

Several cross plots has been made in order to identify zones of interest regarding mineralogy and fluid content. Density has been plotted against depth to identify areas of high/low densities. The average density is around 2.38 g/cm^3 decreasing slightly upwards from 3037mRKB (Figure 5-2).

The porosity has been plotted against depth (Figure 5-3) where the porosity values range between 0 and 43% with an average around 13%. Several abnormal porosity spikes can be observed ($>25\%$) and is related is related to low densities. No clear trends are visible except a general increase in porosities above 3040mRKB most likely related to presence of hydrocarbon and corresponding decrease in bulk density. On top we see values reaching 0% that correspond to the Draupne Formation (hot shale).

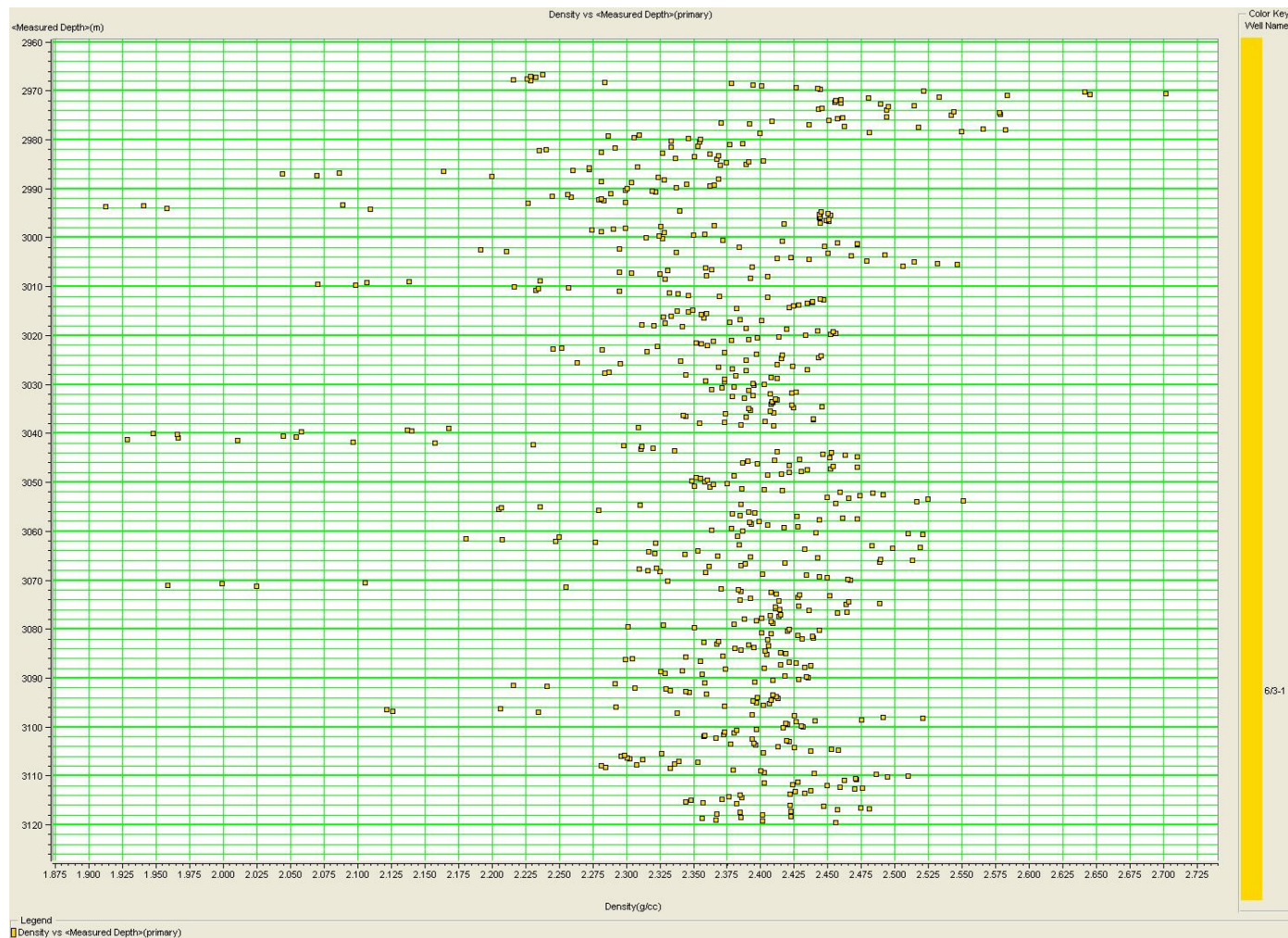


Figure 5-2. Density – Depth cross plot of the cored reservoir interval in well 6/3-1

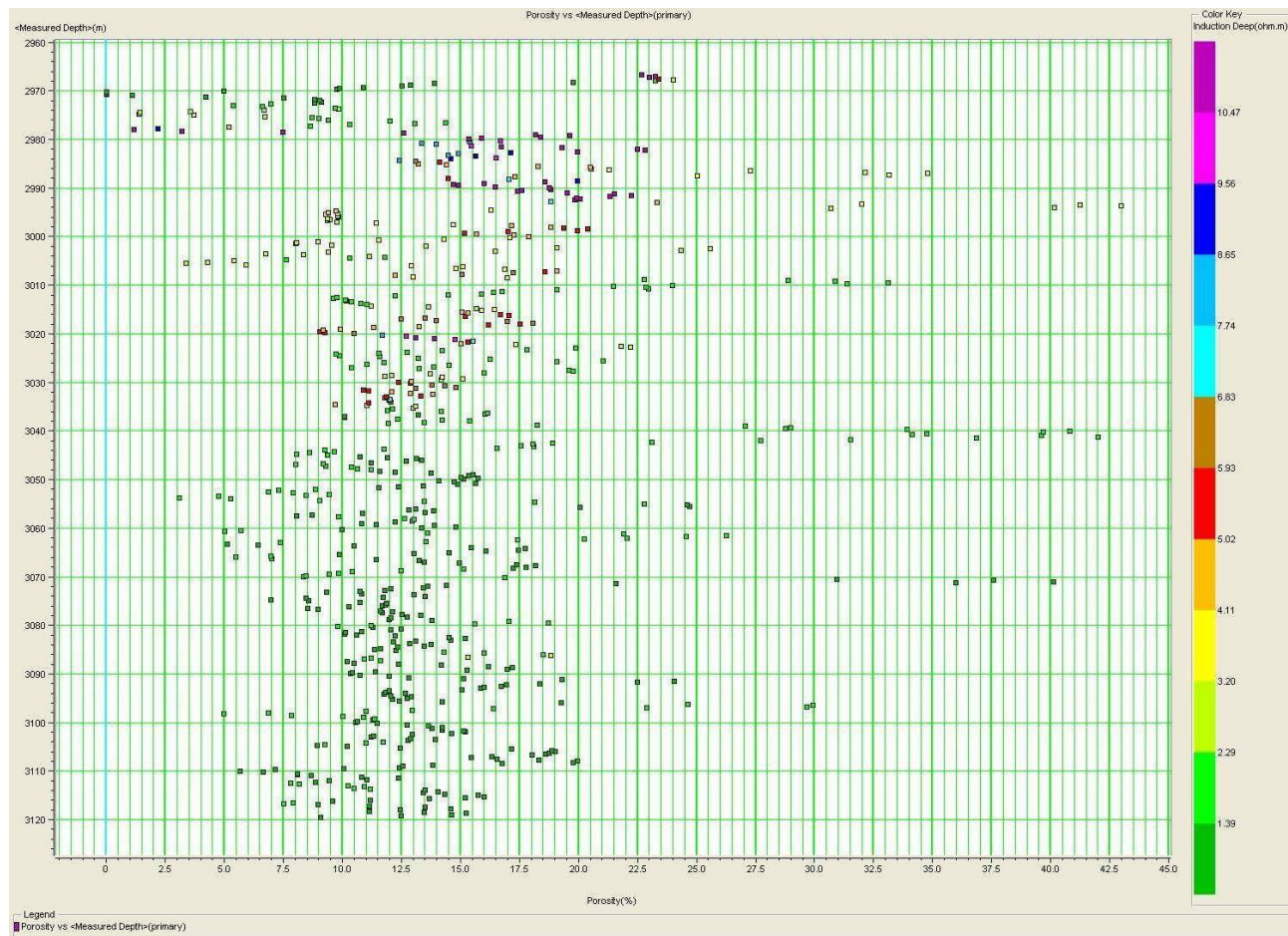


Figure 5-3. Porosity – depth cross plot with color coded deep induction measurements. Notice that high deep induction readings only can be located above proven OWC contact is at 3017mRKB. Abnormal high porosities can be related to very low densities associated with cemented areas

Presence of hydrocarbon in the well can be seen by the change in sonic transit time trends with depth (p-wave affected by fluids) (Figure 5-4) where a decrease in sonic transit time is expected in the hydrocarbon zone in comparison to the water filled area. As with the induction readings in Figure 5-1 the oil bearing zones can be mapped out by cross plotting gamma-ray values with depth and color code the induction. Five hydrocarbon bearing zones have been identified (Figure 5-5) based on low gamma value (<75API) and high deep induction values. Good reservoir quality is expected to be within these zones with respect to both porosity and permeability.

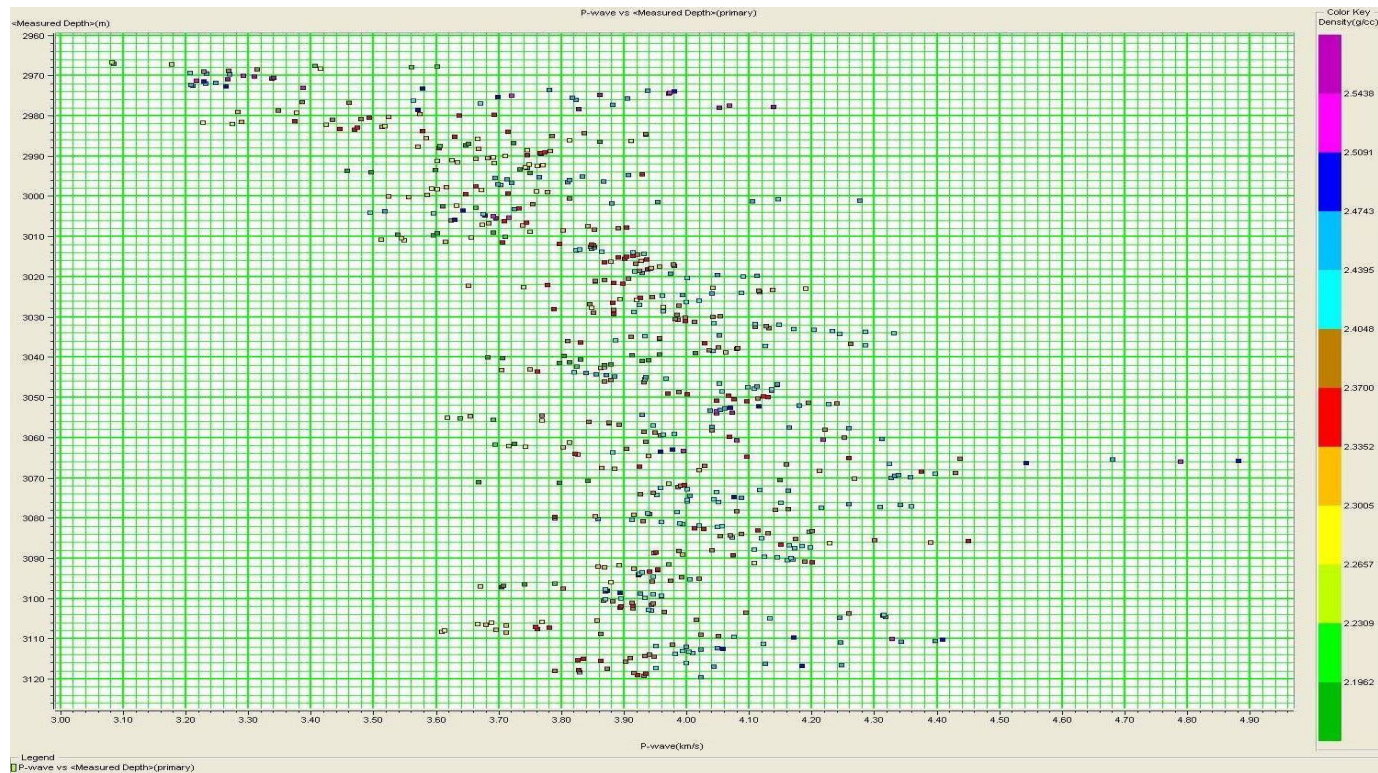


Figure 5-4. P-Wave – Depth cross plot with color coded density. Higher density areas are associated with cemented intervals and low porosity while lower density is associated with high porosity (presence fluids (water/gas/oil) sandstone. Notice that the shift in P-wave trend occurring at OWC contact, indicating an influence on P-wave velocity by hydrocarbon filled pores

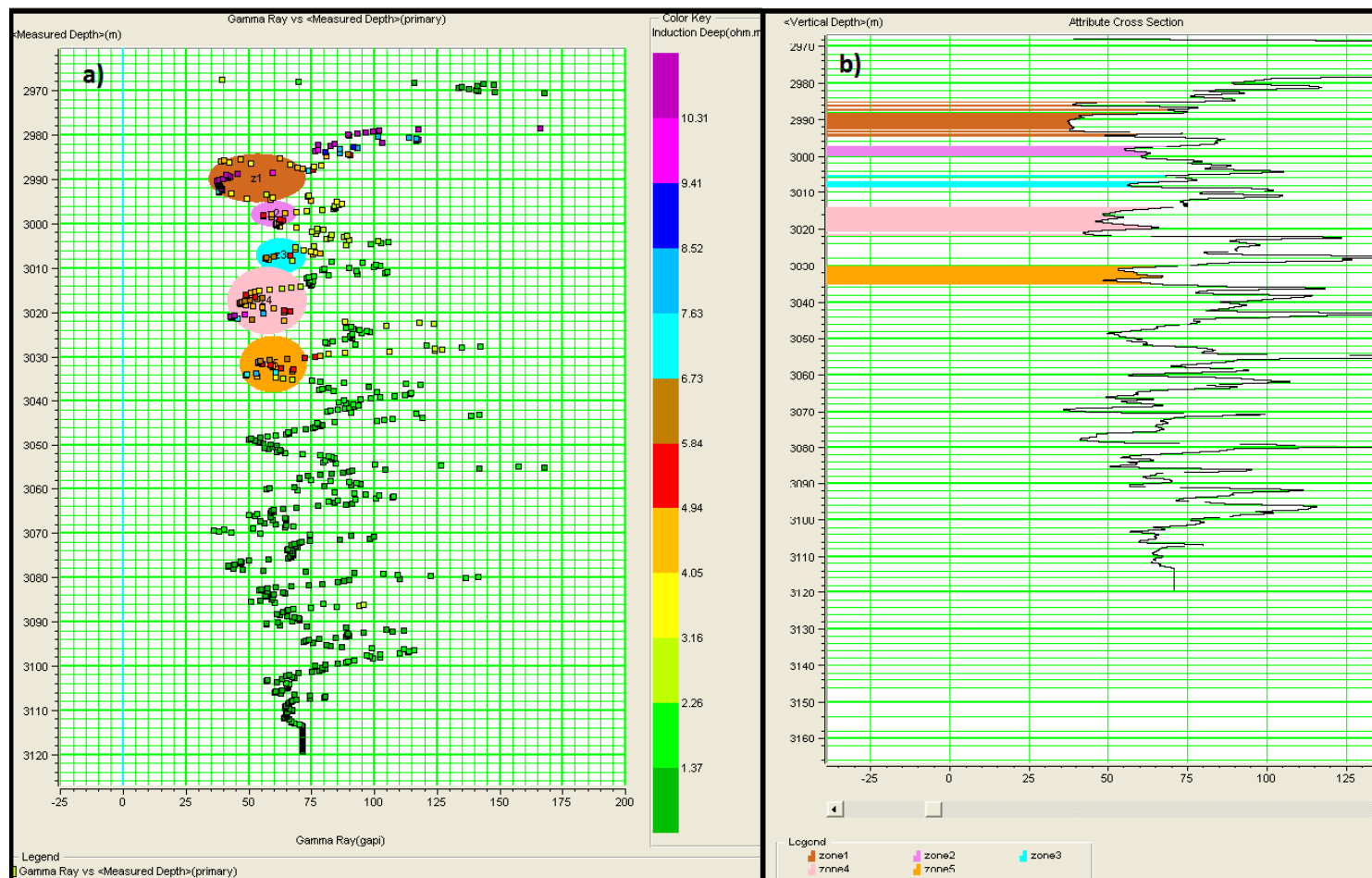


Figure 5-5. Well 6/3-1 a) Gamma ray plotted against depth with color coded induction deep. Five zones with low gamma-ray (<75API) and high induction values have been marked by 5 different zones. b) Cross section of gamma log against depth with depth intervals belonging to different points marked by zones in a)

The complete mineralogical response on wire line logs is difficult to interpret and require a lot of calibrated data in order to minimize uncertainties. The author has not calibrated any wireline log and big uncertainties are related to the interpretation, however they should provide a general impression of the wells. Neutron porosity and density have been cross plotted to identify different lithologies in the data (Figure 5-6a). The three different zones indicate lithology trends (purple = dolomite, yellow = sandstone, cyan = limestone) and are based on standard values by Schlumberger. The cross section (Figure 5-6b) color code the corresponding zones with depth and the lithological trends is shown. The varying lithologies show an abundance of carbonate cement (dolostone/limestone) looks which is most likely overrated. However specific depths of dolostone can be correlated to porosity spikes from Figure 5-1 and Figure 5-3.

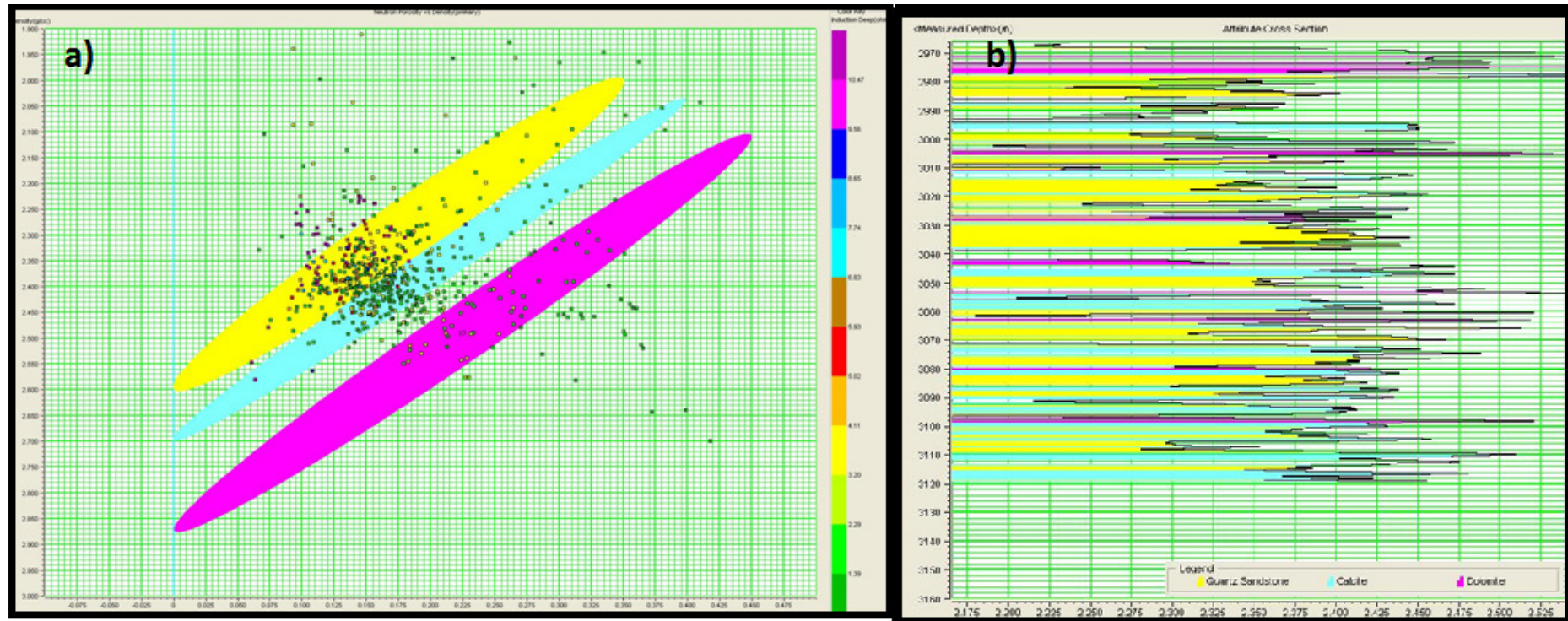


Figure 5-6. Well 6/3-1. a) NPHI - Density cross plot with zones used for identifying lithologies (Yellow = sandstone, Cyan = limestone, Purple = dolomite). Data points are color coded by deep induction (resistivity). b) Cross section of zone values from Figure 6-4 plotted with the density values against depth

Porosity against permeability plot has been made for selected samples from Table 4.2 belonging to well 7/8-4 (Figure 5-7). It is based on core plug measurements given in the completion log. This plot shows that an increase in porosity gives an increase in both horizontal and vertical permeability. Good permabilities can only be seen with porosity values exceeding 15%. Porosity values from core plugs will be higher than thin section quantified porosities due to presence of microporosity not visible in thin sections.

A more complex cross plot has been made in the water filled well 7/8-4 by LMR (Lamba-Mhu-Rho). The S-wave was calculated by the Castagna Equation and default values in Hampson Russel were used to calculate Lamda-rho and Mhu-rho. Five zones have been made according to its lithological response: grey = cemented sandstone, yellow = sandstone, blue = shale, cyan = coal, brown = carbonates. The zones were plotted against depth which gives a rough lithology log. It should be noted that most of the sand and cemented sand is located in the upper section. Presence of coal is indicated in the uppermost part of the section, this however was not observed in the core description log or indicated by the wireline log in Figure 5-1. Similar plot has not been made for well 6/3-1 due to its increasing complexity with different combination of pore fluids affecting pore fluid density.

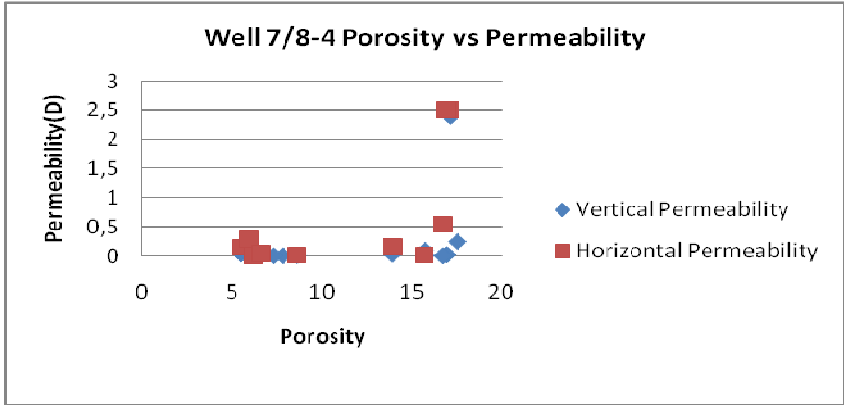


Figure 5-7. Well 7/8-4. Porosity (He porosity from core plug) against permeability (core plug), indicating high permeability (>0,5D) is present when porosity reaches around 15%

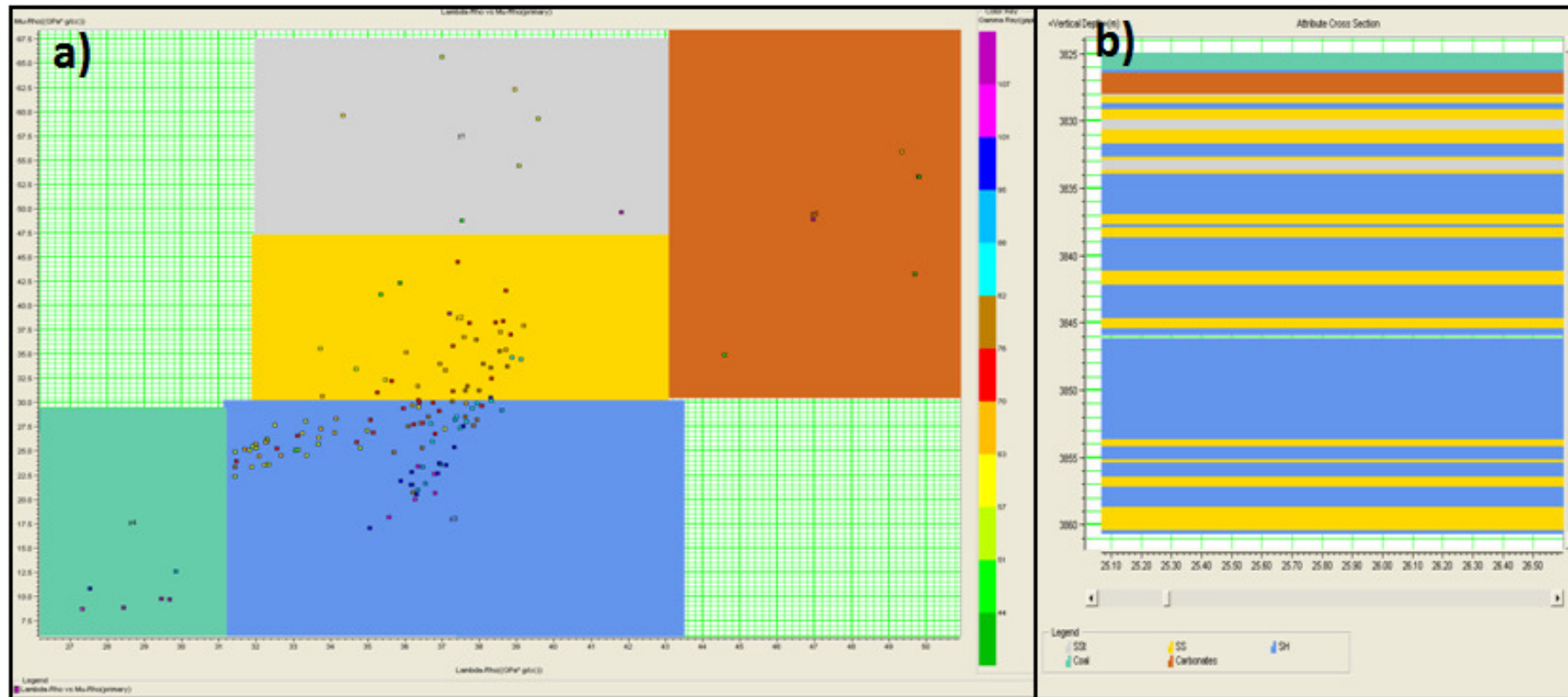


Figure 5-8. Well 7/8-4 a) LMR (Lambda-Mhu-Rho) cross plot. Orthogonal boundaries represents different lithologies: grey = cemented sandstone, yellow = sandstone, blue = shale, moss green = coal, brown = carbonates. b) Cross section with depth on y-axis and the interpreted zones from a)

6. Discussion

6.1 Clay minerals

Clay minerals associated in the wells from the study area are dominated by illite and chlorite with subordinate amounts of kaolin and trace amount of smectite. Kaolin, illite and chlorite will be further discussed in the same section. SEM analysis has been done on samples from well 6/3-1.

6.1.1 Kaolin

Authigenic kaolin has a distinct morphology and usually occurs as pseudo-hexagonal plates, while detrital kaolin lacks this crystalline habit (Wilson and Pittman 1977). Based on this criterion a distinction of authigenic and detrital kaolin could be done. Pore-filling authigenic kaolin (Figure 4-23d) and detrital kaolin (Figure 4-23b) has been identified from SEM-SEI.

Kaolin can also be observed by SEM-BSE (Figure 4-27a). The distinction between kaolinite and dickite is difficult to do in SEM, although (Srodon 1999) suggest that the polytypic transition (kaolinite to dickite) is reflected in morphological change from vermiform to blocky. The authigenic kaolin observed in SEM-SEI has a slightly blocky morphology which might be interpreted as a transition between kaolinite and dickite. According to Ehrenberg et al. (1993) this transition occurs at temperature around 120°C, matching the present day temperature in the shallow reservoir interval in well 6/3-1 (Figure 3-1). The distinction between kaolinite and dickite remains unclear, thus the term kaolin will be used.

Distribution of kaolin

The distribution of kaolin is limited to the upper part of well 6/3-1. The abundance of kaolin varies depending on lithology, small amounts are found in well sorted medium grained sandstone (Figure 4-18, Figure 4-22) while large amounts can be found in silty shale units (Figure 4-22, Figure 6-1). One poorly sorted silty shale sample (Appendix II) within the restricted kaolin interval, has no kaolin (Figure 4-18). The kaolin in the sandstone units are generally fine grained moderately sorted with moderate/high porosity (Appendix IIb). The high amount of kaolin in the silty shale suggests a detrital origin while the small amounts in the sandstone suggest an authigenic origin. This implies a facies control on authigenic kaolin.

Source of authigenic kaolin

The distribution of authigenic kaolin is restricted to sandstone beds of moderately sorted fine sandstone with moderate/high porosity (Appendix IIb). This implies an initial porosity and permeability within the sandstones during precipitation of kaolin suggesting a fluid flow from meteoric origin. This observation of authigenic kaolin distribution is supported by Bjørlykke (1984) claiming that meteoric water leaching has the highest potential to occur in sandstones with higher primary and an initial permeability.

The kaolin content is low in carbonate cemented sandstone, suggesting more leaching and higher permeabilities in sandstones without carbonate cement. However authigenic kaolin has been found where dissolution of carbonate cement occurred (Figure 4-28). These two observations has also been made by Khanna et al.(1997) where extensively carbonate cemented intervals had lower permeability thus less potential for meteoric water leaching of feldspar and mica, and that meteoric water flow would cause dissolution of carbonate cement together with feldspar and mica.

The precipitation of authigenic kaolin requires that K^+ , Na^+ and silica are removed by fluid flow (Bjørlykke 1998). Meteoric water flow is the most significant fluid transport mechanism on a regional scale where the pore water fluxes may be several orders of magnitude higher than compaction driven flow (Bjørlykke 1994). Fluid flow is constrained by both pressure gradients and the supply of fluids and three types can be identified by their origin and driving mechanism in a sedimentary basin: density flow, compaction flow and meteoric water flow (Bjørlykke 1994). Density driven flow can be neglected as the subsurface is too heterogeneous to generate large convection cells (Bjørlykke and Egeberg 1993, Bjørlykke 1994). The volume of water in the basin and dehydration of clay minerals limit the compaction driven flow. The sedimentation rate is often higher than the compaction driven flow making the pore water move downwards.

Facies related kaolin distribution

The facies distribution of authigenic kaolin is most likely within channel associated sandstone as seen on the box car trends from the wire line logs (Figure 6-1) and associated moderate/high porosities and permeabilities (Appendix IIb). Presence of authigenic kaolin indicates an increase in freshwater flux by meteoric water perhaps caused by a more humid climate. Kaolin has been observed to occur in minor amounts in the Triassic in the North Sea (Bjørlykke and Aagaard (1992)). A gradual increase in humid climate from Late Triassic to Early Jurassic increased the potential for meteoric water leaching through the sediments (Sørli, 1996), supporting the presence of authigenic kaolin in the Upper Triassic in well 6/3-1. Palynological data from the Upper Triassic suggest a period of increase in rainfall during the middle to late Carnian (Upper Triassic), with high kaolinite/illite ratios (Simms and Ruffell 1989). The high kaolinite/illite ratio is also supported by the data (Figure 4-18) which further supports an increase in freshwater flux in the Late Triassic.

The facies distribution of detrital kaolin is most likely related to inter-channel facies such as sheetfloods/overbank seen by the poor sorting and high gamma log value from wire line log response (Figure 5-1). Detrital kaolin has only been observed in a channel sandstone associated facies (Figure 4-23b), as analysis by SEM-SEI was done on porous sandstone, however if kaolin is present in silty shale units it is most likely detrital kaolin. This assumption is also supported by Khanna et al.(1997) as they reported that that detrital kaolin is more abundant in the overbank sandstones than in the channel sandstone. Detrital kaolin is usually associated to warm, moist regions as a weathering product (Moore and Reynolds 1997). Humprey et al.(1989) reported an increase in detrital kaolinite in Late Rhaetic (Upper Triassic) and early Jurassic, which supports the detrital kaolinite findings in the Late Triassic.

The amount of kaolin is higher in the detrital kaolin associated facies (7 XRD%) than the authigenic associated facies (0.2-2 XRD%). A similar distribution was found by Khanna et al.(1997) as they reported kaolin content for overbank deposits to be 2-7% while isolated sequences of channel sandstones contained values of 2-8% in Upper-Triassic Lower-Jurassic sequences in the Tampen Spur area.

Presence of both authigenic and detrital kaolin would suggest a more humid climate in the Upper Triassic towards the Lower Jurassic.

Consequences for reservoir quality

Precipitation of kaolin causes a reduction in permeability due to the pore-filling properties of the kaolin (Figure 4-23d, Figure 4-27a, Figure 4-28b). Microporosity occurs between kaolin plates (Figure 4-28b), however these microporosities are too small to be filled with oil, because of their high capillary entry pressure, thus reducing oil saturation potential for the sandstone (Bjørlykke 2010). The distribution and abundance of kaolin in this study is mainly influenced by the climate and fresh water flux, thus being facies controlled. Prediction of reservoir quality is thereby related to facies.

6.1.2 Illite

XRD and petrographic observations reflect that illite is the most abundant clay mineral together with chlorite (Figure 4-15-Figure 4-18). Visually the illite has been identified in SEM-SEI (Figure 4-24b, Figure 4-25c Figure 4-26bc) and SEM-BSI (Figure 4-30abf). The pore-filling fibrous morphology indicates an authigenic origin while the finer grained deformed illite suggests detrital (allogenic) origin. Most of the illite observed by SEM-SEI indicates an authigenic origin.

Distribution of illite

Illite is present in all of the wells (6/3-1, 7/8-4, 7/11-9 and 7/11-8) in varying amounts (0-81 XRD% (Figure 4-15 - Figure 4-18)). The percentage of authigenic illite is difficult to quantify in XRD (e.g., Bjørlykke (1998), due to interference of clastic illite and mica with authigenic illite (Moore and Reynolds 1997). Presence of authigenic illite can only be seen by SEM-SEI, thus making its distribution and abundance difficult to determine.

High XRD% amounts of illite is found close to/in silty shales or shale units, and occurs as minor amount in sandstone bodies (Figure 4-22). The silty shale or shale units most likely represent floodplain or lacustrine deposits (assuming that the Triassic deposition occurred without marine influence). The abundance of illite is most likely controlled by amount of detrital source material while the distribution is mainly controlled by the amount of precursor material (see section below).

Source

The precipitation of illite is mostly controlled by the dissolution of aluminum bearing precursor minerals such as smectite and kaolinite (see simplified equations below).

Kaolin + K-Feldspar = Illite + Quartz + water After Bjørlykke et al. (1995)

smectite + $A^{+3} + K^{+}$ = illite + Si^{+4} After Boles and Franks (1979)

The equation after Bjørlykke et al. (1995) is isochemical implying no supply or removal of ions by pore water flow. It does, however, require that K^{+} and Al^{3+} and silica are removed from the surface of the dissolving K-feldspar and kaolinite to the illite growth area. The most important factors controlling the precipitation of illite at depth is the primary mineral composition with respect to the K-feldspar, smectite content and early diagenetic kaolinite. A correlation between high XRD% amount of illite and low XRD% K-feldspar would be expected if the source of K^{+} came from dissolution of K-Feldspar that is required for the transition from smectite to illite (Figure 4-21 and Figure 4-22). There is a slight decrease of K-feldspar with high amount of Illite, however the semi-quantitative data (XRD) is not accurate enough to establish a certain relationship between the illite and “dissolution” of K-feldspar. Nevertheless it is possible that illitization of smectite occurred, since the morphology is interpreted to come from a smectitic precursor (Figure 4-26b, Figure 4-25c).

The illitization of kaolin requires temperatures of 130-140°C (Bjørlykke et al. 1989). This temperature interval is within the Upper Triassic of well 6/3-1 (Figure 3-1) and Middle Jurassic in well 7/8-4. This might explain the absence of kaolin in the Triassic sandstones in well 7/8-4 (Figure 4-17), as illitization of kaolin might have happened. However the Triassic units in well 7/8-4 is dated by NPD (NPD 2010) to be of Early-Middle Triassic age, deposited in a most likely semi-arid to arid climate (Figure 2-7) making illitization from kaolin unlikely, however due to presence of K-feldspar in all wells it cannot be excluded. Well 6/3-1 might be within the temperature interval of active illitization from kaolin, however authigenic illite seen in SEM-SEI cannot be observed together with kaolinite, as expected if illitization was an ongoing process in the sediment, however due to the small amount of SEM-SEI samples investigated an illitization from kaolin might have happened as K-feldspar is present.

The illitization of smectite occurs in a temperature interval of 60-100 °C (Bjørlykke et al. 1989). In well 7/8-4 the illitization of smectite in the Triassic deposition happened from

Middle Jurassic, while in well 6/3-1 it happened from Paleogene to Neogene. The simplified burial history of 6/3-1 has not been calibrated and some uncertainties is connected with the temperature history as it is only an extrapolation between current bottom hole temperature and a seabed temperature assumption. The morphology of illite and presence of mixed layer smectite/illite (Figure 4-24b, Figure 4-25c Figure 4-26bc) indicate a smectite precursor for the illite.

Facies related distribution of illite

Illite is most abundant in fine grained sediments (silty shale, shale) while being present in minor amounts in sandstones (Figure 4-21, Figure 4-22). Most of the illite identified by SEM-SEI is identified to be authigenic, thus the distribution and abundance of authigenic illite is closely related to its precursor, which in this case is either kaolin + K-feldspar or smectite.

Low concentration of detrital and authigenic illite has been seen by SEM-SEI in the porous sandstones. One possible explanation for the low amount of illite could be related to the pore water as Bjørlykke et al.(1992) reported that lack of smectite in the Brent Group contained too little silica content for smectite to form. The detrital illite is possibly related to weathering products which accumulate during flooding events in floodplain associated facies.

Consequences for reservoir quality

No illitization from kaolinite was observed, however morphological data from SEM-SEI suggest a smectite precursor for the authigenic illite. The authigenic illite occupies pore-space and has a pore-bridging morphology, at a depth around 3km/120C°, thus severely reduces permeability (Figure 4-25bc, Figure 4-30abf). Other studies has observed pore-coating illite (e.g (Storvoll et al. 2002)), however this has not been identified in this study.

6.1.3 Chlorite

Chlorite is the most abundant clay mineral together with illite (Figure 4-15-Figure 4-18). Chlorite has been seen in SEM-SEI (Figure 4-25e, Figure 4-23c) and SEM-BSE (Figure 4-30cd) to be both pore-filling and grain-coating. Chlorite replacing detrital grain within a rock fragment has the same morphology as the pore-filling chlorite (Figure 4-30c). The well defined chlorite crystals indicate an authigenic origin. No detrital chlorite has been found in this study. Similar authigenic chlorite has been observed by Humphreys et al. (1989) in Late Triassic from the Central Graben in the English sector (quadrant 22).

Distribution of chlorite

Chlorite can be found in all the wells (6/3-1, 7/8-4, 7/11-9 and 7/11-8) and in all lithologies with varying amounts ranging between 0-17 XRD%. Pore-filling chlorite was observed at 3016,77mRKB (well 6/3-1) in a sandstone with 5 XRD% total clay, while grain-coating was observed in 3022,65mRKB with a total clay content of 1 XRD%. Areas with high porosities (modal analysis) seems to be related with the amount of chlorite being <5 XRD% (Figure 4-20c, Figure 4-7c). Full grain coating coverage on all the grains is achieved with a chlorite content of 1%, while values above 5% chlorite is associated with pore-filling chlorite (Pers. Comm. Jens Jahren, May 2010). Most of the sandstone samples in this study are thereby related to pore-filling chlorite as the average chlorite XRD% is >6%, however this value is semi quantitative.

The grain coating chlorite has a characteristic honeycomb morphology (Figure 4-25e) which covers the quartz grain. Due to the uncertainty of XRD values, chlorite coated sandstones will be represented by a chlorite XRD% ranging between 0.1 and 3%. Five sandstone with grain dominated framework samples match this criterion and has an average porosity of 9,2%, which is quite high in this data set compared to the total average of all point counted samples which is 4,9% (Appendix IIb). All of the suspected grain coated sandstones are poorly to well sorted medium grained with mostly subrounded grain shape, which most likely have been deposited in a more energetic environment than the fine grained sand, thus perhaps can be attributed to channel associated facies or proximal part of sheetflood associated facies. These sandstone bodies are found within dirtying upward trends (sheetflood?) and box car trends (channel sandstone?) (Figure 6-1).

The pore-filling chlorite consist mainly of crystal plates which occlude most of the pores (Figure 4-30cd)(however some empty spaces occur). The pore-filling chlorite is found in poorly/moderate sorted sandstones with high content of total clay and carbonate cement (Figure 4-22). The wireline logs indicate that they are present at the top of dirtying upward trends, probably associated with floodplain or distal sheetflood associated facies.

Source of chlorite

Based on the honeycomb morphology of the grain coatings seen in SEM-SEI the precursor is most likely a smectite (Figure 4-25e). High amount of chlorite is mostly in silty shale areas (Figure 4-22). There is also a correlation between a high amount of chlorite and presence of carbonate cement with one exception at 3028,77mRKB where also kaolinite is present. Humphreys et al. (1994) and Weibel (1999) have also suggested an smectitic precursor from a honeycomb chlorite morphology through a mixed layer mineral (corrensite).

According to Adestål (2002) high amount of smectite can be found in semi arid/arid periods within palaeosols. This might explain why the highest amount of chlorite can be found within suspected floodplain associated facies with carbonate cement. Lower amounts of smectite (associated with low chlorite content) are most likely caused by weathering products. According to Bjørlykke and Aagaard (1992) smectite is a common clay mineral during the Triassic in the North Sea.

The average composition of grain coating chlorite is ($\text{Mg}_{1,72}, \text{Fe}_{2,35}, \text{Al}_{1,53}$) ($\text{Al}_{0,71}, \text{Si}_{3,29}$) $\text{O}_{10}(\text{OH})_8$ (from section 4.5.3) with a corresponding Fe/Fe+Mg ratio of 0,58 defining the grain coating as Mg-Chamosites according to the terminology Bailey(1980). A Fe/Fe+Mg ratio of 0,64 has been found in similar setting from Lunde- and Statfjord Formation by Sørli (1996), while authigenic grain coating chlorite in the Late Triassic from the Central Graben has a Fe/Fe+Mg ratio of 0,44 (Humphreys et al. 1989).

The use of XRD data to determine the iron content in chlorite should be done with caution, as there is a mismatch between XRD calculated Fe content and the elemental analyses done in SEM. Similar doubt of attributing of Mg-rich or Fe-rich composition of chlorite based on XRD data has been promoted by Humphrey et al. (1989)

Evidence of possibly authigenic smectite can be seen in Figure 4-28) where the smectite is located close to biotite and plagioclase. Sørli (1996) reported that dissolution of biotite and K-feldspar have been possible sources of authigenic smectite. The low porosity and lack of K-feldspar might have limited the illitization of smectite.

Palaeoclimatic implications

The distribution of the precursor smectite is the key to understand the chlorite distribution. According to Singer (1984) the detrital smectite is formed either as a degradation product (in temperature climate) or a neoformation mineral (in semi arid climate). The data suggest that the smectite most likely were of a neoformation origin in a semi arid climate.

Consequences for reservoir quality

Authigenic chlorite exists as both grain-coating and pore-filling, thus having properties that destroy or preserve reservoir quality. Fe-rich chlorite seems to have grain-coating effect that may suppress quartz cementation thus preserving porosity. The effect of the chlorite coating also seems to depend on the amount of coverage on the grains, as Figure 4-25e is partially covered with presence of quartz overgrowth. A quantification of the effect by different degrees of grain coating is wanted, as this might predict areas/facies related to the most effective grain coating effect by chlorite with respect to reservoir quality. High porosities are found where chlorite is around 0.1-3 XRD%.

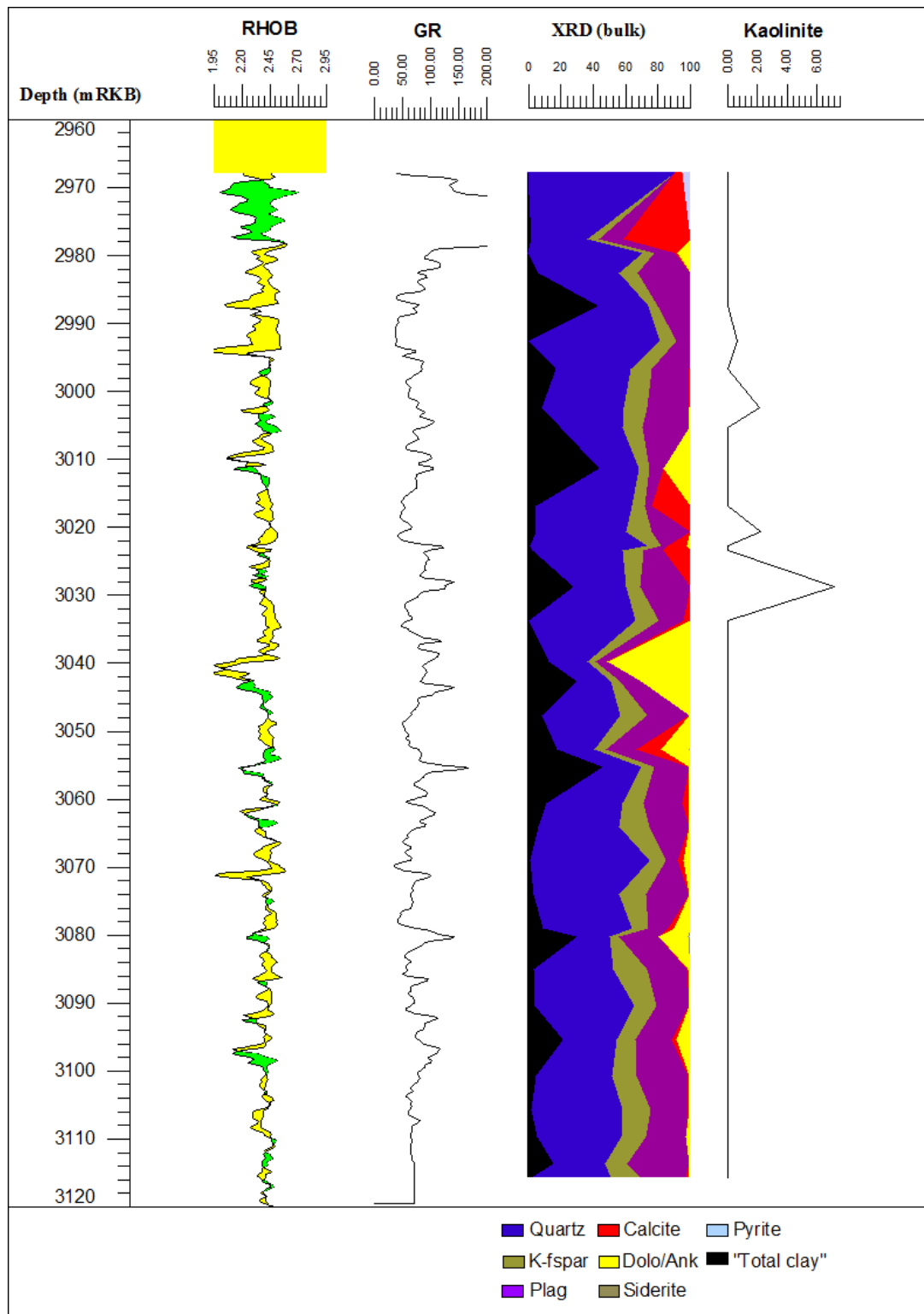


Figure 6-1. Combination of petrophysical data and XRD data with depth. The first tab is NPHI/RHOB cross plot(the NPHI scale is -0,15 at RHOB value of 2,95 and 0,45 at a RHOB value of 1,95), the second plot displays the gamma log values, the third plot is a percentage plot of XRD bulk data, the fourth plot is kaolinite content with depth (XRD %)

6.2 Carbonate cementation

Three types of carbonate cement have been identified: calcite (Figure 4-1cd, Figure 4-28acdef, Figure 4-29), dolomite (Figure 4-27cd, Figure 4-28ace) and ankerite (Figure 4-28e). The cementation occurs as dolomite/ankerite dominated, calcite dominated or in minor amounts of both in the same sample.

Carbonate cementation and petrophysical properties

By assuming that the high values of XRD % of dolomite/ankerite and calcite represent the carbonate cemented intervals several cemented intervals are located (Figure 4-10-Figure 4-13). Highly cemented intervals can be seen in well 6/3-1, 7/8-4 and 7/11-9 while 7/11-8 only contains trace amounts of carbonates. Well 6/3-1 and 7/8-4 will be discussed further in this section due to better data coverage regarding the mineralogical distribution based on XRD analysis.

Suspected cemented intervals were compared to the wire line log to identify any trends associated with cementation. Three cemented areas has been identified in well 7/8-4 (3825,60 mRKB, 3837 mRKB, 3843,15 mRKB and 3855,05 mRKB). A decrease in sonic transit time is observed in all the cemented intervals except at 3855,05 mRKB, which can be explained by the small amount of cementation. An increase in gamma log and a reduction in neutron porosity can be observed in all the cemented intervals. The bulk density only increases at 3837 mRKB while having neutral (no apparent change) responses in the other cemented intervals. A LMR (Lambda-Mu-Rho) cross plot was made with the purpose of identifying the cemented zones and comparing them to the XRD data (Figure 5-8). The grey zones (cemented sandstone) are all located above 3035 mRKB thus immediately excluding the known cemented intervals (based on XRD) at 3837 mRKB, 3843,15 mRKB and 3855,05 mRKB. No significant changes can be observed on the caliper log.

All suspected carbonate cemented intervals (>5 XRD% carbonates) has an increase in sonic transit time (slower P-wave velocity) and a reduction in bulk density (Figure 5-1, Figure 6-1). An increase in neutron porosity and gamma log can also be observed in most of the cemented zones. In contrary to well 7/8-4 significant changes occur in well 6/3-1 with the caliper log, indicating a varying bore hole size throughout Skagerrak Formation (Figure 5-1). Huge variation in density can be seen in the density-depth plot (Figure 5-2), ranging between

1,9 g/cm³ to 2,7 g/cm³. The low density spikes and corresponding high porosity spikes indicate areas of carbonate cementation (Figure 5-1, Figure 5-3). Neutron porosity – density plot was made in order to identify possible lithological trends (Figure 5-6). The lithological distribution based on this cross plot is clearly heterogeneous, changing between sandstone and carbonate cemented intervals (assuming limestone and dolomite represent carbonate cemented intervals). This method (NPHI-density) overestimates the amount of carbonate cemented intervals and thereby fails to position them correctly (if compared to XRD data and point counted thin sections). It also fails identifying the sample with the highest XRD % of Dolomite/Ankerite at 3039,72 mRKB which makes this cross plot schematic at best.

The wire line log trends of the distribution of carbonate cementation seems to follow no clear trends when comparing well 7/8-4 and 6/3-1 other than having high gamma log value, possibly reflecting occurrence of carbonate cement in silty shale or shale units. This relationship is also seen in well 6/3-1 when comparing the lithological log to the XRD bulk data (Figure 4-13) indicating a facies dependant distribution of carbonate cement. The most likely explanation for the poor correlation in log responses between the wells might be due to presence of hydrocarbons in well 6/3-1. The presence of hydrocarbons influences the P-wave velocity by having lower speed in the hydrocarbon filled zone than in the water filled zone (Figure 5-4). The most likely explanation for the abnormally low density and high neutron porosity readings in the carbonate cemented intervals is related to cavings. High borehole size is seen at every carbonate cemented suspected interval. As cavings are mostly related to shale units it also supports a facies control on carbonate cementation.

The LMR method requires calibration of the used parameters and the conversion of a P-wave to an S-wave based on the Castagna equation ($V_p = 1.16V_s + 1.36$ from Castagna et al. (1985)) might be too simplistic in this case. Nevertheless LMR cross plot correctly shows that the upper section of the log is more sand prone than the lower section, however the accuracy is too small and therefore only gives an impression of the lithology distribution in the well.

Highly cemented intervals are expected to have high bulk density and low sonic transit time (high P-wave velocity) due to replacement of pore fluids by cement (Worden and Matray 1998). This is only the case for one suspected carbonate cemented interval in well 7/8-4 (3837mRKB). A possible reason for the large number mismatches in well 7/8-4 is unknown,

however in well 6/3-1 cavings and variation in fluid content (hydrocarbon, water) is most likely the explanation.

Source of carbonate cement

The dominant source for carbonate cements in continental and nearshore sediments are calcretes and dolocrete which develop in warm to hot, arid to semi-arid regions, with low, seasonal rainfall and high evaporation (Morad 1998). Calcrete can form by two ways: i) As phreatic, groundwater, calcrete minerals formed around the water table or as ii) pedogenic (vadose) minerals close to the sediment surface (Wright 1994). Groundwater calcrete can be typically 10 meter thick and associated with drainage channels and playas, in contrast to the pedogenic calcrete that is 1-2 meter thick and associated with stable floodplain periods (Wright 1994).

The textural evidence shows a dominance of small rhombic dolomite crystals together with red colouring suggesting shallow oxic conditions during cementation. The small size of the rhombic dolomite suggests a shallow origin. Several cemented intervals exceed an IGV of above or around 45% which is the assumed original porosity, indicating cementation to occur pre-compaction. Timing of the cementation requires more data, such as oxygen and carbon isotopic data (Giles et al. 1992).

The thickness of the carbonate cemented intervals in well 6/3-1 is of 1-2 meter and assumingly restricted near or within floodplain related facies, thus may reflect a pedogenic origin. Quartz with corrosion related notches has also been observed (Figure 4-2c) which according to Milliken et al.(2007) can indicate humid soil related processes thus supporting the pedogenic origin of carbonate cement. Similar distribution of carbonate cement with pedogenic origin has been found in Chaunoy Formation in the Paris basin by Worden (1998).

Additional sources of Ca might come from dissolution of Ca-plagioclase or albitization of plagioclase (Figure 4-28b, Figure 4-27f) as XRD data indicates a relationship between high amount of carbonate cement occurring where low amounts of plagioclase is located (Blatt 1992). These two processes has also been suggested to be the source of Ca by Sørli (1996) in the Lunde- and Statfjord Formation. However most clastic plagioclases have an An content of 10-30% which results in very small amounts of dissolved calcium (Blatt 1992).

In well 6/3-1 the distribution of calcrete seems to be in samples with low amount of clay minerals, whereas dolocrete is usually in units with high amount of clay minerals. This suggests a more proximal associated facies for calcrete and more distal associated facies for dolocrete (Figure 4-13). This is further supported by grain size association with type of carbonate cement, as fine/medium grained sediments contain more calcite while siltstone/very fine grained sediments contain more dolomite (Appendix II, IIb). This distribution of carbonate cement is also suggested by Morad (1998) where he claims that dolocretes are common in fine grained distal fluvial facies while calcrete is dominate in coarse grained proximal facies.

Consequences for reservoir quality in well 7/8-4 and 6/3-1

Carbonate cementation is an important process influencing fluid flow that can reduce the net pay of a reservoir and compartmentalize the reservoir distribution. The carbonate cementation halts the mechanical compaction thus having high IGV%.

6.3 Quartz cementation

The amount of quartz cement in the samples from well 6/3-1 range between 0 and 11% (Figure 6-2, Appendix IIb), with the majority of samples having low amounts of quartz cement (<5%). The samples with more than 5% quartz cement are generally very fine grained subrounded moderate sorted sandstones (Appendix II), implying that large surface areas promote quartz cementation. The most cemented (thin section) samples have thin clay laminae within the sample, most likely mica (Appendix II). The quartz cement found in SEM-SEI grow into the pore space (Figure 4-24a, Figure 4-25b, Figure 4-26e). Quartz overgrowths require a clean surface, as grains with grain coatings are less quartz cemented than grains without grain coatings.

No quartz cementation was found by SEM-BSE, as SEM-BSE identification of the quartz cement is usually combined with CL (cathodoluminescence) for easier discrimination between detrital quartz and quartz overgrowth (e.g. Götze et al. (2001) and references therein). CL was not performed in this study.

Source of silica cement

Possible sources of silica for quartz cementation could be pressure-solution along stylolites, clay mineral transformations where silica is released into the pore water (e.g. illitization from smectite and kaolinite (Bjørlykke and Egeberg 1993)) or dissolution on grain to grain contacts.

An external source for silica has not been investigated as mass balance calculations for an upward compactional fluid flow is too slow and that fluid flow from a meteoric groundwater flow or a thermal convection cell is highly unlikely to support quartz cementation (e.g. (Bjørlykke et al. 1989, Bjørlykke and Egeberg 1993, Bjørlykke 1994, Walderhaug 1994, 1996, Bjørlykke 1999)).

A silica source from grain-to-grain contacts can also be excluded as volumetrically important since high amounts of quartz cement is found in high IGV(%) rocks. A decrease of IGV(%) would be expected due to closer packaging if the silica source grain-to-grain contact dissolution (Figure 6-2).

The most likely source of quartz would be from stylolites, as small stylolites are observed in the sandstones (Figure 4-2a) and that the sandstones with the most quartz cement contain thin clay laminae. Calculations have also shown that flat stylolites may generate silica supersaturation which is sufficient for quartz precipitation (Jahren and Ramm 2000), thus if the clay laminae seen in the thin section are stylolites they might be an important source for quartz cement.

Dissolution on stylolites has been adapted into the so called I-MID model (Illite – Mica Induced Dissolution) (Bjørkum et al. 1998, Oelkers et al. 2000). This model assumes that the source of the silica cement is quartz surfaces adjoining mica and/or clay grains at stylolite interfaces within the sandstones.

Timing of quartz cementation

By petrographical observations the quartz cement occurred after the precipitation of chlorite coatings (Figure 4-26e). Large quartz overgrowths are seen in porous sandstone indicating that the mechanical framework is stable. No quartz overgrowth can be observed in carbonate cemented samples, suggesting that quartz cementation occurred after carbonate cementation and framework stabilization.

According to Chuhan et al. (2002) the framework stabilization prior to fracturing occurs at stresses higher than >20MPa. If we assume hydrostatic pressure this is equivalent to a burial depth of 2km (Bjørlykke 1999), which corresponds to a temperature of 80°C based on the simplified burial history (Figure 3-1).

According to Walderhaug (1994) the quartz cementation takes place above 75°C and continues as long as it takes to cement the rock. By using this temperature the quartz cementation started in Eocene for both well 6/3-1 (Figure 3-1) and well 7/8-4 (Figure 3-2) and is still ongoing. The cored reservoir interval in well 6/3-1 has a temperature around 120°C while well 7/8-4 has a temperature around 160°C, this means that the rate of quartz precipitation, based on, temperature increases 16-fold in well 7/8-4 compared to well 6/3-1. More quartz cement is also expected in well 7/8-4 than well 6/3-1 due to a larger time-temperature-interval (Figure 3-1, Figure 3-2). This is also the case as the average quartz cement for 6/3-1 (ranging between 0%-11%) is 3,42% while the average for well 7/8-4 is 7,2% ranging between 2,9%-9,2%).

Consequences for reservoir quality in well 6/3-1 due to quartz cementation

The quartz cementation destroys the porosity due to precipitation on grain surfaces and into the pore volumes thus reducing reservoir quality severely. Modeling the quartz cementation is important to predict porosity loss. Mechanism that may prevent/halt quartz cementation is vital regarding reservoir quality. From the model presented in Oelkers et al. (2000) it is expected that all similar samples should with the same time-temperature-interval contain the same amount of quartz cement. The range of quartz cement amounts found in this study suggests that there is a mechanism in the cored reservoir interval in well 6/3-1 that prevents quartz cementation to occur. As seen in the porosity trend (Figure 4-20) chlorite has a porosity-preserving effect if present in low amounts. The porosity preserving effect is most likely by preventing quartz cementation to occur. Clay mineral distribution and growth morphology is therefor an important factor in order to predict reservoir quality. The amount of quartz cement is not dependant on the amount of IGV in this dataset due to the low amount of quartz cement.

6.4 IGV

The intergranular volume is the maximum porosity of the rock in the absence of matrix and cementation. As seen in Figure 4-6 the IGV of the wells vary with depth between 20-50%. Due to more data only the effect of IGV will be discussed from well 6/3-1. Several processes involved in reducing sandstone porosity will be discussed.

Carbonate cementation

In some samples extensive carbonate cementation occurs prior to compaction filling most of the available pore space (stopping mechanical compaction) (Figure 4-1cd, Figure 4-28acdef, Figure 4-29) resulting in high IGV.

Mechanical compaction

Different types of deformation of grains can be seen in the thin sections. The deformation occurs as fracturing (Figure 4-2e, Figure 4-27abd and Figure 4-30ac), ductile bending of grains (Figure 4-2e and Figure 4-27ab) and long grain-to-grain contacts (Figure 4-28df). This is consistent with Bjørlykke (1998, 1999, 2003) description of the main processes involved in mechanical compaction (rearrangement of grains, ductile and bending deformation of grains and breakage of grains). All of these physical processes will most likely reduce the IGV, as the grains get more densely packed.

Grain size

Coarse grains are more fractured than smaller grains (Figure 4-1c), which would imply that coarse grains has less IGV than fine grained sand. The average IGV for medium grained sand is 32,8 IGV%, while very fine sand has 35,94 IGV% (Appendix IIb), implying that medium grained compact more than very fine grained sand.

Sorting

Well sorted sediments seem to have higher porosities than poorly sorted sediments (Figure 4-7). This finding is in agreement with earlier studies (e.g Rogers and Head (1961), Beard and Weyl (1973)). Poorly sorted sediments also contain more clay than well sorted

sediments (Figure 4-8). IGV(%) seems to vary with a small degree with sorting (Figure 4-9), where well sorted sediments has a higher IGV(%) than poorly and moderate sorted sandstone.

Grain shape

Most common grain shape in this study are subrounded/subangular. Only one sample with angular grains have been point counted with a very high IGV of 44,2 (Appendix IIb). The average IGV for the different sorting are: angular = 44,2(n=1), subangular = 32,5(n=4), subrounded = 32(n=8), where n = number of samples. This gives an indication of increasing IGV as a function of grain angularity. The resistance of mechanical compaction by reorientation of angular grains have been reported by Ramm (1992).

Chemical compaction

Stylolites (pressure solution) has been observed (Figure 4-2a) which causes a reduction in rock volume and precipitation of cement. This process is then both affecting the amount of quartz cement within the sandstone, and a reduction in IGV due to the dissolution of grains close to the stylolite. Dissolution of feldspar might increase the IGV (Figure 4-30f), however the volumetric importance of feldspar dissolution is difficult to quantify.

Extensive quartz cementation (>5% in this data set) can mostly be found in very fine sandstones, while low amount of quartz cement is found in fine to coarse grained sandstone (Figure 6-2, Appendix IIb). The high amount of quartz cement in very fine grained sandstone is most likely due to the larger grain surfaces exposed to quartz cementation.

Grain coatings

Grain coatings are potentially important to IGV as they might prohibit formation of quartz cement, as mechanical compaction is not stopped as effectively. Only chlorite coating was identified in this study, thus the chlorite coating is believed to have a porosity preserving effect by covering quartz grains. Coated sandstones are expected to have little quartz cement, while partially coated sandstones are expected to have more quartz cement. This is not the case in this data set as, suspected grain coated sandstones (chlorite 0,1-3,0 XRD%) averages 4,7% quartz cement while the suspected uncoated sandstones (chlorite >3,0XRD%) averages 3,0% quartz cement(Figure 6-2,Appendix IIb). As quartz cement is low throughout the data

set (averages 3,0%) no clear trends between coated chlorite sandstone and uncoated sandstone.

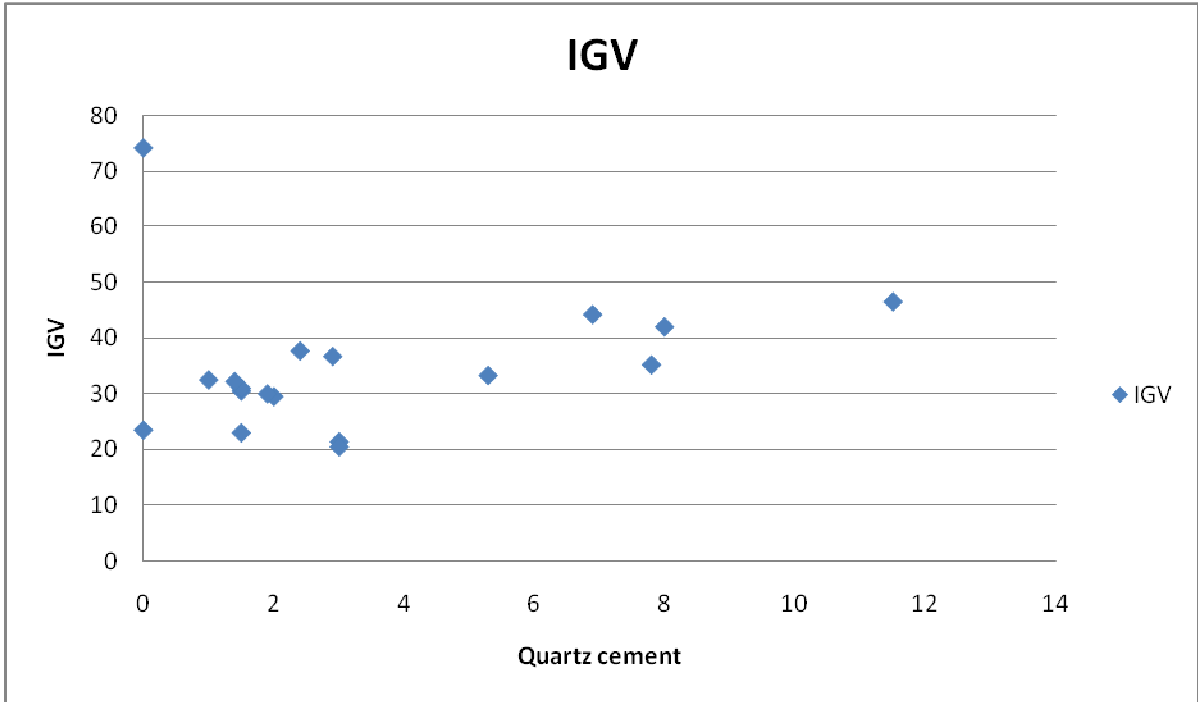


Figure 6-2. IGV plotted against IGV. All samples are from well 6/3-1 and between 2967 mRKB and 3015 mRKB

7. Conclusion

- Grain coating chlorite, with an average composition of $(\text{Mg}_{1,71}, \text{Fe}_{2,35}, \text{Al}_{1,53}) (\text{Al}_{0,70}, \text{Si}_{3,30})$, has a porosity preserving effect that prevent/halt quartz cementation, thus making its distribution (and abundance) important for reservoir quality prediction
- Authigenic kaolin in the Upper Triassic indicates an increase in freshwater flux. Detrital kaolin indicate humid climate, thus Upper Triassic is most likely a transition period from a dry Triassic climate towards the more humid Jurassic period. The distribution of authigenic kaolin seems to be facies dependant as it has been found in permeable sandstone. In the deepest well kaolin may have been dissolved and replaced by illite. Authigenic chlorite and illite is most likely related to a smectite precursor
- An increase of 7% quartz cement in the cored reservoir interval in the Triassic between well 6/3-1 (~3km/128°C) and 7/8-4 (~3,8km/150°C) can be explained by different time-temperature intervals
- The petrophysical location of carbonate cemented zones was done by comparing XRD data with wire line logs and interpreting the log response. Cross plots (i.e LMR, NPHI-Density) proved too difficult to use due the amount of calibration needed for accurate mapping because of the subarkosic composition and variable fluid content. The distribution of carbonate cemented intervals is related to facies and the transition between sandstone and silty shale
- The abundance of carbonates and chlorite minerals combined with a low concentration of kaolin consistent with a rather dry climate in the Triassic
- Intergranular volume – quartz cement relationships indicate both higher IGV and more quartz cement in the very fine grained sand than in medium grained sandstone. High IGV can be ascribed to less mechanical compaction and more quartz cement to the higher surface area for quartz cement to precipitate in fine grained sandstones. Based on this porosity will be lost faster in fine grained sandstone compared to coarse grained sandstones in deep (>4000m) reservoirs

8. References

- Adams, A., MacKenzie, W. and Guilford, C. 1986. *Atlas of sedimentary rocks under the microscope*. New York, NY. 112 pp.
- Adestål, V. 2002. *Paleoclimatic conditions during late Triassic to early Jurassic, northeren North Sea: Evidence from clay mineralogy*, Institutionen för geovetenskaper, Uppsala universitet, Uppsala. 34.
- Anderson, P., Gray, F. and Inc, V. 2001. Using LMR for dual attribute lithology identification. *71st Ann Internat Mtg: Soc of Expl Geophys*, 201-202.
- Asquith, G. and Krygowski, D. 2004. *Basic well log analysis*. Methods in Exploration Series 16, Tulsa, Oklahoma: AAPG 244 pp.
- Bailey, S. 1980. Summary of recommendation of the AIPEA nomenclature committee. *Canadian Mineralogist* 18, 143-150.
- Bartholomew, I., Peters, J. and Powell, C. 1993. Regional structural evolution of the North Sea: oblique slip and the reactivation of basement lineaments, 1109-1122.
- Beard, D. and Weyl, P. 1973. Influence of texture on porosity and permeability of unconsolidated sand. *AAPG bulletin* 57, 349-369.
- Bjørkum, P., Oelkers, E., Nadeau, P., Walderhaug, O. and Murphy, W. 1998. Porosity prediction in quartzose sandstones as a function of time, temperature, depth, stylolite frequency, and hydrocarbon saturation. *AAPG Bulletin-American Association of Petroleum Geologists* 82, 637.
- Bjørlykke, K. 1984. Formation of secondary porosity: how important is it. *Clastic diagenesis: AAPG Memoir* 37, 277-286.
- Bjørlykke, K. 1994. Fluid-flow processes and diagenesis in sedimentary basins. *Geological Society London Special Publications* 78, 127-140.
- Bjørlykke, K. 1998. Clay mineral diagenesis in sedimentary basins-a key to the prediction of rock properties. Examples from the North Sea Basin. *Clay minerals* 33, 15-34.
- Bjørlykke, K. 1999. An overview of factors controlling rates of compaction and fluid flow in sedimentary basins. In Jamtveit, B. and Meakin, P. (eds). *Growth, dissolution and pattern formation in geosystems*. Netherlands: Kluwer Academic Publishers, 381-404.
- Bjørlykke, K. 2010. (in press) *Petroleum Geoscience: From Sedimentary Environments to Rock Physics*: Springer; 1st Edition. edition (Jun 12 2010) 340 pp.
- Bjørlykke, K. and Aagaard, P. 1992. Clay minerals in North Sea sandstones. *Origin, Diagenesis and Petrophysics of Clay Minerals in Sandstones*, 65-80.
- Bjørlykke, K., Aagaard, P., Egeberg, P. and Simmons, S. 1995. Geochemical constraints from formation water analyses from the North Sea and the Gulf Coast Basins on quartz, feldspar and illite precipitation in reservoir rocks. *Geological Society London Special Publications* 86, 33.

- Bjørlykke, K. and Egeberg, P. 1993. Quartz cementation in sedimentary basins. *AAPG bulletin* 77, 1538-1538.
- Bjørlykke, K., Nedkvitne, T., Ramm, M. and Saigal, G. 1992. Diagenetic processes in the Brent Group (Middle Jurassic) reservoirs of the North Sea: an overview. *Geological Society London Special Publications* 61, 263-287.
- Bjørlykke, K., Ramm, M. and Saigal, G. 1989. Sandstone diagenesis and porosity modification during basin evolution. *International Journal of Earth Sciences* 78, 243-268.
- Blatt, H. 1992. *Sedimentary petrology* 2, Salt Lake City, UT (United States): W.H. Freeman and Co. 514 pp.
- Bloch, S. and Helmold, K. 1995. Approaches to predicting reservoir quality in sandstones. *AAPG Bulletin-American Association of Petroleum Geologists* 79, 97-115.
- Boles, J. and Franks, S. 1979. Clay diagenesis in Wilcox sandstones of southwest Texas: implications of smectite diagenesis on sandstone cementation. *Journal of Sedimentary Petrology* 49, 55-70.
- Bragg, W. and Bragg, W. 1913. The reflection of x-rays by crystals. *Proceedings of the Royal Society of London Series A, Containing Papers of a Mathematical and Physical Character*, 428-438.
- Castagna, J., Batzle, M. and Eastwood, R. 1985. Relationships between compressional-wave and shear-wave velocities in clastic silicate rocks. *Geophysics* 50, 571-581.
- Cecil, C. 1990. Paleoclimate controls on stratigraphic repetition of chemical and siliciclastic rocks. *Geology* 18, 533-536.
- Choh, S., Milliken, K. and McBride, E. 2003. A tutorial for sandstone petrology: architecture and development of an interactive program for teaching highly visual material* 1. *Computers & Geosciences* 29, 1127-1135.
- Chuhan, F., Kjeldstad, A., Bjørlykke, K. and Høeg, K. 2002. Porosity loss in sand by grain crushing—Experimental evidence and relevance to reservoir quality. *Marine and Petroleum Geology* 19, 39-53.
- Deegan, C. and Scull, B. 1977. *A standard lithostratigraphic nomenclature for the Central and Northern North Sea*: HMSO.
- Ehrenberg, S. 1995. Measuring sandstone compaction from modal analyses of thin sections: how to do it and what the results mean. *Journal of Sedimentary Research-Section A-Sedimentary Petrology and Processes* 65, 369-379.
- Ehrenberg, S., Aagaard, P., Wilson, M., Fraser, A. and Duthie, D. 1993. Depth-dependent transformation of kaolinite to dickite in sandstones of the Norwegian continental shelf. *Clay minerals* 28, 325-352.

- Erratt, D., Thomas, G. and Wall, G. 1999. The evolution of the central North Sea Rift. *Petroleum Geology of Northwest Europe: Proceedings of the 5th Conference*, 63-82.
- Evans, D., Graham, C., Armour, A. and Bathurst, P. 2003. *The Millennium Atlas: Petroleum geology of the central and northern North Sea: London: Geological Society of London*. 989 pp.
- Evans, J., Hogg, A., Hopkins, M. and Howarth, R. 1994. Quantification of quartz cements using combined SEM, CL, and image analysis. *Journal of Sedimentary Research-Section A-Sedimentary Petrology and Processes* 64, 334-338.
- Feist-Burkhardt, S., Gotz, A., Geluk, M., Haas, j., Hornung, J., Jordan, P., Kempf, O., Michalik, j., Nawrocki, J. and Reinhardt, L. 2008. Triassic. In Pankhurst, B. (ed). *The Geology of Central Europe: Mesozoic and Cenozoic: Geological Society Pub House*, 2, 749-823.
- Galehouse, J. 1971. Point counting. *Procedures in sedimentary petrology: New York, Wiley-Interscience* 653, 385-407.
- Giles, M., Stevenson, S., Martin, S., Cannon, S., Hamilton, P., Marshall, J. and Samways, G. 1992. The reservoir properties and diagenesis of the Brent Group: a regional perspective. *Geological Society London Special Publications* 61, 289-327.
- Glennie, K. 1998. *Petroleum geology of the North Sea: basic concepts and recent advances: Blackwell Pub*.
- Goldsmith, P., Hudson, G. and Van Veen, P. 2003. Triassic. *The millenium atlas: Petroleum geology of the central and northern North Sea: Geological Society (London)*, 105.
- Goldsmith, P., Rich, B. and Standring, J. 1995. Triassic correlation and stratigraphy in the South Central Graben, UK North Sea. *Geological Society London Special Publications* 91, 123-143.
- Gowers, M., Holtar, E. and Swensson, E. 1993. The structure of the Norwegian Central trough (Central Graben area). *Petroleum Geology of Northwest Europe: Proceedings of the 4th Conference*, 1245-1254.
- Götze, J., Plötze, M. and Habermann, D. 2001. Origin, spectral characteristics and practical applications of the cathodoluminescence (CL) of quartz—a review. *Mineralogy and Petrology* 71, 225-250.
- Hillier, S. 2003. Quantitative analysis of clay and other minerals in sandstones by X-ray powder diffraction (XRPD). *Clay mineral cements in sandstones*, 213–251.
- Hodgson, N., Farnsworth, J. and Fraser, A. 1992. Salt-related tectonics, sedimentation and hydrocarbon plays in the Central Graben, North Sea, UKCS. *Geological Society London Special Publications* 67, 31-63.
- Humphreys, B., Kemp, S. and Lott, G. 1994. Origin of grain-coating chlorite by smectite transformation; an example from Miocene sandstones, North Sumatra back-arc basin, Indonesia. *Clay minerals* 29, 681-692.

- Humphreys, B., Smith, S. and Strong, G. 1989. Authigenic chlorite formation in Late Triassic sandstones from the Central Graben, North Sea. *Clay minerals* 24, 427-444.
- Høiland, O., Kristensen, J. and Monsen, T. 1993. Mesozoic evolution of the Jæren High area, Norwegian Central North Sea. *Petroleum Geology of Northwest Europe: Proceedings of the 4th Conference*, 1189-1195.
- Jahren, J. and Ramm, M. 2000. The porosity-preserving effects of microcrystalline quartz coatings in arenitic sandstones: examples from the Norwegian continental shelf. *Quartz Cementation in Sandstones* (29), 271-280.
- Khanna, M., Saigal, G. and Bjørlykke, K. 1997. Kaolinitization of the Upper Triassic–Lower Jurassic sandstones of the Tamper Spur area, North Sea: implications for early diagenesis and fluid flow. *Basin-wide Diagenetic Patterns: Integrated Petrologic, Geochemical and Hydrological Considerations*, 253–268.
- Lander, R. and Walderhaug, O. 1999. Predicting porosity through simulating sandstone compaction and quartz cementation. *AAPG bulletin* 83, 433-449.
- Longiaru, S. 1987. Visual comparators for estimating the degree of sorting from plane and thin section. *Journal of Sedimentary Research* 57, 791.
- Lundegard, P. 1992. Sandstone porosity loss—a “big picture” view of the importance of compaction. *Journal of Sedimentary Petrology* 62, 250-260.
- Marshall, J. and Hewett, A. 2003. *Devonian*. Edited by Evans, D., Graham, C., Armour, A. and Bathurst, P. The Millennium Atlas: petroleum geology of the central and northern North Sea: Geological Society of London.
- McKenzie, D. 1978. Some remarks on the development of sedimentary basins. *Earth and Planetary Science Letters* 40, 25-32.
- McKie, T., Jolley, S. and Kristensen, M. 2010. (In Press) Stratigraphic and structural compartmentalization of dryland fluvial reservoirs: Triassic Heron Cluster, Central North Sea. In Jolley, S., Fisher, Q., Ainsworth, R., Vrolijk, P. and Delisle, S. (eds). *Geological Society London Special Publications*. Reservoir Compartmentalization, XXX, pp.XX-XX.
- McKie, T. and Williams, B. 2009. Triassic palaeogeography and fluvial dispersal across the northwest European Basins. *Geological Journal* 44, 711-741.
- Milliken, K., Choh, S. and McBride, E. 2007. *Sandstone Petrology: a Tutorial Petrographic Image Atlas*: AAPG/Datapages.
- Moore, D. and Reynolds, R. 1997. *X-ray Diffraction and the Identification and Analysis of Clay Minerals*: Oxford University Press Oxford.

- Morad, S. 1998. Carbonate cementation in sandstones: distribution patterns and geochemical evolution. In Morad, S. (ed). *Carbonate Cementation in Sandstones*. Special Publication Number 26 of the International Association of Sedimentologists: Blackwell Science, 1-27.
- NPD. 2010. Norwegian Petroleum Directorate Fact-pages 2010 [Accessed: 2010]. Available at <http://www.npd.no/engelsk/cwi/pbl/en/index.htm>
- O'Connor, B. and Chang, W. 1986. The amorphous character and particle size distributions of powders produced with the micronizing mill for quantitative X-ray powder diffractometry. *X-ray Spectrometry* 15.
- Oelkers, E., Bjørkum, P., Walderhaug, O., Nadeau, P. and Murphy, W. 2000. Making diagenesis obey thermodynamics and kinetics: the case of quartz cementation in sandstones from offshore mid-Norway. *Applied geochemistry* 15, 295-309.
- Parrish, J. 1993. Climate of the supercontinent Pangea. *The Journal of Geology* 101, 215-233.
- Peltonen, C., Marcussen, O., Bjorlykke, K. and Jahren, J. 2008. Mineralogical control on mudstone compaction: a study of Late Cretaceous to Early Tertiary mudstones of the Voring and More basins, Norwegian Sea. *Petroleum Geoscience* 14, 127.
- Ramm, M. 1991. On quantitative mineral analysis of sandstones using XRD. *Dept Geol Oslo, Intern Skr Ser* 62, 1-28.
- Ramm, M. 1992. Porosity-depth trends in reservoir sandstones: theoretical models related to Jurassic sandstones offshore Norway. *Marine and Petroleum Geology* 9, 553-567.
- Rogers, J. and Head, W. 1961. Relationships between porosity, median size, and sorting coefficients of synthetic sands. *Journal of Sedimentary Petrology* 31, 467-470.
- Rønnevik, H., Van Den Bosch, W. and Bandlien, E. 1975. A proposed nomenclature for the main structural features in the Norwegian North Sea, 28-30.
- Sclater, J. and Christie, P. 1980. Continental stretching: an explanation of the post-mid-Cretaceous subsidence of the central North Sea basin. *Journal of Geophysical Research* 85, 3711-3739.
- Sears, R., Harbury, A., Protoy, A. and Stewart, D. 1993. Structural styles from the Central Graben in the UK and Norway, 1231.
- Simms, M. and Ruffell, A. 1989. Synchronicity of climatic change and extinctions in the Late Triassic. *Geology* 17, 265-268.
- Singer, A. 1984. The paleoclimatic interpretation of clay minerals in sediments--a review. *Earth-Science Reviews* 21, 251-293.
- Skjervén, J., Rijs, F. and Kalheim, J. 1983. Late Paleozoic to Early Cenozoic structural development of the south-southeastern Norwegian North Sea. *Geologie en Mijnbouw* 62, 35-45.

- Smith, R., Hodgson, N. and Fulton, M. 1993. Salt control on Triassic reservoir distribution, UKCS Central North Sea, 547.
- Snyder, R. and Bish, D. 1989. Quantitative analysis. *Reviews in Mineralogy*, 20 pp 101.
- Srodon, J. 1999. Use of clay minerals in reconstructing geological processes: recent advances and some perspectives. *Clay minerals* 34, 27-27.
- Stokes, S. 1851. *On the effect of the internal friction of fluids on the motion of pendulums*: Pitt Press.
- Storvoll, V., Bjørlykke, K., Karlsen, D. and Saigal, G. 2002. Porosity preservation in reservoir sandstones due to grain-coating illite: a study of the Jurassic Garn Formation from the Kristin and Lavrans fields, offshore Mid-Norway. *Marine and Petroleum Geology* 19, 767-781.
- Sørli, R. 1996. *Diagenetisk utvikling i Lunda- og Statfjordformasjonens slam- og sandsteiner på Snorrefeltet*, Institutt for Geologi Avdeling for Sedimentologi, Universitetet i Oslo, Oslo.
- Walderhaug, O. 1994. Temperatures of quartz cementation in Jurassic sandstones from the Norwegian continental shelf-evidence from fluid inclusions. *Journal of Sedimentary Research-Section A-Sedimentary Petrology and Processes* 64, 311-323.
- Walderhaug, O. 1996. Kinetic modeling of quartz cementation and porosity loss in deeply buried sandstone reservoirs. *AAPG Bulletin-American Association of Petroleum Geologists* 80, 731-745.
- Weibel, R. 1999. Effects of burial on the clay assemblages in the Triassic Skagerrak Formation, Denmark. *Clay minerals* 34, 619-635.
- Weltje, G. 2002. Quantitative analysis of detrital modes: statistically rigorous confidence regions in ternary diagrams and their use in sedimentary petrology. *Earth Science Reviews* 57, 211-253.
- Welton, J. 1984. SEM petrology atlas. Methods in Exploration Series. *Tulsa, AAPG*, 237p.
- Wilson, M. and Pittman, E. 1977. Authigenic clays in sandstones: recognition and influence on reservoir properties and paleoenvironmental analysis. *Journal of Sedimentary Petrology* 47, 3-31.
- Worden, R. 1998. Dolomite cement distribution in a sandstone from core and wireline data: the Triassic fluvial Chaunoy Formation, Paris Basin. *Geological Society London Special Publications* 136, 197.
- Worden, R. and Matray, J. 1998. Carbonate cement in the Triassic Chaunoy Formation of the Paris Basin: distribution and effect on flow properties. *Carbonate cementation in sandstones: distribution patterns and geochemical evolution*, 163-177.

- Wright, V. 1994. Postgraduate Research Institute for Sedimentology, The University, P. O. Box 22 7, Whiteknights, Reading, RG6 2AB, UK. *Quantitative diagenesis: recent developments and applications to reservoir geology*, 95.
- Zanella, E. and Coward, M. 2003. Structural framework. *The Millennium Atlas: Petroleum Geology of the Central and Northern North Sea Geological Society, London*, 45–59.
- Ziegler, P. 1975. Geologic evolution of North Sea and its tectonic framework. *AAPG Bull* 59, 1073-1097.
- Ziegler, P. 1980. Geology and hydrocarbon provinces of the North Sea. *GeoJournal* 1, 7-32.
- Ziegler, P. 1990. *Geological atlas of western and central Europe*: Geological Society.
- Ziegler, P. and Van Hoorn, B. 1989. Evolution of North Sea rift system. *Extensional tectonics and stratigraphy of the North Atlantic margins: AAPG Memoir* 46, 471–500.

Appendix

Appendix I – XRD data

Appendix Ib – Excel spreadsheet of XRD data

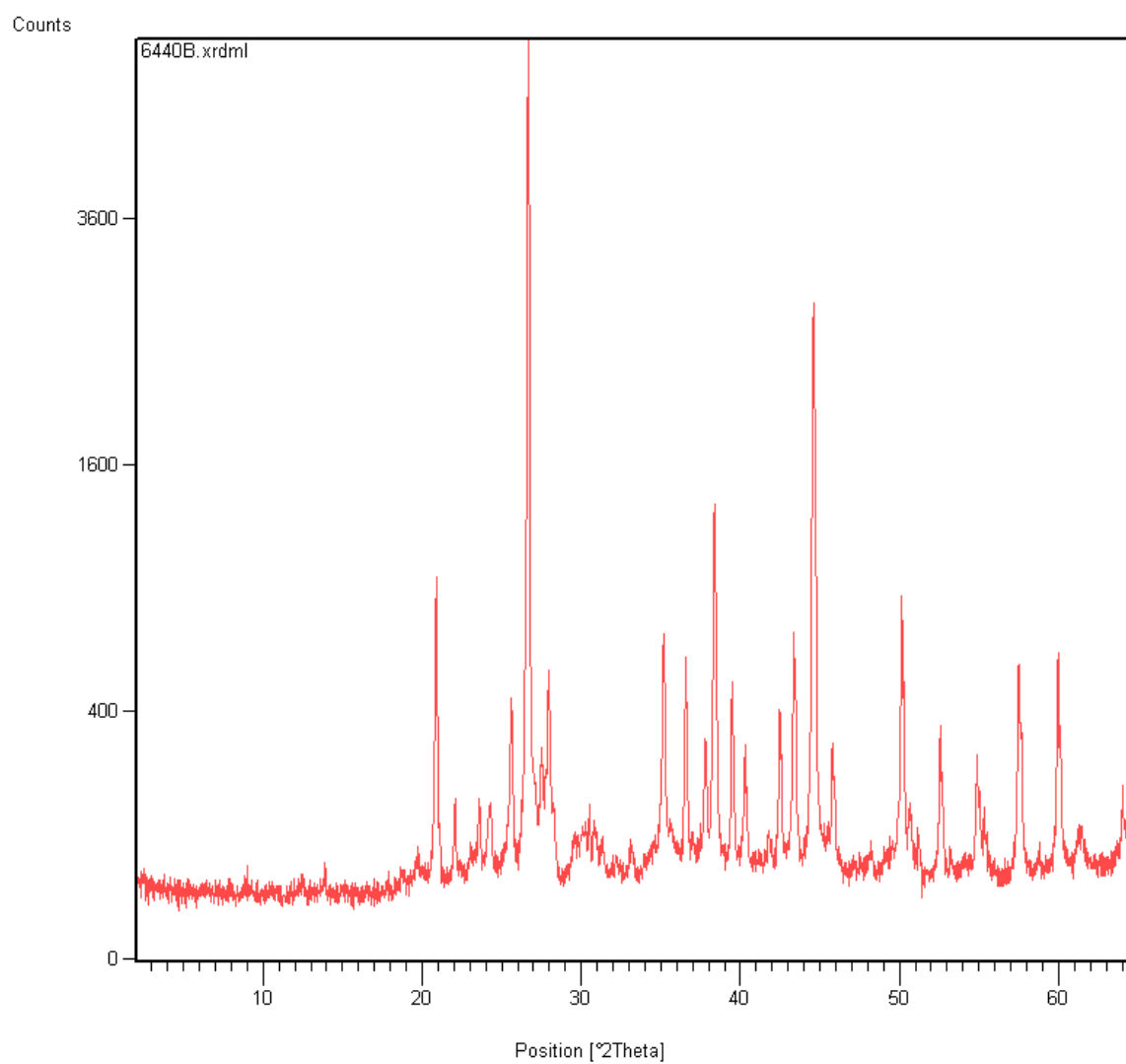
Appendix II – Thin section analysis

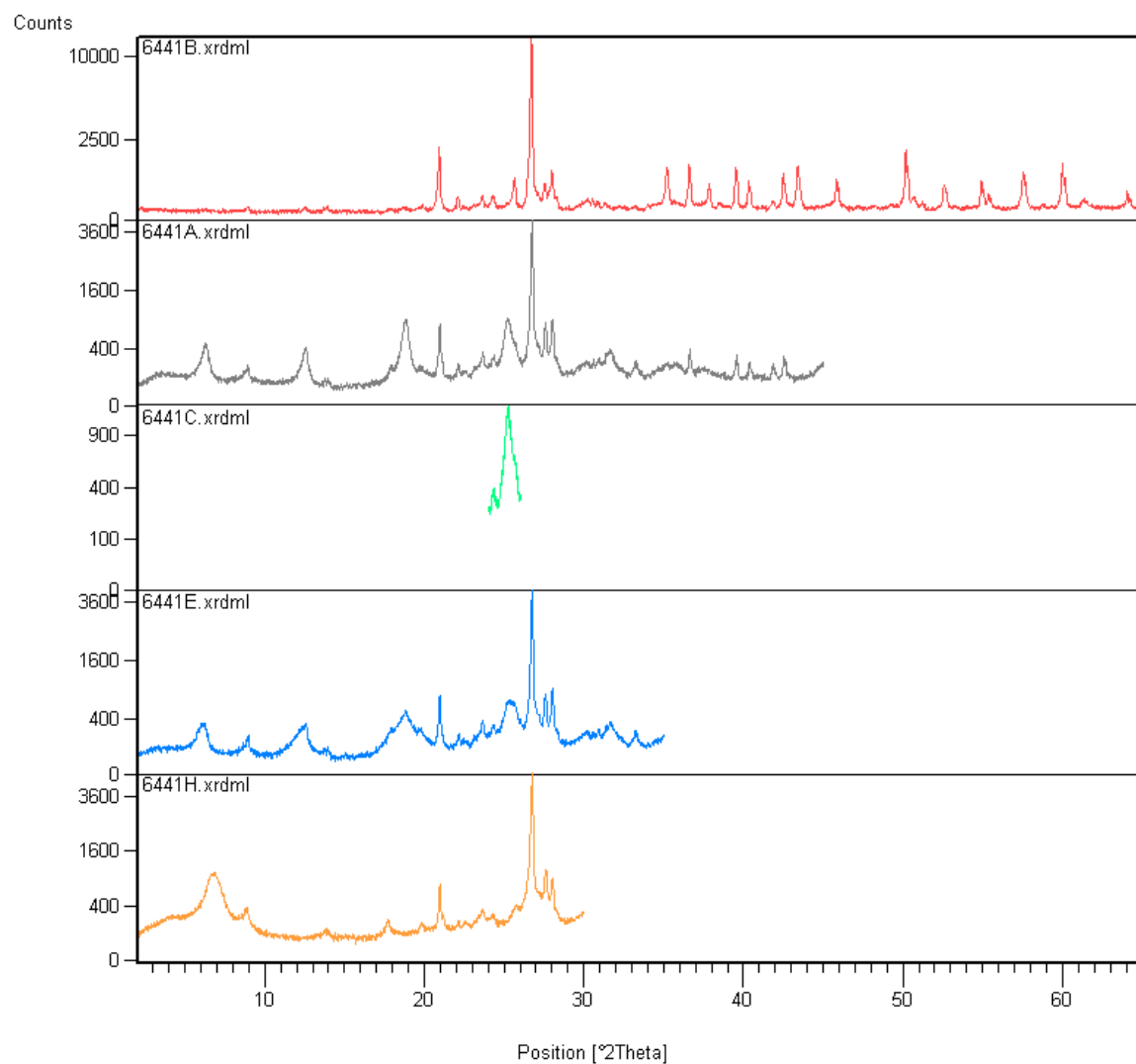
Appendix IIb – Point counting

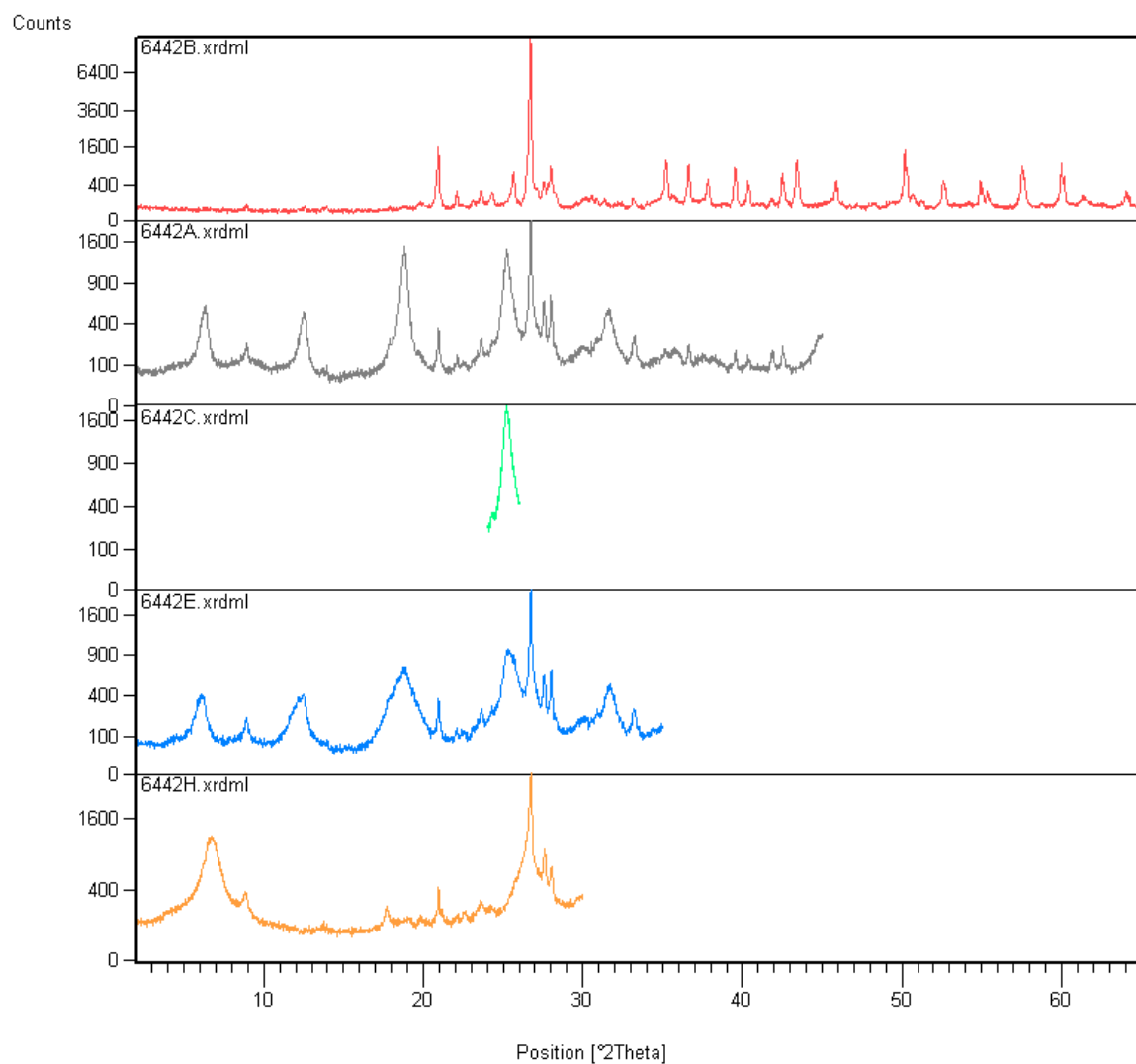
Appendix IIc – Fractures caused by thin section preparation

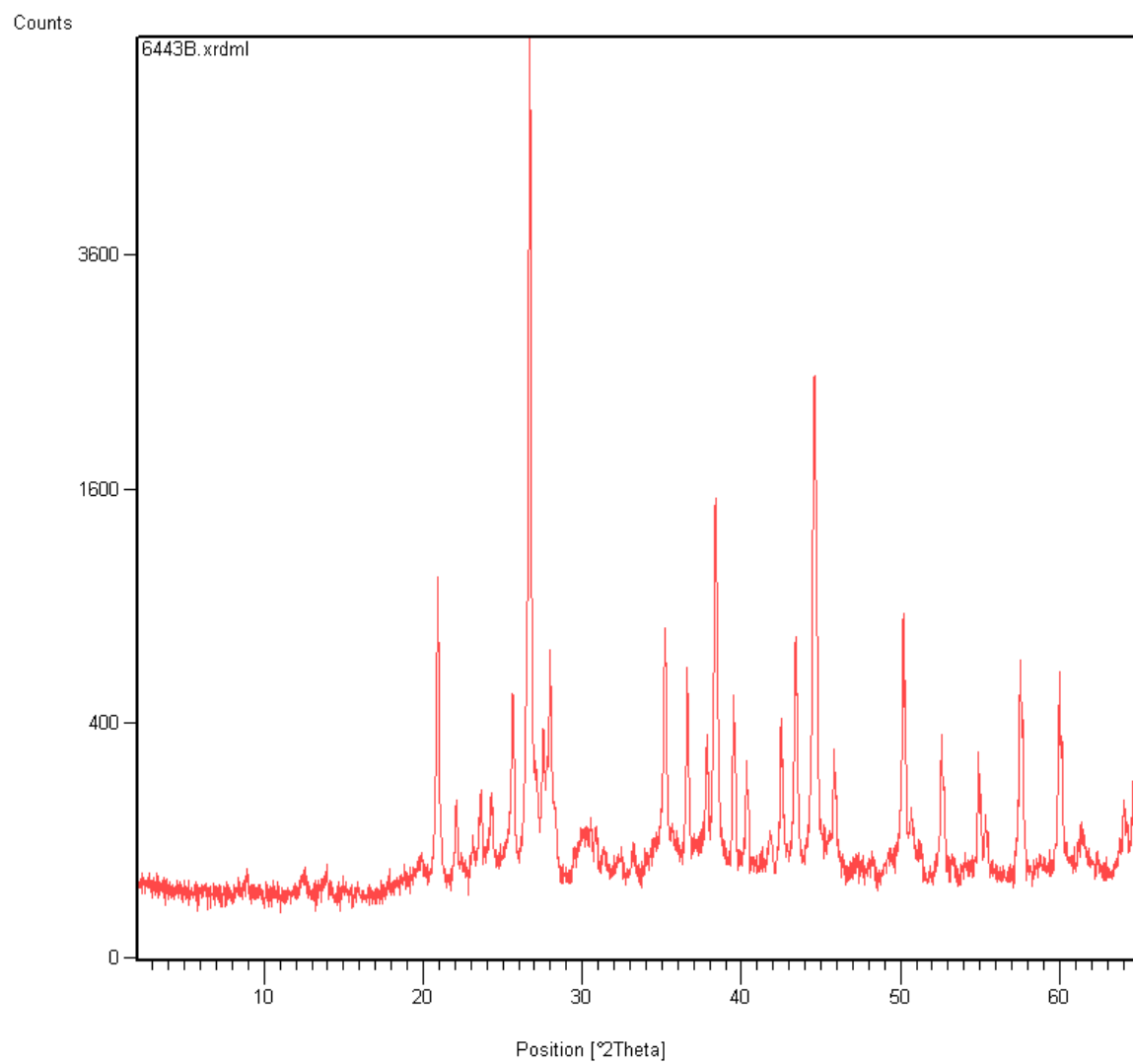
Appendix III – Chlorite composition

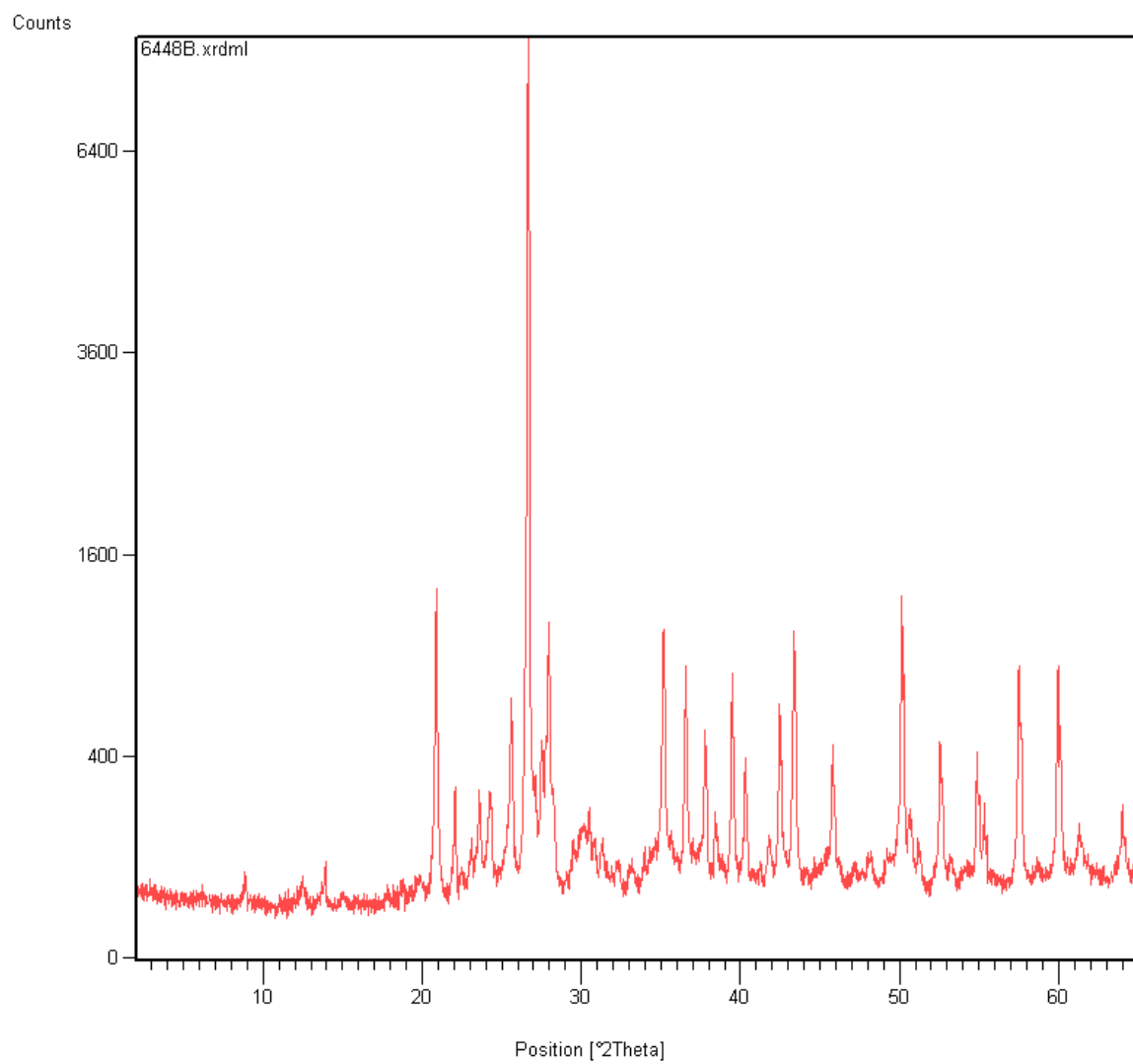
Appendix I – XRD data

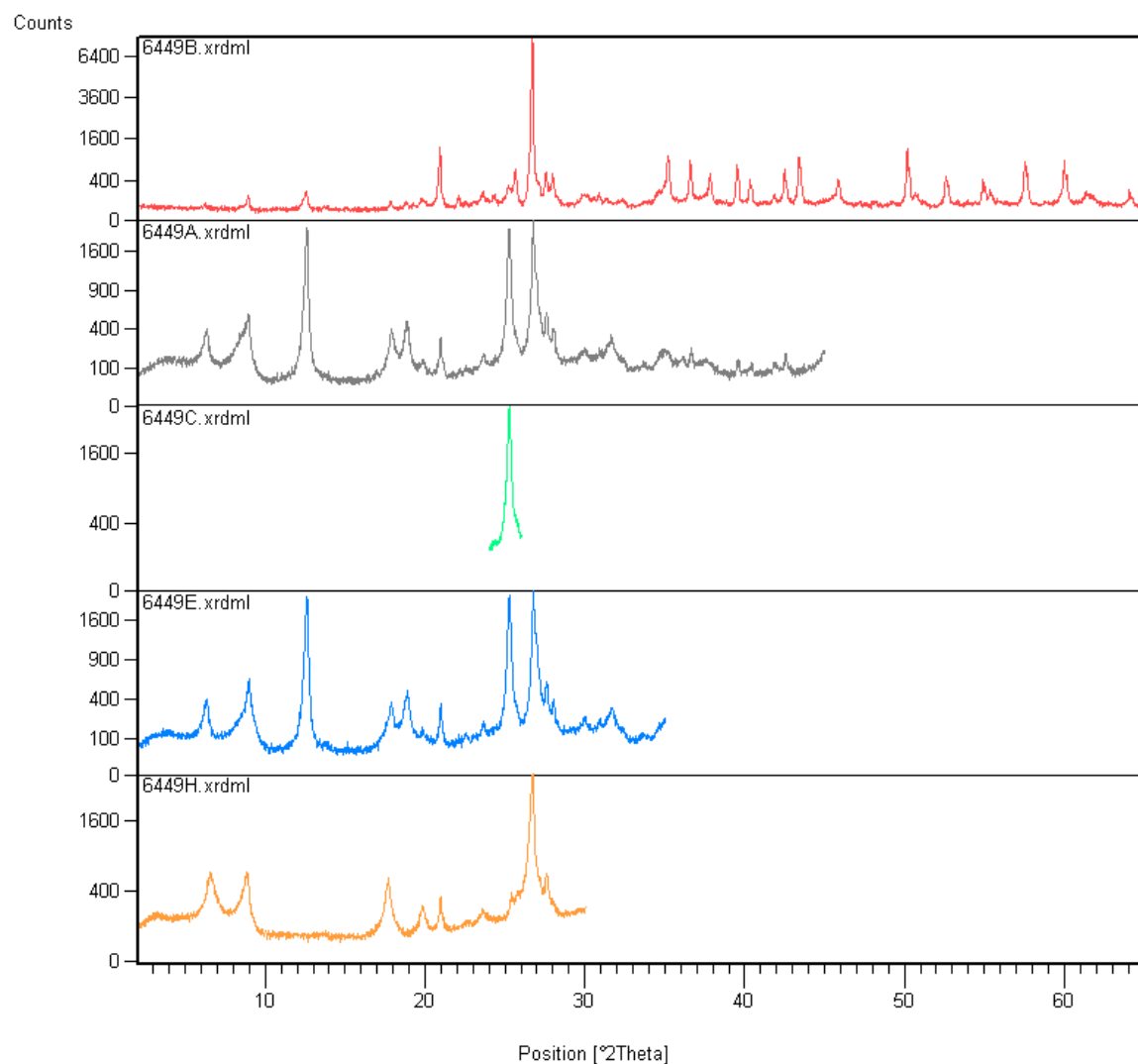


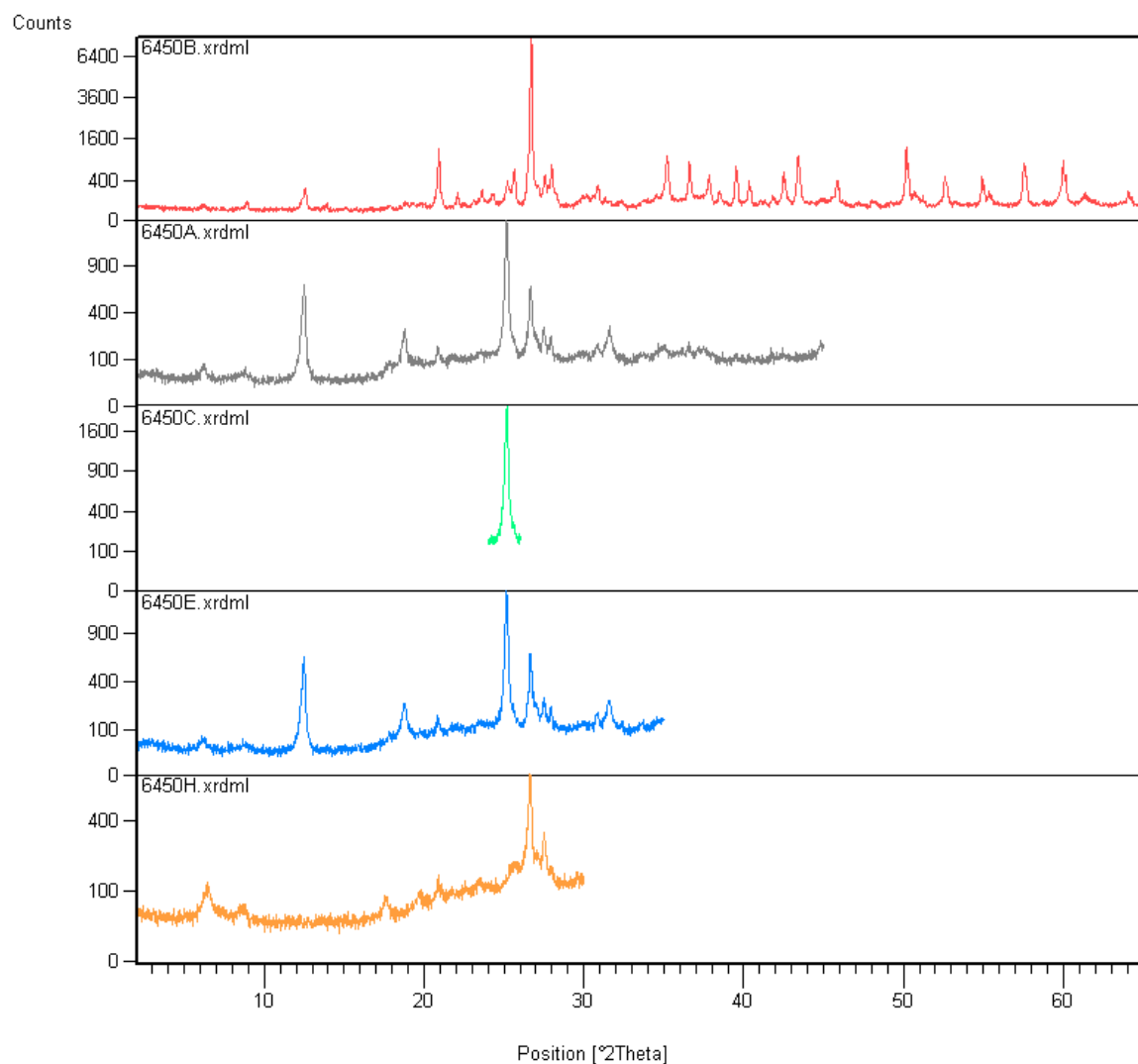


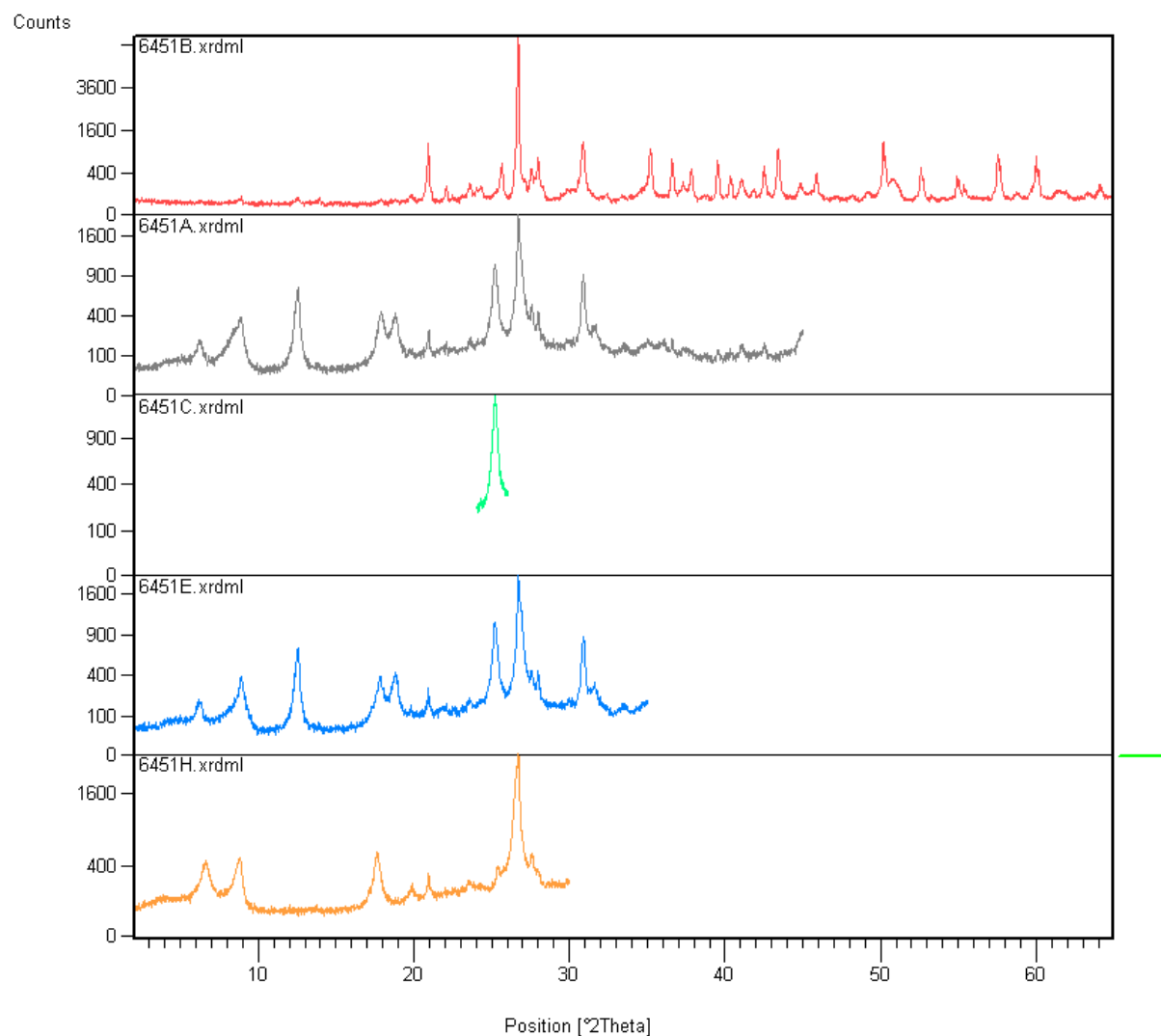


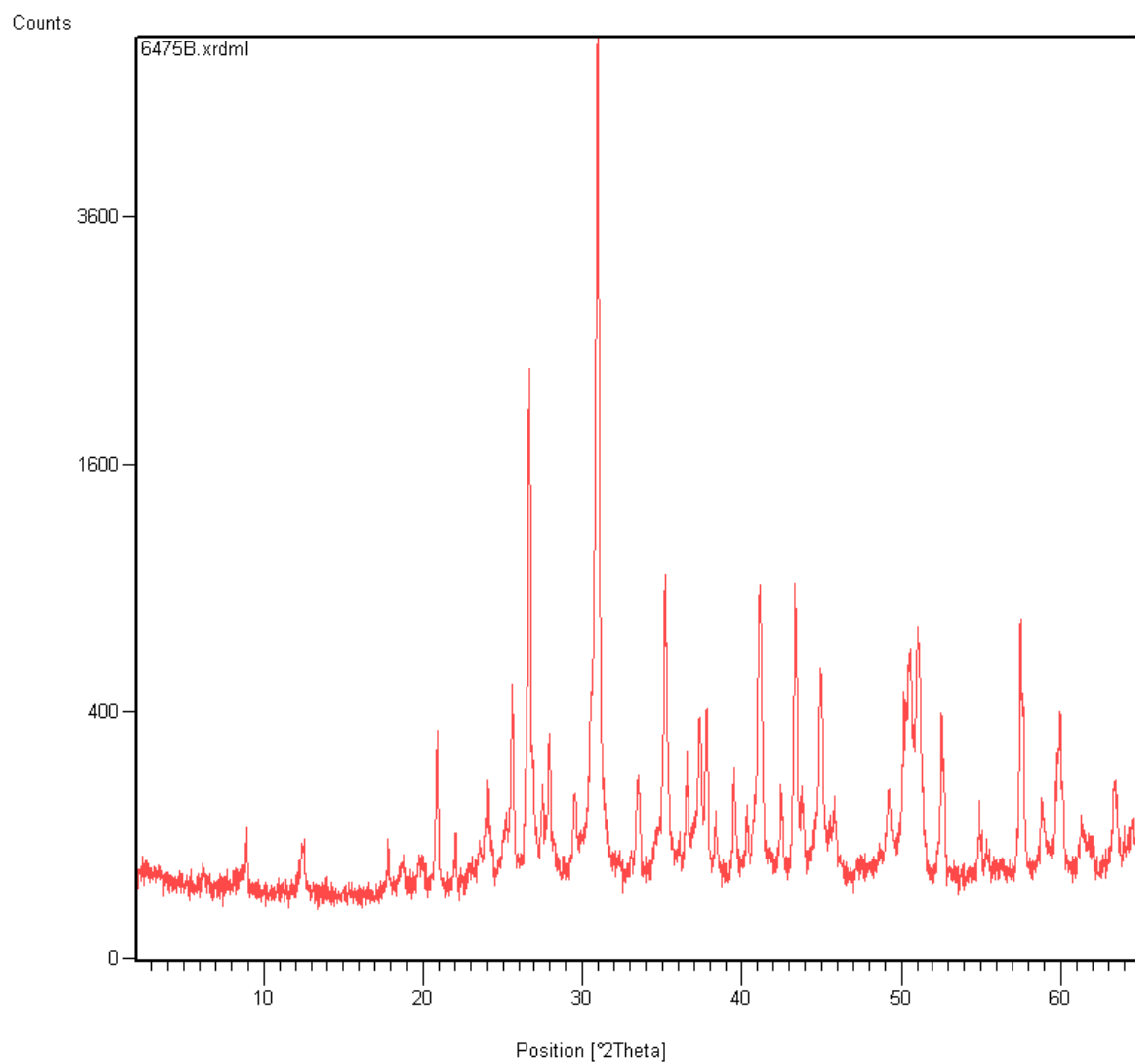


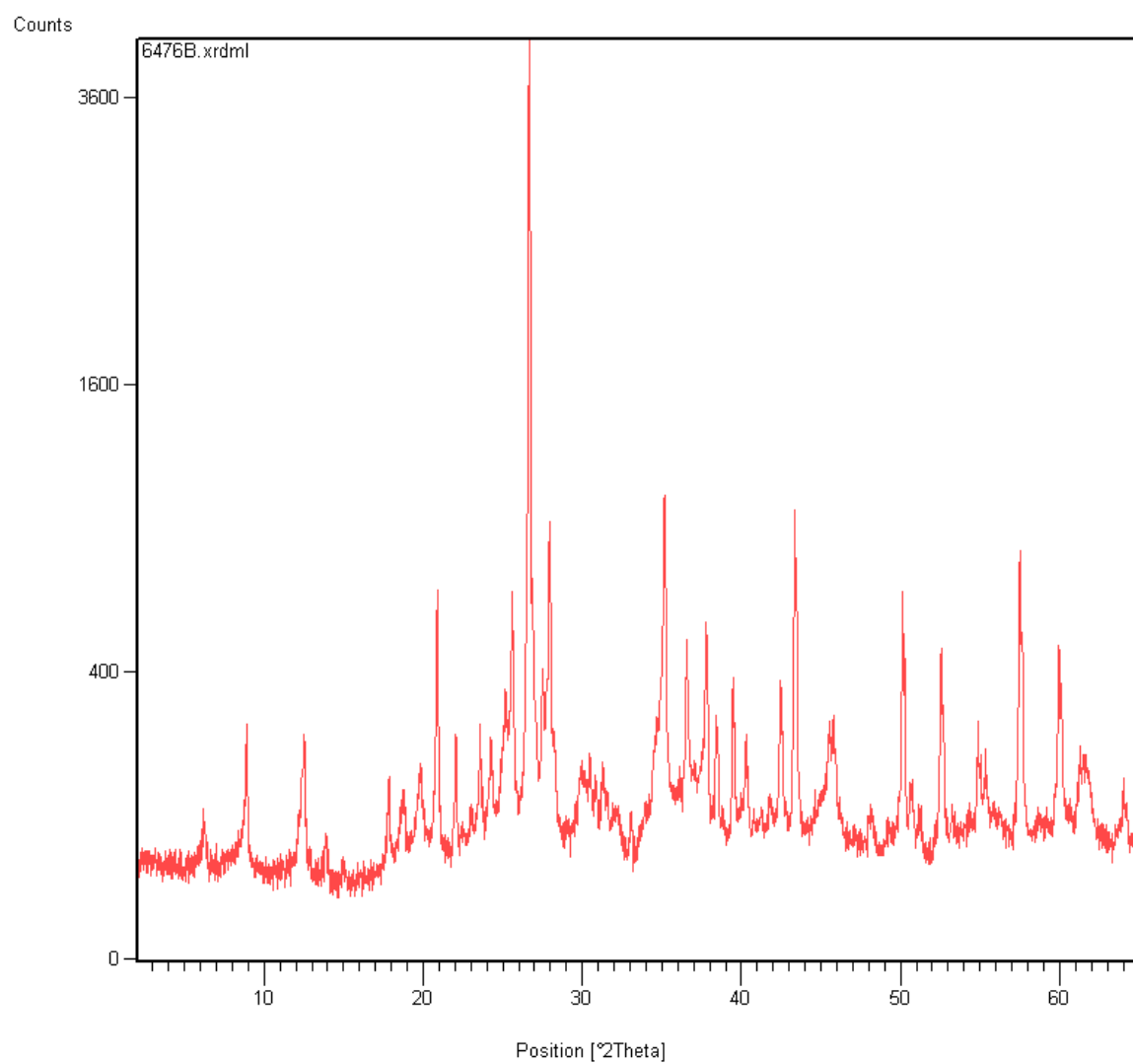


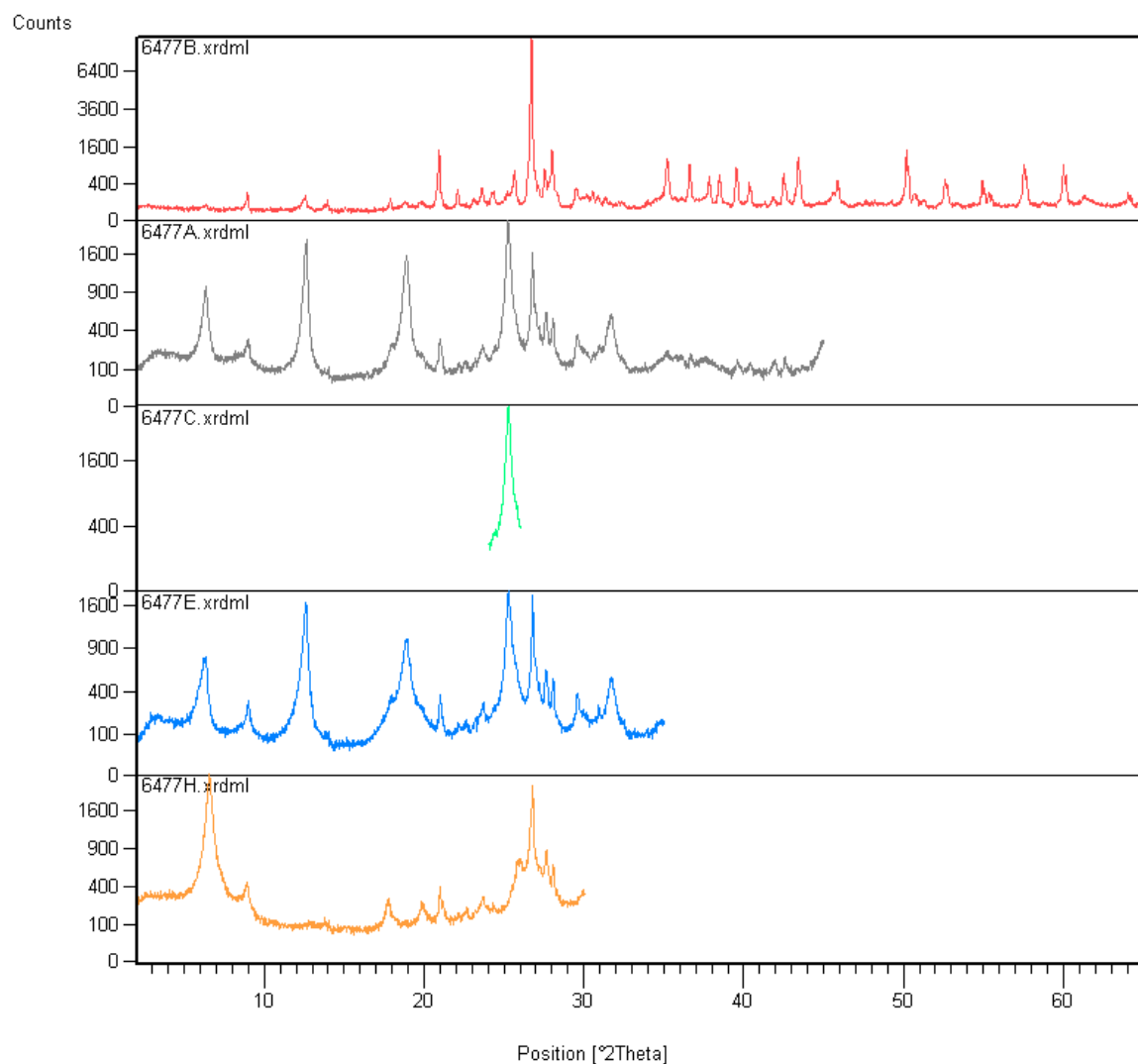


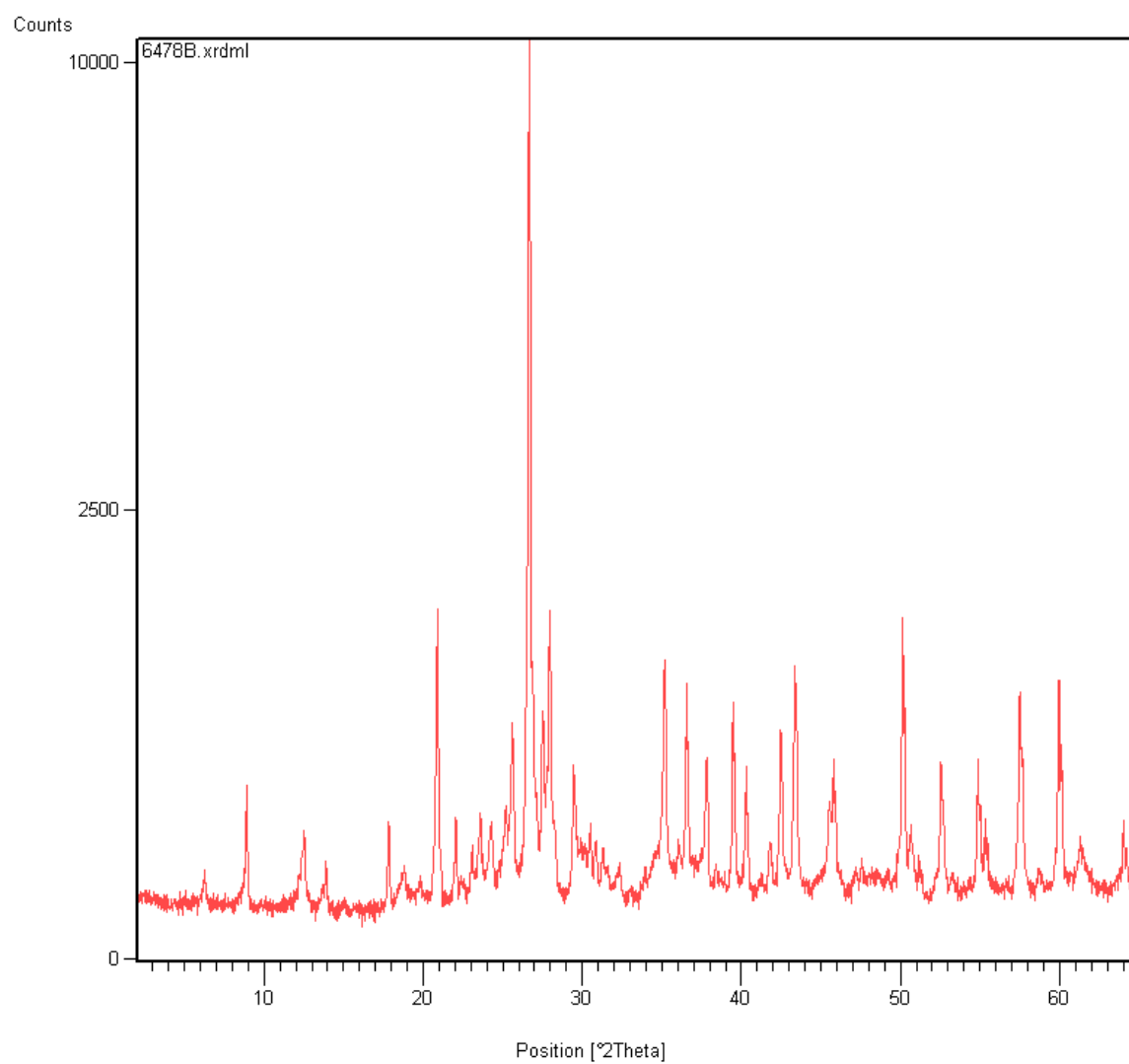


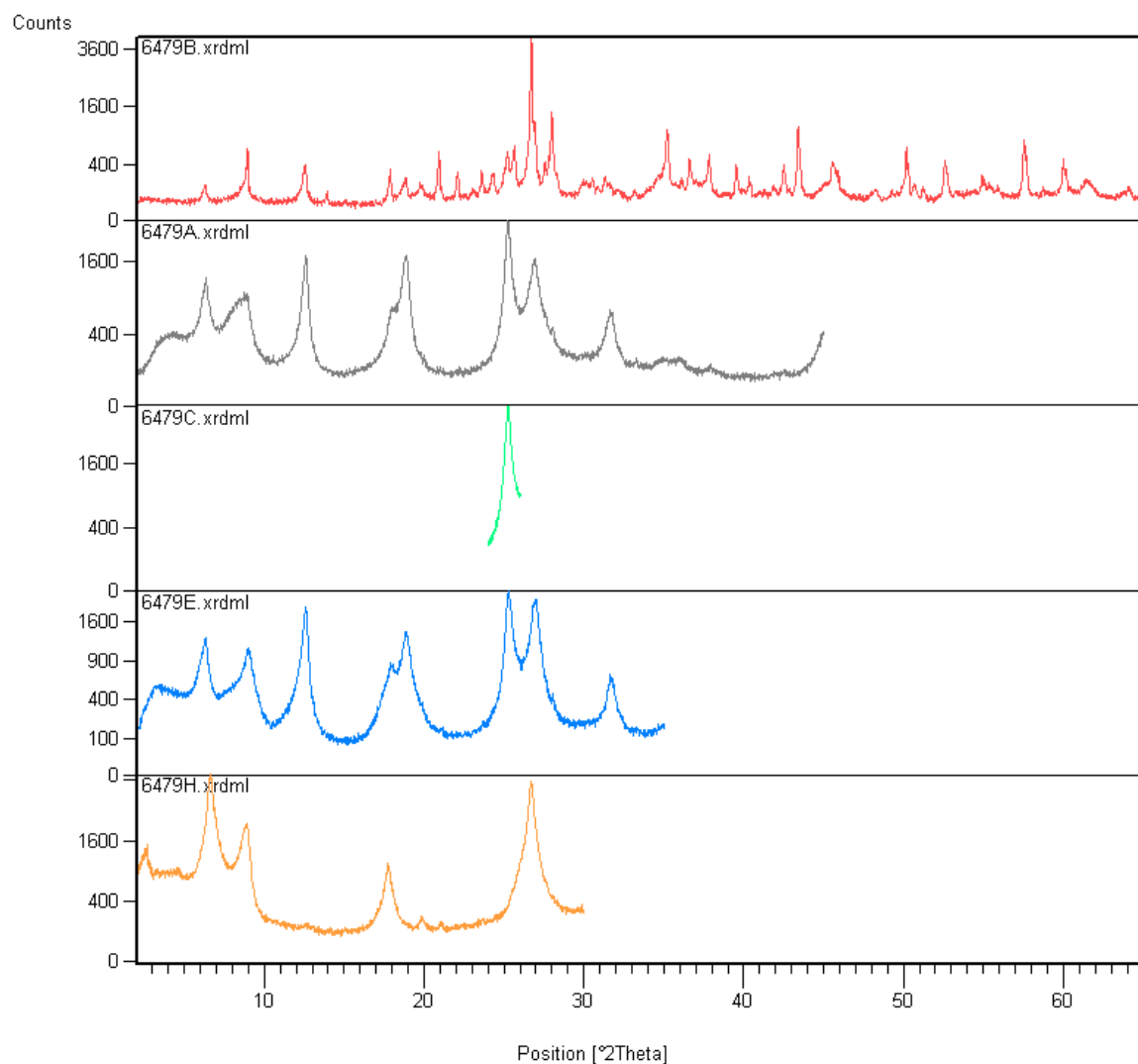


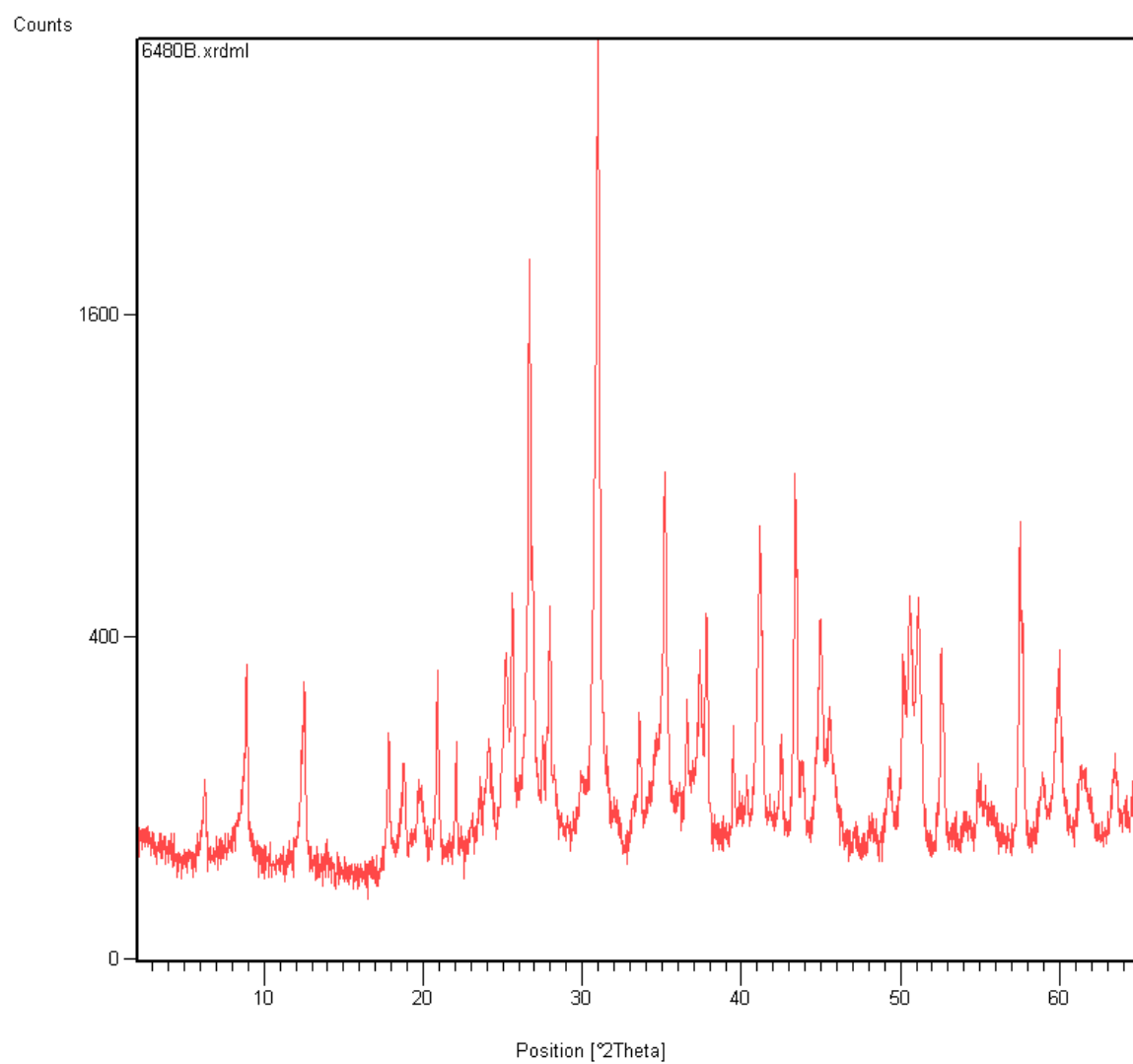


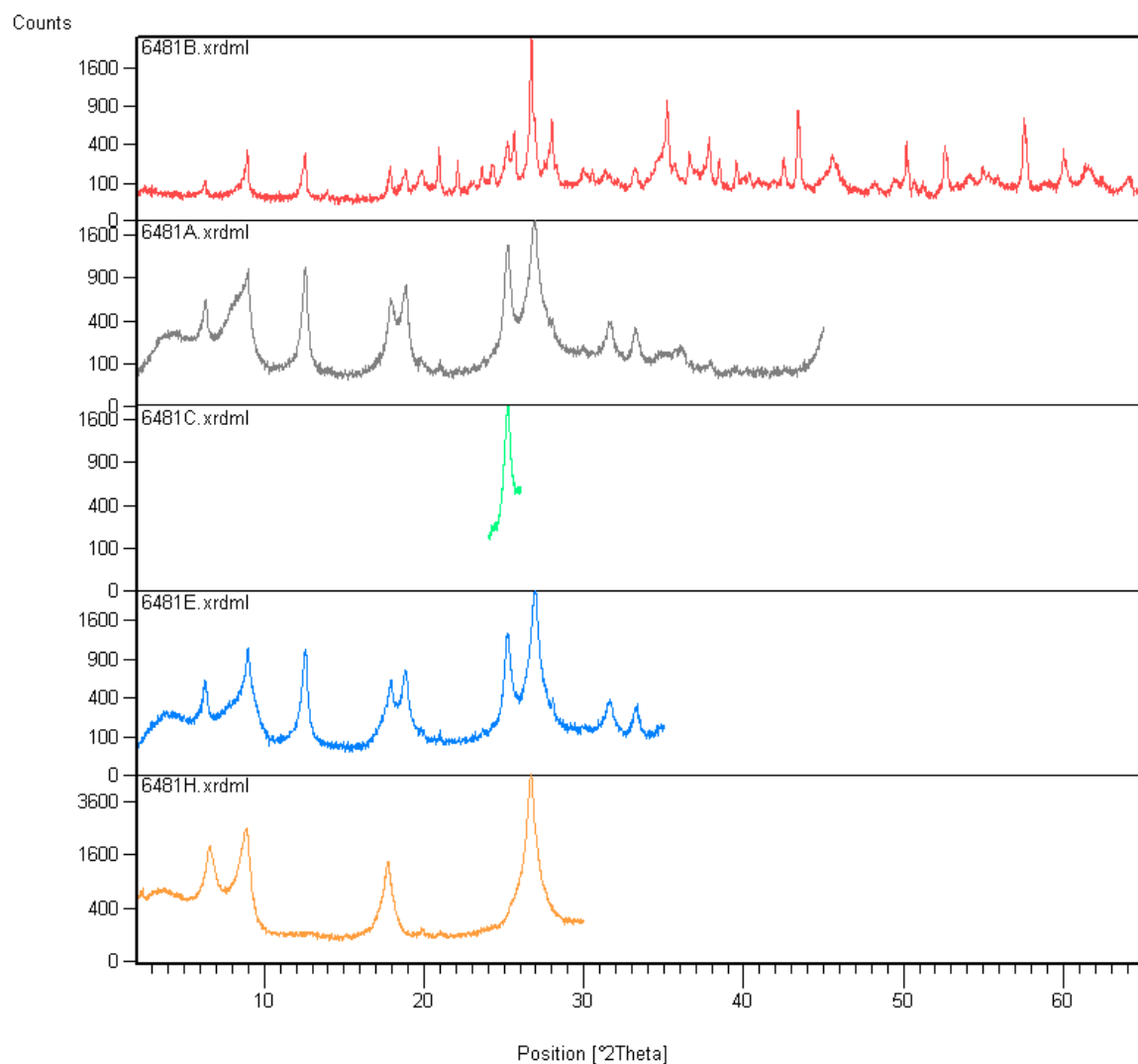


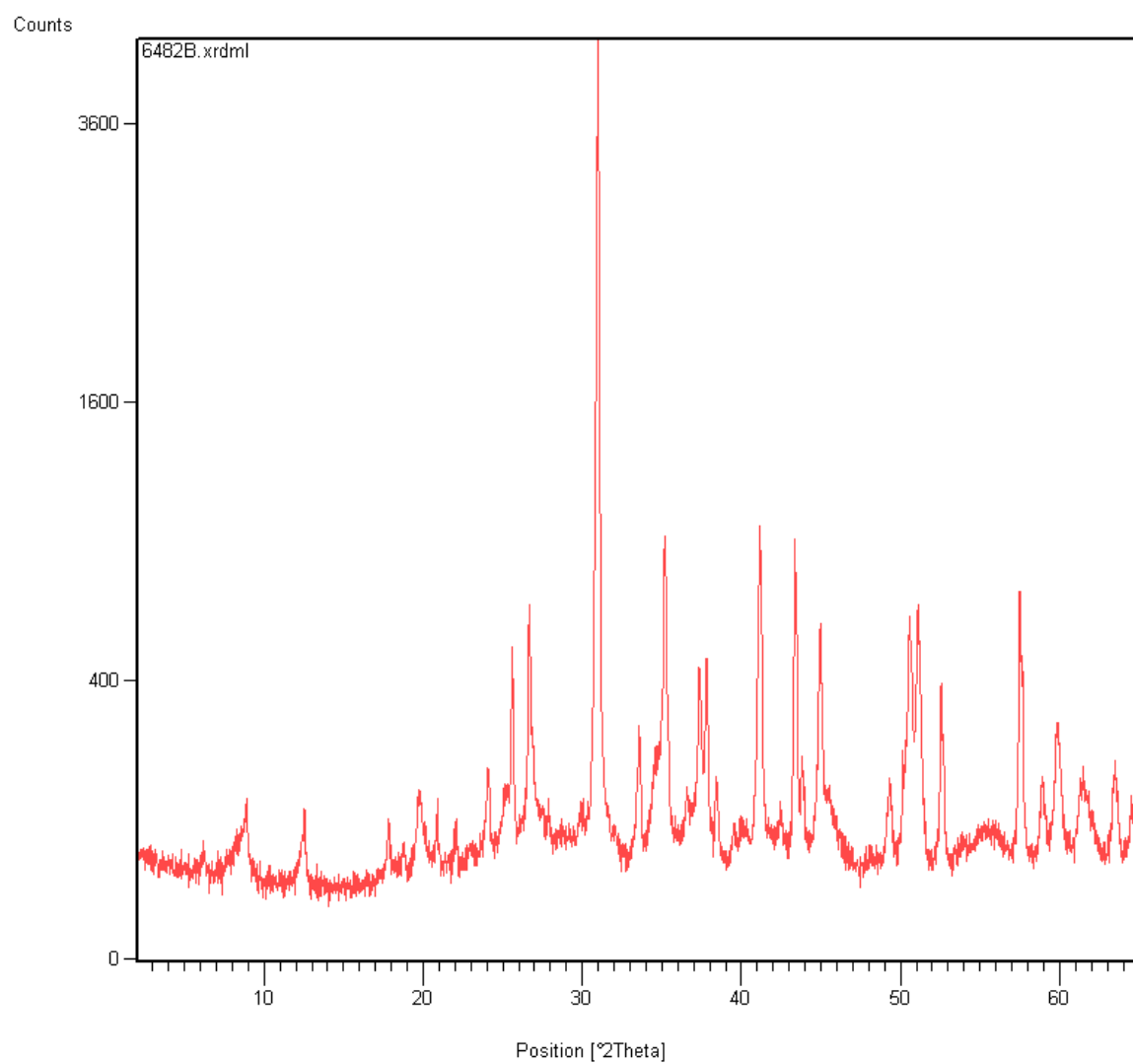


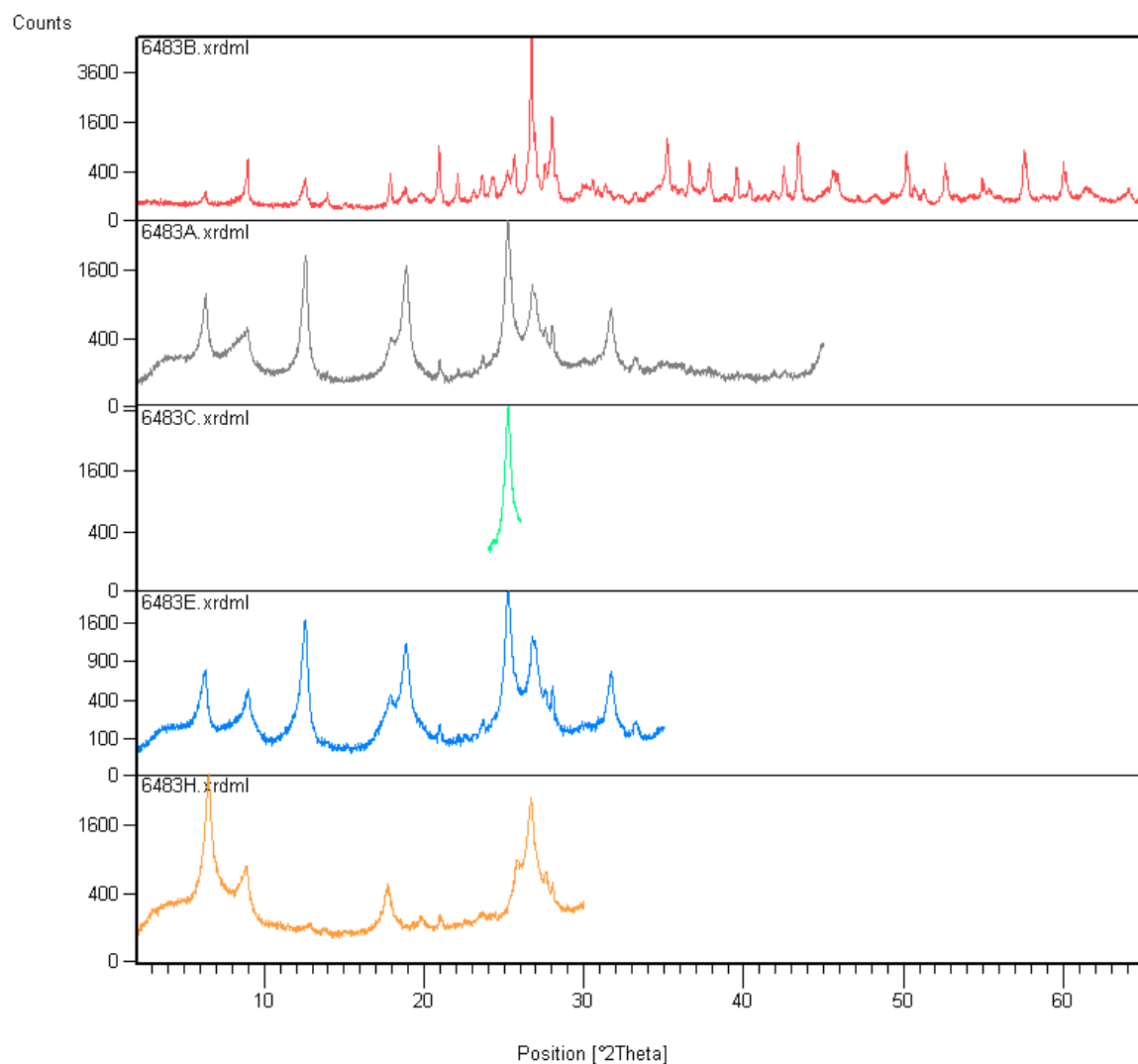


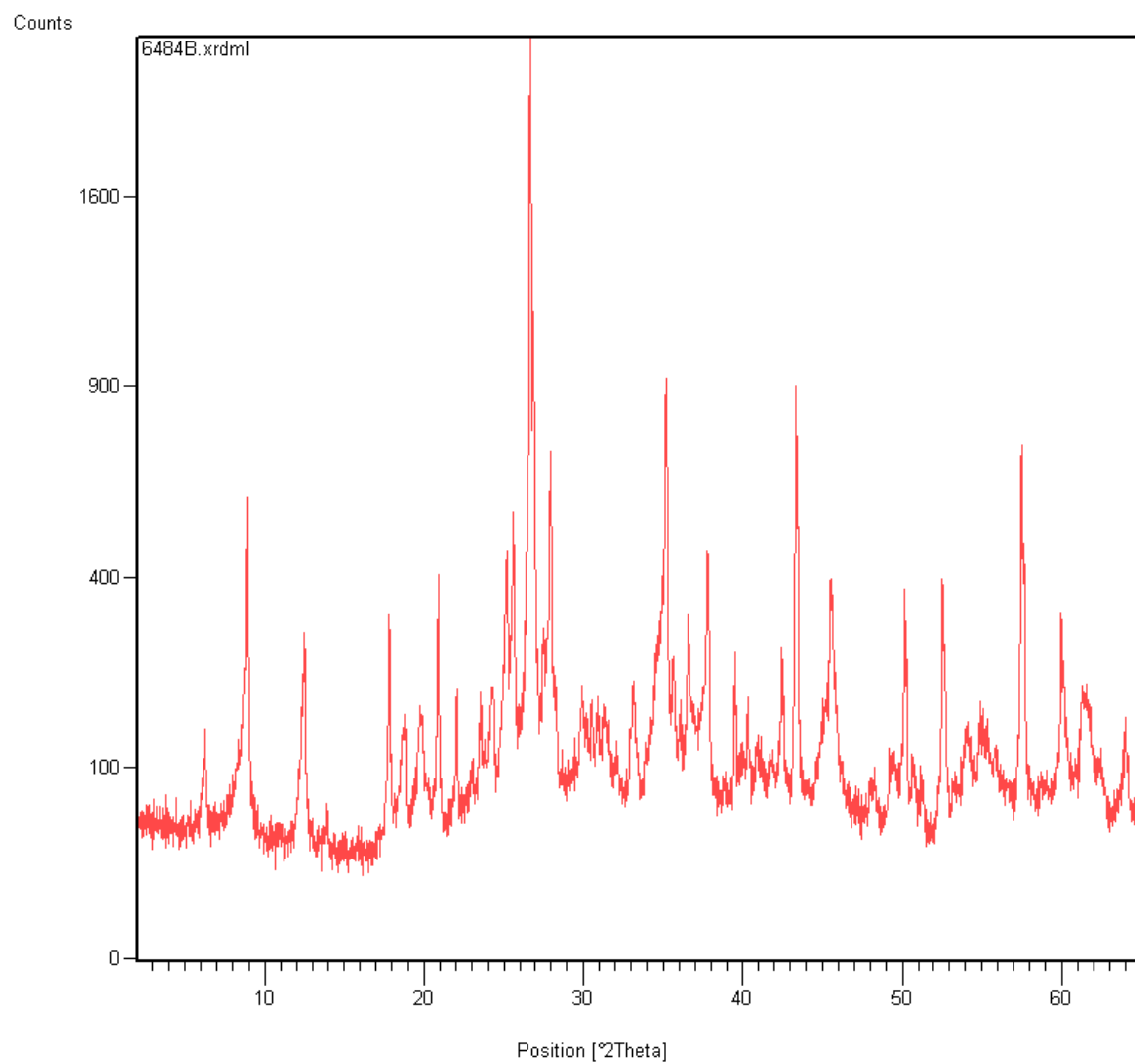


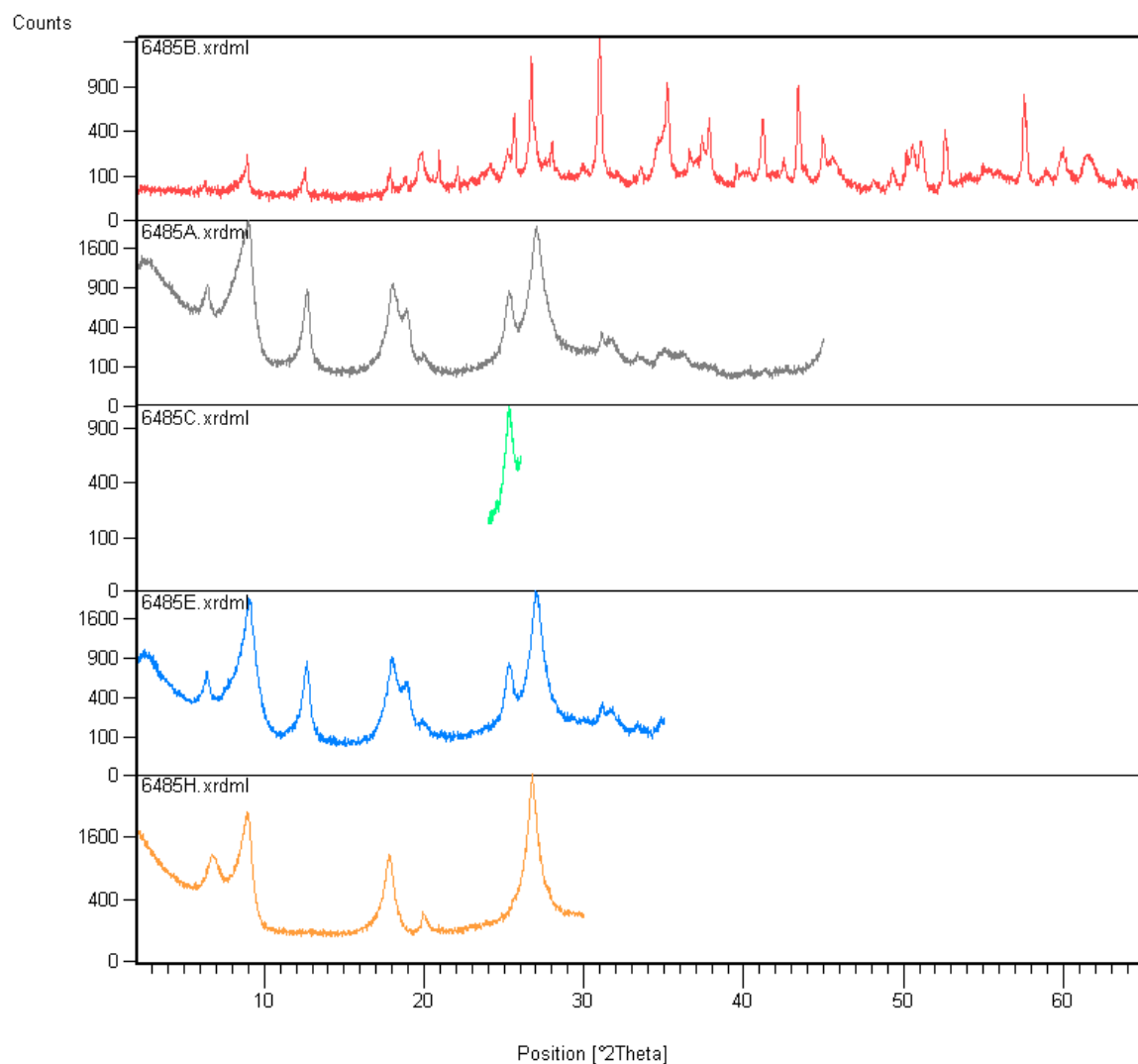


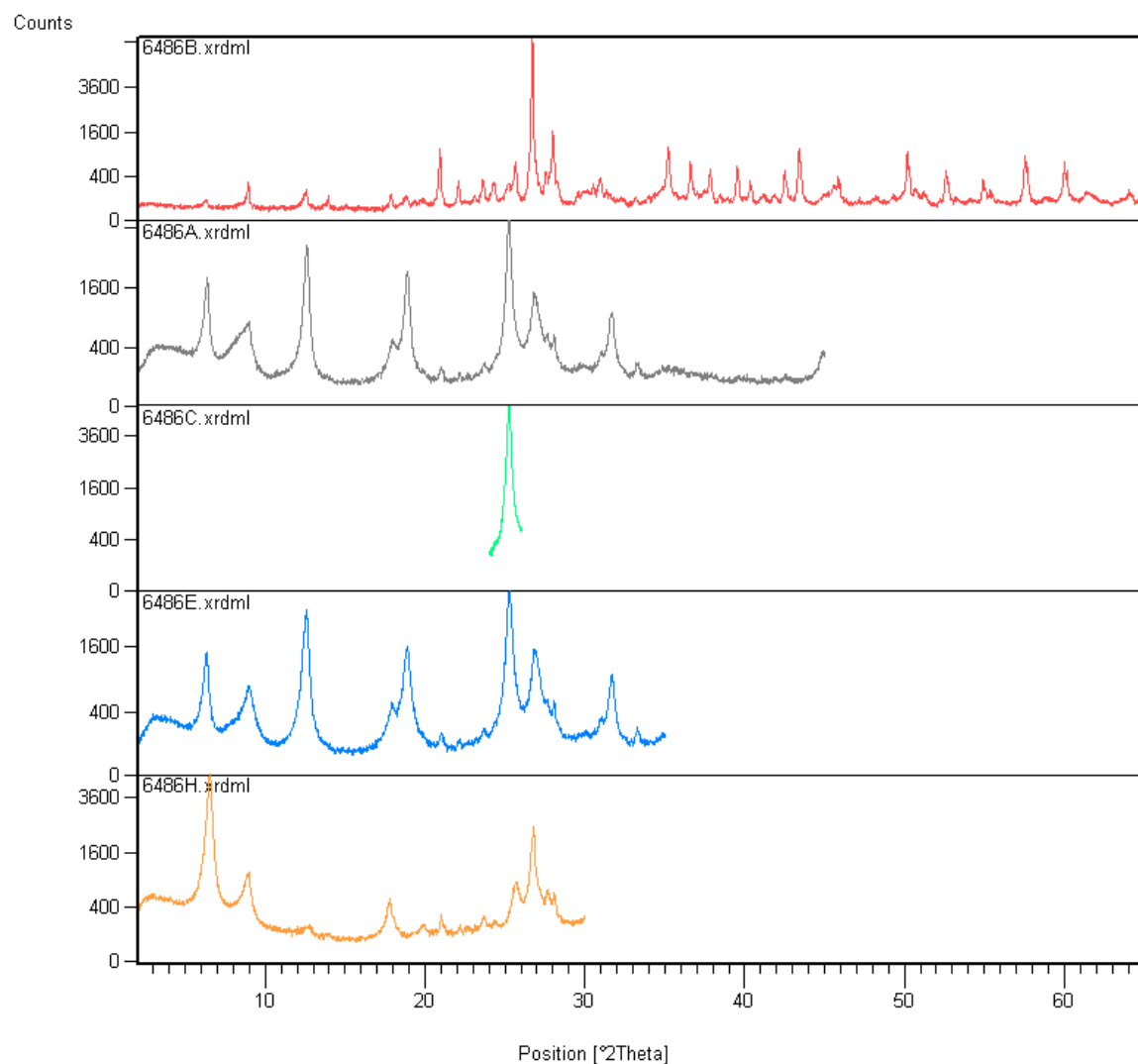


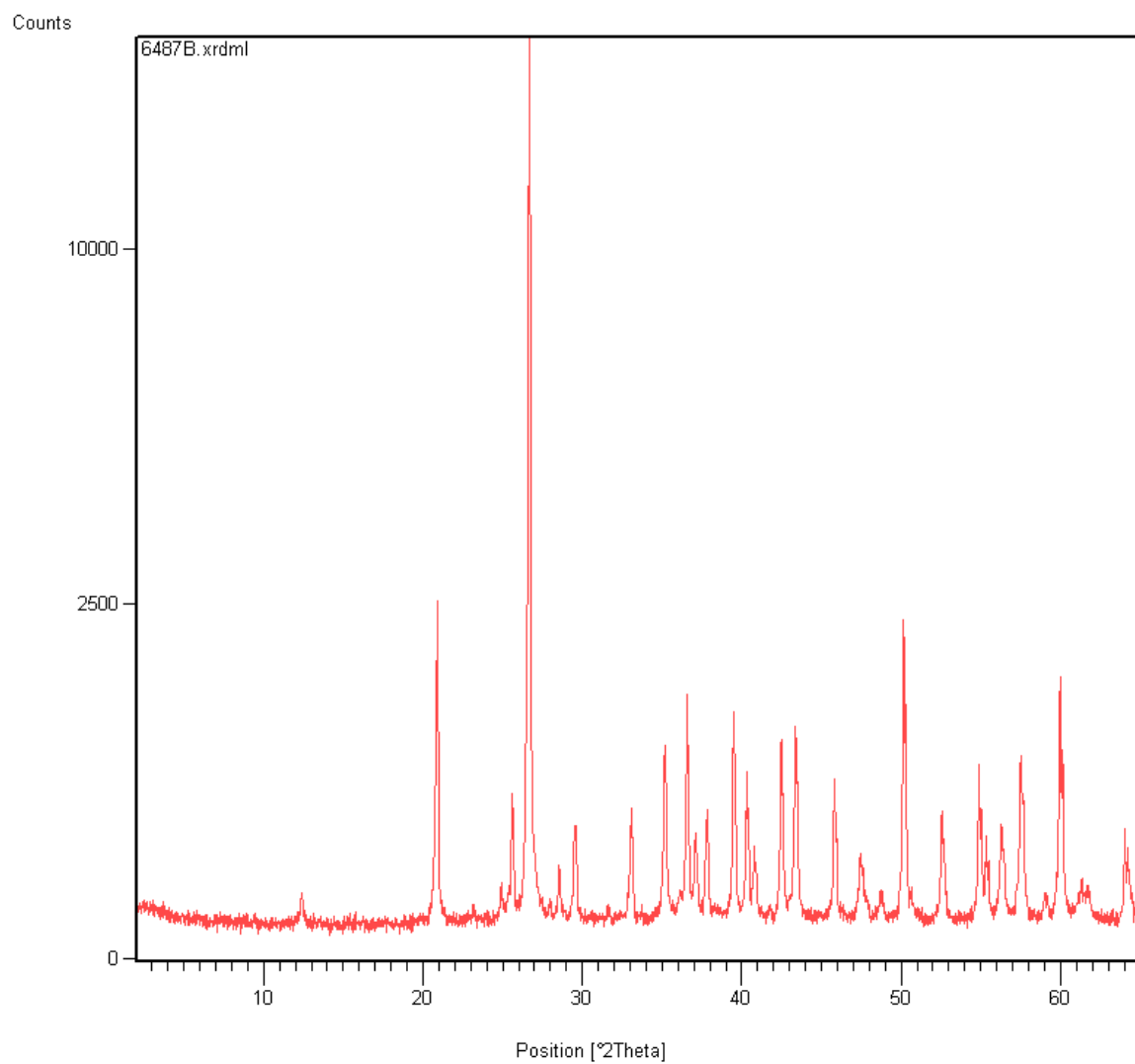


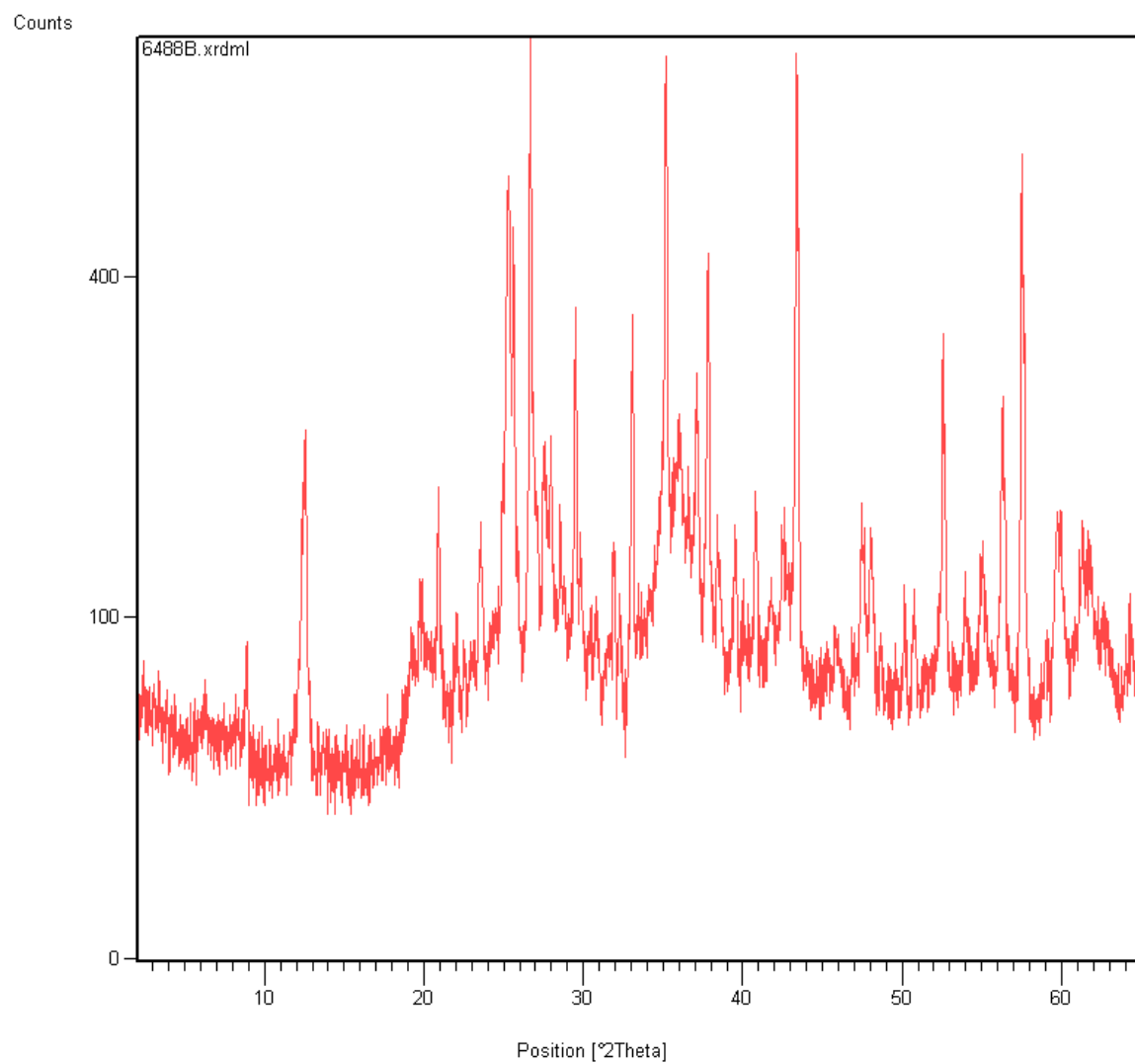


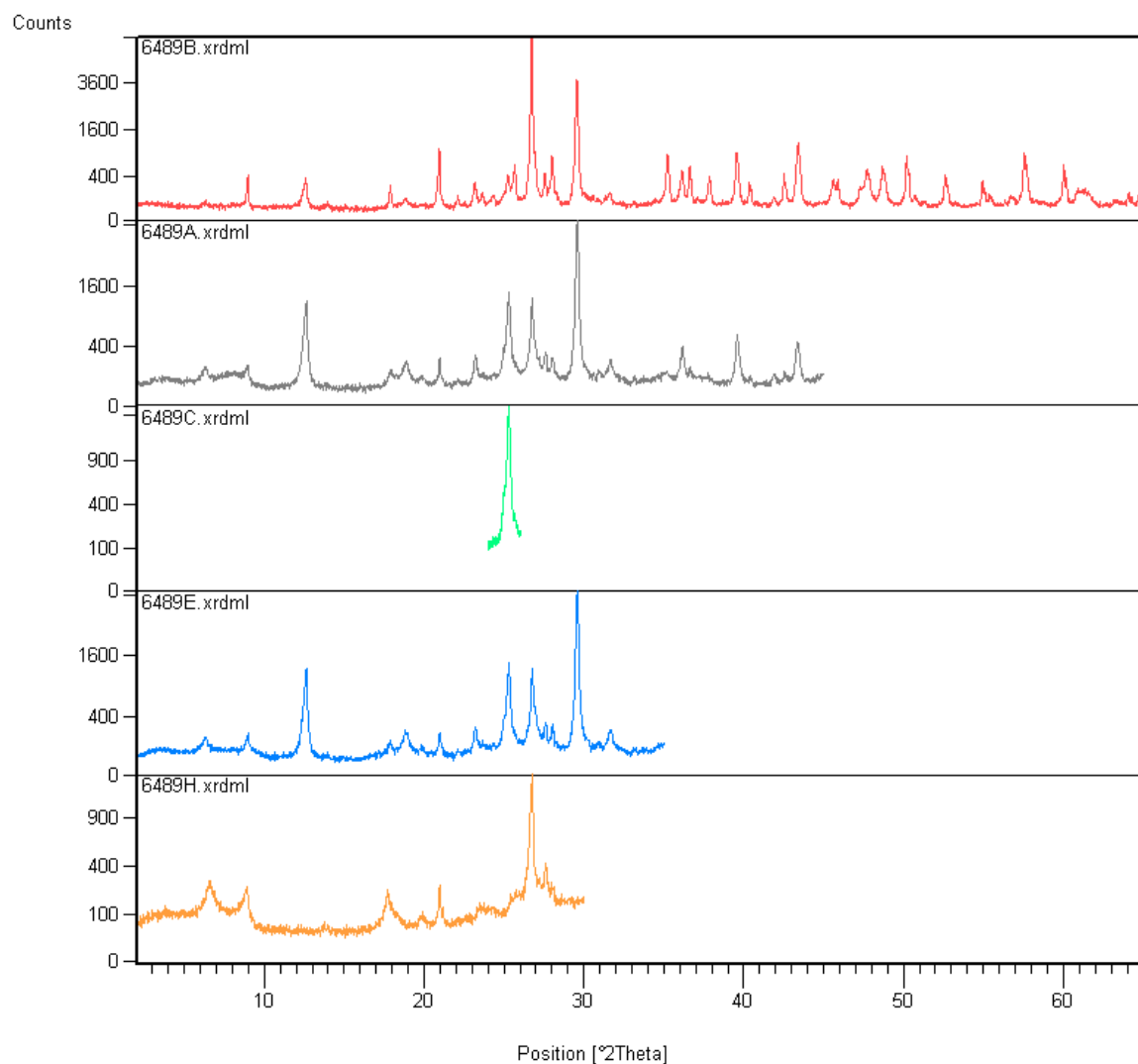


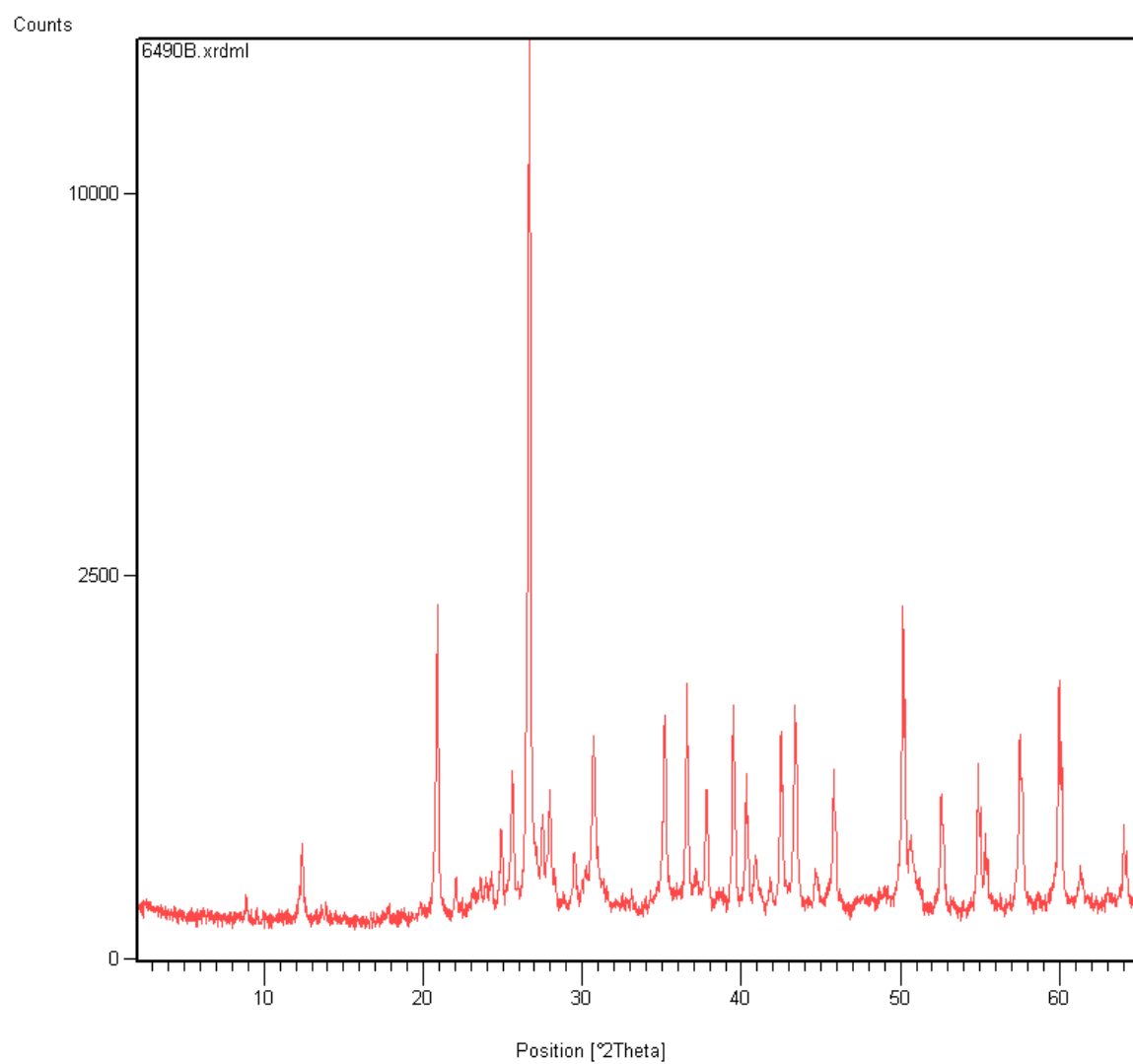


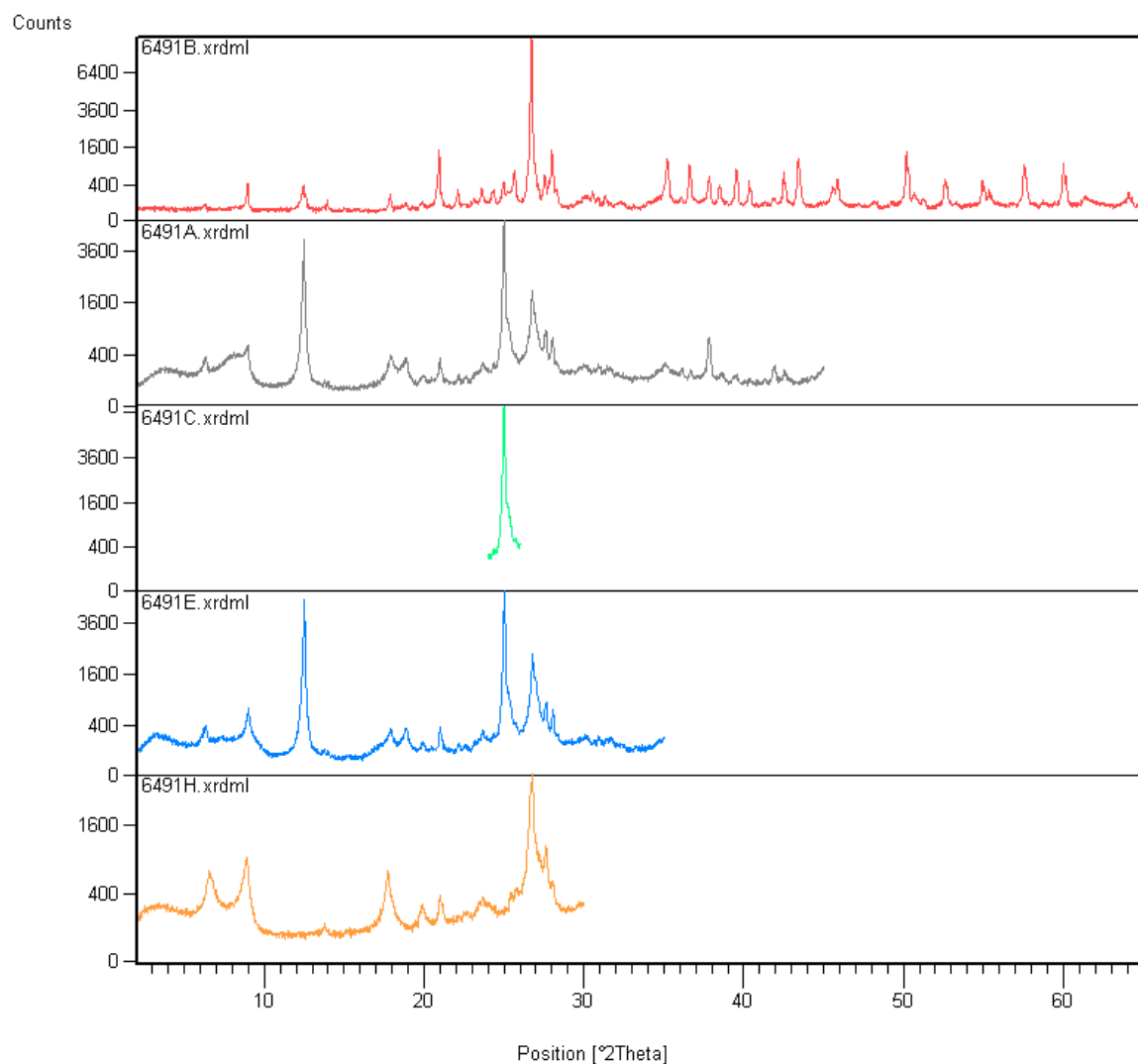


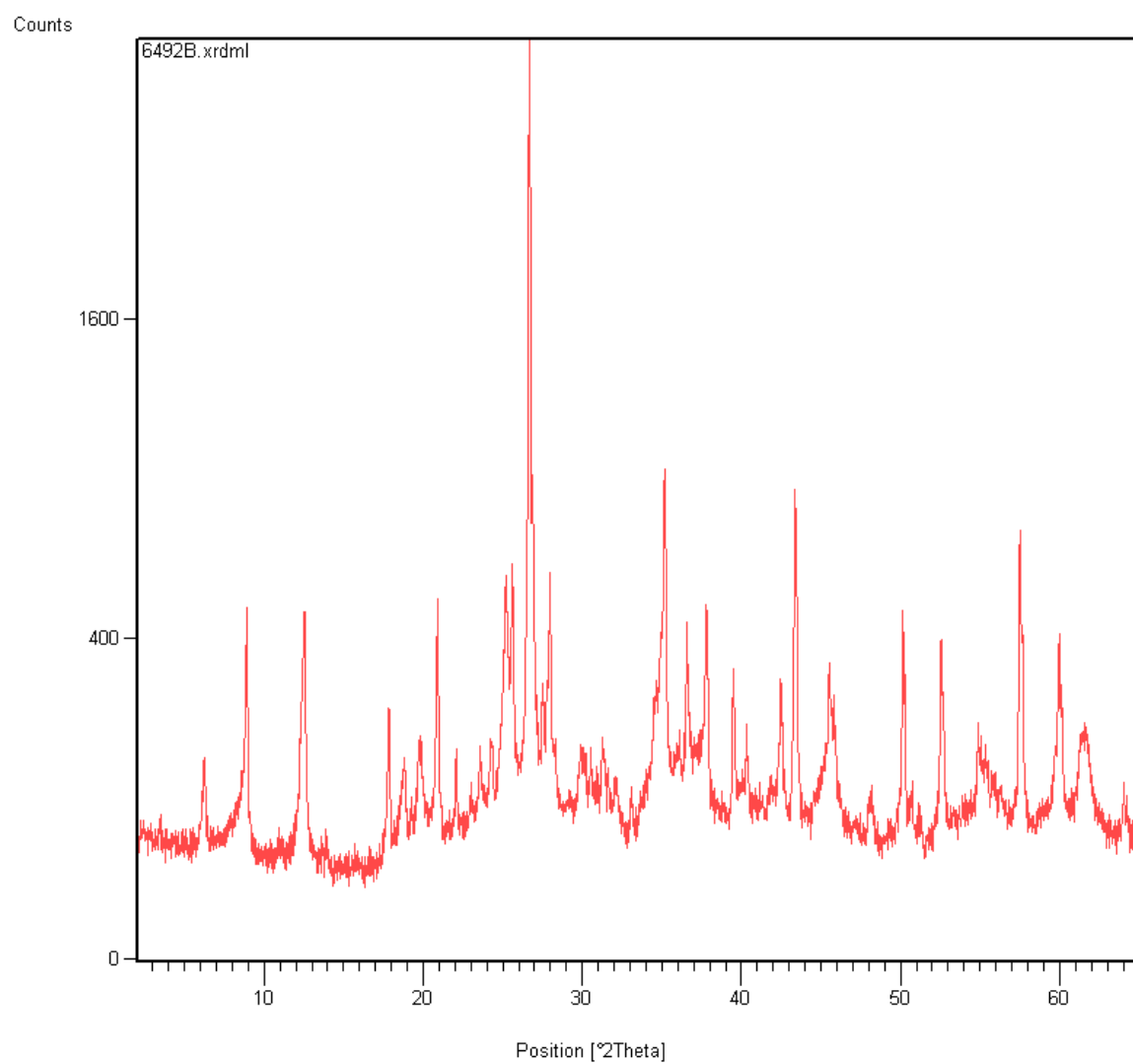


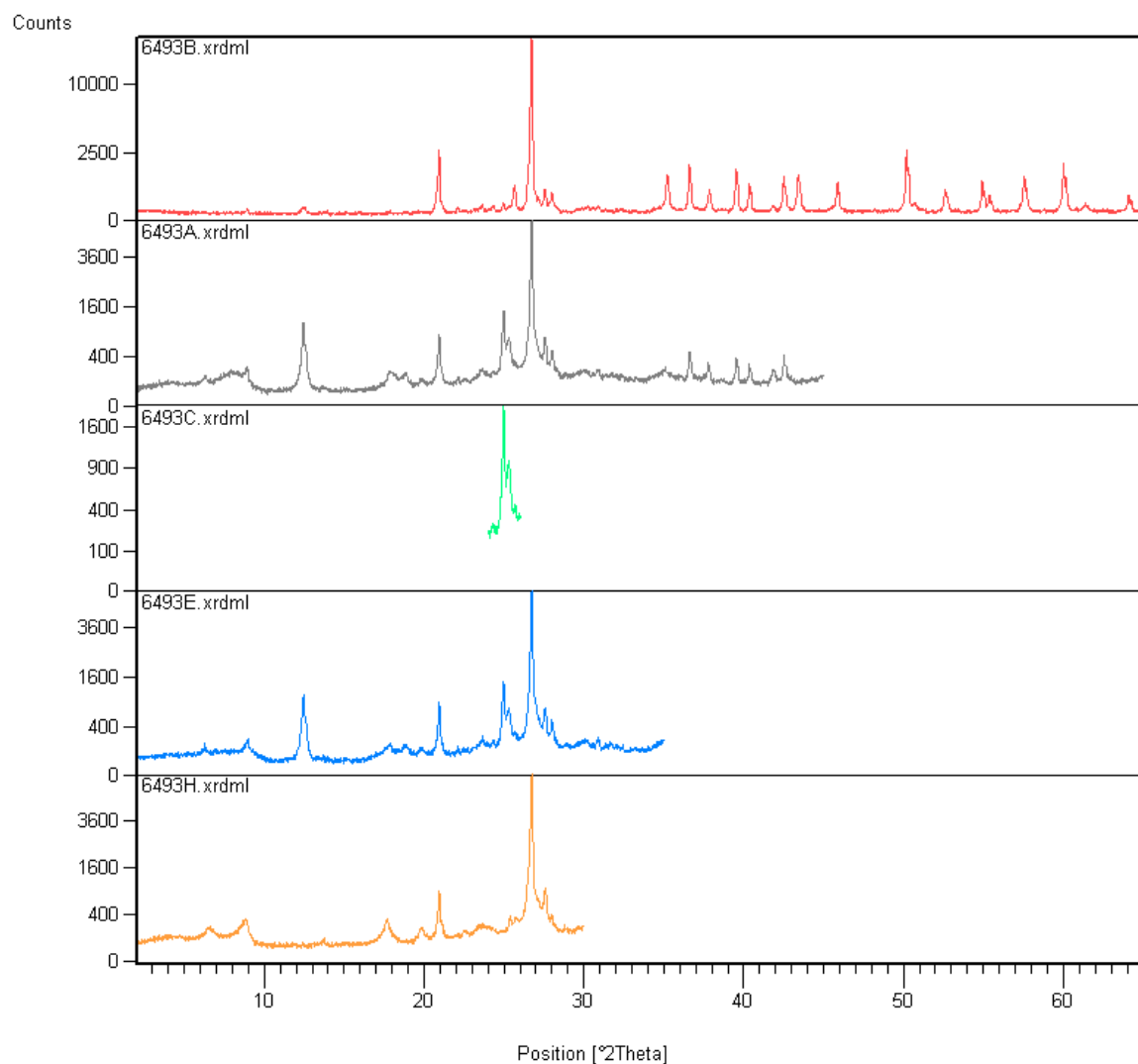


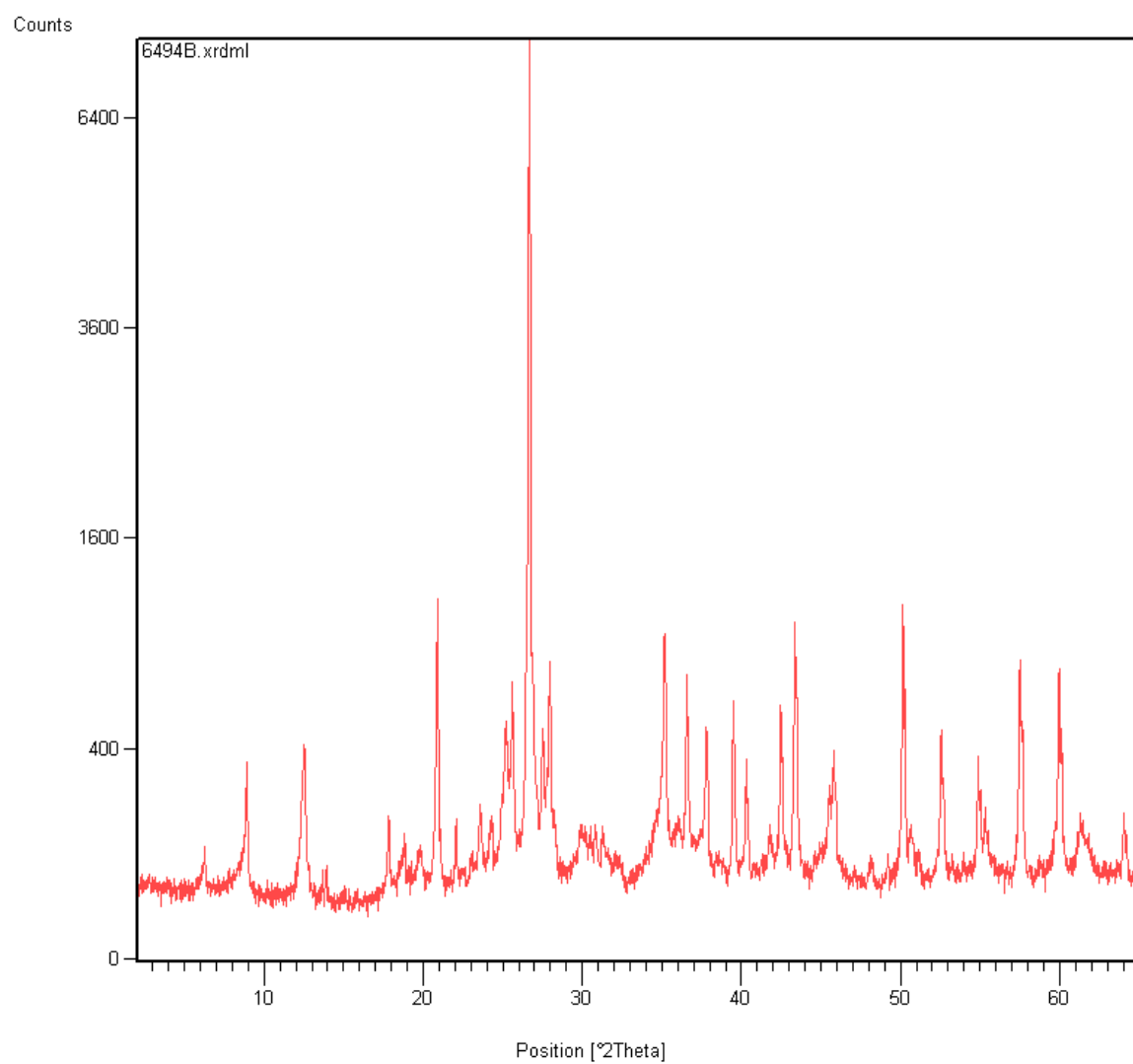


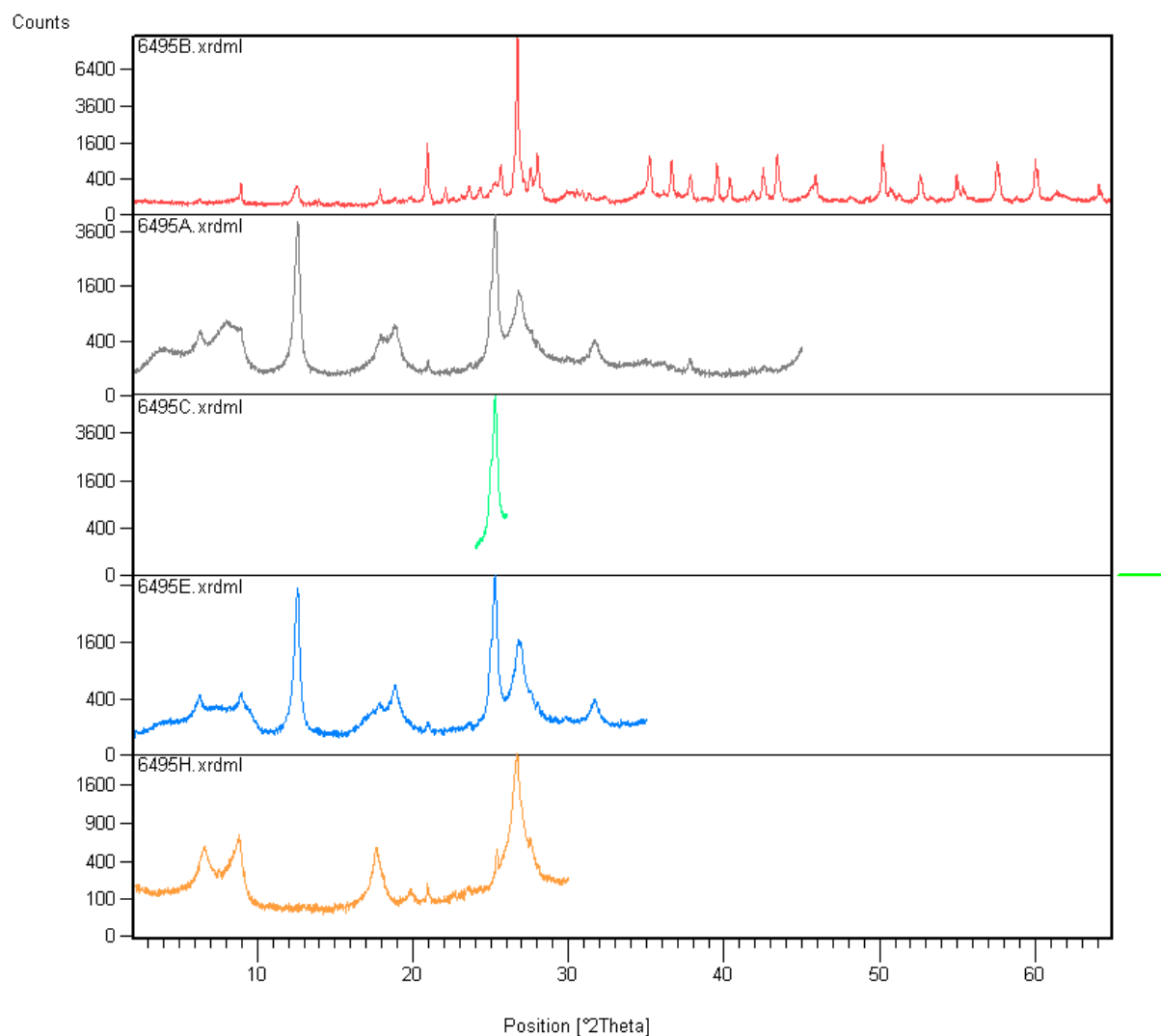


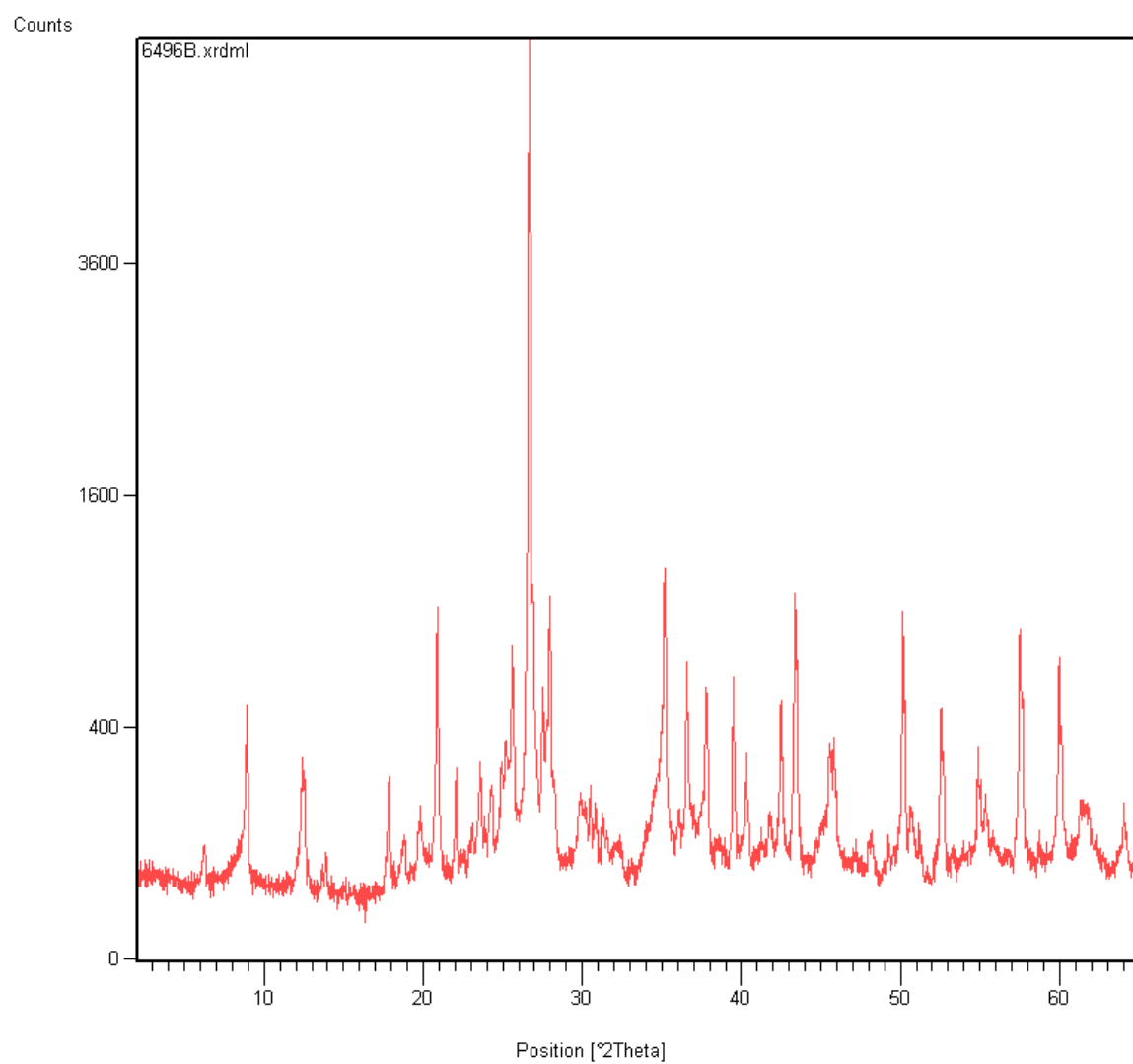


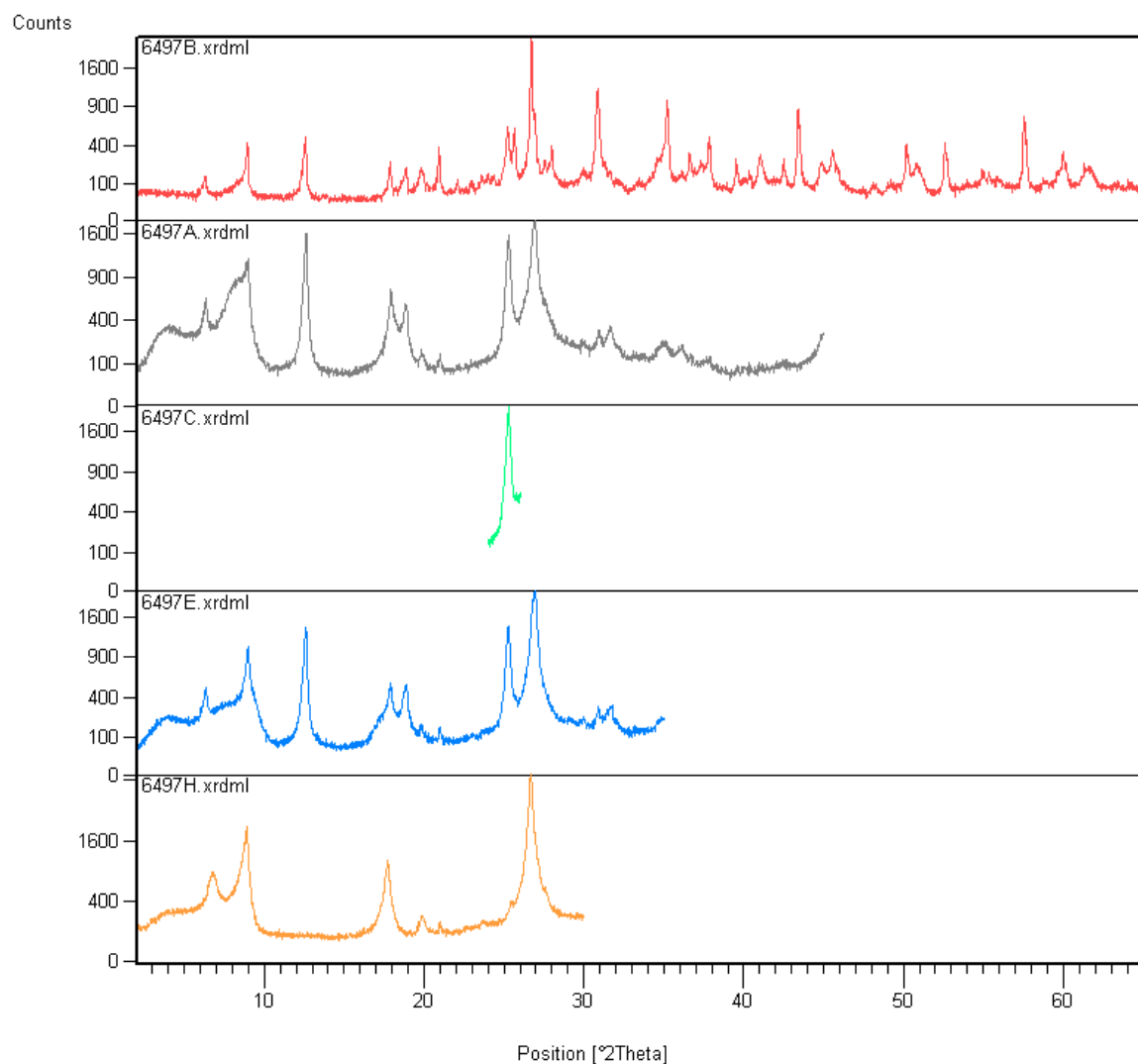


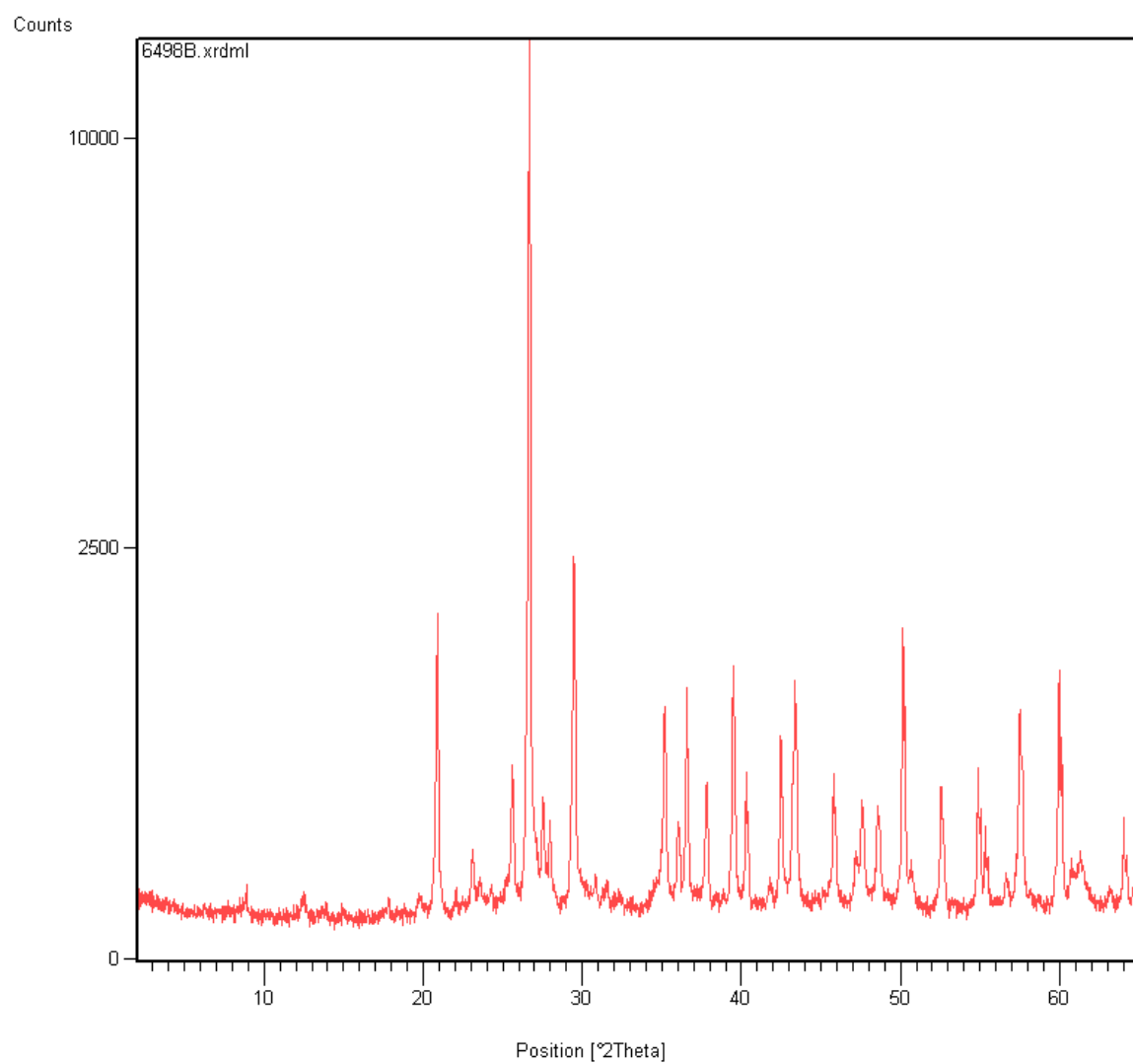


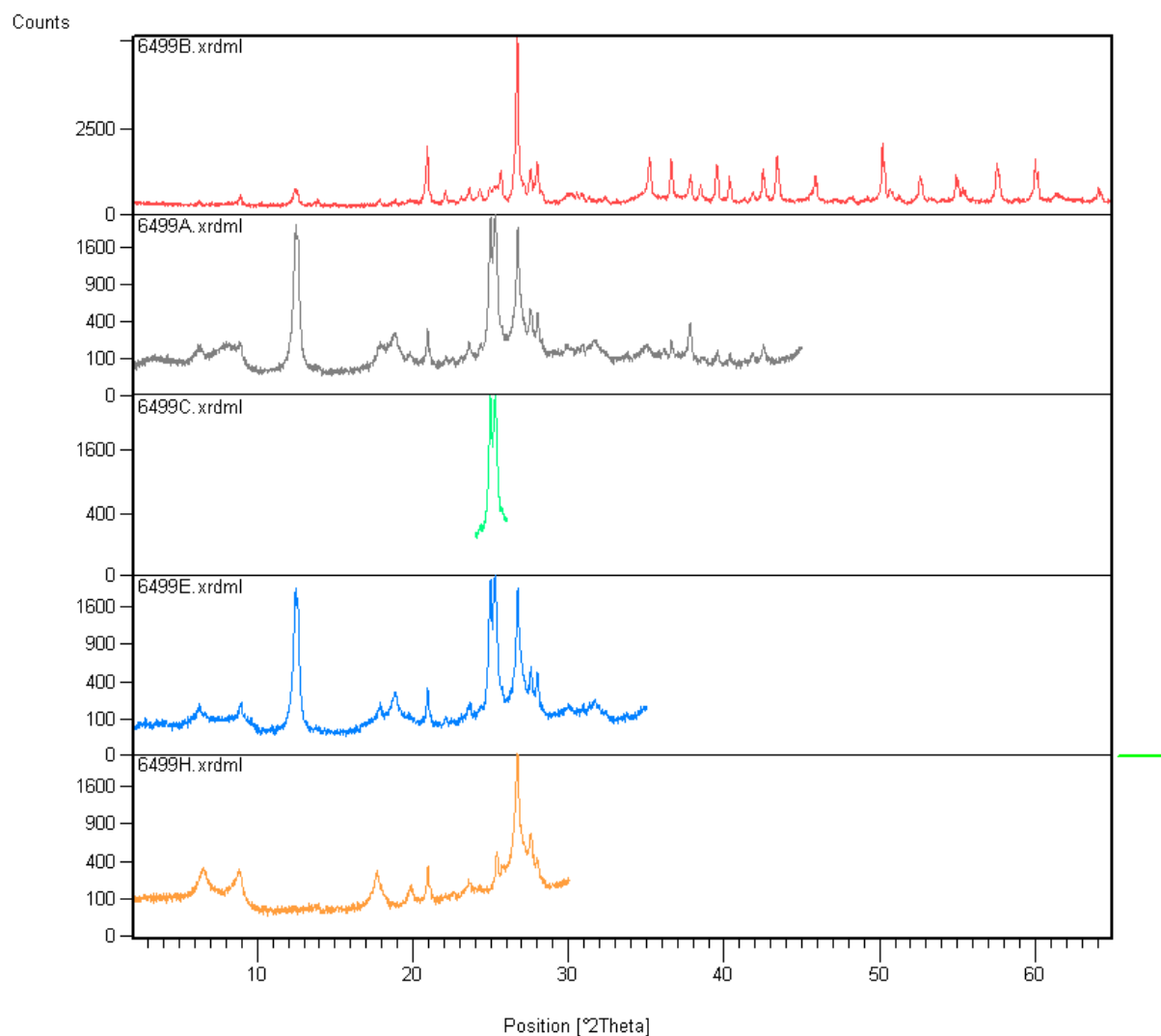


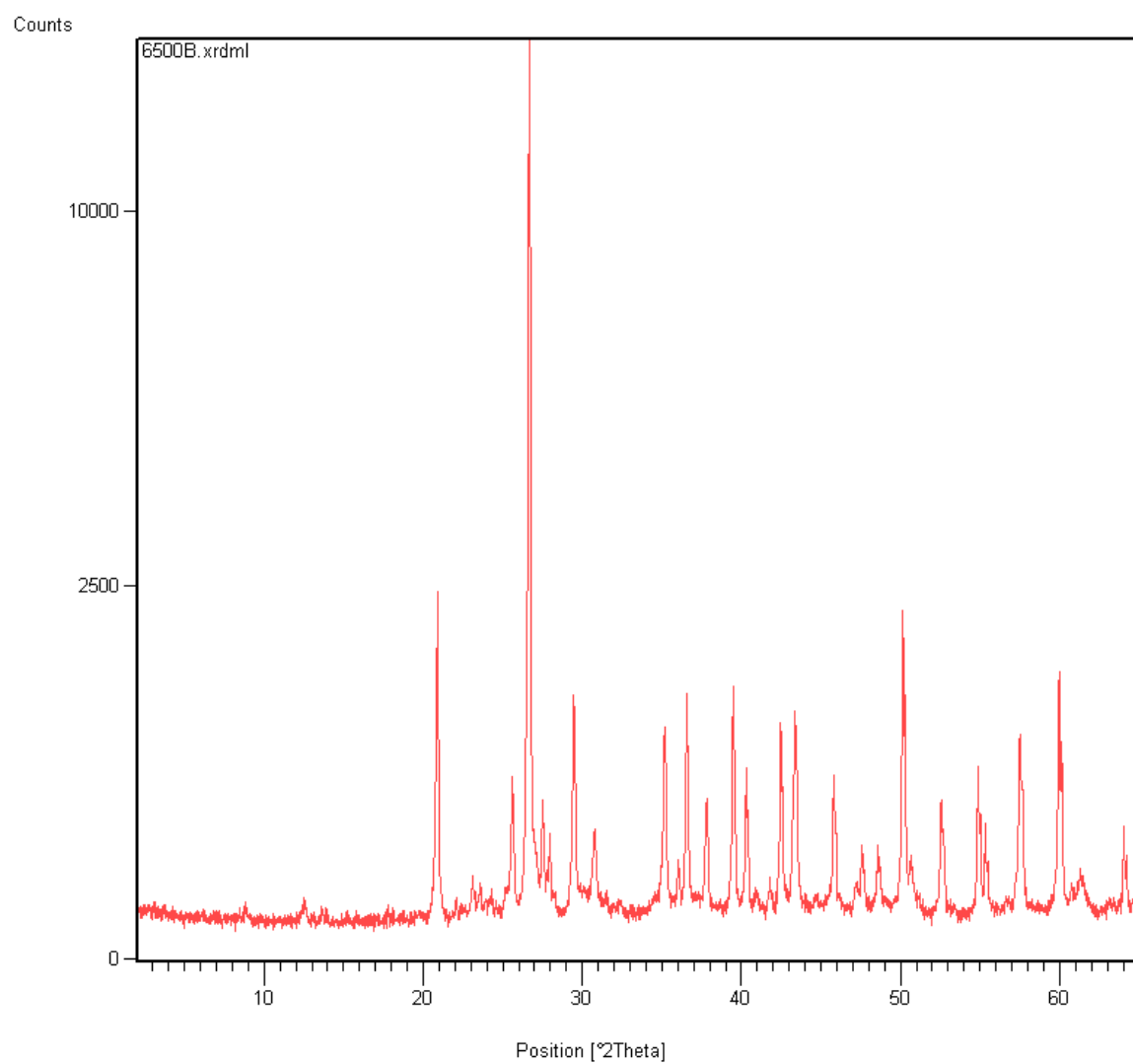


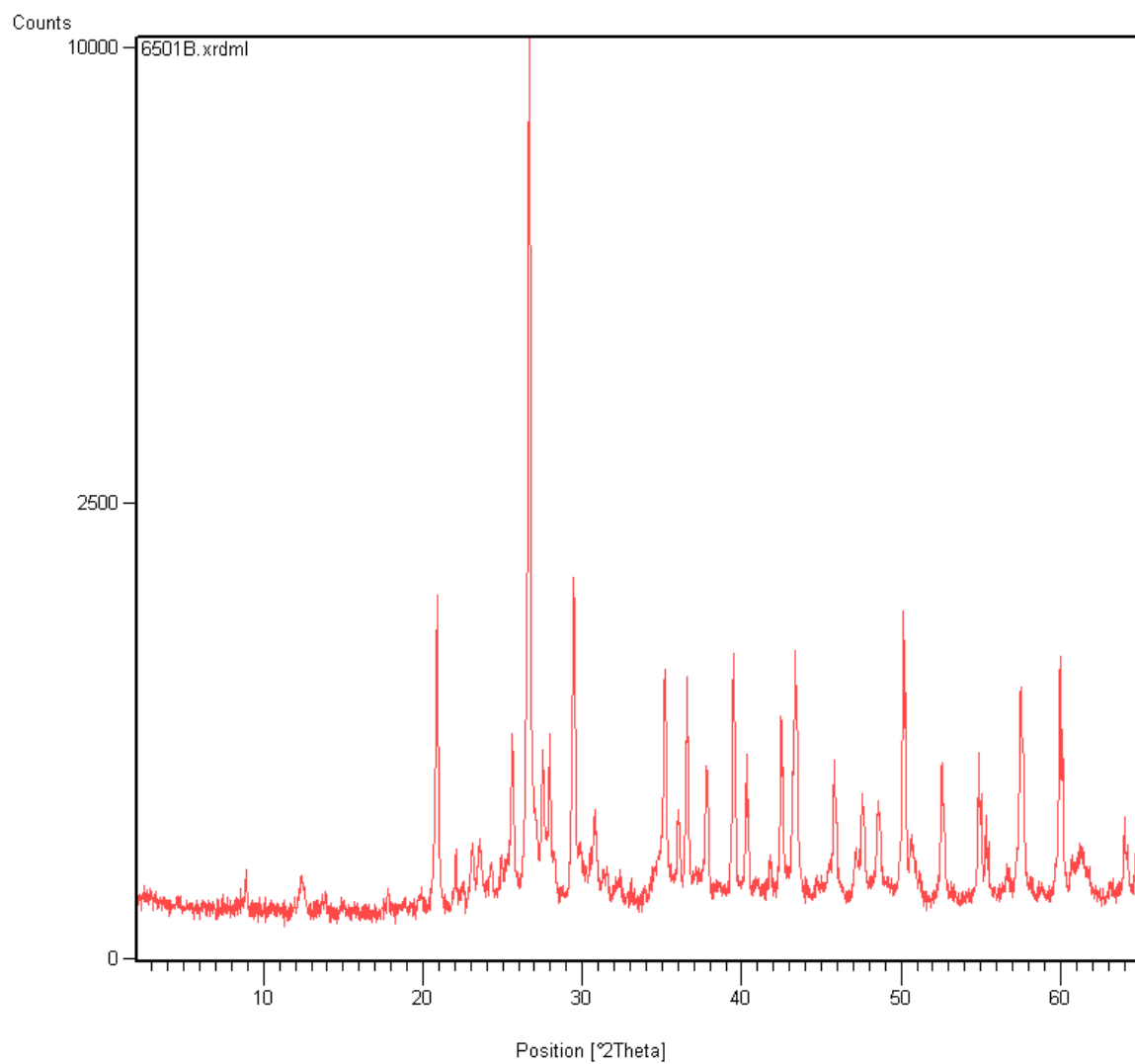


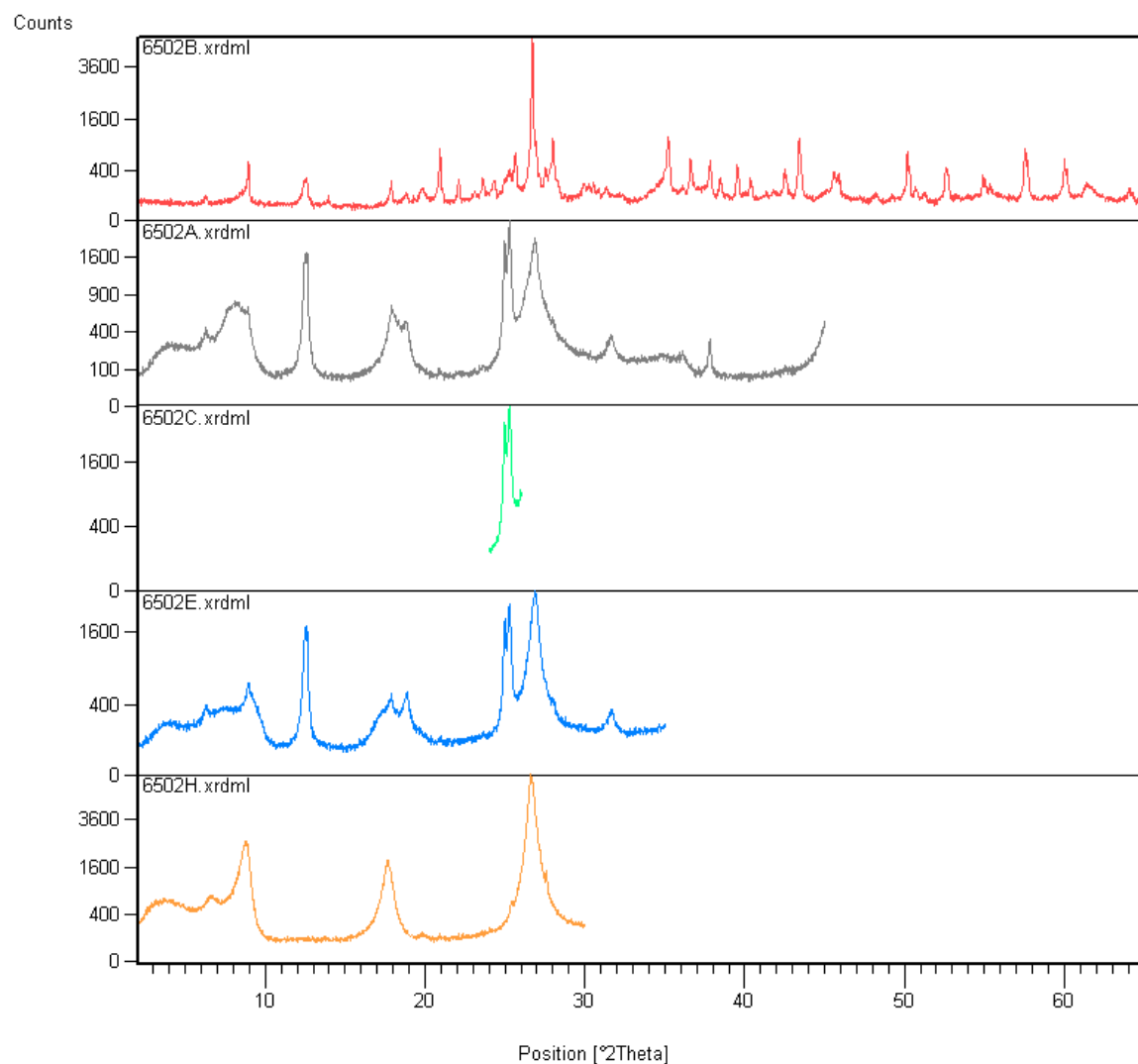


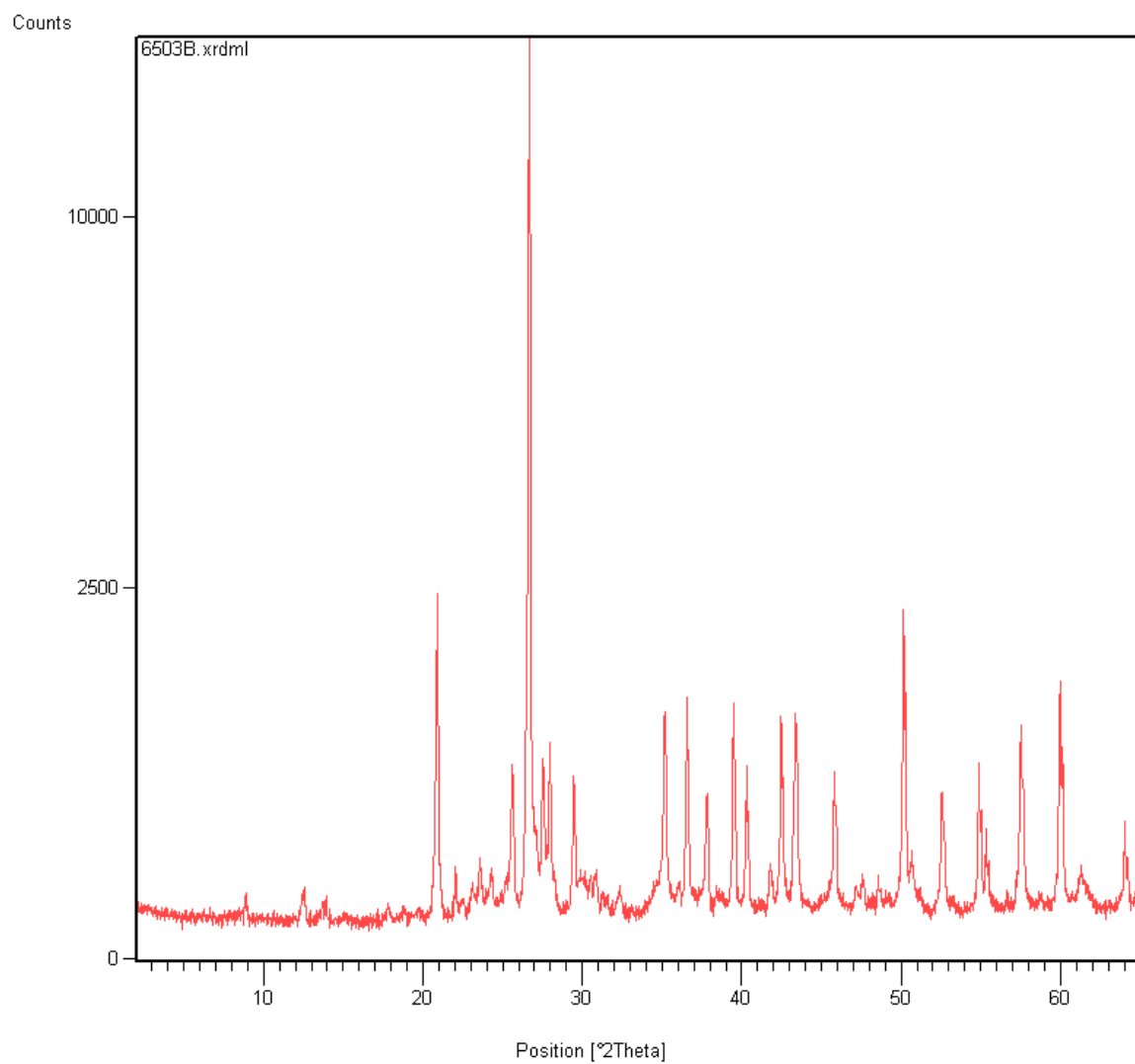


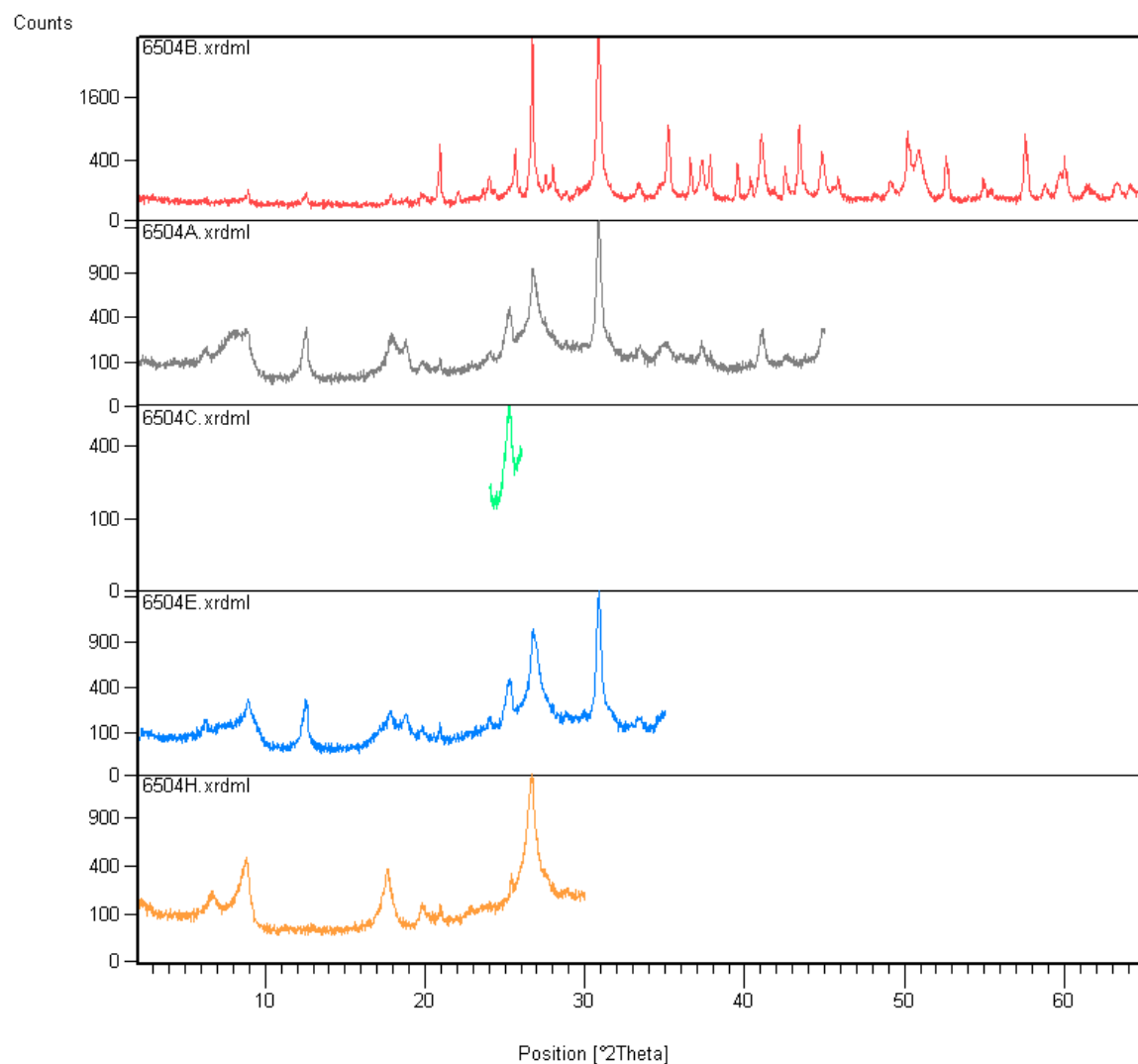


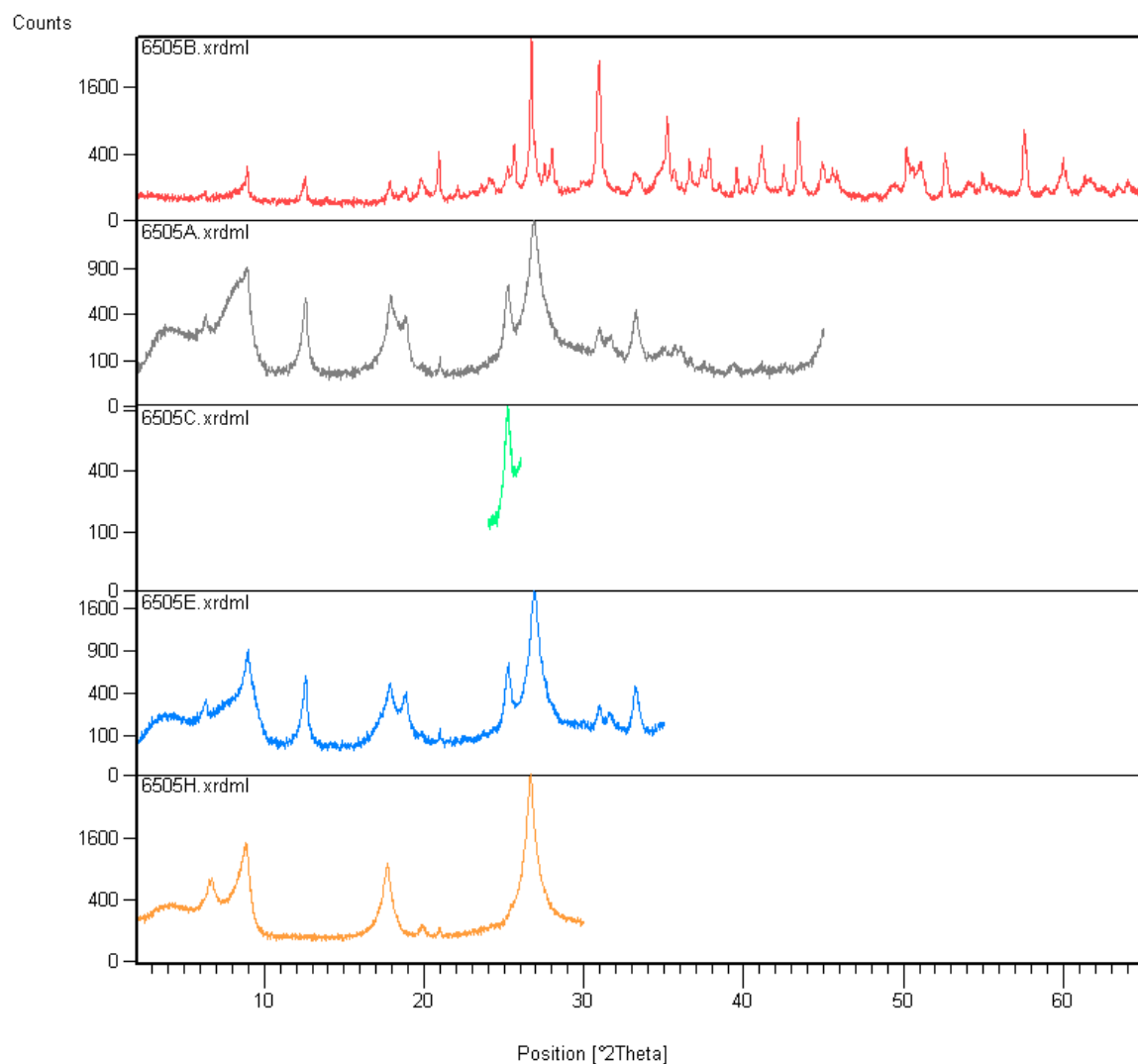


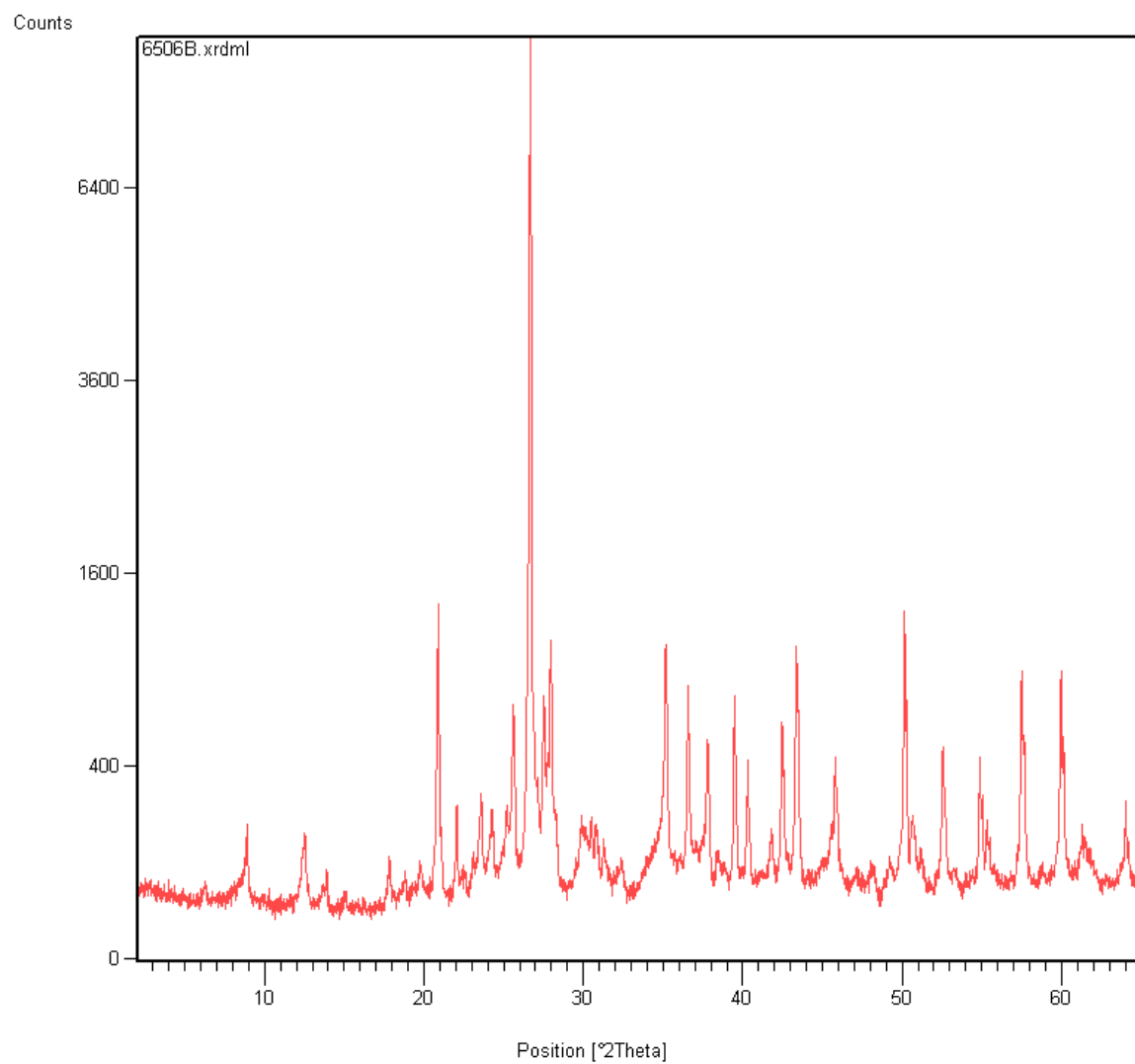


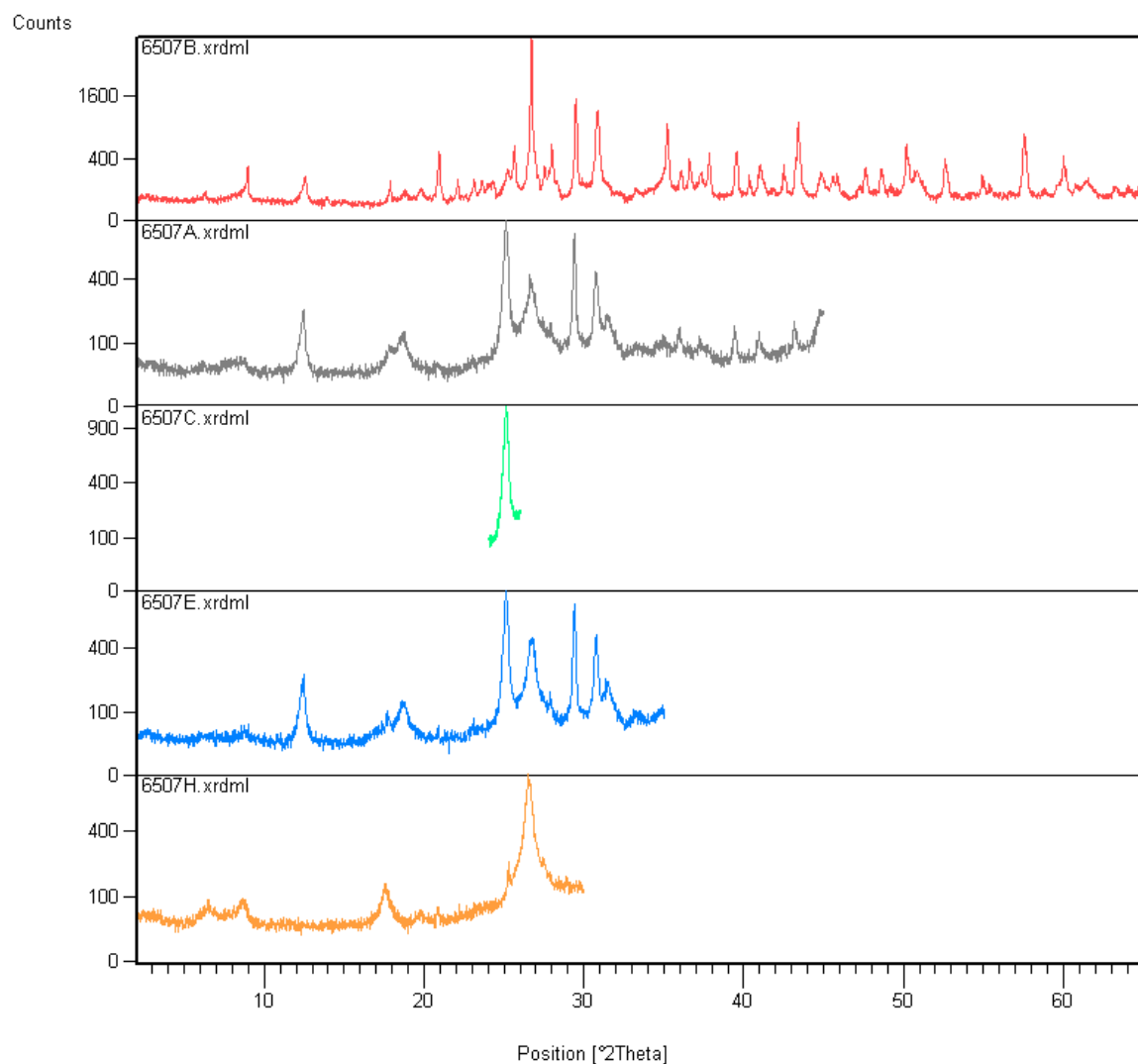


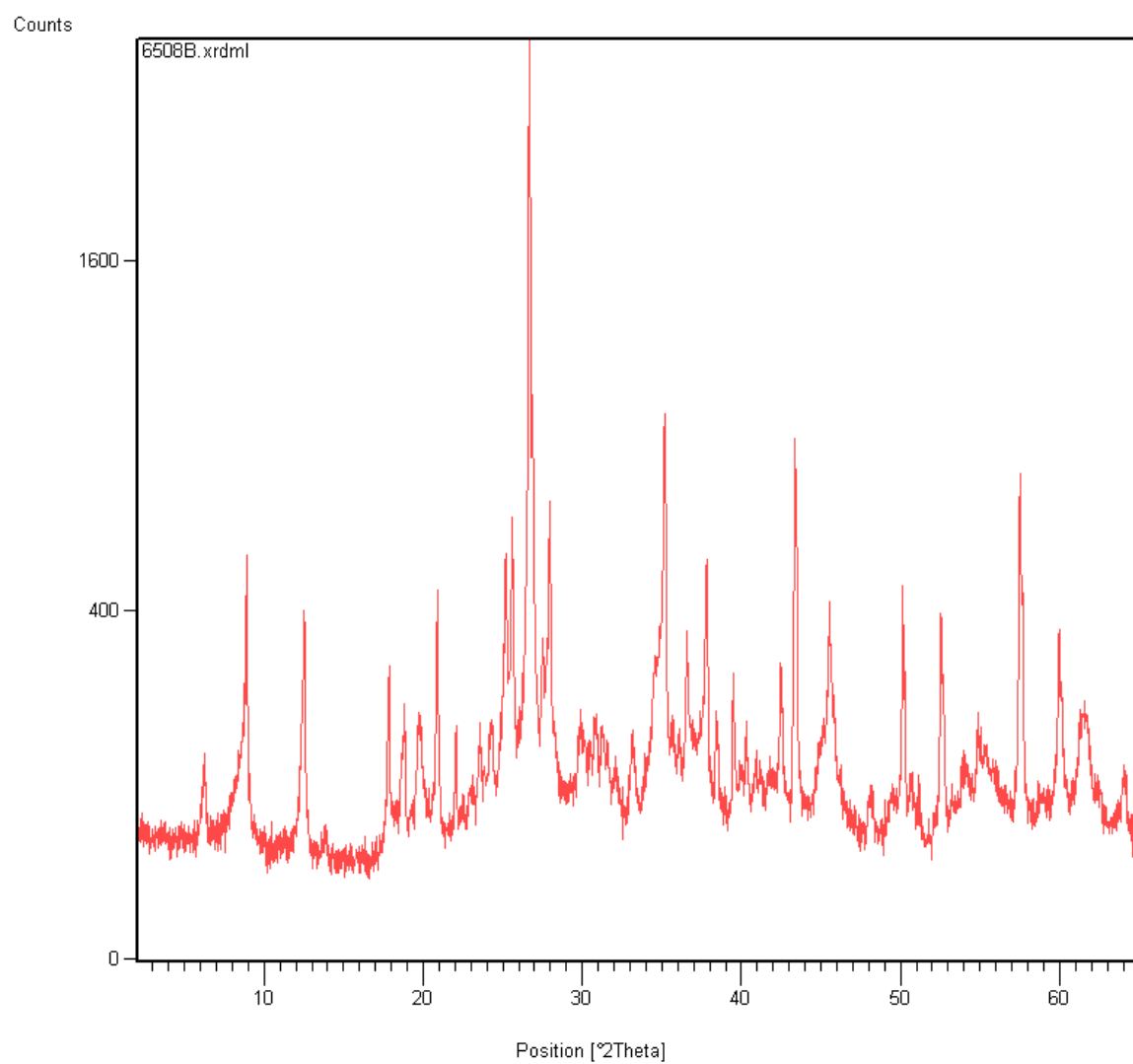


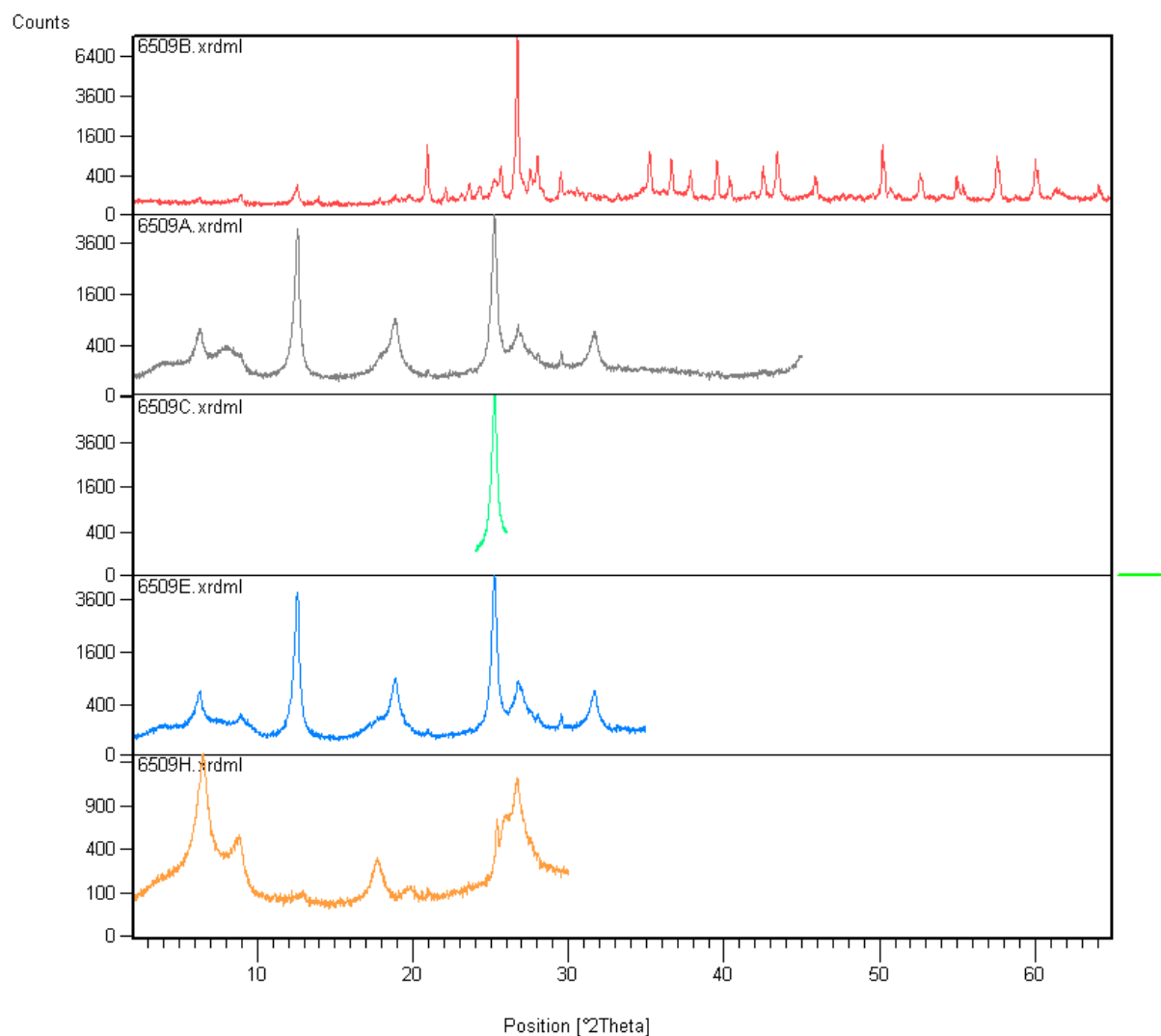


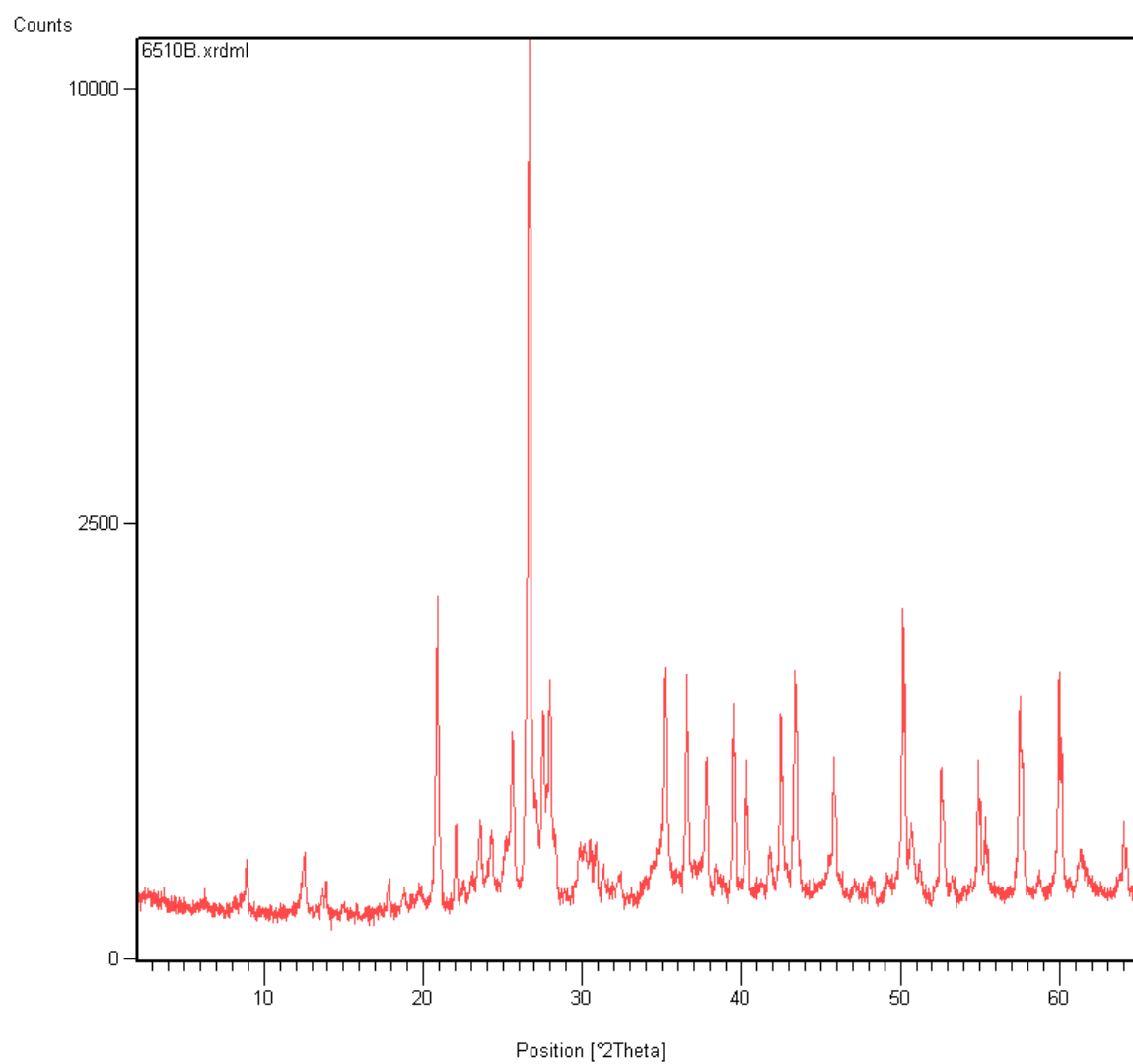


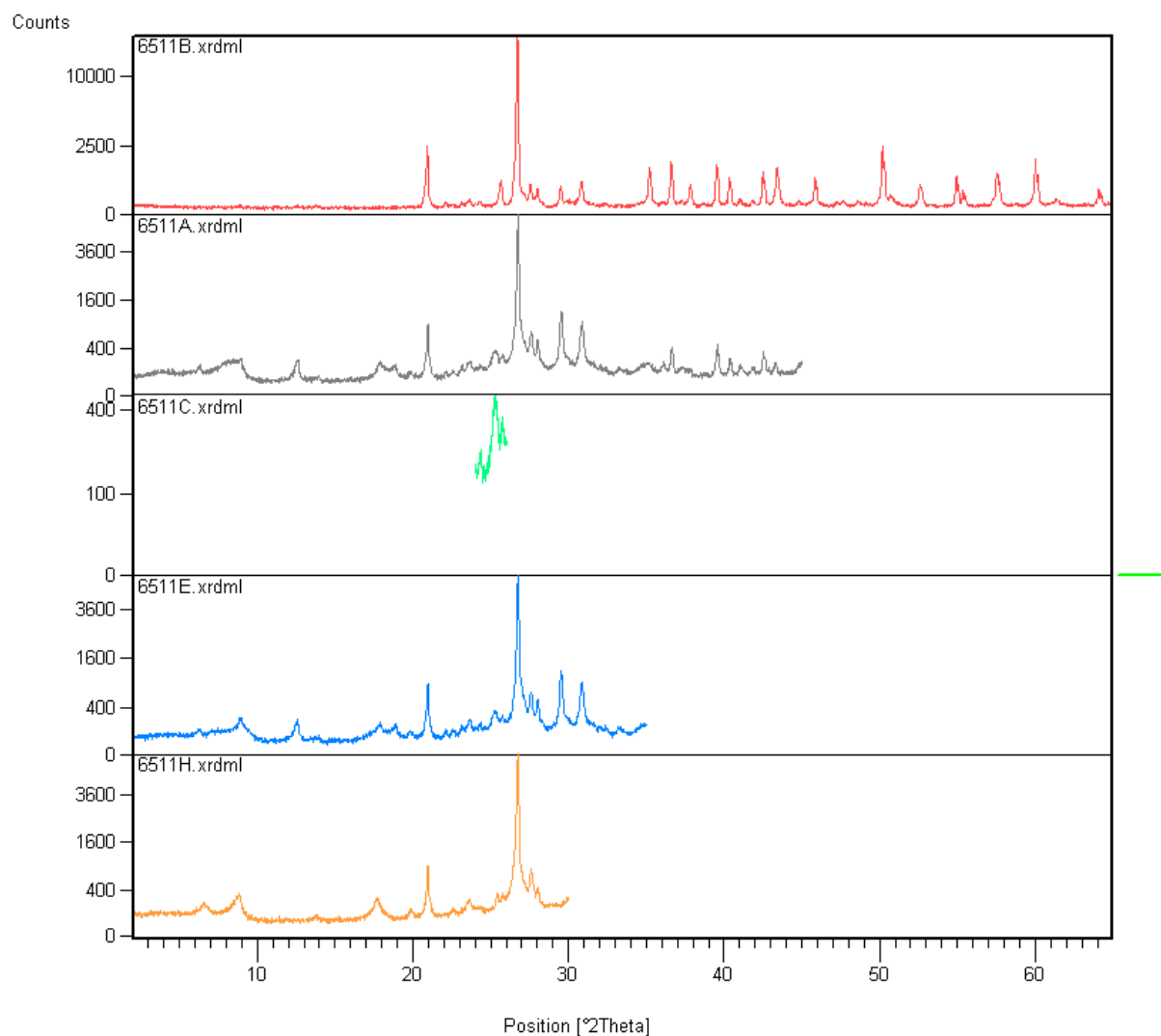


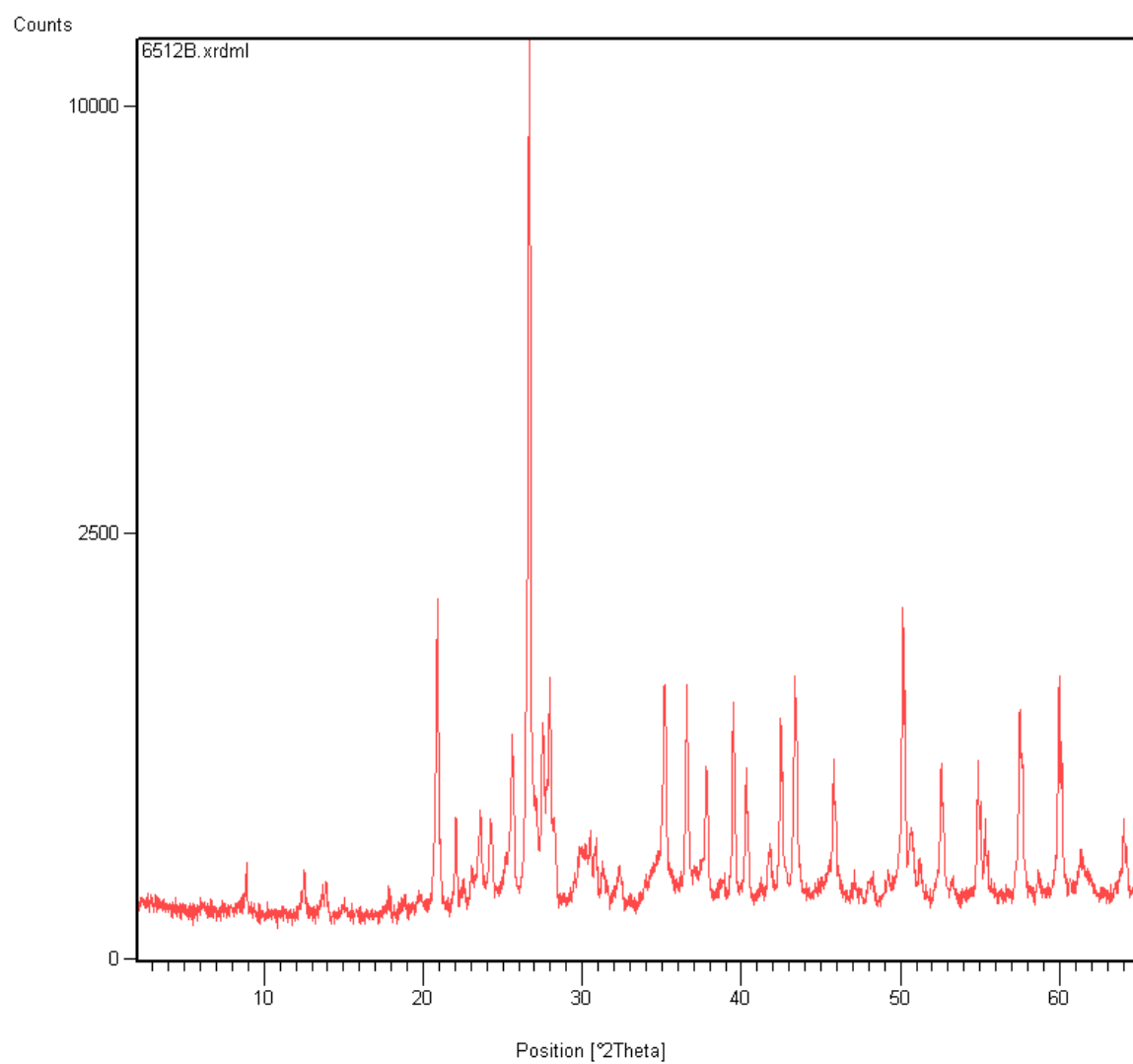


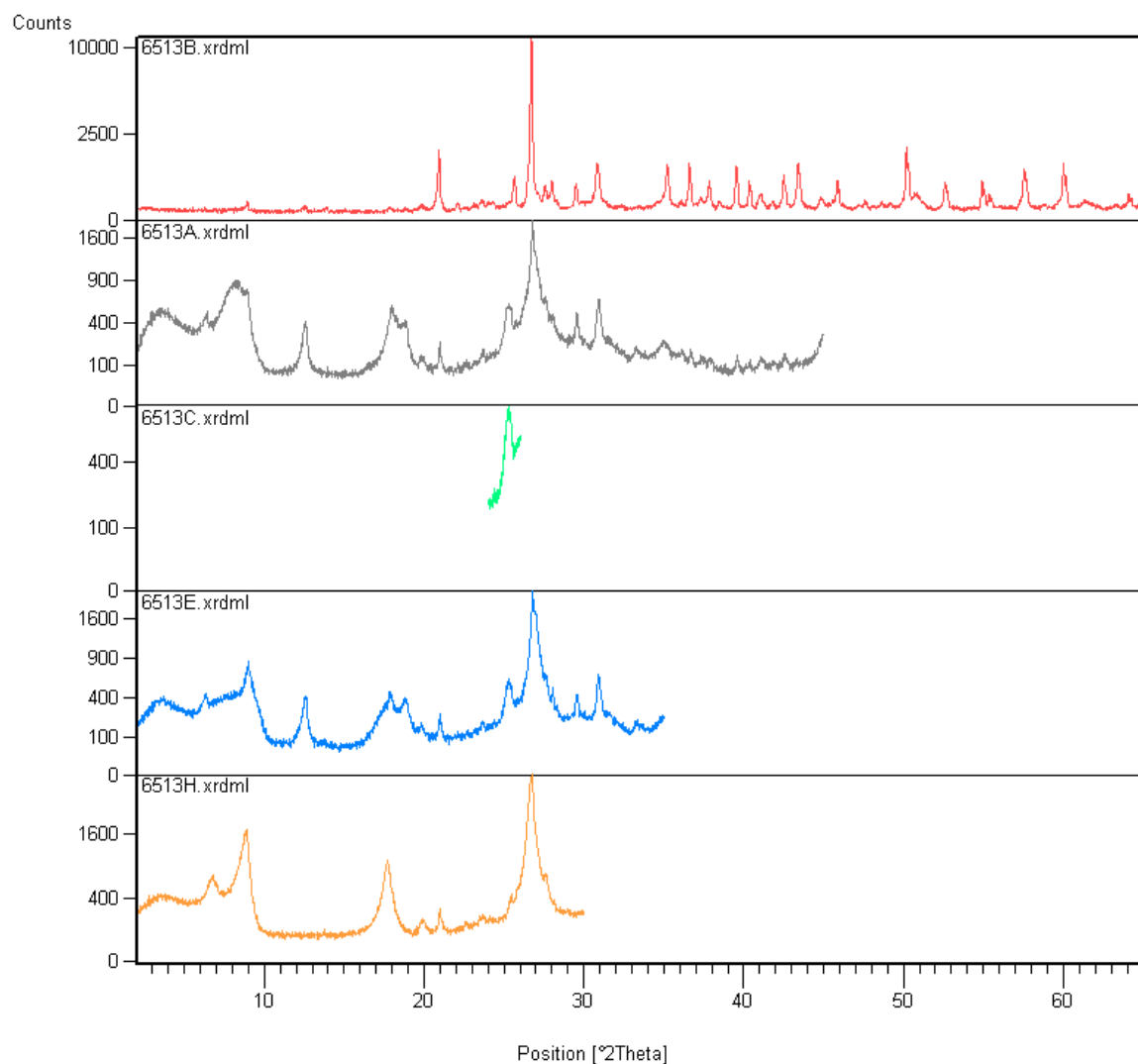


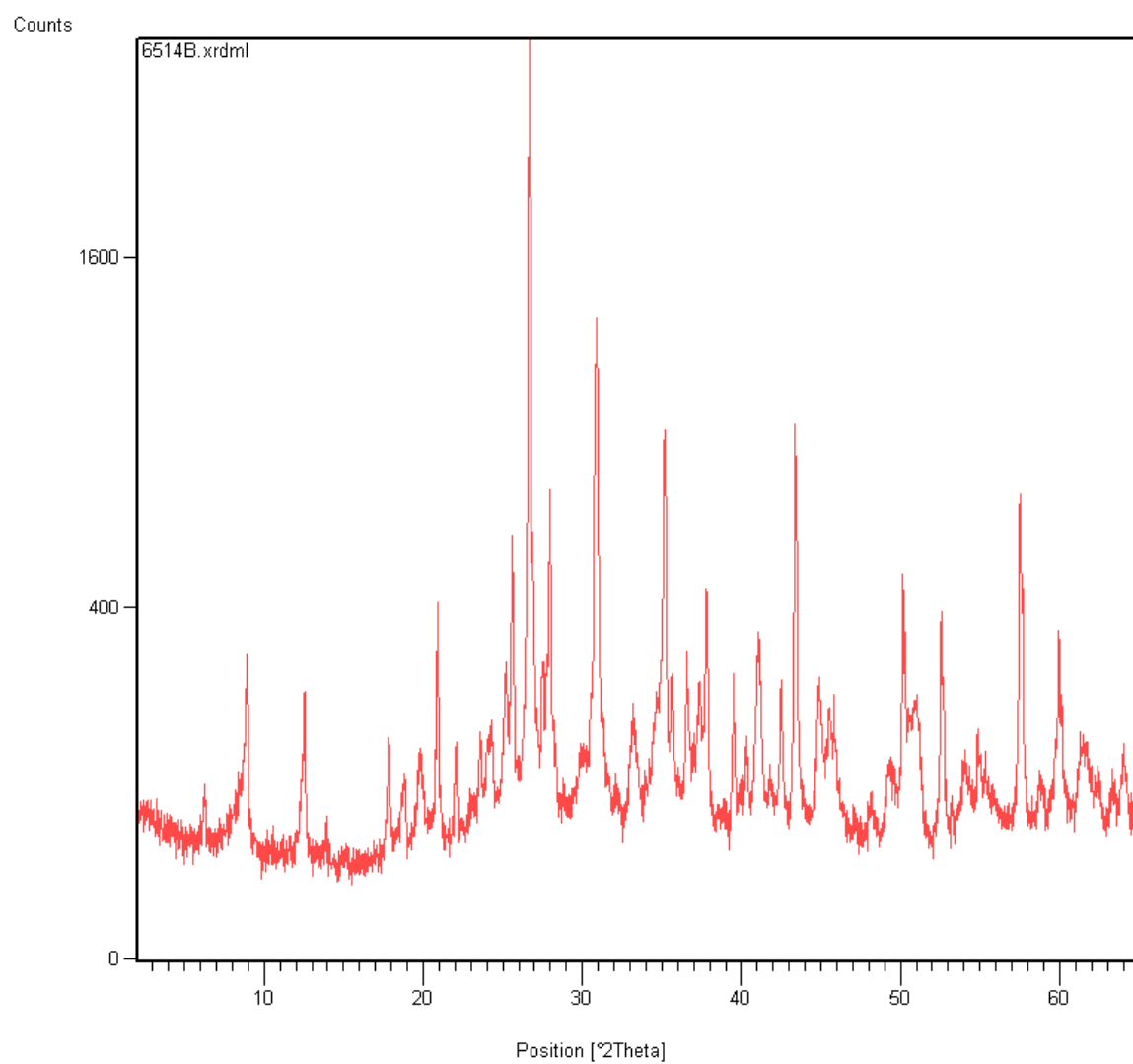


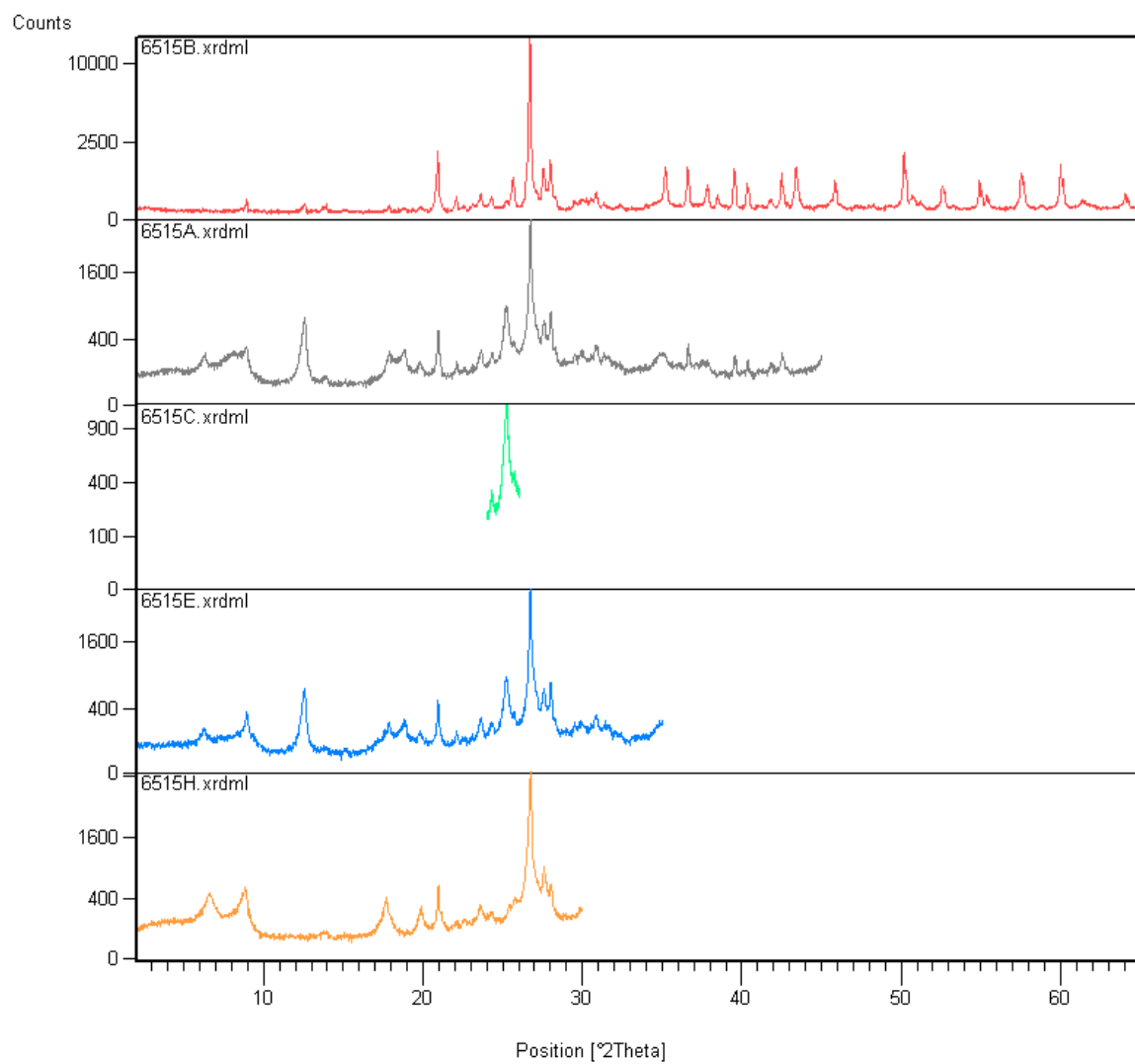


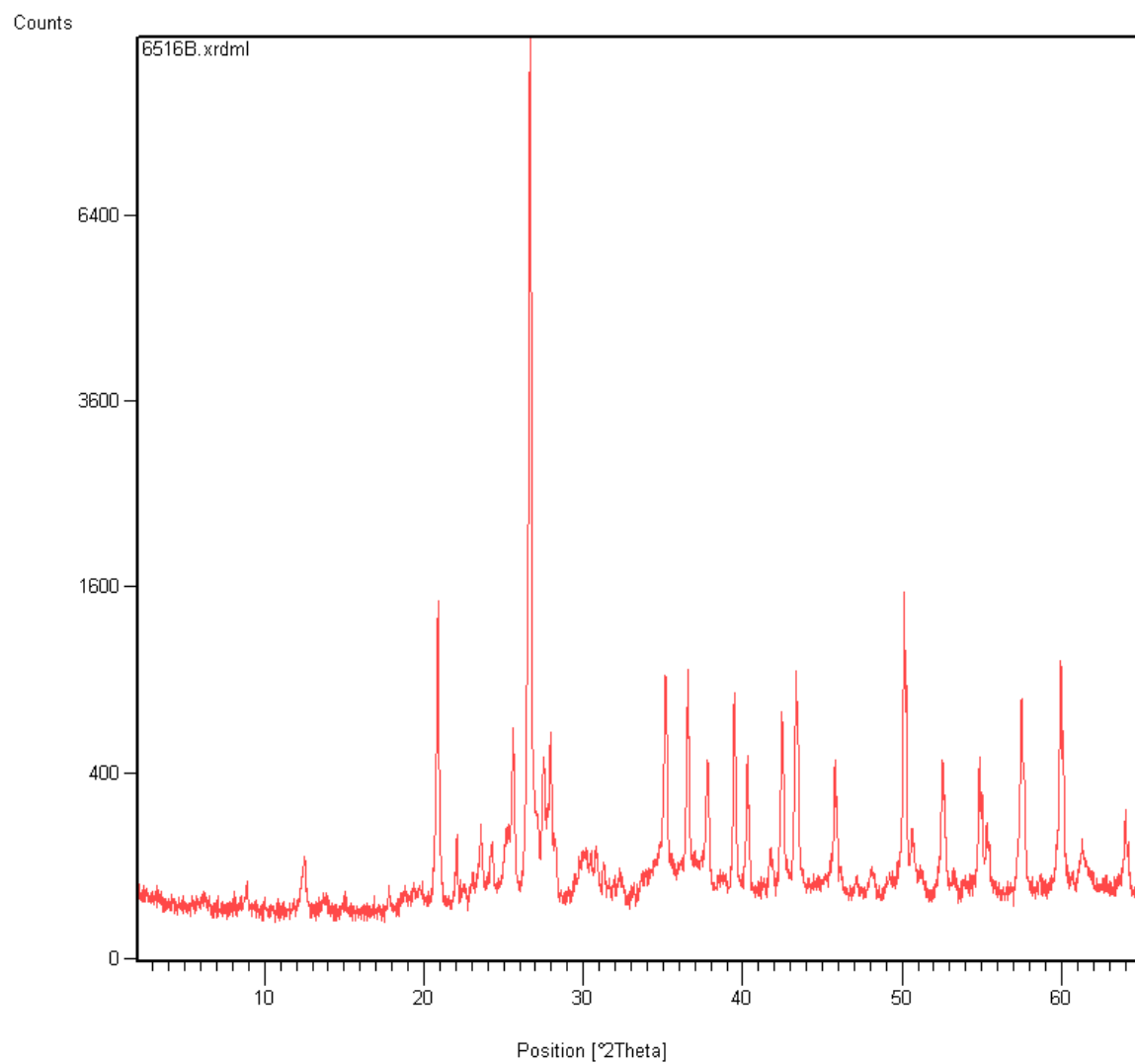


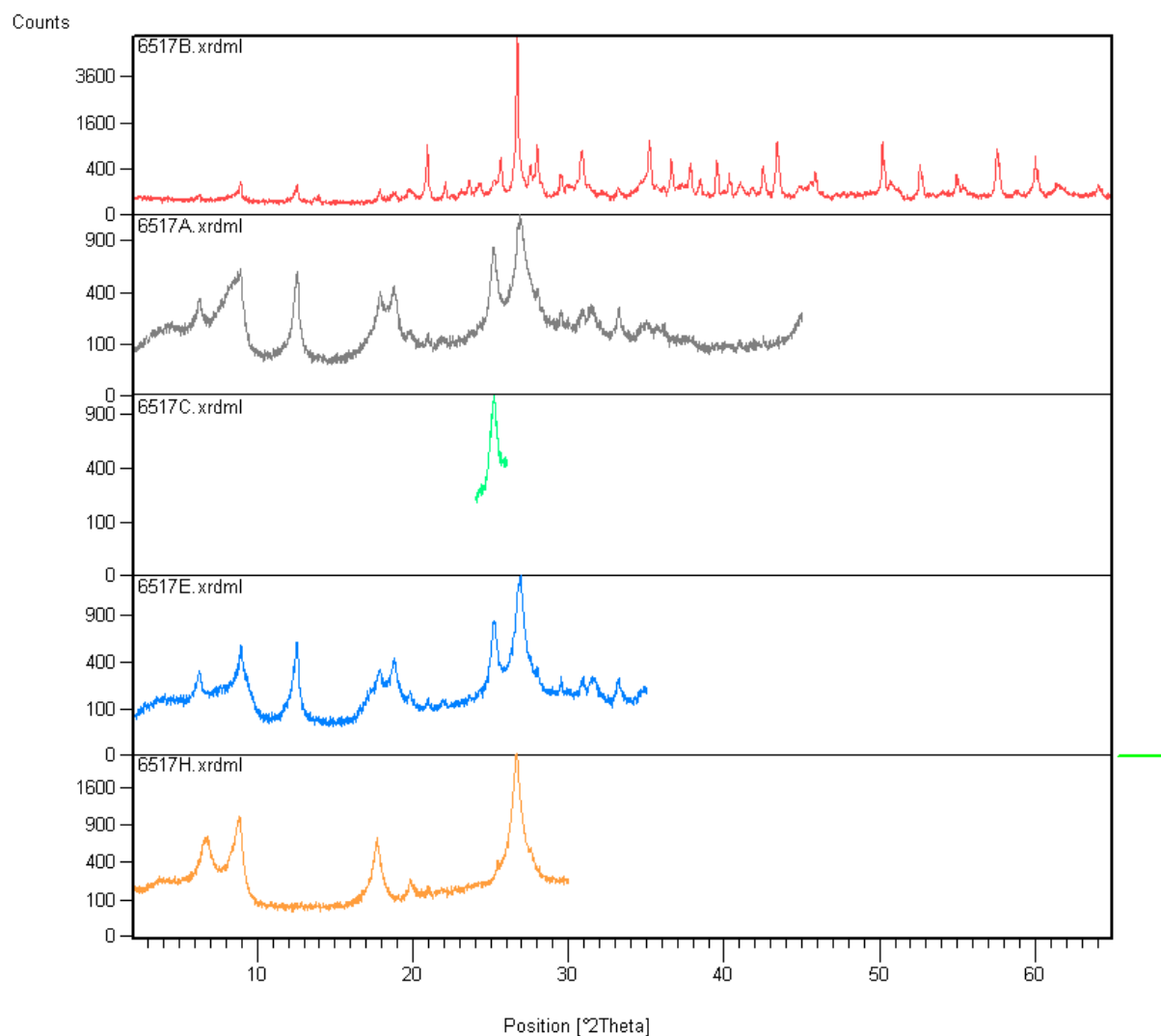


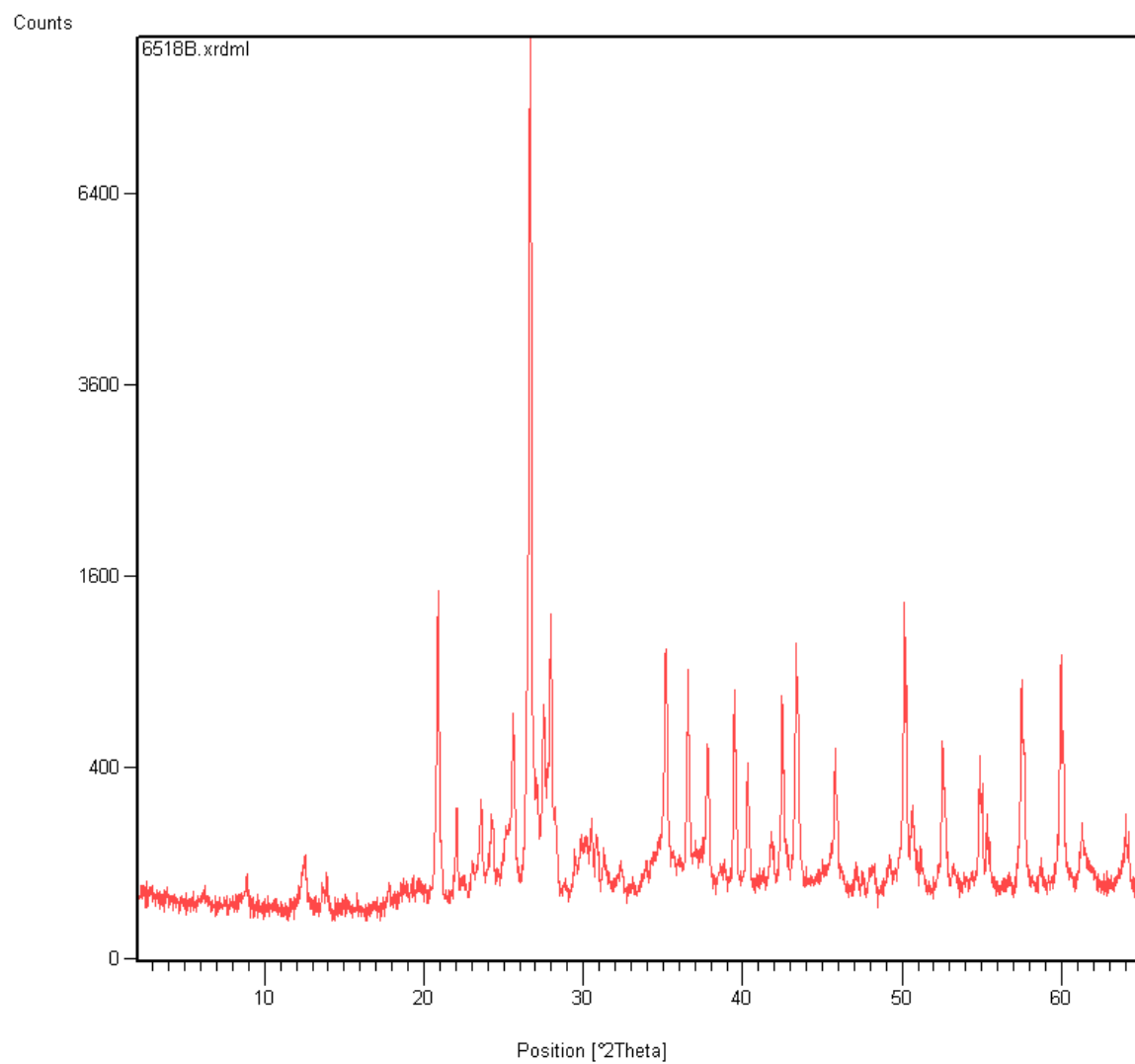


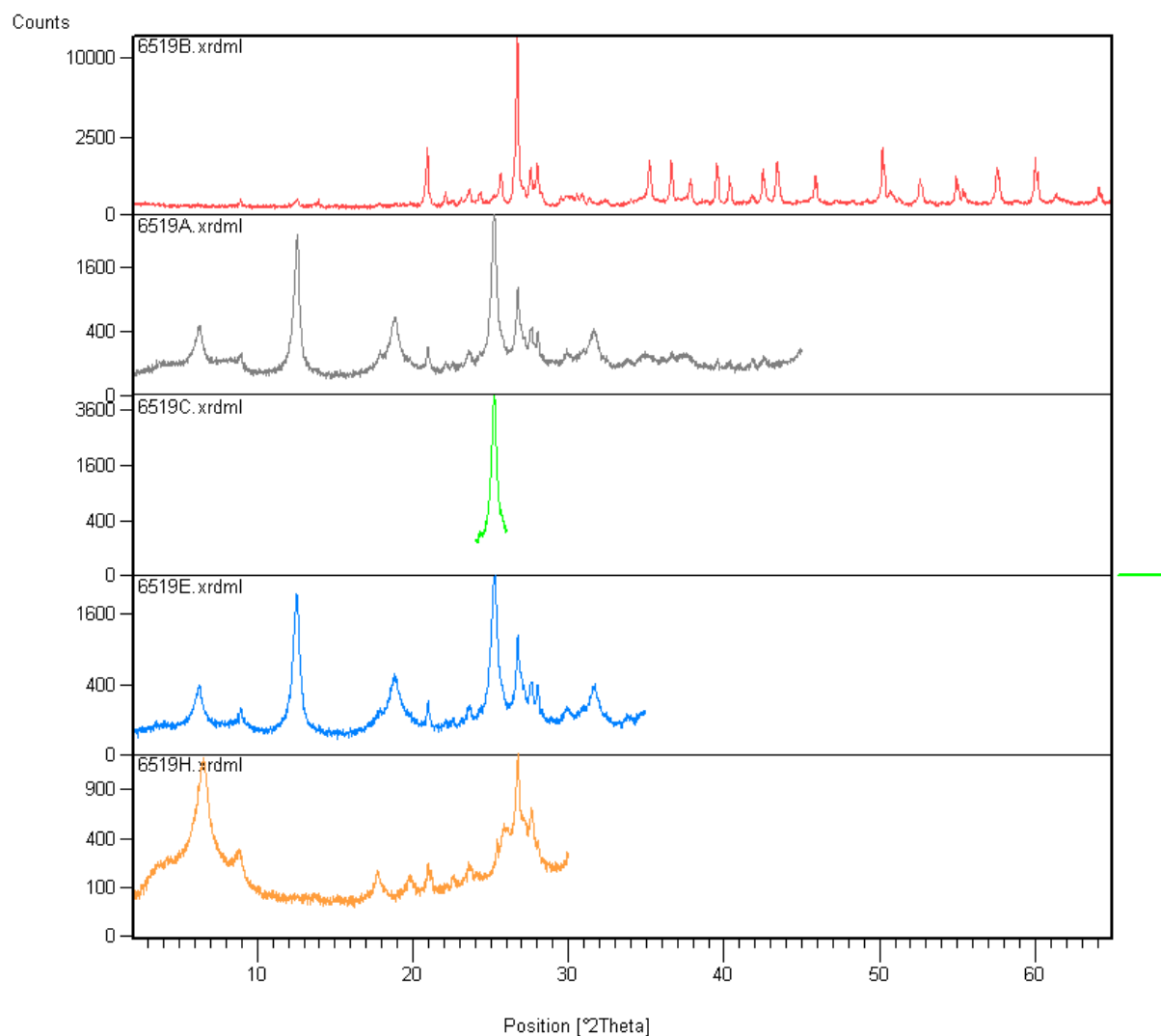


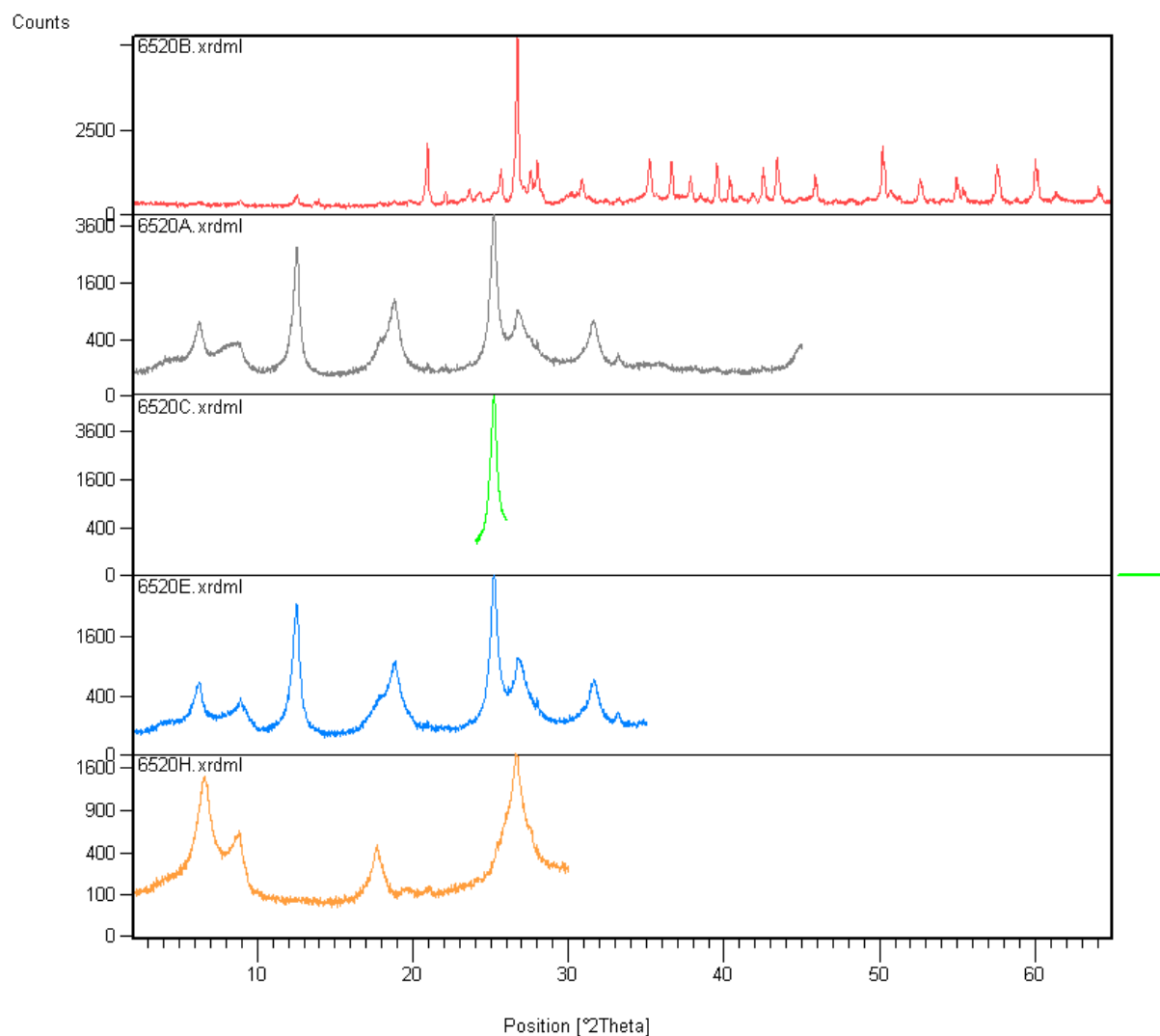


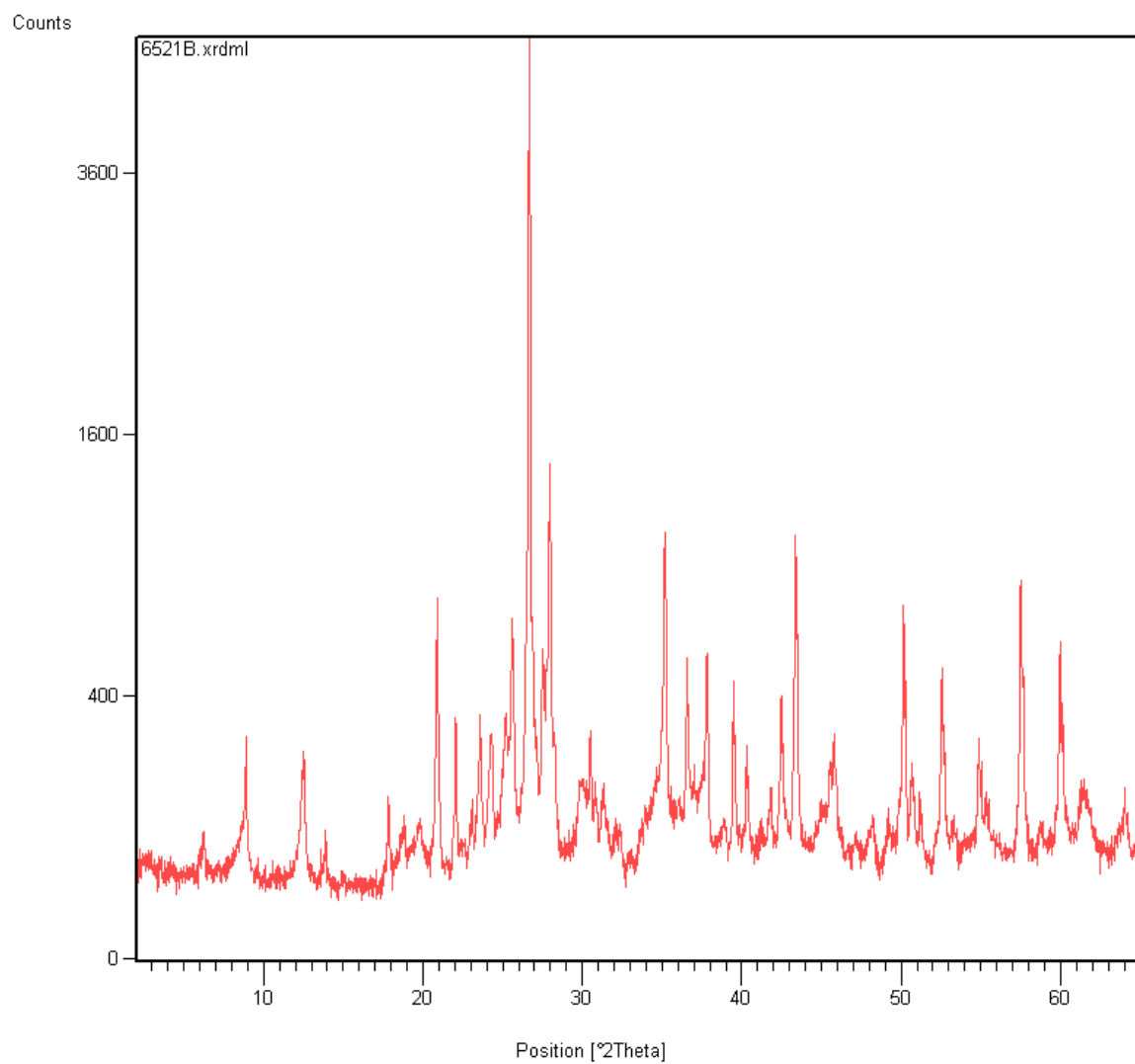


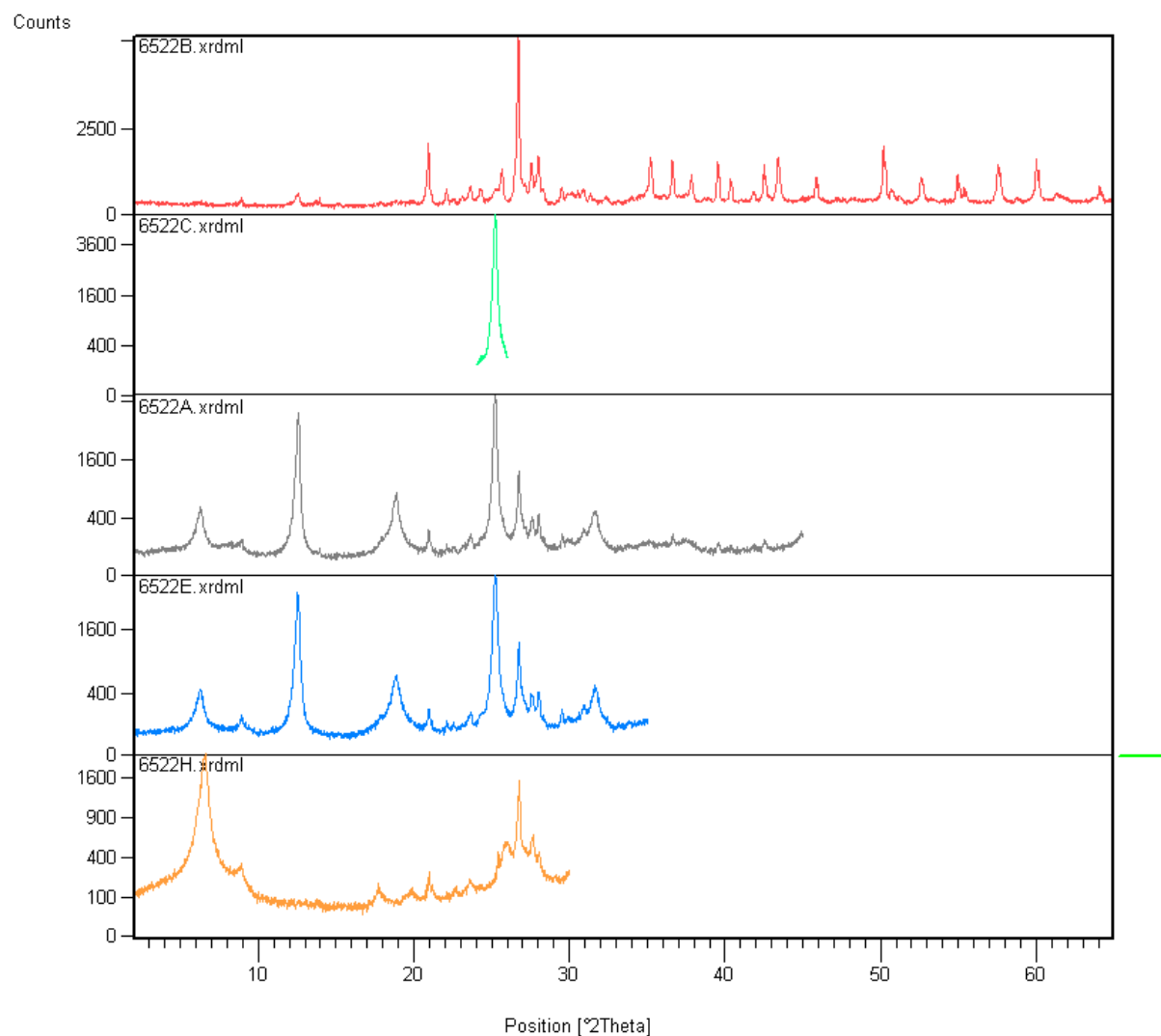












Appendix 1b – Excel spreadsheet of XRD data

XRD Bulk

[illegible]

XRD Clay Fraction

		Area of XRD diffractogram (calc by pseudo voigt function)						Area multiplied by weight factor					Relative percentage				
Well ID	Depth	XRD ID	Kaolinite	Chlorite	Illite	Smectite / IS	Sum	Kaolinite	Chlorite	Illite	Smectite / IS	Sum (wf)	Kaolinite	Chlorite	Illite	Smectite / IS	Total %
		D-Value	3.57	3.53	1	17		%	%	%	%		%	%			
		Weight factor	1	1	1	0.5							%	%	%	%	
7/11-8	3735.70	6441	0	12209	1533	0	13742	0	12209	1533	0	13742	0.0	88.8	11.2	0.0	100.0
	3736.70	6442	0	19249	2110	0	21359	0	19249	2110	0	21359	0.0	90.1	9.9	0.0	100.0
	4183.66	6449	0	34815	17823	0	52638	0	34815	17823	0	52638	0.0	66.1	33.9	0.0	100.0
	4186.70	6450	0	8890	0	0	8890	0	8890	0	0	8890	0.0	100.0	0.0	0.0	100.0
7/8-4	4191.85	6451	0	14705	12083	0	26788	0	14705	12083	0	26788	0.0	54.9	45.1	0.0	100.0
	3830.00	6477	0	45159	4074	0	49233	0	45159	4074	0	49233	0.0	91.7	8.3	0.0	100.0
	3834.00	6479	0	59436	43418	0	102854	0	59436	43418	0	102854	0.0	57.8	42.2	0.0	100.0
	3840.15	6481	0	21890	37604	0	59494	0	21890	37604	0	59494	0.0	36.8	63.2	0.0	100.0
6/3-1	3845.05	6483	0	40584	14020	617	55221	0	40584	14020	308.1	54912.5	0.0	73.9	25.5	0.6	100.0
	3855.05	6485	0	19619	87888	0	107507	0	19619	87888	0	107507	0.0	18.2	81.8	0.0	100.0
	3858.00	6486	0	67502	26050	0	93552	0	67502	26050	0	93552	0.0	72.2	27.8	0.0	100.0
	2197.65	6489	0	18360	2889	0	21249	0	18360	2889	0	21249	0.0	86.4	13.6	0.0	100.0
	2579.65	6490	46999.58	9626.42	15985	0	72611	46999.58	9626.42	15985	0	72611	64.7	13.3	22.0	0.0	100.0
	2582.65	6491	9473.64	4736.82	5344	0	19554.46	9473.64	4736.82	5344	0	19554.46	48.4	24.2	27.3	0.0	100.0
	3002.32	6495	17710.84	45542.16	10029	0	73282	17710.84	45542.16	10029	0	73282	24.2	62.1	13.7	0.0	100.0
	3011.35	6497	0	24815	29757	0	54572	0	24815	29757	0	54572	0.0	45.5	54.5	0.0	100.0
	3020.72	6499	18193.5	18193.5	4444	0	40831	18193.5	18193.5	4444	0	40831	44.6	44.6	10.8	0.0	100.0
	3028.77	6502	13914.9	17007.1	23169	0	54091	13914.9	17007.1	23169	0	54091	25.7	31.4	42.9	0.0	100.0
	3039.72	6504	0	4888	9212	0	14100	0	4888	9212	0	14100	0.0	34.7	65.3	0.0	100.0
	3042.65	6505	0	10094	32856	0	42950	0	10094	32856	0	42950	0.0	23.5	76.5	0.0	100.0
	3052.66	6507	0	4458	330	0	4808	0	4458	330	0	4808	0.0	92.7	7.3	0.0	100.0
	3060.65	6509	0	69273	6519	0	75892	0	69273	6519	0	75892	0.0	91.4	8.6	0.0	100.0
	3069.10	6511	0	3050	6619	0	9669	0	3050	6619	0	9669	0.0	31.5	68.5	0.0	100.0
	3079.05	6513	0	7621	28790	0	36411	0	7621	28790	0	36411	0.0	20.9	79.1	0.0	100.0
3085.00	6515	0	11972	7551	0	19523	0	11972	7551	0	19523	0.0	61.3	38.7	0.0	100.0	
3095.38	6517	0	12178	16176	0	28354	0	12178	16176	0	28354	0.0	42.9	57.1	0.0	100.0	
3105.65	6519	0	45458	2465	0	47923	0	45458	2465	0	47923	0.0	94.9	5.1	0.0	100.0	
3109.65	6520	0	61736	11249	0	72985	0	61736	11249	0	72985	0.0	84.6	15.4	0.0	100.0	
	3115.65	6522	0	51759	1460	0	53219	0	51759	1460	0	53219	0.0	97.3	2.7	0.0	100.0

Appendix II – Thin section analysis

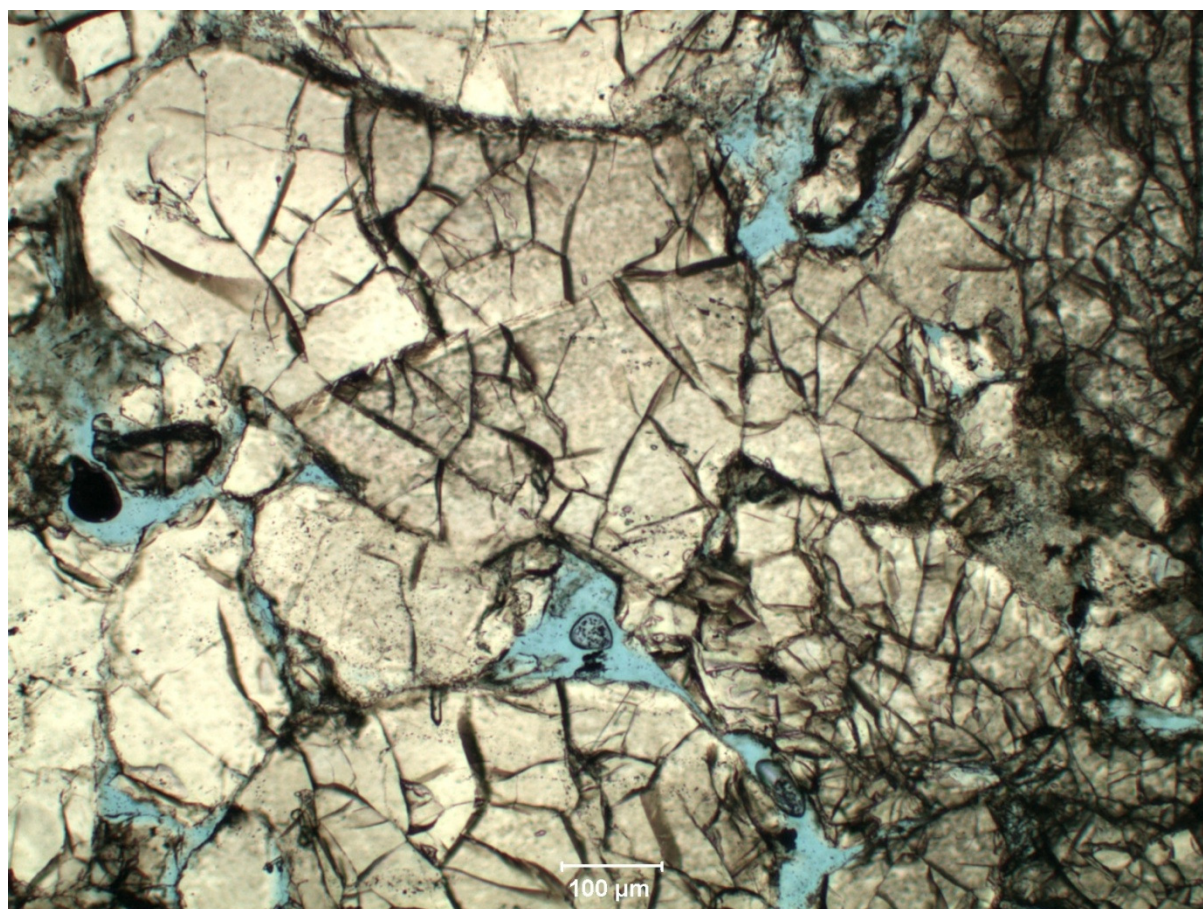
Well 6/3-1								
Formation	Depth (mRKB)	Lithology	BU?	Dominating framework connection	Average grain size (mm)	Most common grain shape	Sorting	Remarks
Intra Draupne Formation	2967.70	SS	BUA	Grain	Medium sand	Subangular	Good	Polycrystalline sutured quartz (Metamorphic source). Carbonate cement. Brittle grains. Undulose extinction quartz both metamorphic and magmatic source). Good porosity. Thin clay layer. 1,75mm largest grainsize
Intra Draupne Formation	2972.85	Shale	BUB	Matrix	Silt	Subrounded	Poor	Brown/grey colored. Microcline present. Dissolved K-spar. Polycrystalline sutured Quartz
Intra Draupne Formation	2977.65	SS	BUC	Matrix	Fine sand	Subangular	Moderate	K-feldspar and Quartz present. Poor porosity, extensive carbonate cemented
Skagerrak Formation	2979.65	SS	BUD	Grain	Coarse sand	Angular	Moderate	Polycrystalline sutured Quartz. Undulating extinction. K-feldsparspar. Dissolved plagioclase
Skagerrak Formation	2982.65	SS	BUE	Grain	Very fine sand	Subangular	Moderate	0,75 largest grainsize. 20% clay? K-spat-plagioclase. Quartz.
Skagerrak Formation	2987.40	Siltstone	BUF	Matrix	Silt	Subrounded	Poor	Feldspar, Qz, Silt beds. No porosity. Mica, undulose extinction, clay filled pores
Skagerrak Formation	2992.65	SS	BUG	Grain	Medium sand	Subrounded	Good	Brittle deformation. Good porosity. Some clay filled pores. Microcline/Qz. Polycrystalline Qz. Dissolved k-skar, qz overgrowth
Skagerrak Formation	2996.65	SS	BUH	Grain	Fine sand	Subangular	Moderate	Clay coating (chlorite?) Dolomite cemented, some brittle deformation, mica, good porosity
Skagerrak Formation	3002.32	SS	BUI	Grain	Fine sand	Subangular	Poor	Bad porosity, clay coating, perthite
Skagerrak Formation	3005.35	SS	BUJ	Grain	Very fine sand	Angular	Poor	Ripple structures. Organic material?. Clay oriented in one direction, qz
Skagerrak Formation	3016.77	SS	BUK	Grain	Medium sand	Subrounded	Good	
Skagerrak Formation	3020.72	SS	BUL	Grain	Medium sand	Subangular	Moderate	Arenite? Polycrystalline quartz, undulose extinction, Mica, Dolomite cemented? Dissolved K-spar. Large polycrystalline grains (Very coarse). Moderate porosity, little clay <5%, qz overgrowth
Skagerrak Formation	3023.42	SS	BUN	Grain	Fine sand	Subangular	Poor	Largest grain = 3mm, smallest = clay. Microcline, Polycrystalline Qz, Mica, Calcite/Dolomite cemented. Albite (multiple twinning). Undulose extinction in quartz. Some cemented areas some not. Poor porosity
Skagerrak Formation	3028.77	Siltstone	BUO	Grain	Silt	Subrounded	Poor	Laminated clay/silt, Qz, Dolomite cemented areas
Skagerrak Formation	3033.65	SS	BUR	Grain	Fine sand	Subangular	Good	Good porosity, cemented areas Calcite/dolomite?, plagioclase, microcline
Skagerrak Formation	3039.72	Siltstone	BUS	Matrix	Silt	Subangular	Moderate	Polycrystalline Qz, <5% clay. Dolomite cemented, plagioclase and microcline. Undulose extinction in Qz
Skagerrak Formation	3042.85	Shale	BUT	Matrix	Clay	Subrounded	Poor	Dolomite cemented, hematite present. Small dolomite crystals (near surface precipitated). Chert present, was opal c/5 -> fine grained
Skagerrak Formation	3047.65	SS	BUU	Grain	Fine sand	Subangular	Poor	Clay coating, mica, qz, k spar, clay >5%, poor porosity, microcline, plagioclase
Skagerrak Formation	3052.66	SS	BUV	Grain	Very fine sand	Subangular	Poor	Bad porosity, clay >5%, mica, one area very cemented (dolomite?)
Skagerrak Formation	3055.30	Shale	BUW	Matrix	silt/clay	Subangular	Poor	Bad porosity, brown stained, calcite/dolomite cemented?
Skagerrak Formation	3060.65	SS	BUX	Grain	Very fine sand	Subangular	Moderate	Chlorite coating(?), clay filled pore space, plagioclase and carlsbad twinning. Dolomite cemented?
Skagerrak Formation	3069.10	SS	BUY	Grain	Medium sand	Subrounded	Poor	Microcline, plagioclase (dissolved), perthite. Coarsest grain = 1.3mm. Locally cemented areas (qz?). Clay coating
Skagerrak Formation	3074.00	SS	BUZ	Grain	Fine sand	Subangular	Moderate	Bad porosity, mica, microcline, qz, plagioclase
Skagerrak Formation	3079.05	SS	BVA	Grain	Medium sand	Subrounded	Poor	Microcline, carb/dolomite cemented areas, polycrystalline qz, moderate porosity
Skagerrak Formation	3080.15	Siltstone	BVB	Grain	Silt	Subangular	Moderate	mica, largest grain = 0.25mm, no porosity
Skagerrak Formation	3085.00	SS	BVC	Grain	Fine sand	Subangular	Moderate	Clay coating, dissolved k spar (kaolinite?), undulose extinction, microcline, polyquartz
Skagerrak Formation	3090.16	SS	BVD	Grain	Fine sand	Subrounded	Moderate	Dissolved k-spar (kaolinite?) mica, perthite, poly qz, clay coating, subhedral grains, plagioclase, brittle deformed grains,
Skagerrak Formation	3095.38	SS	BVE	Grain	Very fine sand	Subrounded	Moderate	largest grain = coarse size, shale, silica cemented?, green mineral coating (chlorite?), bad porosity
Skagerrak Formation	3100.65	SS	BVF	Grain	Fine sand	Subangular	Good	mica, plagioclase, microcline, clay coating, moderate porosity
Skagerrak Formation	3105.65	SS	BVG	Grain	Medium sand	Subrounded	Good	good porosity, plagioclase, clay coating, mica, poly qz
Skagerrak Formation	3109.65	SS	BVH	Grain	Fine sand	Subangular	Moderate	undulose extinction, microcline, plagioclase, dolomite cemented areas, locally cemented areas (dolomite?). Grain with both carlsbad and microcline twinning
Skagerrak Formation	3115.65	SS	BVJ	Grain	Fine sand	Subangular	Good	Laminated mica bands. Quartz cement

Appendix IIb – Point counting

Point counting thin section										
Well 6/3-1										
IGV(volume %) = Vintergran										
Depth	ID	Quartz	Feldspar	Rock Fragment	Matrix	Calcite cement	Primary porosity	Quartz cement	Secondary porosity	IGV
2967.70	BUA	72	1,5	4	9	11,5	8,5	1,5	0	30,5
2977.65	BUC	60	1,9	0,4	34,3	0	0	2,4	1	37,7
2982.65	BUE	60,2	3,9	1,4	27,9	0	0,9	2,9	5	36,7
2992.65	BUG	75	3	2,5	5,5	2	7,9	3	3	21,4
3002.32	BUI	67	1,5	1,5	17,5	6	4	2	0	29,5
3005.35	BUJ	50,8	1,6	3,2	24,5	12,8	0	6,9	0	44,2
3020.72	BUL	66	1,4	2,3	7,6	16,7	3,8	1,9	0	30
3023.42	BUN	57	8	2,5	7	20,5	4	1	0	32,5
3039.72	BUS	23,3	1,9	0	1,9	69,6	1,4	0	1,4	74,3
3052.66	BUV	56	2	0	31,5	2,5	0	8	0	42
3060.65	BUX	73	2,5	1	15	6	2,5	0	0	23,5
3074.00	BUZ	72	5	2,5	13	0	4,5	3	0	20,5
3079.05	BVA	61,5	6,5	1	9,5	13	7	1,5	0	31
3085.00	BVC	63,5	7,5	6	14,5	0,5	6,5	1,5	0	23
3095.38	BVE	50,4	11,6	2,9	4,3	22,8	0,9	5,3	0	33,3
3105.65	BVG	61,2	2,9	2,9	9,8	2,4	10,2	7,8	5	35,2
3115.65	BVJ	47,5	6	0,5	30	2,5	1,5	11,5	1	46,5
3016,77	BUK	60,8	3,3	3,8	8,6	14	7,2	1,4	1	32,2

Well	Sample	Facies descriptio	Depth (mRKB)	Detrital framework grains			Matrix	Mica	Pore filling cement			porosity		IGV
				Quartz	Fld	RF			Qz (macro)	Aut clay	dolomite	Primary	Secondary	
7/11-8'	Tr1	MRB	3726,08	61,9	10,8	2,7	1,8	0,9	0,9	7,2	0	13,5	0,3	23,4
7/11-8'	Tr2	CSRB	3728,36	55,2	4,6	5,6	0	2,8	0,9	11,2	0	19,7	0	31,8
7/11-8'	Tr3	C-MRB	3735,7	56,7	10,4	2,6	2,2	0,6	6,4	0,6	0	18,5	2	27,7
7/11-8'	Tr4	MRB	3736,7	54,7	6,3	7,8	2,7	2,6	3,9	4,3	0	15,7	2	26,6
7/11-8'	Tr5	CSRB	3743,95	58,2	6,5	4,6	5,1	0,4	2,3	6,5	0	15,4	1	29,3
7/8-4'	TR8	Caliche	3825,6	-	-	-	-	-	-	-	100	-	-	-
7/8-4'	TR9	MGB	3831,25	47,1	10,3	8,4	3,1	2,8	8,4	6,6	0	11,3	2	29,4
7/8-4'	TR10	MGB	3831,6	56,9	7,9	3,4	3,7	5,5	8,3	2,7	2,7	8,3	0,6	25,7
7/8-4'	TR11	MGB	3832	51,3	7,8	2,9	5,8	12,7	2,9	4,9	3,9	6,8	1	24,3
7/8-4'	TR12	CRB	3845,65	53,2	8,9	5,8	7,3	0,9	9,2	5,4	0	8,3	1	30,2
7/11-9'	TR13	MGB	4183,66	58,7	7,9	0	26,8	1,1	2,9	1,1	0	1,5	0	32,3
7/11-9'	TR14	C-MGB	4186,7	45,3	4	0	42,7	1,6	2,4	0	3,2	0,8	0	49,1
7/11-9'	TR15	MGB	4191,85	54,4	9,2	0,9	0,4	1,8	1,8	10,1	17,5	3,9	0	33,7
7/11-9'	TR16	Caliche	4192,6	-	-	-	-	-	-	-	100	-	-	-

Appendix IIc – Bad thin section with extensive quartz fractures during preparation



Appendix III – Chlorite composition from SEM-SEI

3015,65mRKB		
1	(Mg _{1,86} , Fe _{2,40} , Al _{1,23}) (Al _{0,24} , Si _{3,76}) O ₁₀ (OH) ₈	
2	(Mg _{1,71} , Fe _{2,53} , Al _{1,52}) (Al _{1,05} , Si _{2,95}) O ₁₀ (OH) ₈	
3	(Mg _{1,94} , Fe _{2,54} , Al _{1,11}) (Al _{0,30} , Si _{3,70}) O ₁₀ (OH) ₈	
4	(Mg _{1,89} , Fe _{1,98} , Al _{1,72}) (Al _{0,90} , Si _{3,10}) O ₁₀ (OH) ₈	
5	(Mg _{1,60} , Fe _{2,13} , Al _{1,75}) (Al _{0,69} , Si _{3,31}) O ₁₀ (OH) ₈	
6	(Mg _{2,03} , Fe _{2,92} , Al _{0,95}) (Al _{0,77} , Si _{3,22}) O ₁₀ (OH) ₈	
7	(Mg _{2,16} , Fe _{1,59} , Al _{1,64}) (Al _{0,42} , Si _{3,58}) O ₁₀ (OH) ₈	
8	(Mg _{2,29} , Fe _{1,83} , Al _{1,53}) (Al _{0,81} , Si _{3,19}) O ₁₀ (OH) ₈	
9	(Mg _{1,96} , Fe _{2,27} , Al _{1,46}) (Al _{0,85} , Si _{3,15}) O ₁₀ (OH) ₈	
10	(Mg _{1,94} , Fe _{2,24} , Al _{1,47}) (Al _{0,75} , Si _{3,25}) O ₁₀ (OH) ₈	
11	(Mg _{1,63} , Fe _{2,96} , Al _{1,33}) (Al _{1,16} , Si _{2,84}) O ₁₀ (OH) ₈	
Avg	(Mg _{1,91} , Fe _{2,31} , Al _{1,43}) (Al _{0,72} , Si _{3,28}) O ₁₀ (OH) ₈	

3060,65mRKB		
1	(Mg _{1,28} , Fe _{3,26} , Al _{1,34}) (Al _{1,10} , Si _{2,90}) O ₁₀ (OH) ₈	
2	(Mg _{1,53} , Fe _{2,26} , Al _{1,75}) (Al _{0,83} , Si _{3,17}) O ₁₀ (OH) ₈	
3	(Mg _{1,59} , Fe _{2,08} , Al _{1,71}) (Al _{0,47} , Si _{3,53}) O ₁₀ (OH) ₈	
4	(Mg _{1,51} , Fe _{1,93} , Al _{1,85}) (Al _{0,44} , Si _{3,56}) O ₁₀ (OH) ₈	
5	(Mg _{1,53} , Fe _{2,54} , Al _{1,60}) (Al _{0,94} , Si _{3,06}) O ₁₀ (OH) ₈	
6	(Mg _{1,25} , Fe _{2,67} , Al _{1,49}) (Al _{0,30} , Si _{3,70}) O ₁₀ (OH) ₈	
7	(Mg _{1,10} , Fe _{2,05} , Al _{2,00}) (Al _{0,31} , Si _{3,69}) O ₁₀ (OH) ₈	
8	(Mg _{2,51} , Fe _{1,30} , Al _{1,60}) (Al _{0,41} , Si _{3,59}) O ₁₀ (OH) ₈	
9	(Mg _{1,34} , Fe _{2,35} , Al _{1,80}) (Al _{0,80} , Si _{3,20}) O ₁₀ (OH) ₈	
10	(Mg _{1,38} , Fe _{3,33} , Al _{1,18}) (Al _{0,98} , Si _{3,02}) O ₁₀ (OH) ₈	
11	(Mg _{1,63} , Fe _{1,88} , Al _{1,85}) (Al _{0,56} , Si _{3,44}) O ₁₀ (OH) ₈	
12	(Mg _{1,45} , Fe _{2,75} , Al _{1,52}) (Al _{0,95} , Si _{3,05}) O ₁₀ (OH) ₈	
13	(Mg _{1,72} , Fe _{2,25} , Al _{1,63}) (Al _{0,82} , Si _{3,18}) O ₁₀ (OH) ₈	
14	(Mg _{1,33} , Fe _{3,25} , Al _{1,21}) (Al _{0,79} , Si _{3,21}) O ₁₀ (OH) ₈	
15	(Mg _{1,61} , Fe _{1,90} , Al _{1,89}) (Al _{0,66} , Si _{3,34}) O ₁₀ (OH) ₈	
Average	(Mg _{1,52} , Fe _{2,39} , Al _{1,63}) (Al _{0,69} , Si _{3,31}) O ₁₀ (OH) ₈	

